UNIVERSITÉ SORBONNE PARIS CITÉ

Thèse preparée

à l'UNIVERSITÉ PARIS DIDEROT

École doctorale STEP'UP – ED 560

Laboratoire Astroparticule et Cosmologie (APC)

Antenna-Coupled LEKIDs for Multi-Band CMB Polarization Sensitive Pixel

Par

Alessandro Traini

Thèse de doctorat de l'USPC, specialité Physique de l'Univers
Dirigée par Michel Piat

Présentée et soutenue publiquement à l'APC (Université Paris Diderot) le
1 Octobre 2018

Devant un jury composé de :

Président du jury:	Alessandra Tonazzo, Professeur à l'Université Paris Diderot
Rapporteur:	Bruno Maffei, Professeur à l'Université Paris-Saclay
Rapporteur:	Mario Zannoni, Chercheur à l'Université Milano-Bicocca
Examinateur:	Andrea Catalano, Chercheur au CNRS (Grenoble)
Examinateur:	Hervé Geoffray, Ingénieur au CNES
Directeur de Thèse:	Michel Piat, Professeur à l'Université Paris Diderot

Résumé

La prochaine génération d'instruments pour l'observation de la polarisation du fond diffus cosmologique est partiulièrement exigeante en termes de nombre de détecteurs, de qualité de la mesure et d'efficacité de remplissage du plan focal. De plus, pour détecter les modes-B de polarisation provenant de l'inflation, il faut observer le ciel avec plusieurs bandes de fréquence afin de soustraire les avant-plans. Dans ce contexte, les détecteurs à inductance cinétique (KIDs) représentent une technologie très prometteuse en raison de leur grand facteur de multiplexage et de leur facilité de réalisation, tandis que le couplage avec une antenne peut fournir des solutions multi-bandes et double-polarisation dans un design compacte. Les KIDs à éléments localisés (LEKID) couplé à une antenne développé dans cette thèse sont sensibles à la polarisation avec deux sous-bandes à 140 GHz et 160 GHz chacune avec une bande passante de 10%. L'architecture proposée utilise une antenne à fente excitée par une ligne microruban et deux filtres passe-bande vers deux résonateurs. Ces derniers sont couplés capacitivement avec l'antenne et comprennent une ligne microruban en Aluminium comme absorbeur. Cette architecture est particulièrement simple à fabriquer, sans via et ne nécessite que de deux niveaux de métallisation. La transition ne nécessite aucun dépôt de diélectrique au-dessus du résonateur, évitant ainsi les limitations de toute source de bruit due au substrat non-monocristallin (TLS). En outre, la même technique de couplage peut être appliquée à de nombreux types d'antennes excitées par une ligne microruban, ce qui permet de s'adapter aux filtres passe-bande.

Mots clefs: détecteurs à inductance cinétique, supraconductivité, cosmologie

Abstract

Next generation telescopes for observing the Cosmic Microwave Background are demanding in terms of number of detectors and focal plane area filling efficiency. Moreover, foreground reduction in B-Mode polarimetry requires sky observation with multiple frequency bands. In this context KIDs are promising technology because of their large multiplexing rate, while antenna coupling can provide multi-band and dual-polarization solutions in compact design. The proposed polarization sensitive antenna-coupled LEKID is operating at 140 GHz and 160 GHz with a bandwidth of almost 10% for each sub-band. The design involves a microstrip excited slot antenna and two open-stub band-pass filters to direct the signal toward two resonators. These are lumped elements capacitively coupled to the antenna and include an Aluminium strip as absorber. The architecture proposed is particularly simple to fabricate, via-less and only involves two metallization levels. The transition does not require any dielectric deposition above the resonator, thus preventing limitations from any source of noise due to non-monocrystalline substrate (TLS). Furthermore, the same coupling technique can be applied to many types of microstrip excited antennas, which allow to accommodate band-pass filters.

Keywords: kinetic inductance detectors, superconductivity, cosmology

Acknowledgments

I wish to thank all the people who made the present work possible.

Firstly, I would like to thank Michel Piat, who gave me the opportunity to carry on this research on resonant detectors.

I would also like to express my appreciation to all members of the millimeter lab, I am grateful for having been part of such an enthusiastic group.

Thanks to Damien, Andrea and Guillaume, their assistance has been crucial for my work and I am indebted for their constant guidance.

I'm equally thankful to Yannick and Ken for their advice and assistance during these three years.

A special thanks goes to the APC students and postdocs who shared with me the PhD life: Pierros, Mikhail, Tuan, Thuong, Camille, Eleonora, Ranajoy, Cyrille, Calum, Maria and Donatella.

The present work couldn't be accomplished without the collaboration of the GEPI group at Paris Observatory. In particular, I would like to thank Faouzi, Samir and Christine for the time they spent with me and for teaching me the practices on microfabrication.

I am also grateful to Alessandro for his prompt support at Institut NEEL.

Lastly, I would like to thank my family for the endless support and encouragement.

Contents

Table of Acronyms

CEB: Cold-Electorn Bolometer

CMB: Cosmic Microwave Background

COBE: Cosmic Background Explorer

CSO: Caltech Submillimeter Observatory

FFT: Fast Fourier Transform

FEM: Finite Element Method

FIT: Finite Integration Technique

FP-7: Seventh Framework Programme

FWHP*:* Full Width to Half Power

HFSS: High Frequency Structural Simulator

KID: Kinetic Inductance Detector

LEKID: Lumped Element Kinetic Inductance Detector

MGEs*:* Maxwell's Grid Equations

MPI*:* Martin-Pupplet Interferometer

MoM: Method of Moments

NEP: Noise Equivalent Power

NIKA: Néel IRAM KIDs Array

PEC: Perfect Electric Conductor

PID: Proportional Integral Derivative

TE: Transverse Electric

TEM: Transverse Electromagnetic

TES: Transition Edge Sensor Bolometer

TM: Transverse Magnetic

TRL: Technology Readiness Level

VNA: Vector Network Analyzer

WMAP: Wilkinson Microwave Anisotropy Probe

Introduction

Kinetic Inductance Detectors (KIDs) are promising technology for future high-sensitive observational astronomy, with particular advantages for millimeter-wave and far infrared detection. Frequencies up to 600 GHz are of great interest for observing the Cosmic Microwave Background (CMB), which is the first light emitted after the Big Bang, and its polarization.

About 10% of the CMB signal is linearly polarized by Thomson scattering. As I will explain in Chapter 1, the polarization process requires a quadrupole distribution of matter, which might be generated by primordial gravitational waves originated during the inflationary epoch. These waves form tensor perturbations that imprint on CMB photons a special polarization pattern, called B-mode in analogy with electromagnetism, which is distinguishable due to their unique behavior under parity inversion. CMB polarization contains more information than the temperature anisotropy and B-mode detection would open a window to the inflationary epoch, occurred before recombination.

Currently, the sensitivity needed for B-modes detection is still unknown, with an upper limit set by data from Bicep2 experiment, Keck array and Planck. Since ongoing observations have already reached the photon noise limit, the instrument sensitivity can be improved by increasing the number of detectors on focal plane. The main goal for future CMB observatories (both ground and space based) is to push down the B-modes upper limit of about two orders of magnitude, which results in the technological challenge of implementing large detector arrays on focal plane. Furthermore, B-mode observation is limited by foreground contamination. Main sources of noises are gravitational lensing, synchrotron emission and thermal dust. Components separation requires observations with a wide spectral coverage, roughly between $40GHz - 600GHz$. These requirements lead to what is called CMB

"stage-4" for ground based projects, which demands large arrays containing about 10^5 detectors. Space observatories are necessary to fulfill the full spectral coverage, which is not observable from the ground due to the atmosphere opacity, setting some extra constraints in terms of weight and physical size of focal plane.

Next generation focal planes are oriented toward planar antenna-coupled detectors. Antenna-coupling is advantageous because it can provide multi-band and dual-polarization solutions in compact design: this kind of arrangement is particularly convenient for space based telescopes, where the mass and focal plane area is a constrain. I will illustrate in Chapter 2 some techniques commonly used in microwave engineering to process high frequency signals. Basic antenna properties and the dipole antenna I have used in this work are described in Chapter 3.

Kinetic Inductance Detectors are a very interesting alternative to bolometers. As described in Chapter 4, KIDs are LC resonators that exploit the kinetic inductance which arises from the two fluids model of superconductivity to detect photons. The basic idea is that a resonant circuit has a natural frequency which depends on the value of its capacitance C and inductance L. Under certain circumstances photons can be absorbed in the superconducting metal, altering the factor L of the circuit, and so change the natural frequency. Resonators are coupled to a readout line; a measure of the resonant frequency is directly proportional to the power absorbed in the circuit. The readout line provides a tone to the resonator and the measure is carried out by fast electronic at room temperature. A signal with multiple tones is used to read an array of several resonators in a multiplexed way. The multiplexing rate allows for using a single readout cable to measure the resonance of hundreds of detectors. This is a clear advantage compared to more common bolometers which require superconducting electronics (SQUIDs) working at low temperature for a lower multiplexing rate.

In order to shrink the pixel size it is common to develop lumped elements (LEKIDs) with a large capacitor. The latter can be implemented as a planar structure, like the interdigital capacitor. LEKIDs also have the advantage of a more uniform current distribution across the inductor. Despite the LEKID design can be polarization sensitive, each pixel is limited to one frequency band. Ground based experiments, for which the atmosphere allows few windows in the millimeter domain, can be upgraded time by time to detect different frequencies. Space observatories lack of

this feature and the multi-frequency design has to be implemented on pixel. For this reason the CMB community is currently focusing on antenna coupled KIDs. Cameras operating with antenna coupled bolometers are already active on ground based telescopes and we aim to recover the same sensitivity and performance with KID technology.

In this thesis I have developed an original architecture for coupling a lumped element KID with a microstrip excited antenna. In Chapter 5 I will discuss the simulated performance of each component. I have used full wave simulation software (CST Microwave Studio) to design a dual-resonant slot antenna, which is the receiver of the detection chain. The high frequency signal is then filtered on a diplexer that I have simulated with Sonnet Software. I have developed a microstrip-to-coplanar transition design to couple each filter with one resonator. Such a transition is the critical part of my work and it has been simulated with both CST and Sonnet. I have firstly considered the NIKA (New IRAM KID Array) pixel as a starting design of the LEKID geometry. I then adapted it to deal with all the requirements needed for the antenna coupling.

The fabrication of few demonstrators took place at Paris Observatory within a collaboration with the GEPI group. I did not actively participate in the fabrication process except for the design of the photomasks as described in Chapter 6.

I have arranged the setup of a cryostat at APC to test some demonstrators at low temperature in collaboration with the millimeter lab group members. In addition, the Institut NEEL in Grenoble provided the equipment for a full pixel characterization in terms of noise and spectral sensitivity. Experimental set up and measurements are discussed in Chapter 7.

Preliminary tests presented a number of unexpected features. I will discuss in Chapter 8 the development of a new optimized design according to these results. New demonstrators are currently under fabrication and will be tested both at APC and Institut NEEL.

During these three years I have also participated in the Cosmic Origin Explorer (COrE) collaboration. COrE was an ESA M5 proposal for a space based telescope dedicated to B-Modes observation [core-mission.org]. The focal plane of COrE consisted of more that 2000 detectors arranged in 19 frequency bands from 60 GHz to

600 GHz using KIDs as baseline technology. Unfortunately, the proposal has been rejected because the total cost of the mission was exceeding the given budget for a M5 mission. Nevertheless, new technological solutions for large focal plane arrays are currently under investigation and the CMB community is particularly active in KIDs development.

Chapter 1

Science Background

The Copernican system and the embrace of the heliocentric model during the XVI sec. started a scientific revolution in cosmology. After then and the first observations with the Galilean telescope in the XVII sec., astronomers become aware of the possibility to understand the laws that regulate the universe, its composition and evolution through time.

After the Newtonian description of gravity, cosmology were stuck on a stability problem. As Newton itself wrote in the second edition of *Principia Mathematica*, the universe must extend to infinity in all directions in order for the gravitational attraction to be uniform and null. Otherwise, the gravitational attraction between celestial bodies will eventually make the universe collapse.

Many cosmologists and mathematicians in the XVIII sec. started to take into account non-euclidean geometries to describe the universe [1]. Einstein was the first to link the geometry of space with gravity. He realized that light is bent under the effect of a gravitational field. To describe the space curvature under the effect of gravity Einstein consulted his mathematician friend Marcel Grossmann. The collaboration between the two led to the development of the general theory of relativity. Later in 1917 he published his model of a static and closed universe which aimed to solve the problem of Newtonian cosmology.

Since then, the technological advancements allowed astronomers to expand their knowledge to all the frequency spectrum. I will start this chapter by describing the historical steps which led to the Big Bang theory and modern cosmological models.

Then I will focus more on the Cosmic Microwave Background (CMB) science, which is the main motivation for the present work. I will illustrate the main open problems in cosmology and how the inflation theory may provide a solution to them. Current models can be validated experimentally with high sensitivity measurements of the CMB polarization. I will present an historical introduction on the CMB discovery, the current status of observations and the technological challenges we are facing for next generation CMB observations.

1.1 Expanding universe

The first evidence of the expanding universe was obtained in the early 1900 by Vesto Melvin Slipher from the Lowell Observatory in Flagstaff, Arizona. He was the first astronomer to detect celestial body spectra with enough signal-to-noise ratio for Doppler shift measurement [5]. He observed spectra for 25 spiral nebulae and discovered that four of these had a radial velocity toward the observer (blue-shifted), the others were receding from the observer (red-shifted). He calculated the recession speed in the range of $150-1100\ km/s$ [6]. The mean value he found was thirty times larger than the average velocity of the stars. This measure led to the *'island-universe'* hypothesis, in which spiral nebulae were distinct galaxies, not gravitationally bound to the Milky Way.

Later in 1920, the astronomer Edwin Hubble was working at the Mount Wilson Observatory in California, equipped with a 2.5 m telescope, the Hooker Telescope, which was the largest telescope in the word at that time. By taking advantage of the relationship between Cepheid variables luminosity and their pulsation period, Hubble calculated the distance of three nebulae observed by Slipher. He discovered that those objects were far away from the Milky Way, supporting the island-universe model.

Hubble also studied the relationship between the recession velocity and the distance form the observer. He estimated the distance for 24 extra-galactic nebulae for whom he knew the radial velocity. His measurement lead to a linear correlation between distances and velocities [7]. He also combined the nebulae into 9 groups according to proximity in direction and distance, finding again a linear correlation with distances (Figure1.1.1). Calling v the radial velocity and D the distance from the observer,

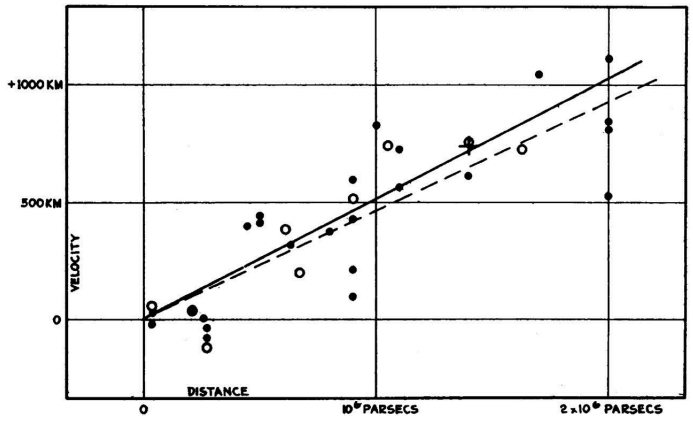

Figure 1.1.1: Plot published by Hubble in 1929 [7]. The full line represents the linear correlation between nebulae radial velocities (black dots) and their distance from the observer. The dotted line represents the linear correlation calculated from combining nebulae into groups (white disks).

we can write the *Hubble's law*:

$$v = H_0 D \tag{1.1.1}$$

where H_0 is known as the *Hubble Constant* and has the dimension of the inverse of time. The value of H_0 calculated form the Hubble plot was 500 $Km\,s^{-1}Mpc^{-1}$. Currently, the estimated value of H_0 is in the range of 68 $Km\,s^{-1}Mpc^{-1} \lesssim H_0 \lesssim$ 89 $Km\,s^{-1}Mpc^{-1}$ obtained from different methods and cosmological models [8].

It is notable that despite the universe is expanding, objects that are bound gravitationally, like galaxies in the local group, are not moving apart from each other. Thanks to local non-homogeneity of matter distribution and peculiar motions, gravitationally bound systems can interact and collapse into more massive systems and form the structures that we observe today. The expansion becomes homogeneous at large scale where these local irregularities can be neglected. Modern cosmology has adopted the so called '*Cosmological Principle*', which states that the properties of the universe at large scale are the same for every observer at any location. In other worlds, the universe is homogeneous and isotropic when the scale is large enough, and there is not any special location in the universe. Notice that isotropy implies homogeneity since we assume the universe to be isotropic for every observer, but a homogeneous universe can be anisotropic. Furthermore, the universe appears to be isotropic for every observer since we assume the observers to be in free falling [9].

1.2 Cosmological distances

We can parameterize the expansion of the universe by using a time-dependent *scale factor* $a(t)$ [10]. It relates the distances between any two objects taken at any moment in time with those taken at a reference time, that is arbitrarily chosen to be the present. In such a reference, the scale factor at t_0, the present epoch, is $a(t_0) = 1$. We call the distance of two objects *proper distance*. It changes during time due to the expanding universe. If we scale the proper distance by the scale factor, we obtain the proper distance $d(t)$ at time t. Calling d_0 the proper distance at $t = t_0$ we can write:

$$d(t) = a(t)d_0 \tag{1.2.1}$$

The recession speed of two galaxies is the derivative of their proper distance, so from 1.2.1 we can obtain:

$$\dot{d}(t) = \dot{a}(t)t_0 \tag{1.2.2}$$

Combining 1.2.1 and 1.2.2 we obtain:

$$\dot{d}(t) = \frac{\dot{a}(t)}{a(t)}d(t)$$

The latter is the Hubble law written as a function of the scale factor. We can infer the Hubble constant as:

$$H_0 = \frac{\dot{a}(t)}{a(t)} \tag{1.2.3}$$

In modern cosmology it is useful to use the *comoving distance*, the distance between two objects which remains constant at any time, thus comoving with the expansion. The comoving distance r can be calculated as:

$$r = \frac{d(t)}{a(t)} \tag{1.2.4}$$

1.3 Friedman models

We can write the metric of our universe by considering the spatial increment dl in polar coordinates (r, ϕ, θ) of a two dimensional space on a surface of a sphere. Along with the assumption an expanding, homogeneous and isotropic universe we obtain

the invariant interval [11, 12, 13]:

$$ds^2 = dt^2 - \frac{a^2(t)}{c^2}\left[\frac{dr_c^2}{1-kr_c^2} + r_c^2\left(d\theta^2 + sin^2\theta d\phi^2\right)\right] \tag{1.3.1}$$

where $k = 1/R_0$, with R_0 the radius of curvature of the universe at $t = t_0$, and $r_c = R_0 sin\,(r/R_0)$ being the comoving angular diameter distance. The metric in 1.3.1 is the *Robertson-Walker metric*[1]. The value of k determines the geometry of the universe. We can distinguish three cases:

- $k = 0$: the radius of curvature is $R_0 = \infty$ so the universe is flat (or Euclidean). In this case the shortest path between two points is a straight line. Two parallel lines never meet each other.

- $k > 0$: it corresponds to a closed (or spherical) universe. This geometry allows two parallel lines to converge at a certain point. The sum of the angles of a triangle is greater than 180 degrees.

- $k < 0$: it corresponds to an open (or hyperbolic) universe. In this case two parallel lines are always divergent. The sum of the angles of a triangle is lesser than 180 degrees.

Notice that the geometry of the universe in the Robertson-Walker metric changes as $a^{-2}(t)$ and the scale factor contains all the information about the expansion.

In order to have access to the dynamics of expansion we must solve the Einstein's field equations. The Robertson-Walker metric provides a solution to those as follows:

$$\ddot{a} = -\frac{4\pi G}{3}a\left(\rho + \frac{3p}{c^2}\right) + \frac{1}{3}\Lambda a \tag{1.3.2}$$

$$\dot{a}^2 = \frac{8\pi\rho G}{3}a^2 - \frac{c^2}{R_0^2} + \frac{1}{3}\Lambda a^2 \tag{1.3.3}$$

where ρ is the total inertial mass density of the matter and radiation in the universe, p its pressure and G the gravitational constant. Equations 1.3.2 and 1.3.3 are commonly called *Friedman's equation.* The 1.3.3 has the form of an energy equation and contains the *cosmological constant* Λ. The first term on the right side represents the gravitational potential energy of the expanding universe.

[1] *Also called Friedmann-Lemaitre-Robertson-Walker metric or FLRW.*

Since the total mass is conserved during the expansion, we can express ρ as a function of its value today ρ_0 and the scale factor as:

$$\rho = a^{-3}\rho_0 \tag{1.3.4}$$

assuming the volume $V \propto a^3$. Also, the total energy ε_t associated with the mass density can be written as $\varepsilon_t = \rho c^2$. With these assumptions, equation 1.3.2 can be inferred from the derivative of 1.3.3 by substituting $\dot{\rho}$ with the first law of thermodynamics in relativistic form written as follows:

$$\frac{d\rho}{da} + 3\frac{\left(\rho + \frac{p}{c^2}\right)}{a} = 0$$

Equation 1.3.2 has the form of a force equation and makes more evident the purpose of the cosmological constant. The first term on the right side has a negative sign, thus represents the total gravitational force that prevents the expansion. The second term on the right side contains Λ and has a positive sign. It represents the force involved on the expansion that keeps the universe from contracting due to gravitational interactions. The cosmological constant was firstly used by Einstein in 1917, before the Hubble discovery of the expansion. Einstein introduced Λ in an attempt to describe a model of static universe, which was widely accepted at that time.

Solutions of equation 1.3.3 are called *Friedman world models*. We can distinguish two cases: solutions where we consider $\Lambda = 0$, thus we do not take into account its repulsive effect, and solutions with $\Lambda \neq 0$. Today we link the cosmological constant effect with *dark energy*, the nature of which is still unknown.

Before we start studying the dynamics of Friedman's world models, it is better to introduce the *critical density* ρ_c and the *density parameter* Ω_M as follows:

$$\Omega_M = \frac{\rho_0}{\rho_c} = \frac{8\pi G\rho_0}{3H_0^2} \tag{1.3.5}$$

These quantities will be used to rewrite Friedman's equations in more useful form.

1.3.1 Dust

World model with $\Lambda = 0$ and $p = 0$ is called *dust*. With these assumptions and 1.3.5 Friedman's equations become:

$$\ddot{a} = -\frac{\Omega_M H_0^2}{2a^2} \tag{1.3.6}$$

$$\dot{a}^2 = \frac{\Omega_M H_0^2}{a} - \frac{c^2}{R_0^2} \tag{1.3.7}$$

where we have also assumed $\rho = \rho_0 a^{-3}$. The dust model is particularly friendly for calculating the spatial curvature k at the present epoch. Considering $t = t_0$, $a = 1$ and $\dot{a} = H_0$ we obtain from 1.3.7:

$$k = \frac{1}{R_0} = \frac{(\Omega_M - 1)}{(c/H_0)^2} \tag{1.3.8}$$

Depending on the value of Ω_M we get different dynamics:

- $\Omega_M < 1$: the universe is open and expands to $a = \infty$.
- $\Omega_M > 1$: the universe is closed and stops expanding when $a = a_{max}$ at the cosmic time $t_{max} = \pi\Omega_0 \left[2H_0 \left(\Omega_M - 1\right)^{3/2}\right]$. At time $t = 2\,t_{max}$ the universe collapse to the so called *Big Crunch*.
- $\Omega_M = 1$: it is often called *Einstein-De Sitter* model. The universe is flat and the expansion eventually stops at a certain cosmic time. The scale factor depends on t as $a = (t/t_0)^{2/3}$ where the current age of the universe is $t_0 = (2/3)\ H_0^{-1}$.
- $\Omega_M = 0$: the universe is open and the velocity of the expansion is constant. The current age of the universe is $t_0 = H_0^{-1}$. This model is called *Milne* model.

Different world model dynamics for some values of Ω_0 are shown in Fig. 1.3.1.

1.3.2 Effect of Λ on world models

The cosmological constant introduces a repulsive force on Friedman's equations that allows the universe to accelerate and contrasts the gravitational attractions at large scale. Despite its nature is still misunderstood, it can be represented as repulsion of the vacuum. Thus, we can associate to the cosmological constant a negative pressure

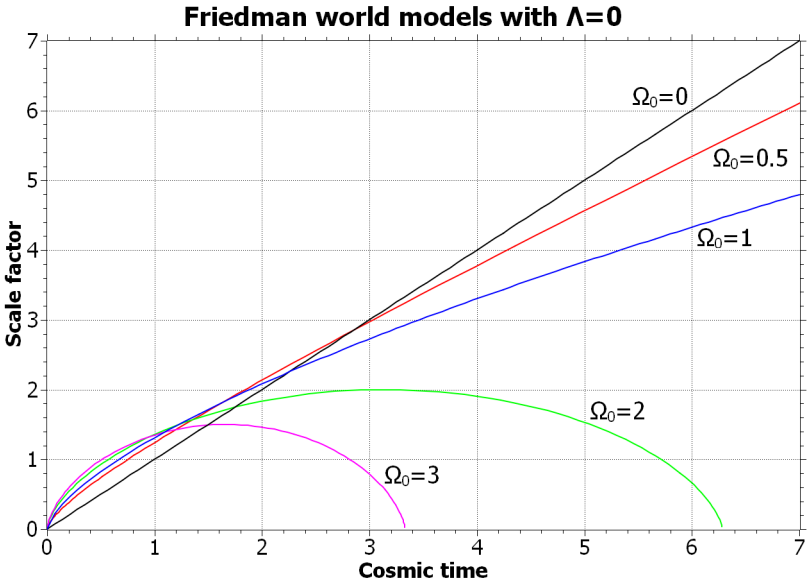

Figure 1.3.1: Plots of the scale factor with $H_0 = 1$. At the present age $a = 1$ and $t = t_0$, for different values of Ω_0 we obtain $H_0 t_0 = 1$ for $\Omega_0 = 0$, $H_0 t_0 = 2/3$ for $\Omega_0 = 1$, $H_0 t_0 = 0.57$ for $\Omega_0 = 2$ and $H_0 t_0 = 0.51$ for $\Omega_0 = 3$.

of the type $p_v = -\rho_v c^2$ with a constant[2] mass density ρ_v. As in the case of $\Lambda = 0$, it is convenient to introduce a density parameter Ω_Λ associated to dark energy. We assume again the dust model where the matter and radiation pressure p_m is null. In such a scenario the Friedman's equation can be written in the form:

$$\ddot{a} = -\frac{\Omega_M H_0^2}{2a^2} + \Omega_\Lambda H_0^2 a \tag{1.3.9}$$

$$\dot{a}^2 = \frac{\Omega_M H_0^2}{a} - \frac{c^2}{R_0^2} + \Omega_\Lambda H_0^2 a^2 \tag{1.3.10}$$

where the cosmological constant $\Lambda = 8\pi G \rho_v$ and the density parameter:

$$\Omega_\Lambda = \frac{8\pi G \rho_v}{3H_0^2}$$

We can infer the the effect of Λ on the curvature of the universe by considering equation 1.3.10 at the present age, thus substituting $a = 1$ and $\dot{a} = H_0$. We obtain:

$$k = \frac{1}{R_0^2} = \frac{[(\Omega_M + \Omega_\Lambda) - 1]}{(c^2/H_0^2)}$$

From the latter we obtain the condition $\Omega_{tot} = (\Omega_M + \Omega_\Lambda) = 1$ for a flat universe. Notice that the curvature of the universe is open in case of $\Omega_{tot} < 1$ and closed in

[2]It can be demonstrated from the first law of thermodynamics with the assumption of $V \propto a^3$.

case of $\Omega_{tot} > 1$.

World model dynamics with a non-zero cosmological constant have been particularly interesting since latest observations [14] reported $\Omega_\Lambda \neq 0$. We can summarize those models by setting $\ddot{a} = 0$ in 1.3.9 and substituting a_{min} into equation 1.3.10. We obtain:

$$\dot{a}^2_{min} = \frac{3H_0^2}{2}\left(2\Omega_\Lambda \Omega_M^2\right) - \frac{c^2}{R_0^2}$$

From this latter equation we distinguish three cases:

- $\dot{a}^2_{min} > 0$: the universe keeps expanding exponentially from a singularity. At large scale it has the dynamic of a *de Sitter* model.

- $\dot{a}^2_{min} < 0$: in those models the direction of expansion never changes, so the universe can follow two different branches. One where the expansion is not sufficient to prevent the universe to collapse, and the other where the universe keeps expanding. In every case there is no initial singularity and the universe *bounced* form the time at which $a = a_{min}$.

- $\dot{a}_{min} = 0$: the universe starts from a stationary value of a or tends to a constant value of a. This is know as the *Eddington-Lemaitre* model.

It is remarkable that we get different values of the age of the universe for different world models. Considering an empty universe, t_0 is simply obtained from the inverse of the Hubble constant. When the cosmological constant is included, t_0 can be larger than H_0^{-1} depending on the value of Ω_Λ.

The first evidence for dark energy was found in 1998 by the *Supernova Cosmology Project* [15] and the *High-z Supernova Team* [16] that lead to a Nobel prize in 2011. The value of Ω_Λ was inferred from the relationship between the magnitude of type Ia Supernovas and their redshift z. Fig. 1.3.2 shows the plot of the Ω_M, Ω_Λ joint confidence intervals. For a flat universe, they found $\Omega_M = 0.28^{+0.09}_{-0.08}$ with $\Omega_\Lambda = 1 - \Omega_M$. Even with no assumption about the spatial curvature, they found $\Omega_\Lambda > 0$ at the 99.7% confidence level. Furthermore, both groups agreed on a negative deceleration parameter:

$$q_0 = -\left(\frac{a\ddot{a}}{\dot{a}^2}\right)_{t_0} = \frac{\Omega_M}{2} - \Omega_\Lambda$$

indicating that the expansion of the universe is accelerating.

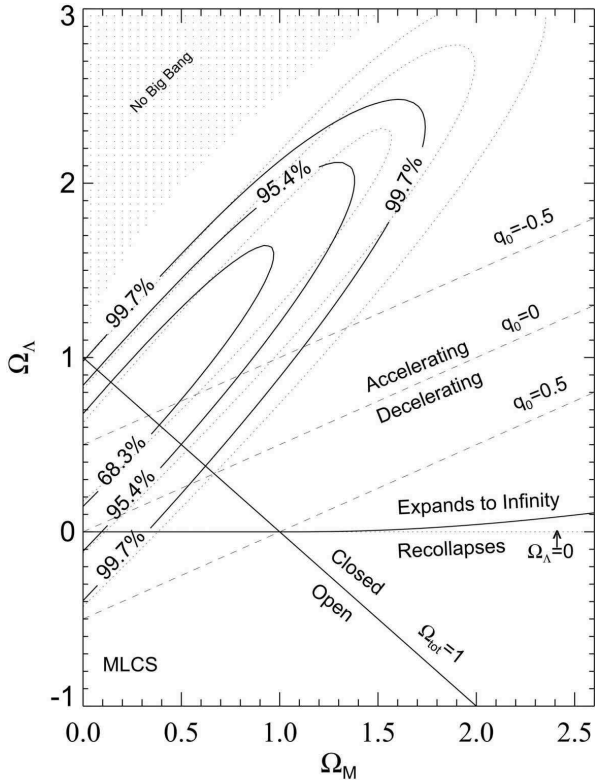

Figure 1.3.2: Joint confidence intervals for $(\Omega_M, \Omega_\Lambda)$. The dotted contours don't take into account unclassified objects SN 1997ck ($z = 0.097$) [16].

1.4 Thermal history of the universe

The expanding universe argument suggests that at some point in the past the scale factor must be zero and the density diverges in what is called the initial *singularity*. That moment is known as the *Big Bang*. Conditions at this point in time are so extreme that physical laws as we know might be not valid anymore and quantum effects apply on cosmological scales [17]. The thermal history of the universe gives us a picture on how galaxies and large scale structures have formed. Key events are shown in Tab. 1.4.1:

- $t < 10^{-6}\ s$: the physics of very high energy ($> 1\ GeV\ \sim 10^{13}\ K$) is is not well established to characterize the very early universe. The universe experienced an exponential expansion associated to an unknown scalar field. This event, called *inflation*, will be discussed more in detail later in this chapter. An extension of the standard model predicts symmetry-breaking transitions [19] all over this period. The asymmetry between matter and anti-matter that we observe today has its origin during the *Baryogenesis*, which is a mechanism

Event	time t	redshift z	temperature T
Inflation	10^{-34} s (?)	–	–
Baryogenesis	?	?	?
EW phase transition	20 ps	10^{15}	100 GeV
QCD phase transition	20 μs	10^{12}	150 MeV
Dark matter freeze-out	?	?	?
Neutrino decoupling	1 s	6×10^9	1 MeV
Electron-positron annihilation	6 s	2×10^9	500 keV
Big Bang nucleosynthesis	3 min	4×10^8	100 keV
Matter-radiation equality	60 kyr	3400	0.75 eV
Recombination	260–380 kyr	1100–1400	0.26–0.33 eV
Photon decoupling	380 kyr	1000–1200	0.23–0.28 eV
Reionization	100–400 Myr	11–30	2.6–7.0 meV
Dark energy-matter equality	9 Gyr	0.4	0.33 meV
Present	13.8 Gyr	0	0.24 meV

Table 1.4.1: Time scale and energy involved for some main events according to the Big Bang theory. Table credit to Daniel Baumann [18].

still not completely understood. The Higgs mechanism becomes effective at $E \sim 100\ GeV$ [18], this event is referred as the *electroweak phase transition*.

- $t \sim \mu s$: at energies of 200 MeV quarks are confined into hadrons. Three quark systems form baryons (like protons) and quark-antiquark pairs form mesons (like pions). In this stage, called *QCD phase transition*, the universe is a hot plasma of nucleons, leptons, pions, their associated neutrinos and photons.

- $t < 1\ s$: when temperature drops to $T < 10^{11}\ K$, muon neutrinos (ν_μ, $\bar{\nu}_\mu$) decouple from the plasma and expand freely, interacting only through weak interaction. Below $10^{11}\ K$ protons are more numerous than neutrons.

- $t \sim 6\ s$: electron-positron annihilation starts. The energy released is only transferred to photons and ν_e, $\bar{\nu}_e$ neutrinos decoupled. For that reason today we observe a photon temperature greater than neutrino temperature. The reduction of e, $\bar{e}$ freeze the n/p ratio since reactions $n + \nu_e \leftrightarrow p + e$ and $n + \bar{e} \leftrightarrow +\bar{\nu}_e$ loose efficiency.

- $t \sim 3\ min$: *nucleosynthesis* started forming some ionized elements like helium and deuterium from protons and neutrons. Neutral atoms became to form while the temperature decreased.

- $t \sim 10^5\ years$: This is the epoch of *recombination*. The reaction $H + \gamma \rightarrow e^- + p$ becomes inefficient, thus, while forming neutral atoms, the number of free electrons decreases drastically as well as the efficiency of Thomson scattering with photons. Therefore, the universe became transparent to photons, which are observed today as the Cosmic Microwave Background.

The epoch of recombination is of great interest for observational cosmology. It is notable that at redshift $z \approx 1500$ the CMB temperature was about $T = \approx 4000\ K$, well below the $1.5 \times 10^5\ K$, corresponding to $h\nu = hT = 13.6\ eV$, necessary to ionize neutral hydrogen. Despite that, the number of photons is several order of magnitude greater than the number of hydrogen atoms. Thus, photons in the Wien region of the spectrum are enough to ionize the gas. It can be found that $T \approx 5600\ K$ is a temperature high enough to largely ionize the intergalactic gas. Considering the present CMB temperature of $2.72\ K$, the universe became ionized at redshift $z \approx 2000$ which corresponds to a scale factor $a \approx 2.72/5600 = 5 \times 10^{-4}$.

1.5 Inflation

Physics before the electron-positron annihilation phase is quite speculative. The standard model of Big Bang cosmology described by the Robinson-Walker metric has a singularity at $t = 0$ where $T \to \infty$. Alan Guth firstly proposed in 1980 [25] the inflation theory for which the universe experienced an exponential growth at its very beginning. This period of time takes the name of *inflationary epoch*, the existence of which may explain three cosmological problems.

Flatness problem

As we have seen in previous sections, considering the scale factor $a = (1+z)^{-1}$, the Hubble's constant varies with redshift as

$$H(z) = \frac{\dot{a}}{a} = H_0 \left[(1+z)^2 (\Omega_0 z + 1) - \Omega_\Lambda z (z+2) \right]^{0.5}$$

and so the density parameter 1.3.5

$$\Omega_M = \frac{8\pi G}{3H_0^2} \rho_0 (1+z)^3 = \frac{\Omega_0}{\left[\frac{\Omega_0 z + 1}{1+z} \right] - \Omega_\Lambda \left[\frac{1}{(1+z)} - \frac{1}{(1+z)^3} \right]} \tag{1.5.1}$$

At large redshift, or $z \gg 1$, the first square bracket in the denominator of 1.5.1 tends to Ω_0, and the second square bracket tend to zero. Consequently, we obtain $\Omega_M \to 1$ regardless of the value of Ω_0 we measure at present time. The dark energy contribution can be neglected at large redshift due to their large different dependence on redshift. We then rewrite 1.5.1 as follows

$$\left(1 - \frac{1}{\Omega_M} \right) = (1+z)^{-1} \left(1 - \frac{1}{\Omega_0} \right)$$

which tell us that if $\Omega_0 \neq 1$ in the past, it must be different from 1 at present time. This property requires a fine tuning of the value Ω_M in the early epoch to result in $\Omega_0 = 1$. The consequent flatness of the early universe is called the *flatness problem*, since there is nothing in the standard model that would require any particular value of Ω_0. The fine tuning is more pronounced including a non-zero cosmological constant [26]. Considering a reference model with $\Omega_\Lambda = 0.7$ and $\Omega_M = 0.3$, we obtain $\Omega_M = 0.999999996$ at $z = 1000$.

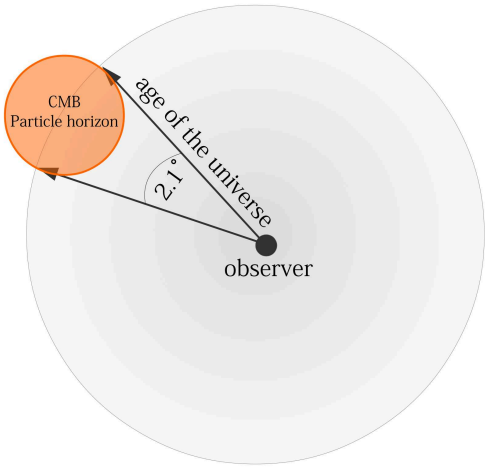

Figure 1.5.1: Particle horizon at the time of CMB formation has an angular size of 2.1° on the sky, which is in contrast with the CMB uniformity we measure today.

Horizon problem

Two points in space-time are said in causal contact if they are close enough to communicate with light signals. Considering an observer at point O in space, the set of points causally connected to O are within a sphere of radius R_h. Because of the universe expansion, the radius is time-dependent. In other words, any light signal received by O at time t must have been emitted at time t' with $0 < t' < t$. The radius R_h can be then calculated as

$$R_h(t) = a(t) \int_0^t \frac{cdt'}{a(t')}$$

which diverges at $a \to 0$ since the observer at the initial singularity is in causal contact with the whole universe. The radius R_h take the name of *particle horizon*. It is remarkable that the recession speed can be greater than the speed of light but if two points were causally connected in the past, they will remain connected forever. This is not the case when considering the Hubble sphere, for which objects located at the sphere border are moving at the speed of light with respect to the center. The existence of a particle horizon rises a question about the structures we observe today on the CMB. Those larger than R_h at the time of CMB formation should be causally disconnected as shown in Fig. 1.5.1. Considering the same reference model discussed in the flatness problem, at $z \approx 1000$ the angular size of the particle horizon is $\theta_h \approx 2.1°$, so regions separated by more than one degree on the CMB sky

are casually disconnected, but the CMB sky is uniform to a precision of 10^{-5}.

Monopole problem

This problem arises from the grand unified theories (GUT). As the universe expanded and cooled, the GUT scalar filed symmetry broke at $T \approx 10^{16}\ GeV$, leaving the field into a particular configuration. This scenario is analogous to that of the magnetism. When molecules are cooled down to a certain critical temperature the magnetic moments align with those of their neighbours. Similarly, when the GUT field freezes, it points to a particular direction like a monopole. The scalar field must be uncorrelated at distances larger than the particle horizon. Thus, if monopoles did not annihilate with each other, their number density would be one monopole per nucleon at present time, enough to dominate the energy density of the universe. This contradiction is known as the *monopole problem*.

Solution

The inflation theory provides an answer to all of these open questions. An inflationary expansion can be described as a universe with a cosmological constant. In such a case the Friedmann equation becomes

$$H^2 = \frac{8\pi G}{3}\rho - \frac{k}{a^2} + \frac{\Lambda}{3} \tag{1.5.2}$$

The first two terms of 1.5.2 become negligible as the expansion proceed while the last term remains constant. Thus, after a while, we can write

$$H^2 = \frac{\dot{a}}{a} = \frac{\Lambda}{3}$$

which has an exponential solution of type

$$a = e^{Ht}$$

As said before, the inflation come from a hypothetical scalar field that permeate the universe. The particle associate to such a field is called *inflaton*, and so the field *inflaton field*. The inflation mechanism is speculative, more details can be found in

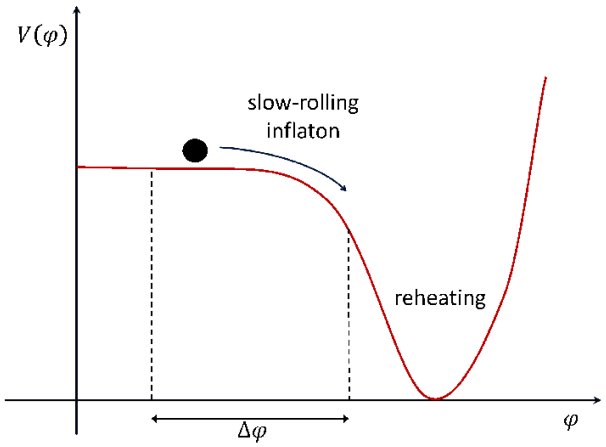

Figure 1.5.2: Example of inflaton potential well with a flat region. After a slow-rolling phase the field oscillates around the minimum and decay in other particles. Credit to [28].

literature. In few words, the potential energy $V(\phi)$ associated to the scalar field ϕ might be time dependent. In this scenario, at the very early epoch $V(\phi)$ is at its minimum. As the universe expands and cools down, the position of the minimum shift and the universe settle to the new minimum as shown in Fig. 1.5.2. The energy released is proportional to ΔV. Another possible scenario involves the inflaton to cross a potential barrier through quantum tunnel in order to find a deeper minimum. This is the case of the universe in a *false vacuum*. We don't know the shape of the potential, but after some time, the inflation must come to end. The inflation phase allows the universe to be in thermal contact in the early epoch, and so solves the horizon problem. Similarly, the huge expansion would have dilute any topological defect, like the monopoles, by a factor e^{300}, thus solving the monopole problem. Moreover, the expansion is so quick that we are unable to see the curvature of the space. During the inflation the scale factor increases exponentially but the energy density of the universe remains constant. Since

$$|\Omega_{tot}(t) - 1| = \frac{|k|}{a^2 H^2}$$

the inflation pushes the value of Ω_{tot} to the unity with an accuracy of many decimal place, thus solving the flatness problem.

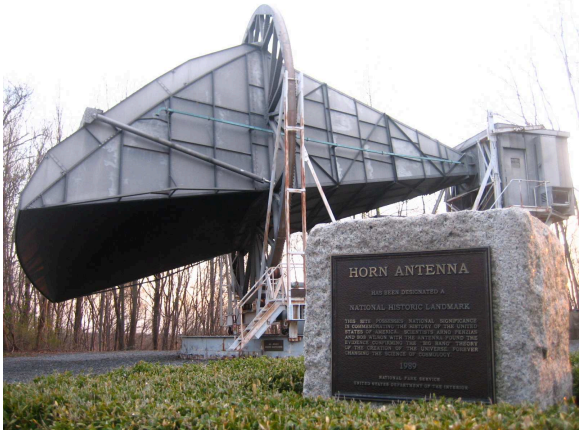

Figure 1.6.1: Original horn antenna used by Penzias and Wilson to characterize the excess noise then recognized as CMB signal. Source: Wikipedia

1.6 Cosmic Microwave Background

1.6.1 Origin

As the universe cooled down with the expansion, photons lost energy until a moment they decoupled from matter and traveled free throughout the universe. The last scattering surface represents the boundary between the opaque and transparent universe to light. Therefore, it sets a limit on observations through electromagnetic signals. The surface of last scattering originated at that particular distance (about 6000 $h^{-1}Mpc$) for which photons have reached us today. The universe is filled with CMB photons with a density of $n_\gamma = 3.7 \times 10^8\ m^{-3}$ and observers in different parts of the universe would see the surface of last scattering with the same radius but centered on their location. The Cosmic Microwave Background was incidentally discovered in 1964 by two radio astronomers at the Bell Telephone Laboratories, Arno Penzias and Robert Wilson, working on a 6 meter horn antenna in New Jersey. They measured an excess isotropic noise at 4080 MHz with a correspondent residual temperature of $3.5 \pm 1.0\ K$ [20]. At the same time, Robert H. Dicke, Jim Peebles, and David Wilkinson were building their own radiotelescope searching for the CMB when they heard about the noise problem of Penzias and Wilson. The two groups published a paper in 1965 [21] explaining the noise problem as a CMB measurement. Penzias and Wilson shared the 1978 Nobel prize in physics for their discovery.

In the early universe photons were created and absorbed continuously, so they were in thermal equilibrium with the environment. As a consequence, the universe was an

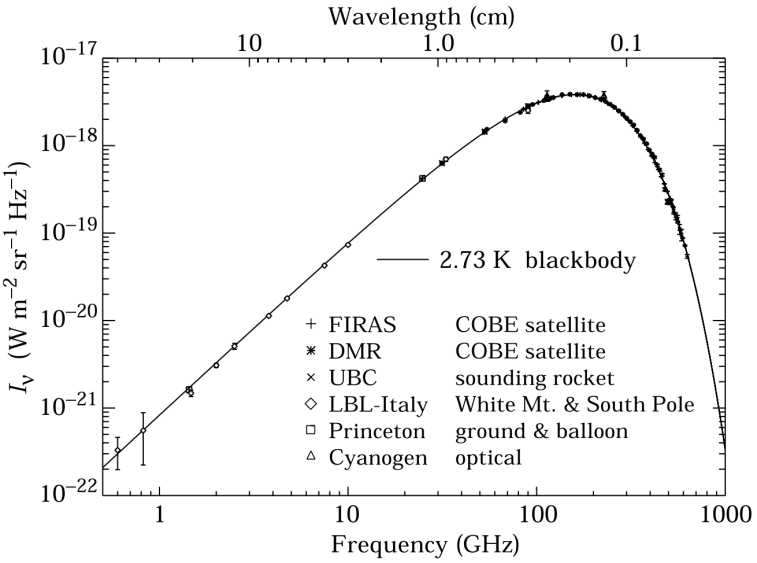

Figure 1.6.2: Black body spectrum of the CMB calculated with different telescopes. Credit: C. Caso et al. (Particle Data Group), The European Physical Journal C3 (1998) 1.

almost perfect black body, for which the intensity I_ν as a function of temperature is given by the Planck's law:

$$I_\nu(T) = \frac{2h\nu^3}{c^2} \frac{1}{\exp\left(\frac{h\nu}{k_B T} - 1\right)} \tag{1.6.1}$$

Since its discovery, the CMB intensity has been measured with several instruments including three space telescopes:

1. **Cosmic Background Explorer** (COBE): lunched in 1989 with three instruments (DMR, FIRAS and DIRBE) [22]. The mission is often referred as the beginning of the precision cosmology era and led to the 2006 Nobel prize in physics shared with George Smoot and John Mather.

2. **Wilkinson Microwave Anisotropy Probe** (WMAP): lunched in 2001, it includes five separate frequency bands from 22 to 90 GHz [23].

3. **Planck**: lunched in 2009 with two instruments (LFI and HFI) both sensitive to polarization in nine frequency bands from 30 to 857 GHz [24].

The inferred spectrum in Fig. 1.6.2 is the best black body source ever measured with a temperature $T = 2.72\ K$. Despite the cosmological redshift, the black body curve has the characteristic of maintaining the shape regardless of the expansion. This can

be demonstrated by substituting $\nu' = \nu_0/(1+z)$ in the Planck's law 1.6.1, so that

$$I(\nu', T)\frac{d\nu'}{(1+z)} = \frac{2h(1+z)^3}{c^2}\frac{(\nu')^3}{\exp\left(\frac{h\nu'(1+z)}{k_B T} - 1\right)}\frac{d\nu'}{(1+z)}$$

Since the temperature has the same variation with z, in other words $T' = T_0(1+z)$, we obtain

$$I(\nu', T)\,d\nu' = \frac{2h(1+z)^3}{c^2}\frac{(\nu')^3}{\exp\left(\frac{h\nu'}{k_B T'} - 1\right)}d\nu'$$

which has exactly the same form of 1.6.1. Nevertheless, the energy density decreases with time by a factor $j' = j(i+z)^{-4}$ since the wavelength decreases by a factor $(1+z)$ and the volume by a factor $(1+z)^3$. Recalling the Stefan-Boltzmann law

$$j = \sigma T^4$$

we obtain

$$T_{CMB} \propto (1+z)$$

The last scattering surface is not generated instantaneously but is rather a transition that corresponds to a redshift interval of $\Delta z \approx 195$. Therefore, the CMB is a layer of a comoving radial distance of about $\Delta r = 42 Mpc$.

1.6.2 CMB anisotropies

Despite the great sky uniformity, quantum fluctuations occurred at the very early epoch. These generated small density fluctuations which, along with the cosmic expansion, led to the structure we observe today. These primordial anisotropies, thus, are of great interest in cosmology and can be observed in terms of temperature fluctuation on the CMB. Fig. 1.6.3 shows the improvement in terms of angular resolution from COBE mission ($> 7°$) to WMAP ($> 0.3°$) and Planck ($> 0.05°$), for which the measured $\Delta T/T \approx 10^{-5}$. Anisotropies on the CMB are caused by three effects [29]:

- The **gravitational redshift** of photons from within the density fluctuations at the last scattering surface. This effect was firstly described by Sachs and Wolfe in 1967. Photons from high-density regions at last scattering experience

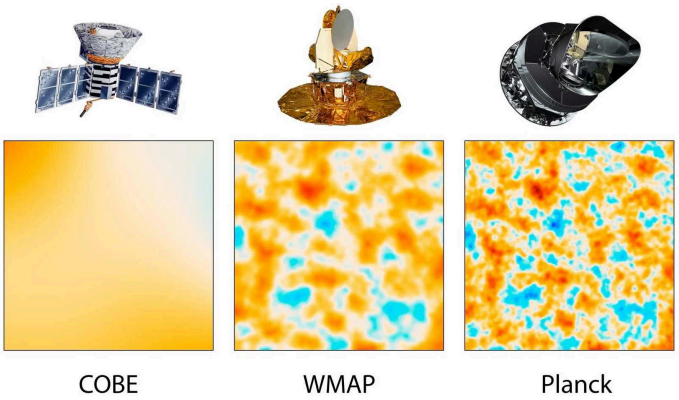

Figure 1.6.3: Evolution in angular resolution of satellite instruments. Source: Wikipedia.

a stronger gravitational field, and are thus redshifted more than photon in low-density regions.

- **Adiabatic perturbations**. In high density regions radiation and matter are more compressed, resulting in higher temperature.

- **Doppler perturbations**. Velocity of plasma at recombination leads to Doppler shift, increasing the temperature.

All of these effects are called *primary anisotropies*, to be distinguished from the *secondary anisotropies* which did not generate at the time of recombination but by all sort of scattering along the line of sight. Temperature fluctuations are projected on the CMB sphere, thus it is convenient to use a spherical decomposition. Angular scales on the sky can be characterized by spherical harmonics $Y_{lm}(\theta, \phi)$ so that

$$\frac{\Delta T}{T}(\theta, \phi) = \sum_{l=0}^{\infty} \sum_{m=-l}^{m=l} a_{lm} Y_{lm}(\theta, \phi)$$

with l being the multipole and $a_{lm}$the fluctuation amplitude coefficient. Fig. 1.6.4 shows graphically the relationship between l and the angular scale. For a given multipole l the size s of a spot in the sky is approximately

$$s \approx \frac{180^\circ}{l}$$

The inflation theory predicts the coefficients a_{lm} to be Gaussian distributed, for which the mean value is null. In this scenario we can introduce the angular power

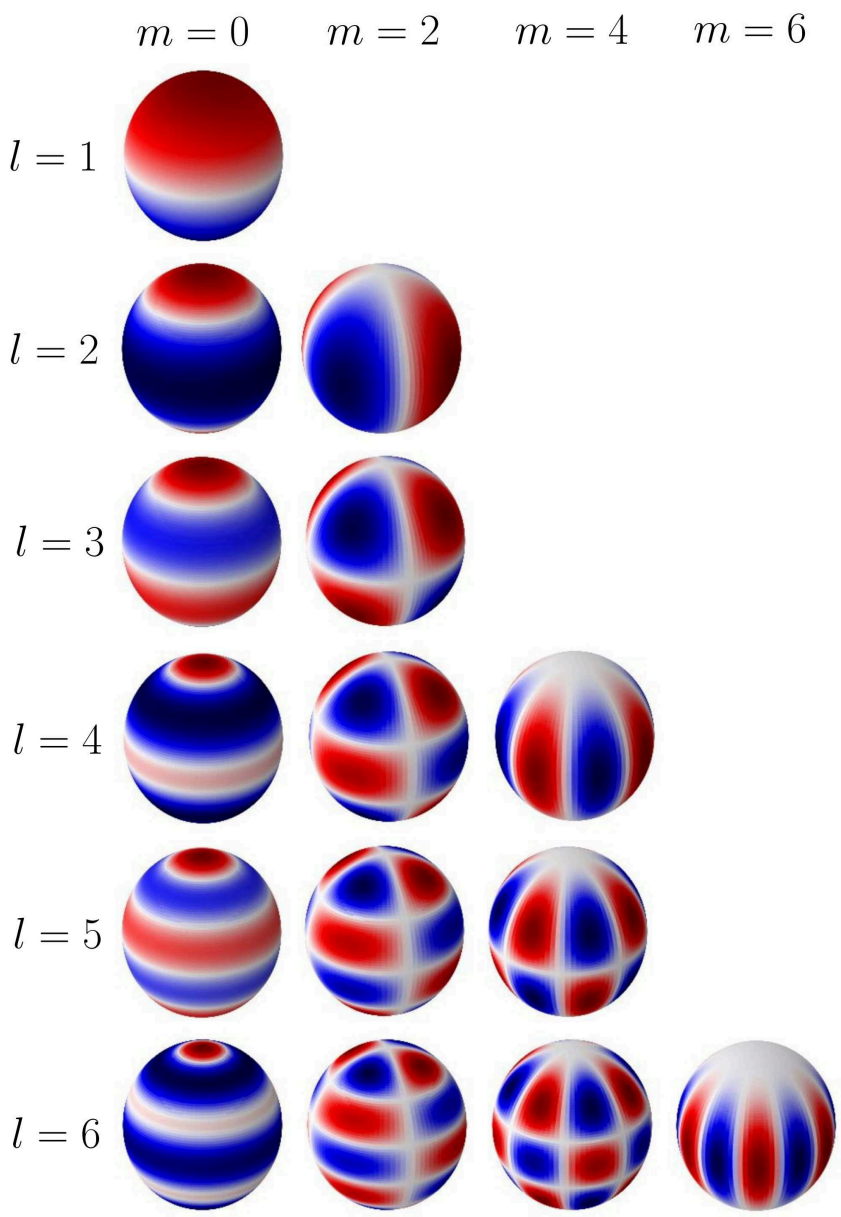

Figure 1.6.4: 3D representation of some multipole components from $l = 1$ to $l = 6$. The angular scale on the sky increases inversely with the multipole order.

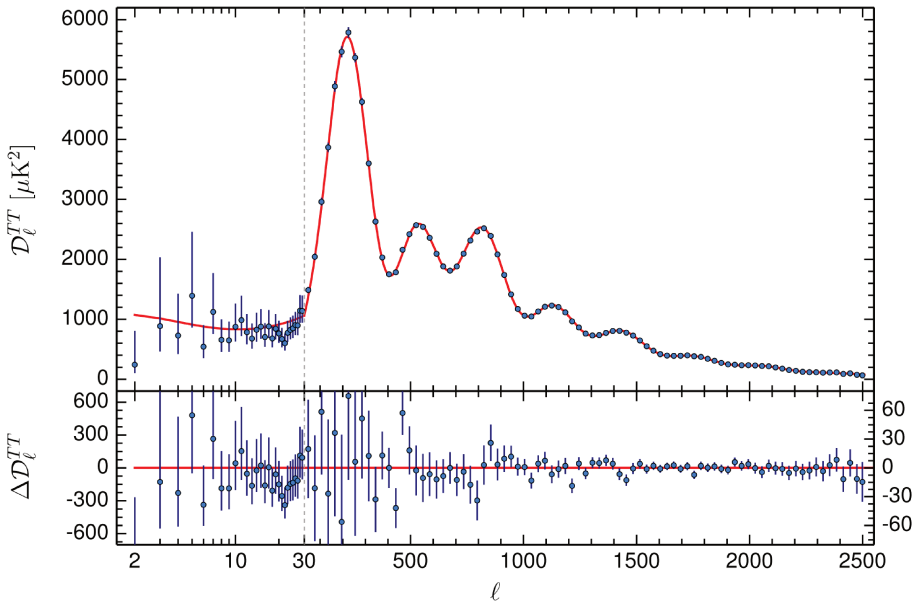

Figure 1.6.5: CMB temperature power spectrum. It is noticeable the effect of cosmic variance at low l and the acoustic peaks. Credit to Planck 2015.

spectrum with a set of coefficient C_l defined as

$$\langle a_{lm} \cdot a^{\star}_{lm} \rangle = C_l \delta_{ll'} \delta_{mm'}$$

The observed power spectrum would be of the form

$$C_l = \frac{1}{2l+1} \sum_{m=-l}^{l} a_{lm} a^{\star}_{lm}$$

The CMB temperature power spectrum is shown in Fig. 1.6.5. Quantum fluctuation from the early epoch generated gradients in density of matter. While the gravity contracts the high density regions, the pressure due to radiation counteracts the compression, resulting in an oscillating region which takes the name of acoustic oscillation. Compressed regions are hotter compared to low density regions. The acoustic oscillation frozen during recombination producing peaks on the temperature power spectrum. These are called *acoustic peaks*. The main features we observe on the temperature power spectrum are the following:

- Value of $l = 1$ corresponds to a dipole pattern in the sky. This is not related to intrinsic CMB properties but rather on the Earth motion relative to it. The dipole is used to infer some parameter like the sun motion around the galaxy and the sun velocity. Therefore, the temperature power spectrum is usually

plotted starting from $l = 2$.

- The error bar increases at small scale due to the cosmic variance. It arises from the fact that there are only $(2l + 1)\, m$ samples at fixed l. The precision limit set by the cosmic variance is given by

$$\Delta C_l = \sqrt{\frac{2}{2l+1}} C_l$$

- The position of the first peak is an indicator of the space curvature. Measurements suggest the peak to be located at $l = 200$, which is consistent with a flat universe.

- Higher peaks give information about the presence of dark baryon and cosmological parameters like Ω_B and Ω_M.

- Photons started to diffuse as the universe becomes transparent to radiation. This diffusion dumped perturbations smaller than the thickness of the last scattering layer. The process is know as *Silk damping* and suppresses or smooths peaks above $l = 500$.

1.6.3 CMB polarization

About 10% of CMB photons are linearly polarized by Thomson scattering. These photons contain more information than the temperature anisotropy and a measure of the polarization power spectrum improves the precision of cosmological parameters. The process of polarization involves the scattering of electromagnetic radiation by a free electron and requires a quadrupole distribution as shown in Fig. 1.6.6. The quadrupole anisotropy can be due to *scalar* ($m = 0$), *vector* ($m = 1$), or *tensor* ($m = 2$) perturbations. Vector perturbations are damped by the expansion, therefore only scalar and tensor perturbations are observable [31]. Scalar perturbations are generated by density gradients on the last scattering surface and are responsible for large scale structure formation. Tensor perturbations arises from primordial gravitational waves which are predicted by the inflation theory. These waves affect the space-time metric along the orthogonal directions with respect to the propagation axis. The compression due to this perturbation generates a quadrupole distribution which polarizes CMB photons. Scalar and tensor perturbations are shown in Fig.

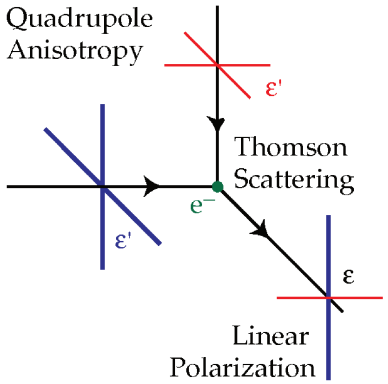

Figure 1.6.6: Effect of Thomson scattering in a quadrupole distribution. Polarization along the radial direction decreases in intensity and the photon flux along the line of sight appears linearly polarized.

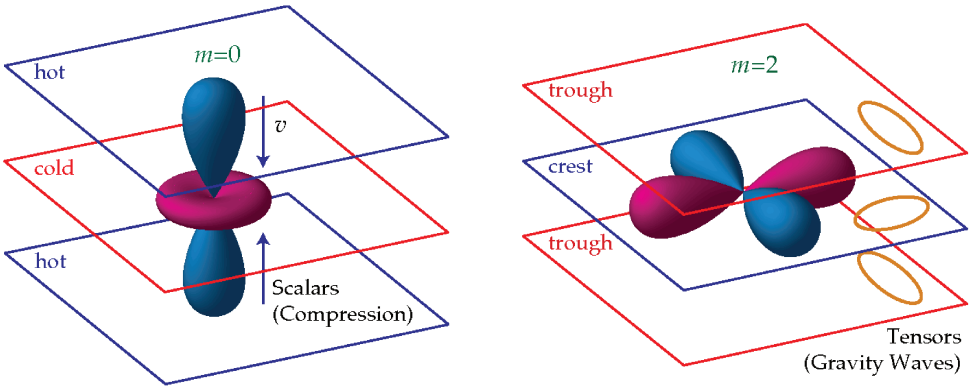

Figure 1.6.7: Scalar perturbation (left) and tensor perturbation (right). Source: [32]

1.6.7. Linear polarization on the sky can be decomposed into two components called E-modes and B-modes depending on the parity[3]. E mode signature is invariant under parity transformation while B mode is not. The effect of parity is shown in Fig. 1.6.8. It is remarkable that:

- Scalar perturbations can only generate E-modes on the sky.
- Tensor perturbations can generate both E-modes and B-modes.

CMB polarization was firstly detected by DASI [30] in 2002. Beside cosmological parameters, polarization is of great interest since gives information about the inflation epoch. In particular, B-modes can be originated only from primordial tensor perturbation. Therefore, the detection of such a polarization pattern will give us the signature on the CMB of primordial gravitational waves.

[3]E modes and B modes are analogous to E and B fields in electromagnetism.

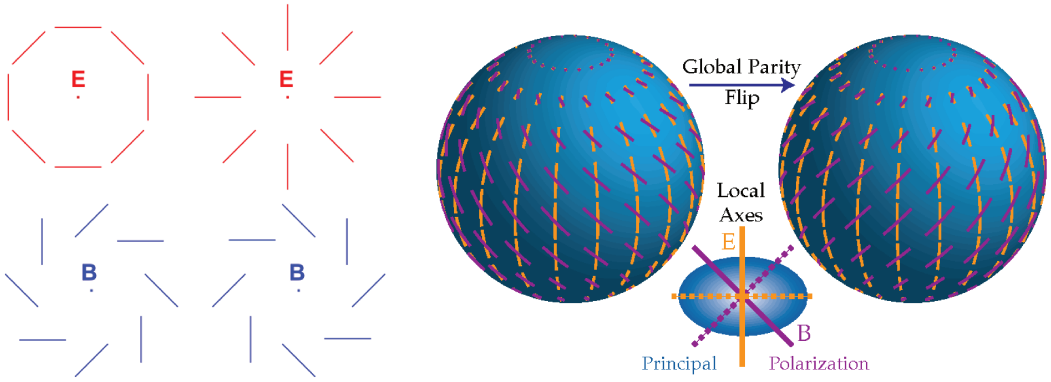

Figure 1.6.8: Polarization patterns of E-modes and B-modes. It is shown their opposite behavior under parity. Source: [32]

1.6.4 Observational challenges for CMB polarimetry

Sensitivity

We can observe four spectra, TT, TE, EE and BB. These are calculated as the temperature difference of unpolarized CMB (T), E-modes (E) and B-modes (B) on two different locations of the sky. The TT curve is the CMB temperature power spectrum discussed in the previous section. Fig. 1.6.9 shows recent measurements of some spectra with data from different experiments, which involves space telescopes, ground based telescopes and balloons. B-modes are still undetected and currently we only have measured an upper limit. Inflation models predict B-modes to be fainter than E-modes of at least one order of magnitude. It is a convention in cosmology to use the tensor-to-scalar ratio r defined as

$$r = \frac{\Delta_T^2}{\Delta_S^2}$$

where Δ_T^2 and Δ_S^2 are the power spectra of tensor and scalar perturbations respectively. We don't know the exact value of r, from current available measures we obtain an upper limit of $r < 0.07$ with 95% confidence. Some theories predict the factor r to be of the order of 10^{-3}or smaller. This value is small enough to set a technological challenge in terms of detection sensitivity. Detectors already reach the fundamental limit given by photon noise, thus, next generation telescopes dedicated to CMB polarimetry require more detectors on focal plane. The community often indicates the current instrumentation development as CMB stage-3 with focal planes having $\sim 10^4$ detectors. As shown in Fig. 1.6.10, during the next few years CMB

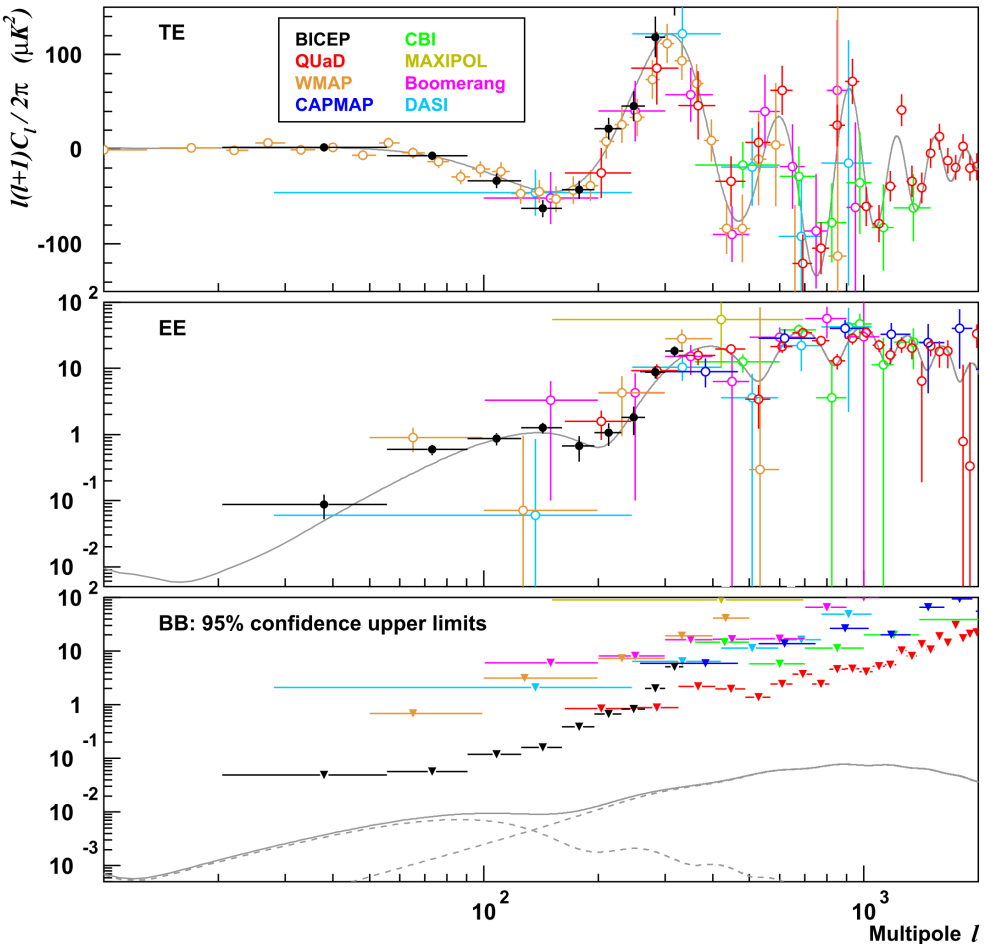

Figure 1.6.9: TE, EE and BB power spectra obtained form several telescope data. Source: [33]

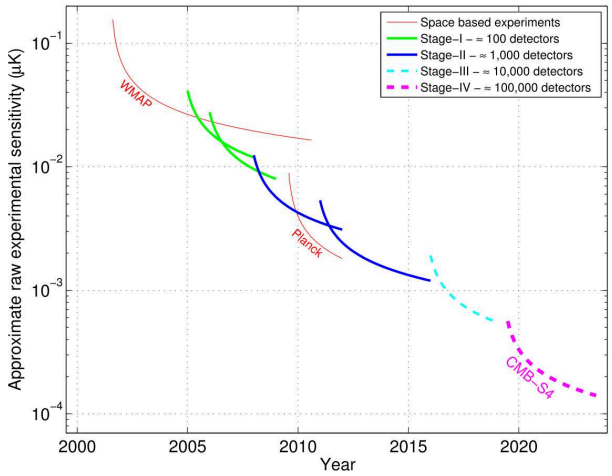

Figure 1.6.10: Evolution in terms of number of detector on focal plane dedicated to CMB observation. Source: CMB-S4 Science Book [34].

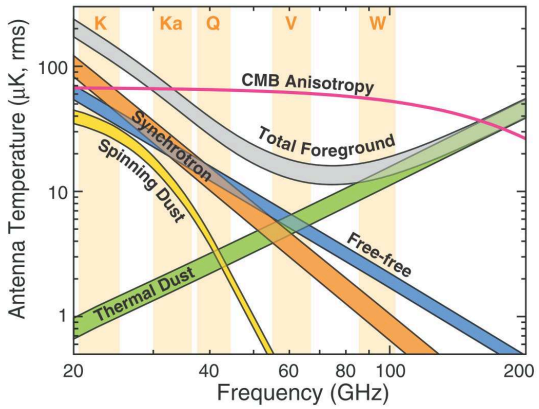

Figure 1.6.11: Spectra of galactic emissions compared to CMB anisotropy. Source: Bennet et al. [36].

stage-4 is supposed to operate with $\sim 10^5$ detectors on focal plane.

Foregrounds

Beside the sensitivity, B-modes observation is limited by foreground contamination. B-mode pattern on the sky can be produced by E-mode polarization bent by interactions with gravitational fields. This process is known as *gravitational lensing*. The B-mode lensing signal can be removed using primordial E-mode map along with the CMB lensing potential [34]. The latter is also a CMB stage-4 measurement goal. Astronomers call this technique *delensing* and it is a crucial approach to reduce the effective noise in primordial B-mode map. Observations are also limited by galactic emissions. Telescopes located at South Pole, like BICEP and Keck Array, benefit of clean sky but still foregrounds are significant compared to B-modes. Galactic emission components shown in Fig. 1.6.11 are characterized by:

- **Synchrotron**: Dominant at low frequencies ($< 40\ GHz$). Synchrotron radiation occurs when cosmic ray electrons interact with the galactic magnetic field. Photons are polarized perpendicular to the field lines.
- **Free-free**: Unpolarized emission due to electron-ion scattering in interstellar plasma.
- **Thermal dust**: Thermal Emission from interstellar dust grain such as graphites and Silicates. This component dominates the foreground above 80 GHz.
- **Spinning dust**: A fainter component of the foreground at low frequencies

($20\ GHz\ -\ 60GHz$) supposed to be originated by spinning particles.

B-mode observation requires component separation on the sky map. Therefore, next generation telescopes must be sensitive on a wide range of frequencies in order to cover the spectrum of each source of contamination.

1.7 Conclusions

CMB polarimetry is a great probe for modern cosmology which may provide informations from the inflationary epoch. B-modes observation is a compelling challenge that is pushing astronomers to develop new technological solutions. Next generation focal planes will require large number of detectors to increase the sensitivity, polarization sensitive pixels and multi-chroic solutions to fabricate large arrays in compact design. In this context, antenna-coupled detectors is the preferred architecture. In particular, microstrip excited planar antennas can provide polarization sensitive receivers and can easily accommodate bandpass filters for multi-chroic design.

Chapter 2

Microwave Circuits

Signal processing for radio and millimeter astronomy requires high frequency circuits. In the millimeter or microwave domain, the frequency is too high for the electronic devices to be efficient. For that reason, direct detectors for frequencies higher than about 100 GHz often rely on superconducting properties of metals to push down the readout electronic operational frequency range.

In the context of antenna-coupled Kinetic Inductance Detectors (KIDs) two types of technologies are involved. First, high frequency signals have to be carried from a receiver (antenna) to a detector. This step may involve signal filtering and impedance matching, which is usually carried out with planar transmission lines. Then, KIDs readout electronic makes use of more traditional circuit components up to 10 GHz.

In this chapter I will introduce the main aspect of microwave engineering that are used for developing electrical circuits and microwave components.

2.1 Planar transmission lines

Before the appearance of planar transmission lines, electromagnetic waves were mainly transmitted by waveguides. A waveguide is defined [38] as a system whose electromagnetic properties do not change along at least one straight line in space. Standard waveguides have the advantage of low loss, but they are bulky and expensive. Therefore, during the 1940s, when printed circuits become popular due to military applications, planar transmission lines were developed. Today they are used

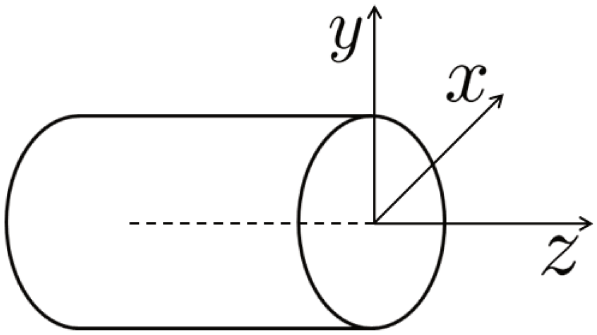

Figure 2.1.1: Notation used. The cross section of the waveguide lies on the x, y plane. The z axis is the waveguide axis of symmetry and also the direction of wave propagation. Electric and magnetic fields have components only along x and y in pure TEM modes.

for integrated circuit, thus a large amount of literature exists for many applications, especially in microwave systems. Waves can propagate along a transmission line in three different ways:

- *Transverse electromagnetic (TEM modes)*: the longitudinal components of the fields are null.
- *Transverse electric (TE modes):* the longitudinal component of the electric field is null.
- *Transverse magnetic (TM modes)*: the longitudinal component of the magnetic field is null.

In each case wave propagates with a propagation constant β, that in the case of lossy lines becomes $\gamma = \alpha + j\beta$, where α is the attenuation coefficient. The propagation constant β can depend on frequency. In these cases there is a cutoff wavenumber $k_c = \sqrt{k^2 - \beta^2}$, which represents the longest possible wavelength for the wave to propagate. We are interested in TEM modes propagation. In this case the cutoff wavenumber k_c is equal to zero. In TE and TM modes k_c is a function of the angular frequency ω and a propagating wave with wavenumber $k < k_c$ corresponds to an exponentially decaying wave called *evanescent mode.*

Propagation of waves along a waveguide can be derived from the Maxwell's equations. Considering a conductor as in Fig. 2.1.1 and a wave propagating along the z axis, they can be written as

$$\nabla \times \mathbf{E} = -j\omega\mu\mathbf{H} \tag{2.1.1}$$

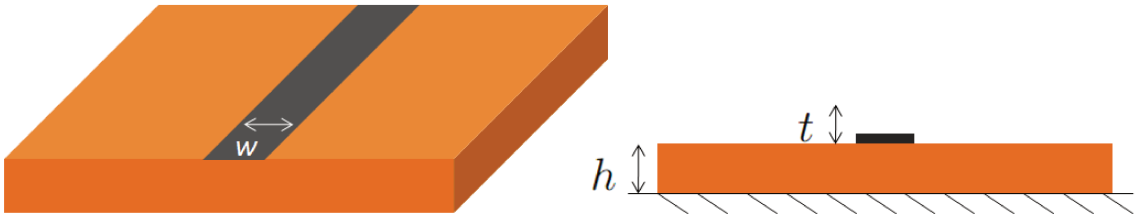

Figure 2.1.2: Face front (left) and section (right) of a microstrip line, a thin metal conductor of thickness t and width w printed over a dielectric substrate of thickness h. The opposite face of the dielectric lies on the ground level.

$$\nabla \times \mathbf{H} = j\omega\epsilon\mathbf{E} \tag{2.1.2}$$

where ϵ, μ are respectively the permittivity and permeability. We used the time dependence in the form of $exp\,(j\omega t)$ and the electric and magnetic fields $\mathbf{E}$, $\mathbf{H}$ are described as follows

$$\mathbf{E}\,(x,y,z) = [\mathbf{e_t}\,(x,y) + \mathbf{e_z}\,(x,y)\,\hat{z}]\exp\,(-j\beta z) \tag{2.1.3}$$

$$\mathbf{H}\,(x,y,z) = [\mathbf{h_t}\,(x,y) + \mathbf{h_z}\,(x,y)\,\hat{z}]\exp\,(-j\beta z) \tag{2.1.4}$$

with $\mathbf{e_t}$ and $\mathbf{e_z}$ being the transverse and longitudinal components of the electric field, $\mathbf{h_t}$ and $\mathbf{h_z}$ the transverse and longitudinal components of the magnetic field. A solution for TEM modes can be found from 2.1.1 and 2.1.2 considering $E_z = H_z = 0$ as follows [40]

$$\beta^2 E_y = \omega^2\mu\epsilon E_y \tag{2.1.5}$$

where $\beta = \omega\sqrt{\mu\epsilon} = k$ and so $k_c = \sqrt{k^2 - \beta^2} = 0$.

A commonly used planar transmission line in microwave frequencies is the microstrip line. It is more economic, compact and lighter than traditional metallic waveguide. The disadvantages are mostly the higher losses and the various consequences of the fact that, unlike waveguide, microstrip is an open structure that can cause some undesired effects like cross-talk, interference and so on. Microstrip lines (Fig. 2.1.2) have a thin conductor of width w that lies over a grounded dielectric substrate of thickness h. Calculation of the fields around the conductor is complicated because the it is not entirely covered by the dielectric and a dielectric-air interface is involved with two different values of relative permittivity. For this reason waves in microstrip lines propagate with a hybrid TM-TE mode. However, if the dielectric thickness is small with respect to the wavelength ($h \ll \lambda$) the fields are *quasi*-TEM. This

means that some components of the electric and magnetic field lines are not null in the direction of propagation. Thus, a small amount of energy is associated with these longitudinal components [39, 43]. Non-TEM lines have propagation constant and characteristic impedance that vary with frequency, this type of lines are called *dispersive*. It is convenient to introduce the effective dielectric constant ε_{eff} of the microstrip line takes into account the fraction of the total energy that exists in the air. The effective dielectric constant is greater than the dielectric constant of air and smaller than the dielectric constant of substrate. An expression for ϵ_{eff} is given by [40]

$$\varepsilon_{eff} = \frac{\varepsilon_r + 1}{2} + \frac{\varepsilon_r - 1}{2} \frac{1}{\sqrt{1 + 12^{\mathrm{h}/\mathrm{w}}}} \tag{2.1.6}$$

Microstrip lines are equivalent to a conductor in a homogeneous material with a dielectric constant ε_{eff} . Waves that propagate along it have a wavelength λ_{eff} reduced by a factor $\lambda_{eff} = \lambda/\sqrt{\varepsilon_{eff}}$ [41]. The characteristic impedance of a microstrip line is given by the thickness of the dielectric, dielectric constant and width of the conductor. Using 2.1.6 it can be calculated as

$$Z_0 = \begin{cases} \dfrac{60}{\sqrt{\varepsilon_{eff}}} \ln\left(\dfrac{8h}{w} + \dfrac{w}{4h}\right) & if\ \dfrac{w}{h} \leq 1 \\ \dfrac{120\pi}{\sqrt{\varepsilon_{eff}}\left[\dfrac{w}{h} + 1.393 + 0.667 \ln\left(\dfrac{w}{h} + 1.444\right)\right]} & if\ \dfrac{w}{h} \geq 1 \end{cases} \tag{2.1.7}$$

Attenuation in a microstrip can be given by the dielectric loss α_d as well as the conductor loss α_c. We can estimate them as follows [40]

$$\alpha_d = \frac{k_0 \epsilon_r \left(\epsilon_{eff} - 1\right) \tan\delta}{2\sqrt{\epsilon_{eff}}\left(\epsilon_r - 1\right)} \left[Np/m\right]; \qquad \alpha_c = \frac{R_s}{Z_0 W} \left[Np/m\right] \tag{2.1.8}$$

where $\tan\delta$ is the loss tangent and $R_s = \sqrt{\omega\mu_0/2\sigma}$ is the surface resistivity.

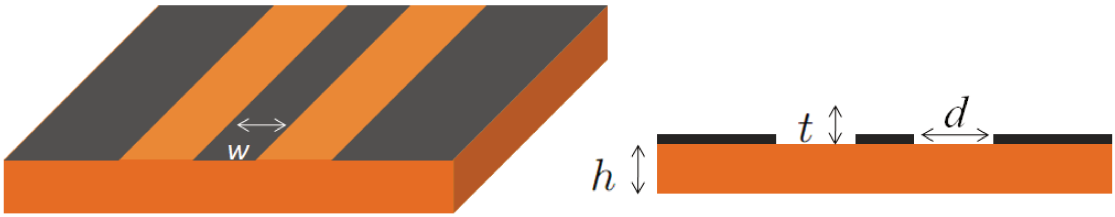

Figure 2.1.3: Face front (left) and section (right) of a coplanar waveguide, a thin metal conductor of thickness t and width w printed over a dielectric substrate of thickness h. The two ground planes lie over the substrate, contrarily to the microstrip, at a distance d from the central conductor.

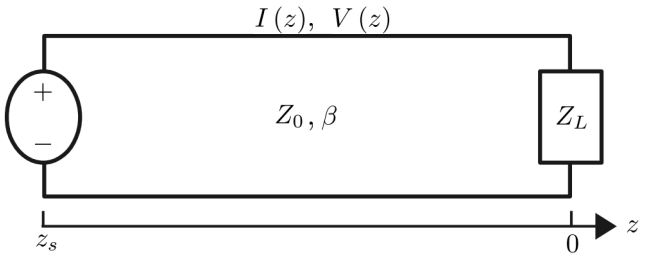

Figure 2.2.1: Transmission line of characteristic impedance Z_0 terminated in a load impedance Z_L. The Ohm's law requires the ratio of voltage to current at the termination to be Z_L. According to this, reflection of the incident wave occurs in the case of a mismatched line, for which $Z_L \neq Z_0$.

For KIDs application microstrip lines are usually adopted along with Coplanar Waveguides (CPW). These are particularly used for the readout node since they can be connected to coaxial cables easier than microstrips. A coplanar waveguide can be described as a planar transmission line of width w in the center of two ground planes at a constant distance d from each side as shown in Fig. 2.1.3. Because of the system symmetry, the coplanar waveguide effective dielectric constant can be written approximately as [42] $\varepsilon_{eff} \approx (\varepsilon_r + 1)/2$, so it is equal to the average dielectric constant of the substrate and the air.

2.2 Impedance matching

2.2.1 Terminations

The basic concept and design of impedance matching and signal filtering can be understood by studying the electrical behavior of terminated transmission lines. We can start considering the general case of a load impedance termination Z_L shown in Fig. 2.2.1. The signal is flowing through a transmission line with characteristic impedance Z_0 and is described by an incident wave which has the form $V_0^+ e^{-j\beta z}$. The wave is generated from a source located at $z = z_s$ with $z_s < 0$. The values of voltage and current along the line are given by the sum of the incident and reflected waves amplitude as follows:

$$V(z) = V_0^+ e^{-j\beta z} + V_0^- e^{j\beta z} \tag{2.2.1}$$

$$I(z) = \frac{V_0^+}{Z_0} e^{-j\beta z} - \frac{V_0^-}{Z_0} e^{j\beta z} \tag{2.2.2}$$

with V_0^- being the reflected wave amplitude. Because of the Ohm's law, the voltage and current at the termination must follow the relation

$$Z_L = \frac{V(0)}{I(0)} = \frac{V_0^+ + V_0^-}{V_0^+ - V_0^-} Z_0$$

We can calculate the amplitude of the reflected wave by using these last three equations, we obtain

$$V_0^- = \frac{Z_L - Z_0}{Z_L + Z_0} V_0^+ = \Gamma V_0^+ \tag{2.2.3}$$

where Γ is the *voltage reflection coefficient* given by the reflected wave amplitude normalized to the amplitude of the incident wave. Equations 2.2.1 and 2.2.2 can be rewritten as

$$V(z) = V_0^+ \left[e^{-j\beta z} + \Gamma e^{j\beta z} \right] \tag{2.2.4}$$

$$I(z) = \frac{V_0^+}{Z_0} \left[e^{-j\beta z} - \Gamma e^{j\beta z} \right] \tag{2.2.5}$$

From these equations we notice that the voltage and current along the line are composed of a superposition of the incident and reflected wave. Hence, a stationary wave forms along the line when $\Gamma \neq 0$. An ideal impedance matching requires $\Gamma = 0$, that occurs when $Z_L = Z_0$ from 2.2.3.

The power P_L delivered to the load will be equal to $P_L = P_I - P_R$, with P_I and P_R being the incident and reflected power respectively. The power loss due to a mismatch is called *return loss* (RL), defined in Decibel as

$$RL = -20 \log |\Gamma| \tag{2.2.6}$$

From the definition above, a matched line has a return loss of ∞ dB. In the case of $\Gamma \neq 0$ the amplitude of the reflected wave can be calculated from 2.2.4 taking into

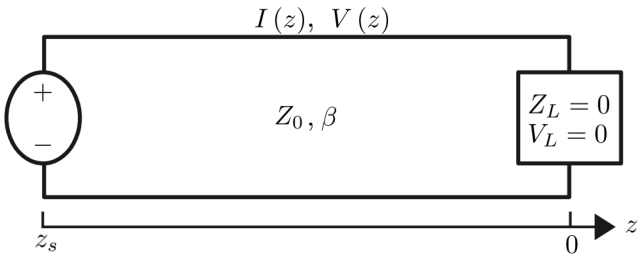

Figure 2.2.2: Lossless terminated transmission line. The voltage drop must be zero across the short circuit, therefore the stationary wave has a node at the termination.

account the definition in 2.2.3. We obtain

$$|V(z)| = \left|V_0^+\right| |1 + |\Gamma| \exp[j(\theta + 2\beta z)]|$$

with θ being the phase of the reflection coefficient. The consequence of having a standing wave is that the voltage amplitude depends on the position along the line. The nodes and peaks are separated by $\lambda/4$ where λ is the signal wavelength through the line. As a result, the input impedance Z_{in} seen along the line becomes

$$Z_{in}(z) = \frac{V(z)}{I(z)} = Z_0 \frac{1 + \Gamma \exp(2j\beta z)}{1 - \Gamma \exp(2j\beta z)} \tag{2.2.7}$$

2.2.2 Short Circuited and Open Circuited Lines

We can now replace the termination load with a short circuit as shown in Fig. 2.2.2. A lossless load is characterized by $Z_L = 0$, thus the voltage drop must be zero and the termination becomes a node of the stationary wave. In this case the input impedance along the line can be calculated by using 2.2.7 with the condition $\Gamma = 1$, we obtain a purely imaginary impedance given by

$$Z_{in}(z) = -jZ_0 \tan(\beta z)$$

The line is only reactive, the voltage and current can be calculated from 2.2.4 and 2.2.5 as follows:

$$V(z) = V_0^+ \left[e^{-j\beta z} - e^{j\beta z}\right] = -2jV_0^+ \sin(\beta z)$$

$$I(z) = \frac{V_0^+}{Z_0} \left[e^{-j\beta z} + e^{j\beta z}\right] = \frac{-2V_0^+}{Z_0} \cos(\beta z)$$

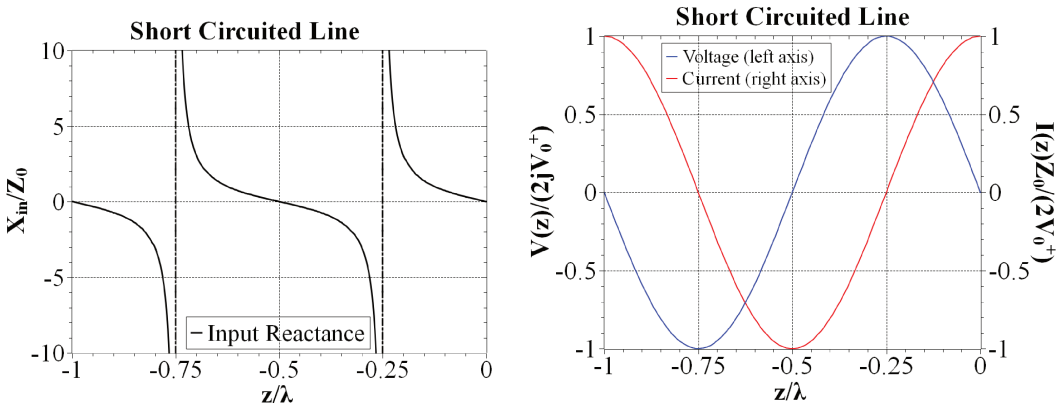

Figure 2.2.3: Input impedance (left) as a funcion of the distance from the short circuit, located at $z = 0$. Standing wave along the line in terms of voltage and current (right).

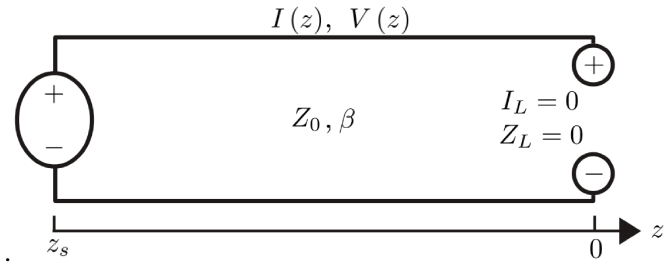

Figure 2.2.4: Transmission line terminated in an open circuit. The current must be zero across the termination, therefore the stationary wave has a maximum at the termination.

Nodes of voltage and current are separated by a quarter wavelength. Fig. 2.2.3 shows the characteristics of a short circuited line as a function of z.

The case of an open circuited line is show in Fig. 2.2.4. This termination is characterized by $Z_L = \infty$, thus the current must be zero and the standing wave along the line has a maximum located at the termination. The input impedance can be calculated as in the short circuit case, we obtain

$$Z_{in}(z) = jZ_0 \cot(\beta z) \tag{2.2.8}$$

Voltage and current are shifted by 45° compared to the short circuited line. These are given by

$$V(z) = V_0^+ \left[e^{-j\beta z} + e^{j\beta z}\right] = 2V_0^+ \cos(\beta z)$$

$$I(z) = \frac{V_0^+}{Z_0}\left[e^{-j\beta z} - e^{j\beta z}\right] = \frac{-2jV_0^+}{Z_0}\sin(\beta z)$$

A plot of $V(z)$ and $I(z)$ is shown in Fig. 2.2.5.

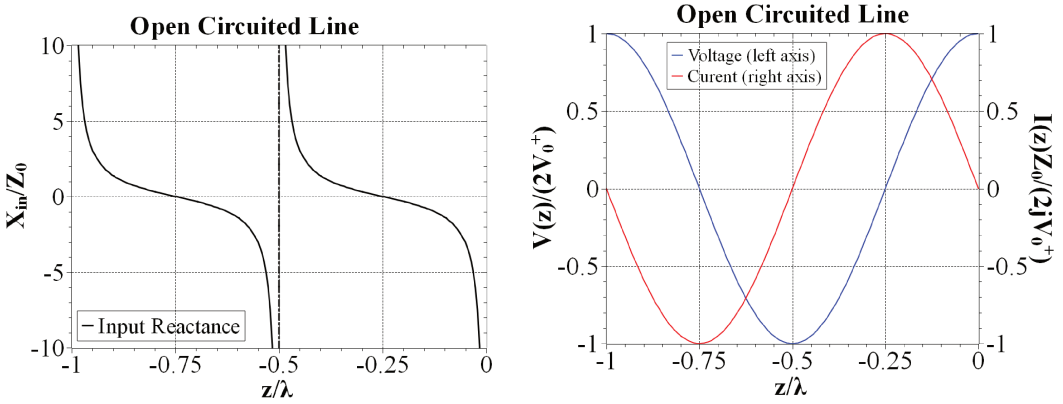

Figure 2.2.5: Input impedance (left) as a funcion of the distance from the open circuit, located at $z = 0$. Voltage and current along the line (right).

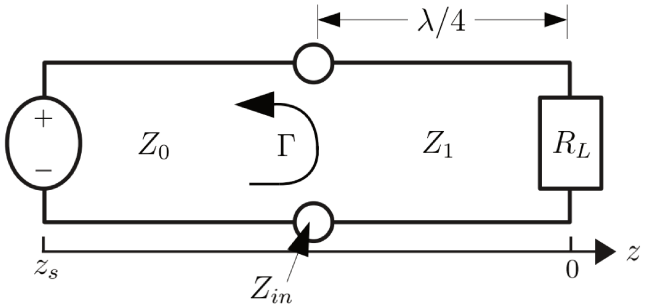

Figure 2.2.6: A line with characteristic impedance Z_0 connected to a quarter wave transformer of characteristic impedance Z_{in}. The $\lambda/4$ segment assures a phase shift of π for the reflected wave at the $Z_0 - Z_1$ interface.

2.2.3 Quarter wave transformer

Considering a resistive load R_L, the complex input impedance 2.2.7 has a real solution for a terminated transmission line of length $\lambda/4$ and characteristic impedance Z_1. With these assumptions we obtain

$$Z_{in} = \frac{Z_1^2}{R_L} \tag{2.2.9}$$

Connecting a transmission line of characteristic impedance $Z_0 = Z_{in}$ at distance $\lambda/4$ from the load does not produce reflected wave when

$$Z_1 = \sqrt{Z_0 R_L} \tag{2.2.10}$$

A quarter wave length transmission line with such a property is called *Quarter Wave Transformer*, shown in Fig. 2.2.6. This circuit element is widely used for impedance matching and is the basic element for different kinds of filters. From the incoming

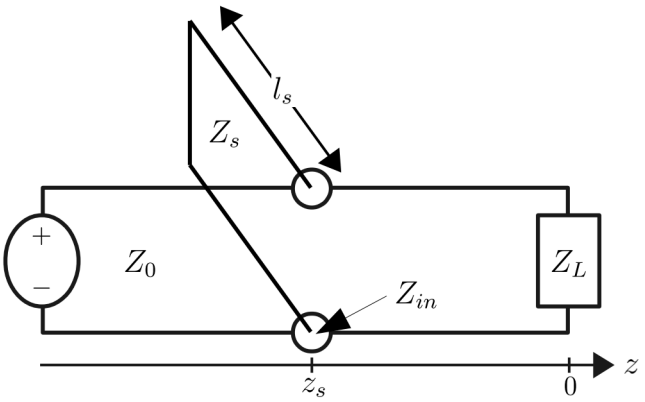

Figure 2.2.7: An open circuit stub of length l_s and characteristic impedance Z_s connected in parallel at distance z_s from a load Z_L.

wave point of view, the circuit does have an impedance mismatch both in the $Z_0 - Z_1$ and $Z_1 - R_L$ interface. Typically, every segment of a quarter wave transformer has a different characteristic impedance, thus $Z_0 \neq Z_1 \neq R_L$. The wave at the $Z_1 - R_L$ interface get reflected on the Z_0 segment with a phase shift of π in case Z_1 has a length of $(2n+1)\,\lambda/4$. This condition together with 2.2.10 assures that the superposition of all the partial reflections along the circuit adds to zero. Thus, the infinite set of waves traveling forward with the same phase velocity combine into a single traveling wave.

2.2.4 Stub matching

When considering superconducting lines, loads are often reactive more than resistive. In such a scenario we may want to use a *stub* to carry out the impedance matching. A stub is a piece of line of fixed length l_s connected in parallel to the transmission line at a certain distance z_s from a load Z_L. A schematic of a stub matching is shown in Fig. 2.2.7. A stub can be terminated both with an open or a short circuit. Since the connection is in parallel, it is more convenient to use the admittance Y. We can infer the input admittance $Y_{in} = 1/Z_{in}$ from 2.2.7 as follows

$$Y_{in} = \frac{1}{Z_0}\left(\frac{1 - \Gamma \exp\left(2j\beta z\right)}{1 + \Gamma \exp\left(2j\beta z\right)}\right)$$

Considering the case of $Z_0 = 50\,\Omega$ and $Z_L = 50 + i50\,\Omega$ we obtain a value of $\Gamma = 0.2 + i0.4$. A plot of the real (Conductance G) and imaginary (Susceptance B) part of Y_{in} is shown in Fig. 2.2.8. The admittance is periodic each $\lambda/2$. Values

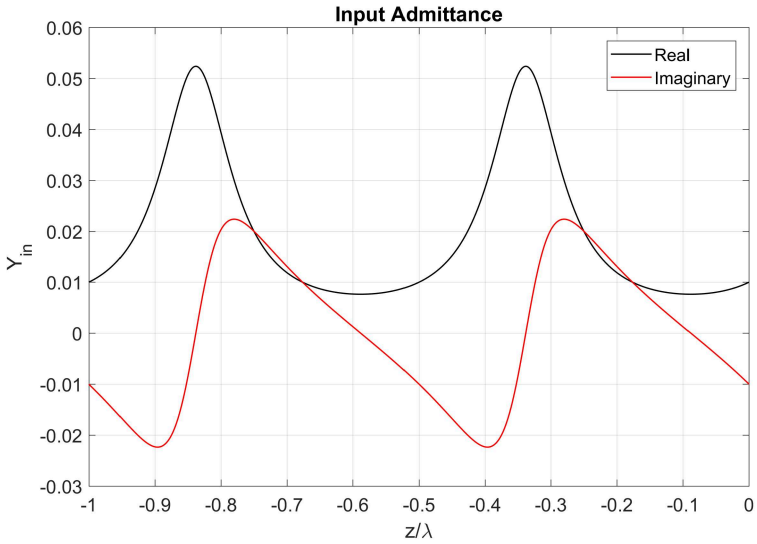

Figure 2.2.8: Real and imaginary part of the input admittance for $Z_0 = 50\,\Omega$ and $Z_L = 50 + i50\,\Omega$.

of $G = 0.02\,S$ are a match for $50\,\Omega$ resistors, they occur at $z_1 = -0.25\lambda - n(\lambda/2)$ and $z_2 = -0.42\lambda - n(\lambda/2)$. At those distances the line is also inductive with $B = 0.02\,S$. By inserting a stub in parallel at z_1 or z_2 with $R = 50\,\Omega$ we obtain a match for the resistance, then the stub length can be tuned to cancel out the reactance at those points. Considering an open circuited stub, the necessary length l_s to obtain $B = -0.02\,S$ is given by the inverse of 2.2.8 and turns out to be $\lambda/2$. For a short circuited stub the length would be a quarter wave. Once every parameter is set, the stub compensates for the load mismatch and no reflection occurs along the transmission line.

2.3 Filters

Microwave and RF filters come in a lot of varieties depending on the desired behavior and characteristics. Signal filtering can results in signal amplification (active filters) or not (passive filters). When designed with planar transmission lines, filters can be realized with stubs, stepped varying characteristic impedance, coupled transmission lines, resonant elements or a combination of them.

2.3.1 Transfer function

A filter can be described by a linear and time-invariant two-port network for which the input I and output O are related by the transfer function $O = T \times I$. The transfer function will take the form of a ratio of polynomials [45]

$$T(p) = \left(\frac{a_n}{b_n}\right) \frac{(p-p_1)(p-p_3)...(p-p_n)}{(p-p_2)(p-p_4)...(p-p_m)} = \frac{N(p)}{D(p)}$$

where $p = \sigma + j\omega$ is the complex frequency. Values of $p = p_1, p_3...p_n$ are zeros for the numerator $N(p)$ and are called finite-frequency transmission *zeros* of the filter. Values of $p = p_2, p_4...p_m$ are zeros for the denominator and are called *poles* of the filter. Those are the natural frequencies of the circuit and are influenced by all the circuit components. Nodes and poles are usually represented on the *complex frequency plane* or *p-plane*, where σ lies on the x axis and $j\omega$ on the y axis. The poles must lie on the second and third quadrant (left half of the p-plane) or on the $j\omega$ axis for the filter to be stable [46]. The zeros can occur anywhere. The p_n, p_m pattern on the p-plane determines the filter response.

As an example of p-plane we can consider a short circuited line as discussed in section 2.2.2. The input impedance of a quarter wavelength long lossless transmission line can be written as

$$Z(p) = Z_0 \frac{\pi p}{2\omega} \prod_{n=1}^{\infty} \left(\frac{2n-1}{2n}\right)^2 \frac{[p+2nj\omega][p-2nj\omega]}{[p+(2n-1)j\omega][p-(2n-1)j\omega]}$$

A lossless line is characterized by $\sigma = 0$, hence the poles and zeros lie on the $j\omega$ axis. These points, shown in Fig. 2.3.1, are respectively

$$poles \rightarrow p = \pm(2n-1)j\omega$$
$$zeros \rightarrow p = \pm 2nj\omega$$

The effect of introducing loss along the line is to shift both the poles and zeros on the negative σ axis. The resulting plot of $|Z(p)|$ would become smoother, with no divergences, and strictly greater than zero.

Unlikely the zeros, poles are characteristic of each network and, except for degenerate cases, are not influenced by all the elements in the circuit. A network composed of

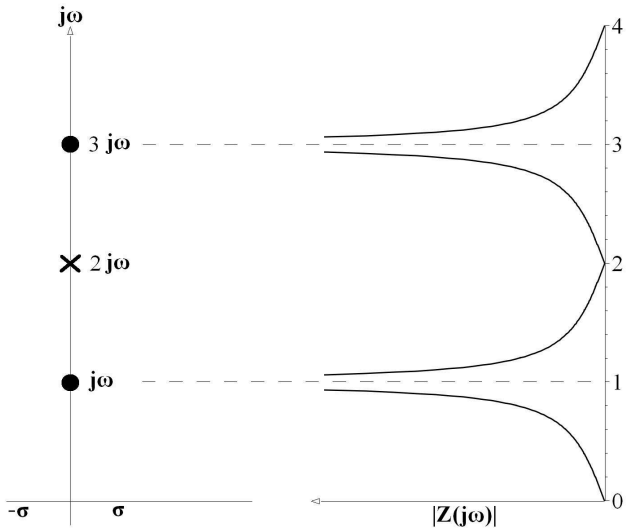

Figure 2.3.1: Zeros (crosses) and Poles (dots) on the p-plane for a short circuited quarter wavelength lossles transmision line.

two networks connected in series will have the poles of both of them.

In the following sections I will explain in more details the response of two of the most common filter approximations for RF and microwave applications.

2.3.2 Butterworth filter

This type of filter is designed to have the maximally flat response along the pass-band. The transfer function of a Butterworth filter can be written in terms of the S_{21} parameter of a two port network as follows [47]:

$$S_{21}(p) = \frac{1}{\prod_{i=1}^{n}(p - p_i)}$$

where

$$p_i = j \exp\left[\frac{(2i-1)\,\pi}{2n}\right]$$

and n is the degree of the filter, which is equal to the number of reactive elements in the circuit. The zeros of the Butterworth transfer function are all at infinity and the poles are equally spaced along the semi circle on the left side of the p-plane. This is due to the fact that

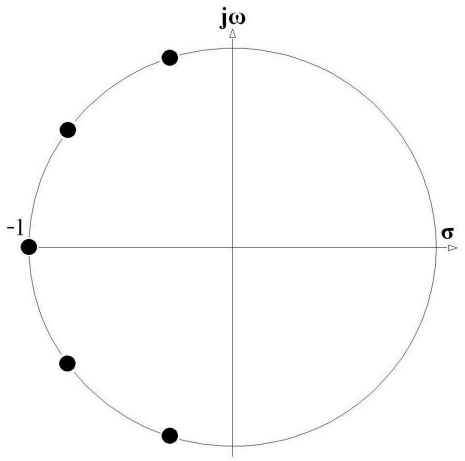

Figure 2.3.2: Pole distribution of a Butterworth filter with $n = 5$.

$$|p_i| = 1$$
$$Arg\ (p_i) = \frac{(2i-1)\,\pi}{2n}$$

Example of pole distribution is shown in Fig. 2.3.2.

2.3.3 Chebyshev filter

The Chebyshev response is designed to have a steeper transition between the pass-band and the stop-band with respect to the Butterworth filter. This kind of filter show ripples across the pass-band. The transfer function can be written as [48]

$$S_{21}(p) = \frac{\prod_{i=1}^{n}\left[\eta^2 + \sin^2\left(\frac{i\pi}{n}\right)\right]^{\frac{1}{2}}}{\prod_{i=1}^{n}(p+p_i)}$$

where

$$p_i = j\cos\left[\sin^{-1} j\eta + \frac{(2i-1)\,\pi}{2n}\right]$$

and n is the degree of the filter. As well as in the case of Butterworth filter, the poles of a Chebyshev filter are located at infinity. For that reason those filters are also referred as *all-poles filters*. An example of pole distributions of a Chebyshev

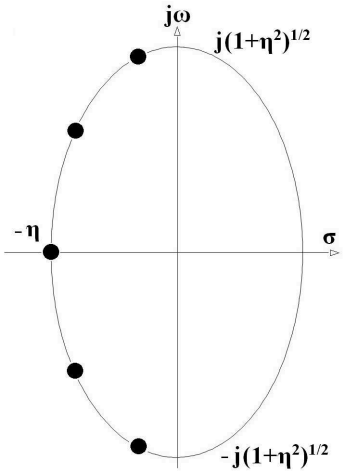

Figure 2.3.3: Pole distribution of a Chebyshev filter with $n = 5$.

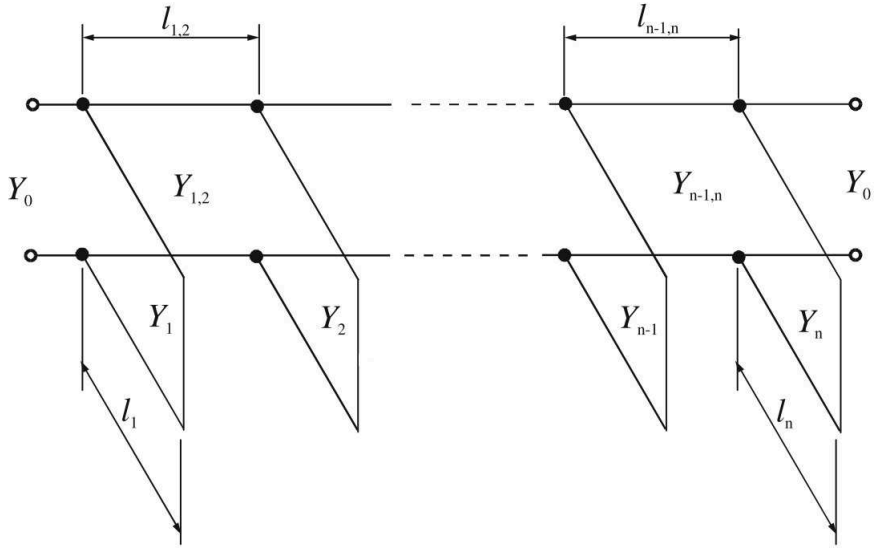

Figure 2.3.4: Bandpass filter modeled with quarter wavelength short circuited stubs along a transmission line. [46]

filter is shown in Fig. 2.3.3. They all lie on an ellipse on the left side of the p-plane. The minor axis has size of η and is oriented as the σ axis. The major axis has size of $\sqrt{1+\eta^2}$ and is oriented as the $j\omega$ axis.

2.3.4 Short circuited stubs Chebyshev bandpass filter

Microstrip line Chebyshev bandpass filters can be modeled with simple quarter wavelength short circuited stubs as shown in Fig. 2.3.4. The filter degree n sets the number of stubs along the transmission line. Stub characteristics depend on the desired filter properties and transmission line impedance. Since the connection is in parallel

it is convenient to use the admittance Y_0 to describe the transmission line and Y_i for the $i-th$ stubs of length l_i. Transmission line admittance between two adjacent stubs $Y_{i,i+1}$ is constant and generally differs from Y_0. Therefore, the separation $l_{i,i+1}$ between two adjacent stubs changes as well. Admittances Y_i for a bandpass filter of order n are given by

$$Y_1 = g_0 Y_0 \left(1 - \frac{h}{2}\right) g_1 \tan\theta + Y_0 \left(N_{1,2} - \frac{J_{1,2}}{Y_0}\right)$$

$$Y_n = Y_0 \left(g_n g_{n+1} - g_0 g_1 \frac{h}{2}\right) \tan\theta + Y_0 \left(N_{n-1,n} - \frac{J_{n-1,n}}{Y_0}\right)$$

$$Y_i = Y_0 \left(N_{i-1,i} + N_{i,i+1} - \frac{J_{i-1,i}}{Y_0} - \frac{J_{i,i+1}}{Y_0}\right) \quad for\ i = 2\ to\ n-1$$

$$Y_{i,i+1} = Y_0 \left(\frac{J_{i,i+1}}{Y_0}\right) \quad for\ i = 1\ to\ n-1$$

where

$$\theta = \frac{\pi}{2}\left(1 - \frac{FBW}{2}\right) \tag{2.3.1}$$

$$h = 2$$

with FBW being the desired fractional bandwidth of the filter and h a dimensionless parameter which sets the filter intern admittance. The others design parameters are calculated as follows:

$$\frac{J_{1,2}}{Y_0} = g_0 \sqrt{\frac{h g_1}{g_2}}$$

$$\frac{J_{n-1,n}}{Y_0} = g_0 \sqrt{\frac{h g_1 g_{n+1}}{g_0 g_{n-1}}}$$

$$\frac{J_{i,i+1}}{Y_0} = \frac{hg_0g_1}{\sqrt{g_ig_{i+1}}} \quad for\ i = 2\ to\ n-2$$

$$N_{i,i+1} = \sqrt{\left(\frac{J_{i,i+1}}{Y_0}\right)^2 + \left(\frac{hg_0g_1\tan\theta}{2}\right)^2}$$

Values of parameters g_i can be found in literature, they determine the amplitude of the Chebyshev ripple along the passband. Tables in Fig. 2.3.5 show element values of g_i as a function of the filter order n and the desired passband ripple. Values of l_i can be inferred from the stub effective dielectric constant as a quarter wavelength: considering the wavelength along the microstrip λ_m we obtain:

$$\frac{\lambda_m}{4} = \frac{75}{f_{GHz}\sqrt{\epsilon_{eff}}}$$

where f_{GHz} is the signal frequency expressed in GHz.

2.3.5 Open circuited stubs Chebyshev bandpass filter

A Chebyshev bandpass filter can also be modeled with open circuited stubs. This solution may provide an easier implementation in most cases[1] but has the drawback of adding complexity on the filter geometry. Compared to the short circuited case, each of the n open circuited stubs is composed by one quarter wavelength piece of line in series with a quarter wavelength open circuited stub. This circuit is equivalent to a half wavelength open circuited stub of discontinuous impedance as shown in Fig. 2.3.6. The open circuited Chebyshev bandpass filter has a peculiar stopband characteristic. At the attenuation pole, the main line sees the stub as a short circuit and the transmission drop to zero. The attenuation pole frequency f_{ap} is a parameter of the filter. In the special case of $f_{ap} = f_0/2$, with f_0 being the bandpass filter central frequency, the admittance Y_{ia} of the quarter wavelength piece of line is equal to the admittance Y_{ib} of quarter wavelength open circuited stub. In the general case these admittances can be inferred from the admittances Y_i of the short circuited stubs Chebyshev bandpass filter in the following manner

[1] Considering a microstrip line, a short circuit requires substrate drilling or extra deposition steps.

For passband ripple L_{Ar} = 0.01 dB										
n	g_1	g_2	g_3	g_4	g_5	g_6	g_7	g_8	g_9	g_{10}
1	0.0960	1.0								
2	0.4489	0.4078	1.1008							
3	0.6292	0.9703	0.6292	1.0						
4	0.7129	1.2004	1.3213	0.6476	1.1008					
5	0.7563	1.3049	1.5773	1.3049	0.7563	1.0				
6	0.7814	1.3600	1.6897	1.5350	1.4970	0.7098	1.1008			
7	0.7970	1.3924	1.7481	1.6331	1.7481	1.3924	0.7970	1.0		
8	0.8073	1.4131	1.7825	1.6833	1.8529	1.6193	1.5555	0.7334	1.1008	
9	0.8145	1.4271	1.8044	1.7125	1.9058	1.7125	1.8044	1.4271	0.8145	1.0
For passband ripple L_{Ar} = 0.04321 dB										
n	g_1	g_2	g_3	g_4	g_5	g_6	g_7	g_8	g_9	g_{10}
1	0.2000	1.0								
2	0.6648	0.5445	1.2210							
3	0.8516	1.1032	0.8516	1.0						
4	0.9314	1.2920	1.5775	0.7628	1.2210					
5	0.9714	1.3721	1.8014	1.3721	0.9714	1.0				
6	0.9940	1.4131	1.8933	1.5506	1.7253	0.8141	1.2210			
7	1.0080	1.4368	1.9398	1.6220	1.9398	1.4368	1.0080	1.0		
8	1.0171	1.4518	1.9667	1.6574	2.0237	1.6107	1.7726	0.8330	1.2210	
9	1.0235	1.4619	1.9837	1.6778	2.0649	1.6778	1.9837	1.4619	1.0235	1.0
For passband ripple L_{Ar} = 0.1 dB										
n	g_1	g_2	g_3	g_4	g_5	g_6	g_7	g_8	g_9	g_{10}
1	0.3052	1.0								
2	0.8431	0.6220	1.3554							
3	1.0316	1.1474	1.0316	1.0						
4	1.1088	1.3062	1.7704	0.8181	1.3554					
5	1.1468	1.3712	1.9750	1.3712	1.1468	1.0				
6	1.1681	1.4040	2.0562	1.5171	1.9029	0.8618	1.3554			
7	1.1812	1.4228	2.0967	1.5734	2.0967	1.4228	1.1812	1.0		
8	1.1898	1.4346	2.1199	1.6010	2.1700	1.5641	1.9445	0.8778	1.3554	
9	1.1957	1.4426	2.1346	1.6167	2.2054	1.6167	2.1346	1.4426	1.1957	1.0

Figure 2.3.5: Parameters g_i for a bandpass Chebyshev filter of order n. Values of g_0 are equal to 1. [46]

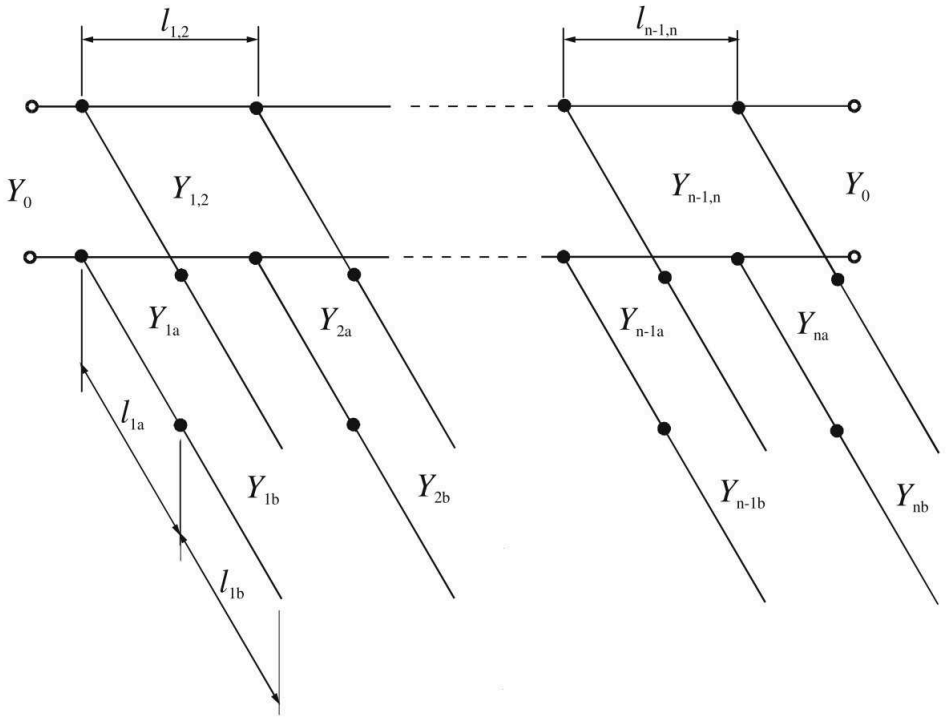

Figure 2.3.6: Bandpass filter on a transmission line modeled with half wavelength open circuited stubs of discontinuous impedance. [46]

$$Y_{ia} = \frac{Y_i \left(\alpha_i \tan^2 \theta - 1\right)}{\left(\alpha_i + 1\right) \tan^2 \theta}$$

$$Y_{ib} = \alpha_i Y_{ia}$$

with θ defined in 2.3.1 and

$$\alpha_i = \cot^2 \left(\frac{\pi f_{ap}}{2 f_0} \right)$$

where f_{ap} must be lower than the filter low band edge frequency.

Chapter 3

Antennas

Most of the detection techniques used in radio and millimeter astronomy rely on Heterodyne systems or direct superconducting detectors. In the first case the radiation is collected by a receiver, like a feed horn, down-converted in frequency and then treated like AC current in standard circuits. These architectures have been used even in recent space missions like Herschel and are suitable for detection of wavelengths up to tens of GHz or high resolution spectroscopy. For photometry, direct detection techniques are more sensitive [49]. Direct superconducting detectors are of great interest for CMB applications and they can benefit from all the advantages provided by antenna-coupling, which can be implemented on-chip in the form of planar structures. This is particularly advantageous in space based telescopes since the payload weight and size are a constraint.

An antenna is a device which emits (or collects) electromagnetic waves propagating through a waveguide and assures the power transmission between the source and free space. Antennas also provide polarization sensitive receivers, which is advantageous in the context of CMB polarimetry. Moreover, planar antennas can be fed with planar transmission lines, which can easily accommodate bandpass filters. These features are appealing for multi-chroic pixels dedicated to CMB stage "4" and have motivated the CMB community to develop antenna-coupled detectors. For this reason, I aim to develop an antenna which has low polarization leakage and large bandwidth. The latter is defined as the antenna operational frequency range, conventionally measured in the spectral region where the antenna reflection is below $-10\ dB$.

Figure 3.1.1: Antenna A with impedance Z_A excited by an electric field E_A on a network of impedance Z_a in front of an antenna B with impedance Z_B.

In this chapter I will discuss some basic antenna properties and the dual-resonant slot-antenna exploited for the development of a dual-color antenna-coulped LEKID discussed in chapter 5.

3.1 Basic properties

3.1.1 Reciprocity Theorem

Antenna properties can be studied in emission or reception. The reciprocity theorem states that properties are the same in both cases. This can be demonstrated considering two antennas A and B consisting only of passive elements as in Fig. 3.1.1. The current on A is given by

$$I_A = \frac{E_A}{Z_a + Z_A}$$

where E_A is the applied electric field and Z_A, Z_a are the impedance of the antenna and the network impedance respectively. The current I_A will generate a current I_B on the antenna B as follows

$$I_B = K\frac{\epsilon}{Z_b + Z_B}$$

with K being a proportionality factor and $\epsilon = K' I_A$. We obtain

$$I_B = KK'\frac{E_A}{(Z_a + Z_A)\,(Z_b + Z_B)}$$

To test the reciprocity we now excite the antenna B. Similarly to the previous case we obtain a current in A equal to

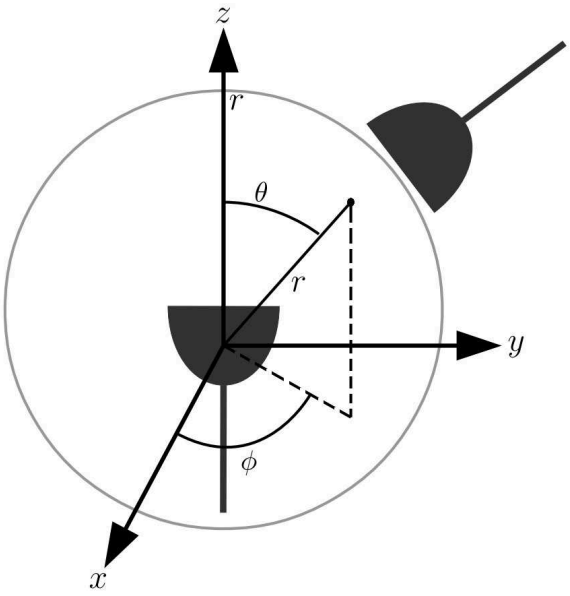

Figure 3.1.2: Measurement of the normalized power pattern. The receiver is scanning the antenna in ϕ and θ at a constant distance r from the transmitter.

$$I'_A = KK' \frac{E_A}{\left(Z'_a + Z'_A\right)\left(Z'_b + Z'_B\right)}$$

Since $I'_A = I_B$ we find that the new impedance Z' must be equal to Z. Therefore, if the antenna is adapted in transmission, it will be adapted in reception in the same way.

3.1.2 Radiation pattern

The radiation pattern of an antenna can be measured by transmitting power to a second antenna located at a constant distance r as shown in Fig. 3.1.2. The receiver scans the power pattern $P(\phi, \theta)$ in spherical coordinates measuring the normalized power pattern

$$P_n(\phi, \theta) = \frac{1}{P_{max}} P(\phi, \theta)$$

Because of the reciprocity theorem, using the fixed antenna as a receiver will not affect the measure. It is necessary that the radius r of the scanning sphere is large enough to be in the farfield region of the emitter. Considering an antenna of diameter D emitting at wavelength λ, this condition is satisfied when the curvature k_r of the wavefront is $k_r \ll 2D^2/\lambda$, and so $r \gg 2D^2/\lambda$ [51].

The total beam solid angle Ω_B of an antenna is given by the power pattern integrated over the entire solid angle as follows

$$\Omega_B = \iint_{4\pi} P_n(\phi, \theta)\, d\Omega \tag{3.1.1}$$

An ideal antenna emits only over a given solid angle and $P(\phi, \theta)$ is null elsewhere. In the real case the power pattern shows one or more main lobes and few side lobes which have a considerably smaller values of $P(\phi, \theta)$. The separation between main lobes and side lobes is a characteristic of the antenna. It is more useful to describe the antenna beam Ω_{MB} only in terms of the main lobe. In this case the integral 3.1.1 is confined in the range of ϕ and θ where the main lobe is present. The main beam efficiency η_B will be given by the ratio $\eta_B = \Omega_{MB}/\Omega_B$, this value is an indicator of the quality of the antenna in terms of directivity. The main lobe is characterized by the *full width to half power* (FWHP), which is the angular extension of the beam where $P(\phi, \theta)$ is the half of its maximum value.

The directive gain $G(\phi, \theta)$ can also be inferred from the power pattern. Even in this case the normalization factor is integrated over the entire solid angle, we obtain

$$G(\phi, \theta) = \frac{4\pi P(\phi, \theta)}{\iint P(\phi, \theta)\, d\Omega} \tag{3.1.2}$$

The amount of power P_d detected by the antenna is expressed by the *effective aperture* $A_e = P_d / |\langle P \rangle|$, where $|\langle P \rangle|$ is the incident power density. The effective aperture has the dimension of m^2 and is related to the antenna beam and the wavelength λ. To show what the relation is we can consider the case of an antenna confined inside a black body at temperature T at thermal equilibrium as shown in Fig. 3.1.3. The antenna directivity D can be inferred from 3.1.2 and 3.1.1 as

$$D = \frac{4\pi}{\Omega_B} \tag{3.1.3}$$

The surface A of the black body intercepted by the lobe is radiating to the antenna with intensity I_ν given by the Rayleigh-Jeans law

$$I_\nu = \frac{2k_B T}{\lambda^2} \Delta\nu \ \left[W m^{-2} H z^{-1} \Omega^{-1} \right] \tag{3.1.4}$$

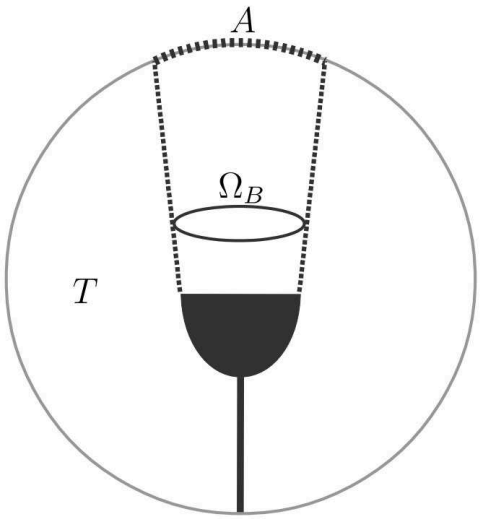

Figure 3.1.3: Antenna confined inside a black body at temperature T. The antenna beam Ω_B intercepts a portion A of the black body surface.

which results in a power W_d detected by the antenna[1] of

$$W_d = A_e \frac{k_B T}{\lambda^2} \Delta\nu \Omega_B \tag{3.1.5}$$

Because of the thermal equilibrium, the antenna radiates over the area A of black body the same amount of power L. This can be calculated by the Nyquist theorem as $L\Delta\nu = kT\Delta\nu$. Taking into account the antenna directivity in 3.1.3 we obtain

$$L'\Delta\nu = k_B T \Delta\nu D \frac{\Omega_B}{4\pi} \tag{3.1.6}$$

with L' being the power fraction incident on the surface A. Since equations 3.1.5 and 3.1.6 have to be numerically the same, we obtain

$$D = \frac{4\pi A_e}{\lambda^2} \tag{3.1.7}$$

None of the quantities in the latter equation depends on the thermodynamic, hence the assumption of thermal equilibrium is valid. Combining 3.1.3 and 3.1.7 we obtain the relation between the beam and the effective aperture as follows

[1]The power collected is divided by a factor 2 because only one polarization component is considered.

$$A_e \Omega_B = \lambda^2$$

which also sets the diffraction limit of an antenna.

3.1.3 Antenna temperature

Every object at thermal equilibrium emits some radiation for which we can associate an equivalent black body temperature. For low frequencies we can use the Rayleigh-Jeans approximation $h\nu \ll k_B T$, valid for $\nu\,[GHz] \ll 20.84\,T\,[K]$. In this regime we obtain

$$\exp\left(\frac{h\nu}{k_B T}\right) \cong 1 + \frac{h\nu}{k_B T}$$

and so we can rewrite the Planck's law 1.6.1 as

$$B_{RJ}\left(\nu, T\right) = \frac{2\nu^2}{c^2} k_B T \tag{3.1.8}$$

The latter shows that the black body brightness increases linearly with the thermodynamic temperature. We can thus define the *brightness temperature*, or equivalent temperature, as the temperature which results in the brightness given by 3.1.8. The thermodynamic temperature of an object in the Rayleigh-Jeans approximation is equal to its equivalent temperature divided by the emissivity ϵ. The latter is a dimensionless parameter of value between 0 and 1 that depends on the molecular structure of the object. Objects with emissivity equal to unity are surfaces of perfect black body. Common objects in millimeter and radio astronomy are the ground, which has an equivalent temperature of $300\,K$, and the sky. When looking at the Zenith the sky equivalent temperature depends on some factors like the weather and is usually below $10\,K$. Near the horizon the equivalent temperature can increase above $100\,K$. These emissions can be detected by the antenna weighted with the power pattern as follows

$$T_A\left(\phi, \theta\right) = \frac{\int_0^{2\pi} \int_0^{\pi} T_B\left(\phi, \theta\right) P\left(\phi - \phi_0, \theta - \theta_0\right) \sin\theta d\phi d\theta}{\int_0^{2\pi} \int_0^{\pi} P\left(\phi, \theta\right) \sin\theta d\phi d\theta}$$

where T_A is the *antenna temperature* and T_B the brightness temperature of the detected object.

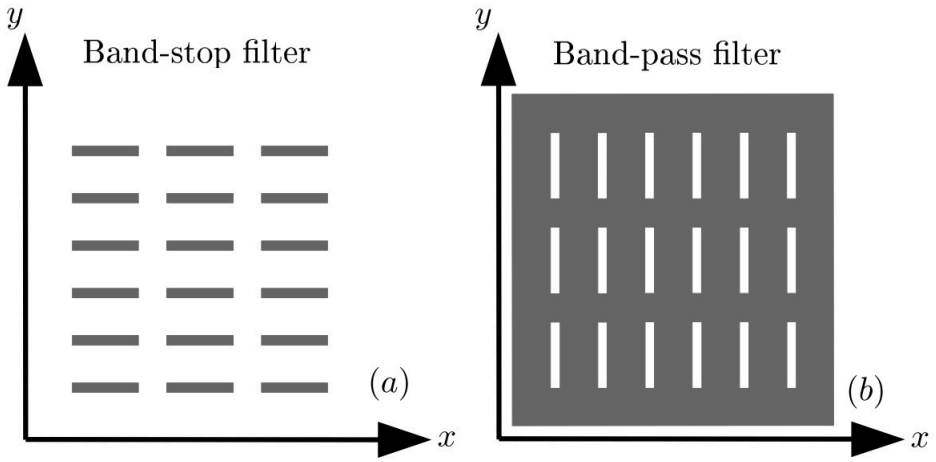

Figure 3.1.4: Metal is represented by gray objects, empty space by white color. Considering a linearly polarized signal along the x axis, the structure in (a) is a band-stop filter for frequencies that correspond to $\lambda/2$ the length of each segment. The complementary structure (b) has the slots oriented along the orthogonal polarization axis to take into account the fields transformation.

For optically thick sources the brightness temperature will be equal to the thermodynamic temperature of the object. The above expression for T_A is incomplete, a full description must take into account the antenna temperature T_P, the equivalent noise temperature and all kind of losses.

3.1.4 Babinet's Principle

Most planar antennas can be modeled as the mirror or dual of standard resonant geometries which can be solved analytically. In these cases the Babinet's principle gives the relationship between an antenna and its complementary structure. The Babinet's principle used in electromagnetism is an extension of the Babinet's principle used in optics, which can be derived from the Huygen's principle [53]. The complementary screen of a perfect electric conductor is a magnetic perfect conductor. Such a conductor can be reproduced by a perfect electric conductor with the condition of exchanging the electric field with the magnetic field and vice-versa. Therefore, when we apply the Babinet's principle, we consider conjugate sources for consistency with the field transformations. An example of this convention is given in Fig. 3.1.4. We can call V_a^- the ratio of the reflected electric field on the surface in 3.1.4 (a) to the reflection due to an infinite metal screen and V_b^- the same corresponding ratio for the surface in 3.1.4 (b). The Babinet's principle states that

$$V_a^- + V_b^- = 1$$

As a consequence, if the structure in (a) behaves like a Bband-stop filter, the structure (b) must behave like a band-pass filter.

3.2 Dipole antenna

I will now discuss the fundamental properties of dipole antennas. Because of the Babinet's principle, a simple slot antenna can be described as the dual of a standard dipole antenna. Slots are planar antennas already exploited by the CMB community. These can be arranged in phase array which has advantageous beam control that does not require optical elements like lenses or bulky components like feed-horns. This is particularly convenient for space applications since the payload weight is a constraint. In the present work I have chosen the model a slot antenna because it requires only few parameters to tune and is faster to simulate with finite element software compared to more complex planar antennas like the sinuous. Moreover, the slot is polarization sensitive and serves as the basic element of more complex design like the seashell or the twin-slot antenna. The latter has the advantage of suppressing potential propagation mode across the focal plane.

3.2.1 Main properties

A full mathematical description of the electromagnetic behavior is possible only for few antennas. One simple case we can consider is a wire of length l and negligible diameter excited at the center. A radiant element defined as such take the name of *dipole*. Considering the wire oriented along the z axis, we can write the current distribution as

$$I(z) = \begin{cases} I_0 \sin\left[k\left(\frac{l}{2} - z\right)\right] & 0 \leq z \leq l/2 \\ \\ I_0 \sin\left[k\left(\frac{l}{2} + z\right)\right] & -l/2 \leq z \leq 0 \end{cases}$$

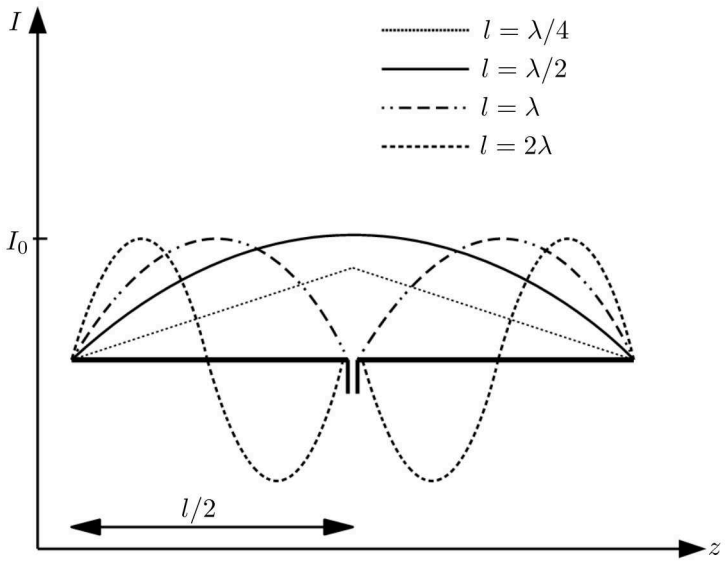

Figure 3.2.1: Current distribution along a dipole of length l excited at the center.

where I_0 is a constant. A plot of the current distribution along z for different values of l is shown in Fig. 3.2.1. The radiated field of a dipole can be calculated as a sum of infinitesimal dipole of length dl located all along the wire. The total field of the antenna is the *pattern multiplication* of each sub-component. The radiated field of one infinitesimal element is inferred starting from the Maxwell equations

$$\nabla \times \vec{H}_A = j\omega\epsilon\vec{E}_A$$
$$\vec{E}_A = -\nabla\varphi - i\omega\vec{A}$$

where $\vec{A}$ is the vector potential and φ the arbitrary scalar function in the Lorentz condition, hence

$$\varphi = -\frac{1}{j\omega\mu\epsilon}\nabla \cdot \vec{A}$$

With these assumption the radiated electric and magnetic field in polar coordinates are given by [52]

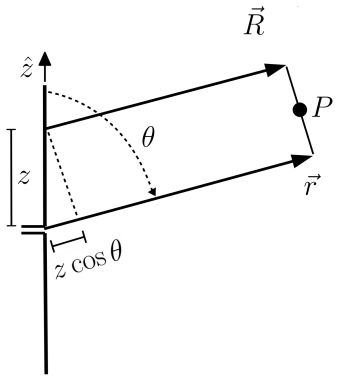

Figure 3.2.2: Notation used to calculate the farfield radiation pattern.

$$E_r = \eta \frac{I_0 l \cos\theta}{2\pi r^2}\left(1 + \frac{1}{jkr}\right) e^{-jkr}$$

$$E_\theta = j\eta \frac{kI_0 l \sin\theta}{4\pi r}\left(1 + \frac{1}{jkr} - \frac{1}{(kr)^2}\right) e^{-jkr}$$

$$H_\phi = j \frac{kI_0 l \sin\theta}{4\pi r}\left(1 + \frac{1}{jkr}\right) e^{-jkr}$$

$$E_\phi = H_r = H_\theta = 0$$

with $\eta = \sqrt{\mu/\epsilon}$ being the intrinsic impedance of the medium where the electromagnetic wave propagates and the vector $\vec{r}$ is calculated from the dipole middle point. We are interested on the farfield region, where $kr \gg 1$. The vector $\vec{R}$ originated at the infinitesimal dipole has the following relationship with $\vec{r}$ as shown in Fig. 3.2.2

$$R \simeq r - z\cos\theta \quad for\ phase\ terms$$
$$R \simeq r \quad for\ amplitude\ terms$$

Under these assumptions we can rewrite the radiated fields for an infinitesimal dipole as follows

$$dE_\theta = j\eta \frac{kI_0 e^{-jkr} \sin\theta}{4\pi r} e^{-jkz\cos\theta} dz$$

$$dH_\phi = j \frac{kI_0 e^{-jkr} \sin\theta}{4\pi r} e^{-jkz\cos\theta} dz$$

$$dE_r \simeq dE_\phi = dH_r = dH_\theta = 0$$

The pattern multiplication involves the integrals of these quantities multiplied by a space factor. More detailed calculations can be found in [52] and result in the following expression for a general dipole of length l

$$E_\theta = j\eta \frac{I_0 e^{-jkr}}{2\pi r} \left[\frac{\cos\left(\frac{kl}{2}\cos\theta\right) - \cos\left(\frac{kl}{2}\right)}{\sin\theta} \right]$$

$$H_\phi = j \frac{I_0 e^{-jkr}}{2\pi r} \left[\frac{\cos\left(\frac{kl}{2}\cos\theta\right) - \cos\left(\frac{kl}{2}\right)}{\sin\theta} \right]$$

Some plots of the dipole radiation pattern for different values of l are shown in Fig. 3.2.3. The beam directivity increases with the dipole length.

3.2.2 Slot Antenna

In the millimeter domain slot antennas cut in metallic ground planes are efficient radiating elements. A slot antenna is the complementary structure of a floating strip. Because of the Babinet's principle, the slot antenna will radiate according to the dipole antenna described in section 3.2.1. The radiating electromagnetic field will be given by the solution for the Maxwell equations in free space

$$\nabla^2 \vec{E} = \mu\epsilon \frac{d^2\vec{E}}{dt^2}$$

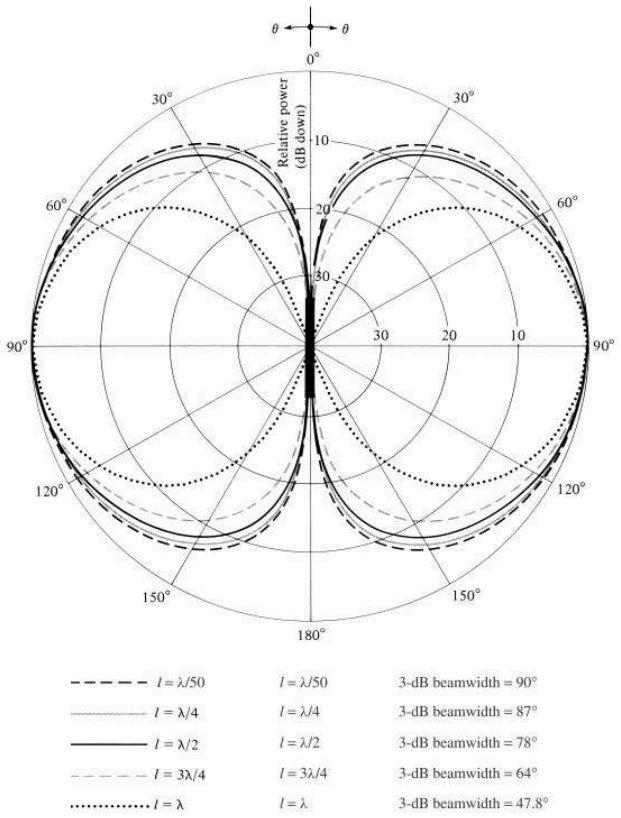

Figure 3.2.3: Dipole beam for different values of l. [52]

$$\nabla^2 \vec{B} = \mu\epsilon \frac{d^2 \vec{H}}{dt^2}$$

$$\nabla \times \vec{E} = -\mu \frac{d\vec{H}}{dt}$$

$$\nabla \times \vec{H} = -\mu \frac{d\vec{E}}{dt}$$

The boundary conditions differ between the slot and the dipole. Considering the coordinate system as in Fig. 3.2.4 and antenna symmetry [52], we obtain for a dipole

$$H_x = 0 \quad \textit{within the dipole region}$$
$$H_y = H_z = 0 \quad \textit{outside the dipole region}$$

Similarly for the slot we obtain

$$E_x = 0 \quad \textit{within the slot region}$$
$$E_y = E_z = 0 \quad \textit{outside the dipole region}$$

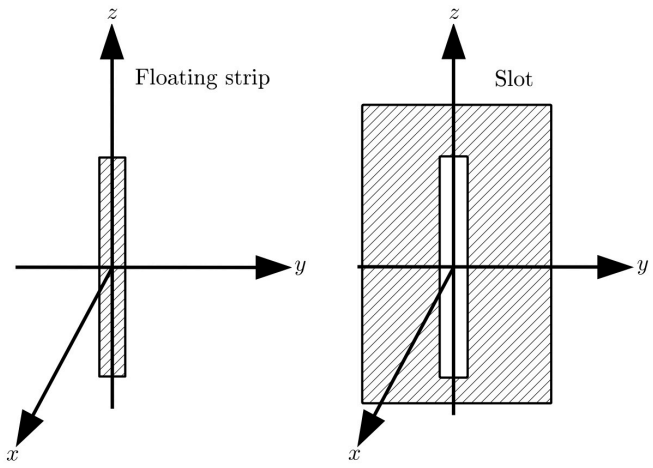

Figure 3.2.4: A floating strip (left) and its complementary plane (right).

For both the radiating elements the problem has the same solution and the fields distribution within the slot will be the same of those in the dipole under the condition of replacing E with H.

Slot antennas can be excited by microstrip coupling. In this case the microstrip crosses the slot along its short axis. The strip termination is crucial to adapt the microstrip to the slot impedance. The slot antenna is surrounded by a magnetic field that takes the name of *magnetic current* in analogy with a standard dipole. The slot impedance depends on the position along the long edge and it is generally proportional to the ratio of the voltage drop across the two facing edges along the small axis to the value of H. The electric field at the slot termination edges must be zero, hence the impedance is null at these points. While moving toward the slot center, the electric field gets larger and reach the maximum value at the center for a slot which is resonating at $\lambda/2$. At this point the impedance Z_s can be inferred considering impedance Z_d of the complementary dipole. By using the Babinet's principle we obtain

$$Z_s Z_d = \frac{\eta^2}{4}$$

where η is the intrinsic impedance of the surrounding media.

3.2.3 Dual-Resonant Slot

Slot antennas are selective in linear polarization, which is essential for CMB observation, but naturally narrow-band with high quality factor. The bandwidth is usually

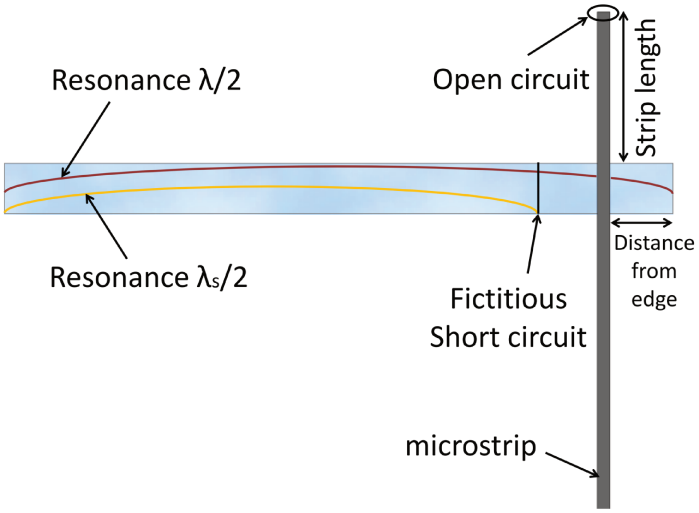

Figure 3.2.5: Microstrip parameters used for the excitation of the dual-resonant slot antenna. The fictitious short circuit sets the antenna edge for the λ_s resonance.

significantly smaller than other microstrip excited antennas like the sinuous. This feature diverges with the antenna-coupling detectors concept for which the same antenna is used to extract more than one band per pixel. Several techniques exist to increase the resonance width; most of them involves special terminations for the microstrip. We consider in this section a technique described in [55] which involves the microstrip generated electric field interference with the slot electric field. Such an interference results in a dual-resonant slot antenna. In order to understand the working principle, we can start considering to excite a slot antenna close to the edge as shown in Fig. 3.2.5. Because of the considerations in 3.2.2, in this configuration the microstrip must be of low impedance. Common dielectrics used for low temperature applications are silicon oxides with dielectric constant below 4 and thickness smaller than $1\,\mu m$. With these parameters, microstrip narrower than few μm are of low characteristic impedance and can be used to excite a slot close to the edge with minimal effort on the design.At one particular frequency above the standard $\lambda/2$ resonance, the electric field generated by the microstrip cancels out the electric field at one point inside the slot. Since the electric field has a null, that point is equivalent to a short circuit. As a result, the microstrip induces a new resonance $\lambda_s/2$ where $\lambda_s < \lambda$ and the electric field is confined between one edge of the slot and the fictitious short circuit. The microstrip is terminated with an open circuit well beyond the slot. The termination acts like a stub for which the length can be tuned to select the resonance λ or λ_s. The existence and location of the fictitious short circuit along the slot is determined by the microstrip characteristic impedance, the

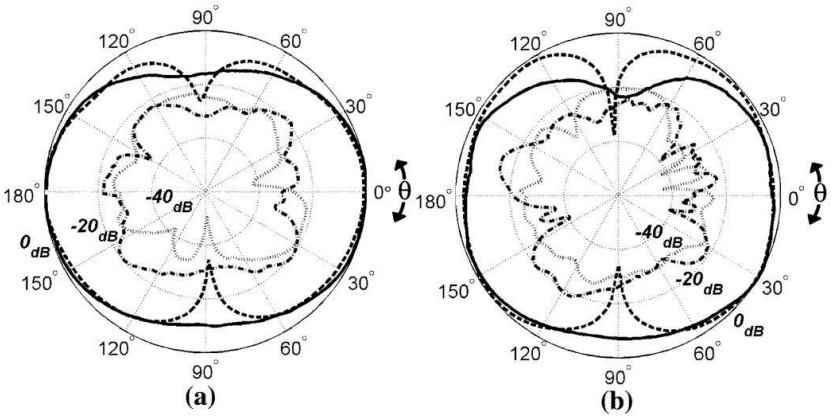

Figure 3.2.6: Radiation patterns of the two frequencies of a dual-resonant slot antenna operating around 3 GHz (a) and 4 GHz (b). Solid lines and solid lines with dots show the H-plane Co-Pol and X-Pol respectively. Dashed lines and dotted lines show the E-plane Co-Pol and X-Pol respectively. [55]

slot width, the distance from the edge and the strip length. In the particular case of λ_s close to λ, which is basically an upper limit on the distance from the edge, it is possible to tune the strip length to an average value that can excite both the resonances. The resultant antenna resonance is wider than a single resonant slot antenna. This technique allows reaching bandwidths larger than 30% retaining the dipole radiation pattern (Fig.) in the whole operational frequency band.

Chapter 4

Kinetic Inductance Detectors

All detectors currently under development for CMB observation exploit superconducting properties of metals. The most common detectors are bolometers in the form of Transition Edge Sensor (TES) that exploits the transition between superconducting and normal phase of metals to detect photons. In this chapter I will explain the working mechanism of Kinetic Inductance Detectors (KIDs) that are high quality factor LC superconducting resonators. Application on photon detection of these devices is quite recent and the theory of KIDs has been developed mostly on the last decade. KIDs are an alternative to TES since they can provide higher multiplexing rate and are easier to fabricate. Therefore, they are advantageous for large focal plane arrays as required for B-modes polarimetry.

I will introduce some important aspects of superconductivity which are crucial for the understanding of KIDs mechanism. The chapter is organized as follows:

- **KIDs theory**: This section introduces the basic properties of resonant circuits which are exploited for KID technology. Then I will describe the mechanism of KIDs as photon detector. The detection occurs when a photon of high enough energy breaks one or more Cooper pairs in the superconducting metal. This event changes the inductance of the circuit, and so the resonant frequency.

- **Superconducting properties of KIDs**: The kinetic inductance in superconductors arises from the two fluids model of superconductivity. I will explain in this section how the Cooper pair density affects the temperature stability of KIDs and why they are more stable than bolometers. The binding energy of a

Cooper pair is a characteristic of each metal. It also sets an energy threshold for photons in order to break a Cooper pair. I will describe the origin of Cooper pairs and why only few metals are suitable for KIDs development. Furthermore, KIDs are fabricated in thin metal layers, I will explain how this aspect influences the metal properties in terms of kinetic inductance.

- **KIDs sensitivity**: I will describe the readout approach used for KIDs arrays and the main sources of noise that are characteristic of superconducting resonators which limit the KIDs sensitivity.

4.1 KIDs theory

4.1.1 Series RLC circuits

To understand the behavior of a KID it is necessary to study some properties of RLC circuits. The main aspect we are interested in is the resonant frequency f_0. It can be calculated considering the input impedance Z_{in} of the circuit, which is the sum of the impedance of every component

$$Z_{in} = R + j\omega L + \frac{1}{j\omega C} = \frac{2P_{in}}{|I|^2} \tag{4.1.1}$$

where ω is the angular frequency, I the current and P_{in} the power delivered to the resonator. The circuit stores energy in the form of magnetic and electric energy. The average value W_e and W_m of those quantities is given by

$$W_e = \frac{1}{4}|I|^2 \frac{1}{\omega^2 C}$$

$$W_m = \frac{1}{4}|I|^2 L$$

Some of the power P_{out} is dissipated by the resistor because of the Joule effect [40]

$$P_{out} = \frac{1}{2}|I|^2 R$$

With those assumptions we can rewrite P_{in} as

$$P_{in} = P_{out} + 2j\omega\left(W_m - W_e\right)$$

and

$$Z_{in} = \frac{2\left(P_{out} + 2j\omega\left(W_m - W_e\right)\right)}{|I|^2}$$

By definition, at resonance the average electric energy equals the average magnetic energy. In other words, the resonant frequency is defined when $W_m = W_e$, which gives

$$Z_{in} = \frac{2P_{out}}{|I|^2} = R$$

The effect of reactive elements is to produce a phase shift φ between voltage and current given by

$$\varphi = \arctan\frac{X}{R}$$

where X is the total reactance of the circuit. From 4.1.1 we obtain

$$X = \omega L - \frac{1}{\omega C}$$

The two components of the reactance must add to zero at resonance, so

$$\omega_0 = \frac{1}{\sqrt{LC}} \tag{4.1.2}$$

The input impedance has a minimum when $\omega = \omega_0$ and is purely real since the inductance and capacitance have the same value with opposite sign. Moving from the resonance to the frequencies where the current drop to $I_0/\sqrt{2}$, which are the cutoff frequencies, $\varphi = 45°$ and the total reactance of the circuit is numerically equivalent to the resistance R. For frequencies $\omega < \omega_0$ the resonator shows a capacitive behavior. For frequencies $\omega > \omega_0$ the behavior is dominated by the inductor.

The resonance of a RLC circuit is characterized by the quality factor Q. It is defined as the angular frequency at resonance multiplied by the ratio of the energy stored in the resonator to the power loss

$$Q = \omega_0 \frac{W_m + W_e}{P_{out}}$$

The quality factor is inversely proportional to the loss of the circuit. It can be calculated at resonances considering $W_e = W_m$ as follows

$$Q(\omega_0) = \omega_o \frac{2W_m}{P_{out}} = \frac{1}{\omega_0 RC} = \omega_0 \frac{L}{R}$$

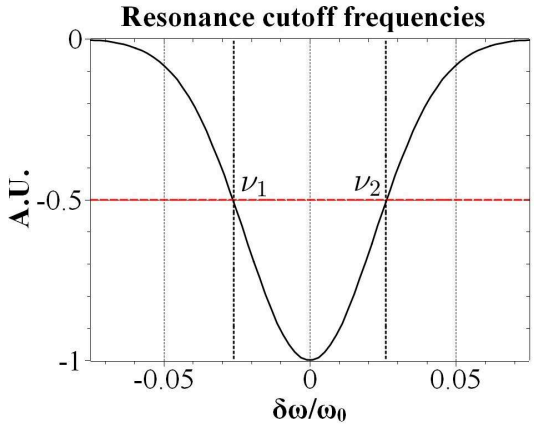

Figure 4.1.1: Example of resonance curve. The two cutoff frequencies are located at $-3\ dB$ from the peak, which corresponds to half of the signal.

In the case of a KID, the resonator is coupled to a feedline. The coupling will be carried out with a certain quality factor Q_c. Therefore, the total quality factor Q_{tot}, or loaded quality factor, of the resonance measured on the feedline will be given by

$$\frac{1}{Q_{tot}} = \frac{1}{Q} + \frac{1}{Q_c} \tag{4.1.3}$$

The bandwidth of the resonance peak is defined at the cutoff frequencies ν_1, ν_2 as $B = \nu_2 - \nu_1$. As shown in Fig. 4.1.1 the two cutoff frequencies are calculated at those points where the signal is half of its value at resonance. The bandwidth is related to the quality factor and the resonant frequency ν_0 as follows

$$Q_{tot} = \frac{\nu_0}{B}$$

It is clear from the latter equation that the quality factor is a measure of the selectivity in frequency. High values of Q means narrow bandwidth resonance. As an example of the advantage in terms of detector multiplexing, working with superconducting resonators having $Q_{tot} = 10^4$ allows to multiplex three resonators within a bandwidth of 1 MHz. Decreasing the loaded quality factor by a factor 10 will result to an increased bandwidth of a factor 10 to accommodate the same number of resonators. The internal quality factor is also related to the voltage across the circuit components. At the resonant frequency the value of Q is equal to the ratio of the voltage drop across the inductor or the capacitor to the voltage drop across the resistance.

The input impedance can be rewritten in terms of the quality factor and resonant

frequency. Combining 4.1.1 and 4.1.2 we obtain

$$Z_{in} = R + j\omega L\left(1 - \frac{1}{\omega^2 LC}\right) = R + j\omega L\left(1 - \frac{\omega^2 - \omega_0^2}{\omega^2}\right)$$

We can now define the distance from the resonance as $\Delta\omega = (\omega - \omega_0)$ and replacing the numerator in the latter equation as follows

$$\omega^2 - \omega_0^2 = (\omega - \omega_0)(\omega + \omega_0) = \Delta\omega\,(2\omega - \Delta\omega) \approx 2\omega\Delta\omega$$

which is valid for small $\Delta\omega$. Therefore, we finally obtain

$$Z_{in} \approx R + j2L\Delta\omega = R + j\frac{2RQ\Delta\omega}{\omega_0}$$

4.1.2 KIDs working principle

As stated in its name, KIDs exploit the kinetic inductance of superconductors to detect photons. The basic idea is that a resonant circuit has a natural frequency which depends on the value of its capacitance C and inductance L. Under certain circumstances photons have the capability of being absorbed by a superconducting metal and alter the factor L of the circuit. This event shifts the resonant frequency to a longer wavelength. Therefore, a measure of such a resonant frequency is directly proportional to the power absorbed on the circuit.

Early KIDs were simple quarter wave resonators coupled to a readout line. These circuits have the disadvantage of a non-uniform current distribution along the transmission line and the fact that the physical size of the structure is a quarter wavelength of the natural frequency. This is problematic since the readout electronic requires low frequency resonant elements, hence quarter wave resonators design involves long transmission lines. Typical readout tones are around $3\,GHz$, which is 10 cm in terms of wavelength. In the context of CMB stage '4', reducing the size of the pixel is critical to optimize the area filling efficiency. Resonators can be reduced in size by adopting lumped RLC circuit instead of the quarter wavelength line. Each element of an RLC circuit can be modeled out of a superconducting transmission line. The resistive and inductive behavior appears from the two fluid model of superconductivity described below in this chapter. The capacitance is mostly given by geometric factors and its presence lowers the natural frequency of the circuit, therefore shrink-

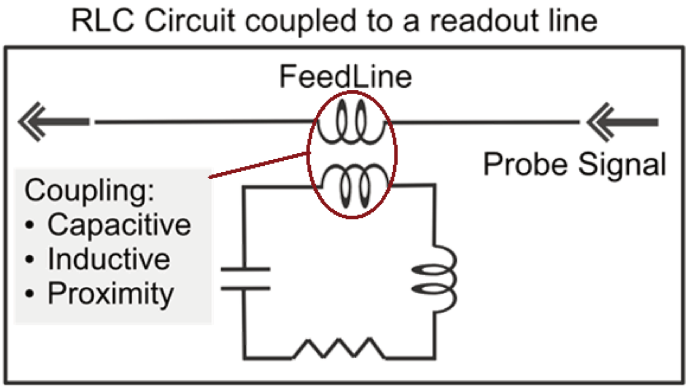

Figure 4.1.2: *RLC* circuit coupled to a readout line. The quality factor measured by the feedline depends on both the quality factor of the resonator and the coupling quality factor.

ing the physical size of the resonator. Detectors developed like that take the name of Lumped Element Kinetic Inductance Detectors (LEKIDs). Those are lumped in the sense that the structure is smaller than the wavelength that excite them. To read the resonant frequency the resonator is coupled to a feedline as shown in Fig. 4.1.2. The coupling technique may vary depending on the design.

The total inductance L_{tot} has two contributions, the internal inductance L_{int} and the external inductance L_{ext} which are defined as follows

- The internal inductance L_{int} is given by the kinetic inductance L_k and the magnetic inductance L_m. The existence of L_k arises from the two fluids model. In two words, the current carried by Cooper pairs in a superconductor have a larger inertia with respect to normal electron and since the effect of scattering is null, the acceleration time under an alternating electric field is not negligible [56]. The inertia causes a delay in the generated current with respect to the voltage phase. This effect reproduces the common behavior of an inductance and is called kinetic inductance.The magnetic inductance L_m is given by the magnetic field generated by the flowing charge carriers along the metal.

- The external inductance L_{ext}, also called geometrical inductance L_g, depends only on the structure geometry and is fixed by the design. Typically, the transmission line designed for resonators is folded in a meander-shape. The value of L_{ext} in these cases will be given by the cross section of the conductor and the geometrical parameters of the meander arms such as the distance between two nearest segments [57].

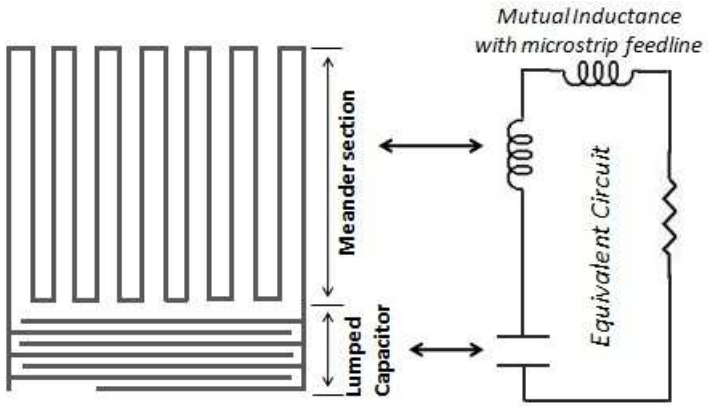

Figure 4.1.3: Example of a Lumped Element Kinetic inductance Detector. The transmission line and the interdigital capacitor form a LC circuit. The physical size of the resonator can be 100 times smaller than λ^2 of the resonant frequency.

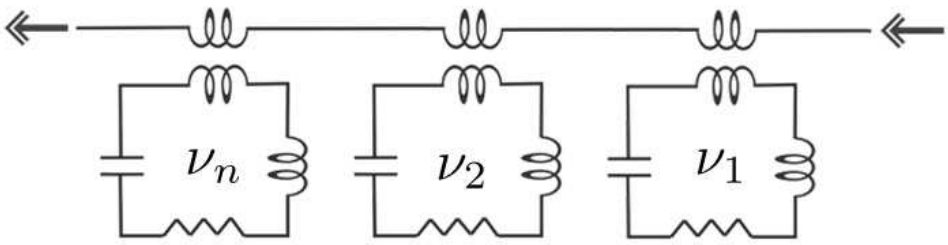

Figure 4.1.4: KIDs multiplexing over a single feedline. Depending on the resonance quality factor and readout electronic, a single feedline can handle up to few thousands resonators.

A signal of frequency f propagating through the feedline is insensitive to the resonator when $f \neq f_0$, with f_0 the natural frequency of the resonator. In the case of $f = f_0$ the energy is stored within the resonator and the transmission parameter of the line suddenly drops, producing a typical resonance peak. The photon absorption occurs along the inductor, which is the section where the current is most important. This is necessary to optimize the detector response.

A common LEKID shape is a meander inductor coupled with an interdigital capacitor. This circuit is shown in Fig. 4.1.3. The entire structure is fabricated as a single metallization level over a silicon substrate. The meander section can be directly illuminated to absorb photons, in such a case the design has to take into account the impedance matching with the free space.

By adjusting one arm length of the interdigital capacitor it is possible to tune the natural frequency of the resonator. This allows to couple several resonators with different resonant frequency to the same readout transmission line as shown in Fig. 4.1.4. The multiplexing factor is the greatest advantage of the KIDs technology over

the more common bolometers. Generally, we want the resonances to be separated by at least three times the full width at half maximum (FWHM). Having the resonators too close to each other can alter or superimpose the resonance curves. Typically, the multiplexing rate can be increased up to few thousands of resonators, it depends on the available bandwidth of the readout electronic and the resonators quality factor. For this reason, each resonator must have a high quality factor, usually above 10^5. This value can be achieved only with superconducting metals deposited in thin layers. Most of the time the metal thickness is small enough that charge carrier behavior is no longer described by classical models and we need a mathematical description of superconductivity in the so-called dirty limit or anomalous limit.

4.2 Superconducting properties of KIDs

4.2.1 Complex conductivity

In 1908 Prof. Heike Kamerlingh Onnes at University of Leiden was the first to liquefy helium and reached a temperature 4 K. That made possible to attain superconductivity in certain metals. Onnes discovered that the resistivity of mercury drop down to zero when temperature decreases below 4.1 K and he gained the Nobel prize in 1913. Superconductivity occurs in some specific metals when the temperature drops below a critic temperature T_c, which is a characteristic of each metal. Above T_c the electrical current is carried by electrons. Because of the scattering events with the positive ions of the metal lattice, metals have a small resistivity ρ which depends on temperature. In a normal metal ρ decreases with the temperature and tends to a finite value for $T \to 0$ as shown in Fig. 4.2.1. In superconductors, below T_c, two electrons can pair together forming a new charge carrier, often called superelectron. This new particle has an integer spin since it forms as the sum of the two electrons spin. Superelectrons follow the Bose-Einstein statistic and don't scatter with the positive ions like electrons do. Such a behavior causes the resistivity to suddenly drop to zero when superelectrons are the charge carriers.

A mathematical description of superconductivity was given by Bardeen, Cooper, and Schrieffer in 1957 (BCS Theory) [61] and led to the Nobel prize in 1972. They explained the superconductivity using an electron-phonon interaction that causes

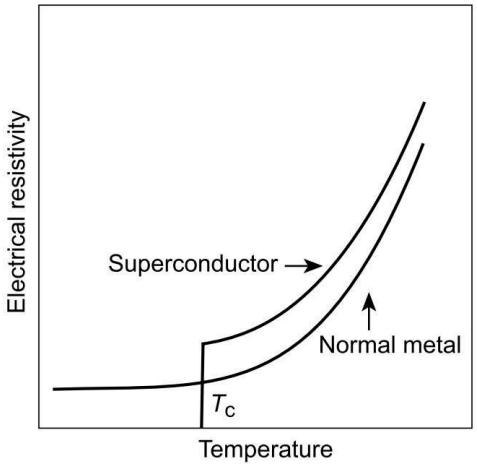

Figure 4.2.1: Temperature dependence of resistivity for normal metals and superconductors. Below T_c the resistivity drops to zero in superconductors. Credit to [60]

the two electrons to couple, so the superelectron takes also the name of *Cooper pair*. The binding energy of a Cooper pair depends on the critical temperature and is typically of the order of few meV. This value is so small that at high temperature the thermal energy brakes the pair into two electrons. Therefore, metals will transit to the superconducting phase only at cryogenic temperature.

Two fluid model

Because of the differences that exist between electrons and Cooper pairs, superconducting transmission lines will have a distinct ability to conduct electrical current when moving from DC to time variable signals. At microwave frequencies superconductors show a resistive effect as was observed by London early in 1940 [62]. This is the main characteristic of superconductors which has been exploited for detector development. An explanation of such phenomena can be derived by using the classical Drude model. It allows us to infer the conductivity of a metal from a kinetic approach. The Drude model considers electrons of mass m_e accelerated by an external electric field $\boldsymbol{E}$. These electrons will move through the metal with an average velocity $\boldsymbol{v}_{av}$. The electrons can scatter with the positive ions of the metal lattice. The average travel time of an electron before its next collision is given by the value of τ, which is called mean free time or relaxation time. The starting electron velocity $\boldsymbol{v}_0$ is assumed to be oriented randomly so that $\boldsymbol{v}_{av}$ has no contribution from $\boldsymbol{v}_0$. Therefore, the average velocity will be given only by the contribution of the electric field. In the case of $\boldsymbol{E}$ constant with time we obtain

$$\boldsymbol{v}_{av} = -\frac{e\boldsymbol{E}\boldsymbol{\tau}}{m_e} \tag{4.2.1}$$

Considering the density of electrons n_e, we can write the current density as

$$\boldsymbol{J} = -n_e e \boldsymbol{v}_{av} = \sigma \boldsymbol{E} \tag{4.2.2}$$

which is the Ohm's law. Combining 4.2.1 and 4.2.2 we obtain

$$\boldsymbol{J} = \left(\frac{n e_e^2 \tau}{m_e}\right) \boldsymbol{E} \longrightarrow \sigma = \left(\frac{n_e e^2 \tau}{m_e}\right) \tag{4.2.3}$$

where σ is the conductivity of the metal in the DC case.

We now consider the AC case; $\boldsymbol{E}$ is no longer time independent but varies accordingly to the angular frequency ω. The equation of motion of the electron will be given by [63]

$$\frac{d\mathbf{p}\left(t\right)}{dt} = -\frac{\mathbf{p}\left(t\right)}{\tau} + f\left(t\right) \tag{4.2.4}$$

where $\boldsymbol{p}\left(t\right)$ is the momentum and $f\left(t\right)$ is the additional momentum given by the influence of $\boldsymbol{E}$. The first term on the right of 4.2.4 represents the frictional dumping due to electrons collisions. Assuming the electric field to vary with time as follows

$$\mathbf{E}\left(t\right) = Re\left(\mathbf{E}\left(\omega\right) e^{-i\omega\tau}\right)$$

we can find a steady-state solution for $\boldsymbol{p}$ of the form

$$\mathbf{p}\left(t\right) = Re\left(\mathbf{p}\left(\omega\right) e^{-i\omega\tau}\right)$$

Combining the latter with 4.2.4 we obtain

$$-i\omega\mathbf{p}\left(\omega\right) = -\frac{\mathbf{p}\left(\omega\right)}{\tau} - e\mathbf{E}\left(\omega\right)$$

The conductivity can be inferred from the definition of the current density like in the stationary case. Therefore

$$\mathbf{J}\left(\omega\right) = \sigma\left(\omega\right)\mathbf{E}\left(\omega\right) = -\frac{n_e e \mathbf{p}\left(\omega\right)}{m_e} = \frac{\left(n_e e^2/m_e\right)\mathbf{E}\left(\omega\right)}{\left(1/\tau\right) - i\omega}$$

which leads to the expression for the conductivity

$$\sigma(\omega) = \sigma_1 - i\sigma_2 = \frac{ne_e^2\tau}{m_e(1+\omega^2\tau^2)} - i\frac{ne_e^2\omega\tau^2}{m_e(1+\omega^2\tau^2)} = \frac{\sigma_0}{(1-i\omega\tau)} \tag{4.2.5}$$

where σ_0 is the conductivity in the DC case. As expected, $\sigma(\omega)$ is composed of a real and an imaginary part. The real part is the term that arises from the scattering events on positive ions and determines the resistance of the metal. The imaginary part is due to the inertia of the electrons. Because of their mass, electrons can't respond instantaneously to the applied electric field, hence there is a delay between the phase of the electric field and the phase of the current. This property is called *Kinetic Inductance*, since the current delay is the typical behavior produced by an inductor. The ratio σ_2/σ_1 is equal to $\omega\tau$ and at microwave frequencies $\omega\tau \ll 1$. To prove this limit we can consider aluminum, for which the concentration of electrons n_e can be calculated considering 3 times[1] the concentration of atoms. Using 4.2.3 we obtain $n = 1.8 \times 10^{-29} m^{-3}$ and $\tau = 7.2 \times 10^{-15} s$. For $\boldsymbol{E}$ varying at 300 GHz corresponds a period of $T = 3.3 \times 10^{-12} s$ and the product $\omega\tau$ is of the order of 10^{-3}. As a consequence, the kinetic inductance in normal metals is negligible. From the point of view of the Drude model, it means that the electrons scatter on a positive ion before being affected by the electric field variation, even at microwave frequencies.

The same approach is valid for superconductors. The conductivity can be inferred with the Drude model with the condition of considering the Cooper pairs as charge carriers. Hence, we swap n_e with n_s, the density of superelectrons, and m_e with m_s, the mass of a Cooper pair. Because of the argument above about the integer spin, we neglect the frictional damping term on the equation of motion. These assumptions led to a pure imaginary conductivity as follows

$$\mathbf{J}(\omega) = i\frac{n_s e^2}{\omega m_e}\mathbf{E} \longrightarrow \sigma_s = -\frac{n_s e^2}{\omega m_e} \tag{4.2.6}$$

As we will see in the next section, the number of Cooper pair is a function of temperature. In the ideal case of $T = 0$ all the available electrons are coupled in Cooper pairs and don't contribute to conductivity, Hence, equation 4.2.6 is valid. On a real case, even below the critical temperature, the thermal energy do not allow some electrons to couple and may contribute as charge carriers. Therefore, the total conductivity

[1] Aluminum has three valence electrons, hence each atom contributes with three electrons to the conductivity.

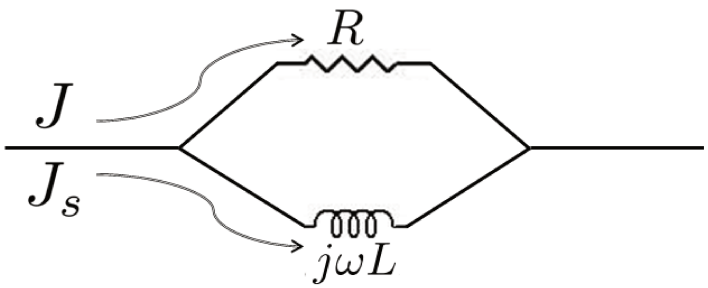

Figure 4.2.2: Two fluid model of superconductivity. The current J generated by normal electrons follow a resistive path of resistance R. The supercurrent J_s is equivalent to an inductor in parallel with R.

σ_{tot} can be written as the sum of the conductivity of each particle that contribute to the current

$$\sigma_t = \frac{n_e e^2 \tau}{m_e} - i\frac{n_s e^2}{m_e \omega} \tag{4.2.7}$$

where the sum $n_e + n_s$ is equal to the density of the charge carriers n. Equation 4.2.7 states that conductivity in superconducting metals depends both on frequency and the ratio n_e/n_s. As a consequence, we get two contributions to the current. Normal electrons are responsible of resistive effect while Cooper pair cause inductive effect along the line. The current generated by Cooper pairs, often called supercurrent J_s, leads to the *two fluid model* of superconductivity as shown in Fig. 4.2.2. It describes the behavior of a superconducting transmission line as an inductance and a resistor in parallel. Considering the DC case, we have $\omega = 0$ and $\sigma_i \to \infty$, hence the inductor is a short circuit over the resistance R and the current will flow carried by Cooper pair. This is exactly what we expected for superconducting lines in direct current. While we increase the frequency, the impedance of the inductor, which is proportional to ωL, increases and part of the current starts to flow on the resistive path led by normal electrons. This is the origin of the resistive effect in superconductors when dealing with high frequency signals such as in the microwave region.

4.2.2 Cooper pair density

We have seen in the previous section that from the two fluid model the ratio n_s/n_e determines the impedance of a superconducting transmission line in terms of resis-

tivity and inductance. We know that at $T = 0$ it has to be

$$\frac{n_s\,(0)}{n} = 1 \tag{4.2.8}$$

since in the ideal case all electrons are coupled in Cooper pairs. To infer the temperature dependence of superelectrons density we consider the Ginzburg-Landau theory described in [65]. Magnetic fields can't penetrate into a superconductor more than a certain length. This effect is known as the *Meissner effect*, for which the magnetic field is rejected on the transition between the normal and superconducting phase. The depth where the magnetic field reduces of a factor e is the *London penetration depth* $\lambda_L\,(T)$, which is temperature dependent and characteristic of each metal [66]. An expression for λ_L is given by

$$\lambda_L\,(T) = \left(\frac{m}{\mu_0 n_s(T) e^2}\right)^{1/2} \tag{4.2.9}$$

and the temperature dependence have the form

$$\lambda_L(T) = \lambda_L(0)\left[1 - \left(\frac{T}{T_c}\right)^4\right]^{-1/2}$$

The value of $\lambda_L(0)$ can be inferred combining 4.2.9 with 4.2.8, then the temperature dependence of n_s can be expressed in terms of the ratio $\lambda(0)/\lambda(T)$ as follows

$$\frac{n_s(T)}{n} = \left(\frac{\lambda_L(0)}{\lambda_L(T)}\right)^2$$

that leads to

$$\frac{n_s(T)}{n} \sim \left[1 - \left(\frac{T}{T_c}\right)^4\right] \tag{4.2.10}$$

which implies

$$\frac{n_e}{n} \sim \left(\frac{T}{T_c}\right)^4$$

Equation 4.2.10 is plotted in Fig. 4.2.3. We can distinguish two regions:

- $T \sim T_c$: the ratio n_s/n depends on the temperature with a slope of -4. This

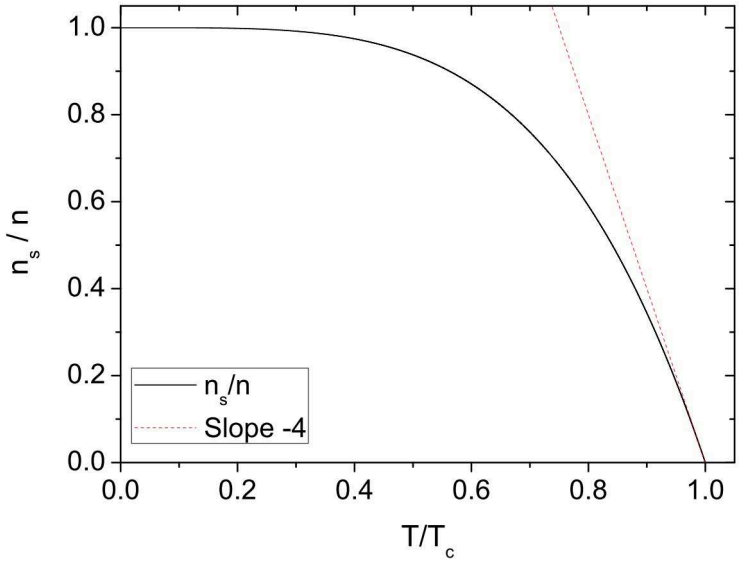

Figure 4.2.3: Cooper pair density normalized to the charge carrier density as a function of the temperature. Near the critical temperature the Cooper pair density increases with temperature with a slope of -4 (dashed red line) and became quite stable below $0.2\ T_c$.

is the region where detectors based on thermal effect, like the Transition Edge Sensors (TES), are more sensitive. Detectors based on Cooper pair counting are inefficient because the sensitivity increases with the number of Cooper pairs and temperature fluctuations affect the measure.

- $T < 0.2\,T_c$: The number of Cooper pairs is quite stable in temperature and the metal is less sensitive to temperature fluctuations.

Values of critical temperature for commonly used superconductors are around $T_c \sim 1\ K$. This involves both pure metals and alloys. As a consequence, superconducting detectors need to be cooled down to temperature $T < 300\ mK$ to perform correctly.

4.2.3 Binding energy

In crystalline solids each atom confines the electrons in quantized energy orbitals. Depending on the lattice, these orbitals can form energy regions available for electrons, the valence band. An energy band can accommodate electrons depending on the availability of the corresponding energy state. Because of their spin, electrons must follow the Pauli exclusion principle, hence the lower state available is given by the sum of all the already occupied states that add up to a lower energy, called the Fermi energy ϵ_F. The ability of conduct electrical current depends on the pres-

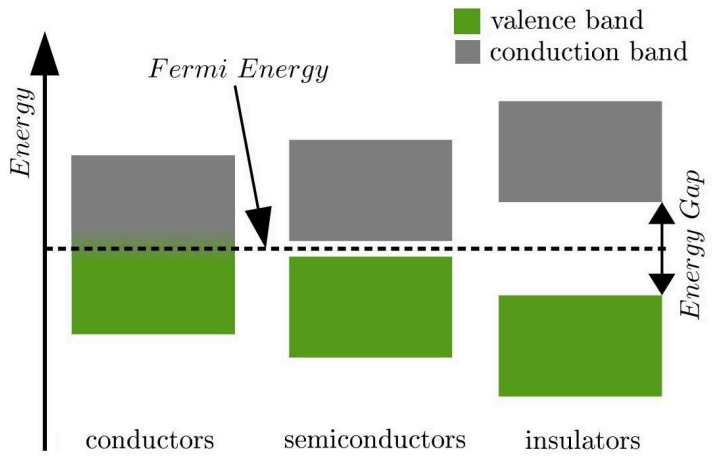

Figure 4.2.4: Valence and conduction bands of solids compared with the Fermi energy. The ability of electrons to jump from a band to another characterizes the conductivity properties of solids.

ence of electrons on the conduction band, in which they are free to move into the lattice.More in general, we can categorize solids into three classes as shown in Fig. 4.2.4:

- Insulators: The Fermi energy is inside an energy gap, or band gap, between the valence and conducting band. The band gap represents a forbidden zone for electrons with no available energy states. It corresponds to the difference in energy between the highest occupied energy state and the lowest unoccupied energy state. In insulators the gap is much larger than $k_B T$ at room temperature and electrons don't have enough energy to jump between the valence and conduction band.

- Semiconductors: The energy gap is small enough that electrons can transit to the conduction band via thermal fluctuation or photon absorption. This effect is exploited by standard sensors for near infrared/visible detection.

- Conductors: The conduction band overlaps with the valence band and electrons can jump between the two bands.

The function $g(E)$, called *density of states,* describes the number of available energy states in an energy range dE around an energy E. At thermal equilibrium $g(E)$ is equal to the Fermi-Dirac density distribution of electrons

$$f_{FD}(E,T) = \frac{1}{1+\exp\left(E-\epsilon_F/k_B T\right)} \tag{4.2.11}$$

VALUES AT $T = 0$			
CONDUCTOR	ξ_0 $[nm]$	λ_L $[nm]$	$k = \lambda_L/\xi_0$
ALUMINIUM	1600	16	0.01
NIOBIUM	38	39	1.02

Table 4.2.1: Values of the coherence length, London penetration depth and Ginzburg-Landau parameter for Aluminum and Niobium. [67]

which can be used to calculate the number of electrons in the conduction band for a given energy gap.

In superconductors the positive ions orbital displacement is due to Coulomb interaction with moving electrons. Because of their masses, ions move slowly compared to electrons. Hence, the positive charged region remains active long enough to attract another electron, which is then coupled to the previous one that created the positive charged region in the first place. This is a simplified explanation of a Cooper pair generation which is well described by the BCS theory [61]. The characteristic length for which two electrons are affected by the coupling is called *coherence length* ξ_0 and is a peculiar property of each metal. It represents the physical size of a Cooper pair within the metal. The coherence length is also related to the minimum spatial extension of the layer between the superconducting and normal state. A mathematical derivation for ξ_0 can be found in [67] and leads to the following expression

$$\xi_0 = \frac{2\hbar v_F}{\pi \Delta_0}$$

where v_F is the electron velocity at the Fermi surface and $\Delta_0 = \Delta(0)$ is the *binding energy*, or energy gap, of a Cooper pair at $T = 0$. The London penetration depth and the coherence length are the fundamental lengths of a superconductors. The first parameter relates how the current density is related to the vector potential and the second is a measure of the range over which the vector potential is averaged to obtain the current density. The ratio λ_L/ξ_0 is called Ginzburg-Landau parameter. Table 4.2.1 shows some values for Aluminum and Niobium at $T = 0$.

The binding energy is the analogous of the energy gap in solids. It represents the minimum energy necessary to break a Cooper pair. If the thermal energy is greater than the binding energy, the superconductivity will be destroyed. The temperature dependence of the binding energy can be found in [68] as follows:

MINIMUM FREQUENCY DETECTABLE			
CONDUCTOR	T_c $[K]$	2Δ $[meV]$	ν_{min} $[GHz]$
Titanium	0.39	0.12	28.6
Gallium	1.1	0.33	80.7
Aluminium	1.2	0.36	88
Indium	3.4	1.03	249.4
Tin	3.7	1.12	271.4
Mercury	4.2	1.27	308
Lead	7.2	2.19	528
Niobium	9.3	2.82	682.1

Table 4.2.2: Minimum frequency detectable for some superconducting metals.

$$\Delta\left(T\right) \approx \Delta(0) \exp\left[-\sqrt{\frac{2\pi k_B T}{\Delta(0)}} \exp\left[\frac{\Delta(0)}{k_B T}\right]\right]$$

Considering $T \sim T_c$, the latter becomes

$$\frac{\Delta(T)}{\Delta(0)} \approx \left[1 - \left(\frac{T}{T_c}\right)^4\right]^{1/2}$$

At $T = 0$ the minimum energy necessary to break a Cooper pair is given by

$$2\Delta(0) \approx 3.52 k_b T_c$$

where the factor two is required by energy conservation. This energy is typically of the order of meV or less for metals with critical temperature less than about 1 K. Superconducting detectors require more than one Cooper pair braking to be efficient. This fact rises up the lower limit on photon energy and therefore frequency. Table 4.2.2 shows values of binding energy and photon energy necessary to break a single Cooper pair for some metals.

4.2.4 Thin metal layers

Superconducting resonators are fabricated in thin films to maximize the kinetic inductance. To achieve high responsive detectors it is necessary to have a metal for which the kinetic inductance dominates over other kinds of reactive contributions. The kinetic inductance fraction depends on the film thickness as shown in Fig. 4.2.5, L_k becomes greater as the metal thickness is reduced.

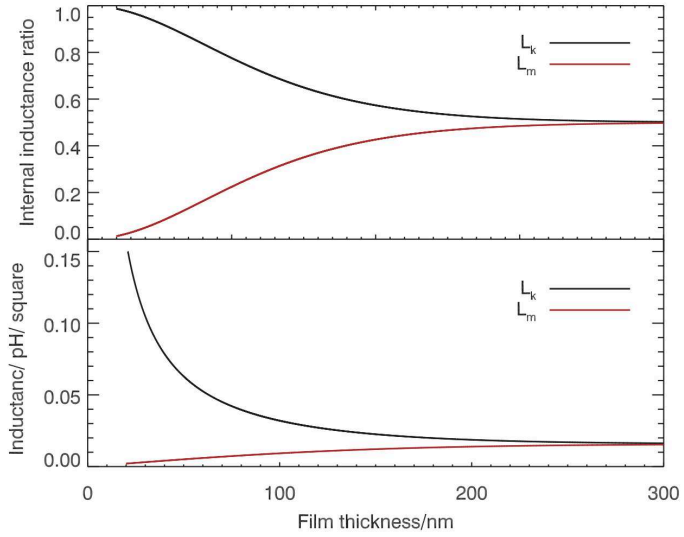

Figure 4.2.5: Ratio of kinetic and magnetic inductance (top) and their values in pH/square considering a superconducting penetration depth of 50 nm. Source: Simon Doyle thesis, 2008 [76].

The mean free path of a Cooper pair $l = v_F \tau$ can be shorter than the film thickness t and the coherence length ξ_0. In this regime, often called *dirty limit*, superelectrons move through the metal by diffusion and the Drude model is not valid anymore. The complex conductivity in the dirty limit can be found in the Mattis-Berdeen theory [69] as follows

$$\frac{\sigma_1(\omega)}{\sigma_n} = \frac{2}{\hbar\nu}\int_{\Delta}^{\infty} \left[f\left(E\right) - f(E+h\nu)\right] g_1(E)dE$$

$$+ \frac{1}{\hbar\nu}\int_{min(\Delta-h\nu,-\Delta)}^{-\Delta} \left[1-2f(E+h\nu)\right] g_1(E)dE$$

$$\frac{\sigma_2(\omega)}{\sigma_n} = \frac{1}{\hbar\nu}\int_{max(\Delta-h\nu,-\Delta)}^{\Delta} \left[1-2f(E+h\nu)\right] g_2(E)dE$$

where σ_n is the normal state conductivity and we are assuming the metal to be in thermal equilibrium, thus the density of states is given by the Fermi-Dirac distribution $f\left(E\right)$ from 4.2.11. The coefficients g_1, g_2 are given by

$$g_1(E) = \frac{E^2 + \Delta^2 + \hbar\nu E}{(E^2 - \Delta^2)^{1/2} \left[(E + \hbar\nu)^2 - \Delta^2\right]^{1/2}}$$

$$= \left(1 + \frac{\Delta^2}{E\,(E + \hbar\nu)}\right) N_s\,(E)\, N_s\,(E + \hbar\nu)$$

$$g_2(E) = \frac{E^2 + \Delta^2 + \hbar\nu E}{(\Delta^2 - E^2)^{1/2} \left[(E + \hbar\nu)^2 - \Delta^2\right]^{1/2}}$$

$$= -i \times g_1(E)$$

The imaginary and real part of the complex conductivity are shown in Fig. 4.2.6 as a function of temperature and frequency. The aluminum has been modeled considering the normal state conductivity $\sigma_0 = 1.95 \times 10^7\ S/m$, $v_F = 1.34 \times 10^6\ m/s$ and assuming $T_c = 1.2\ K$. With these values the aluminum becomes resistive above 90 GHz and gains the ability of absorbing photons. moving at higher frequencies$\sigma_1 \to \sigma_0$. Because of the temperature dependence of the Cooper pair density, we obtain σ_1 to be stable for temperature up to 0.2 K, accordingly with 4.2.10. The niobium has been modeled considering the normal state conductivity $\sigma_0 = 1.23 \times 10^7\ S/m$, $v_F = 0.28 \times 10^6\ m/s$ and assuming $T_c = 9.2\ K$. The real conductivity change drastically around 690 GHz, which corresponds to the Cooper pair breaking energy. Because of the higher critical temperature with respect to aluminum, the niobium shows a complex conductivity which is quite stable for temperature up to 2 K.

The complex conductivity is also related [70] to the complex surface impedance $Z_s\,(\omega, T) = R_s + iX_s$ as follows

$$Z_s\,(\omega, T) = \frac{\int \mathbf{E} d\vec{s}}{\int \mathbf{H} d\vec{s}} = \sqrt{\frac{i\mu_0\omega}{\sigma\,(\omega, T)}} \tag{4.2.12}$$

Rather than the conductivity, the surface impedance is the value measured experimentally for thin layer superconductors. An expression of Z_s for normal metals can be derived from the Ohm's law substituting **J** and **B** with the Maxwell's equations

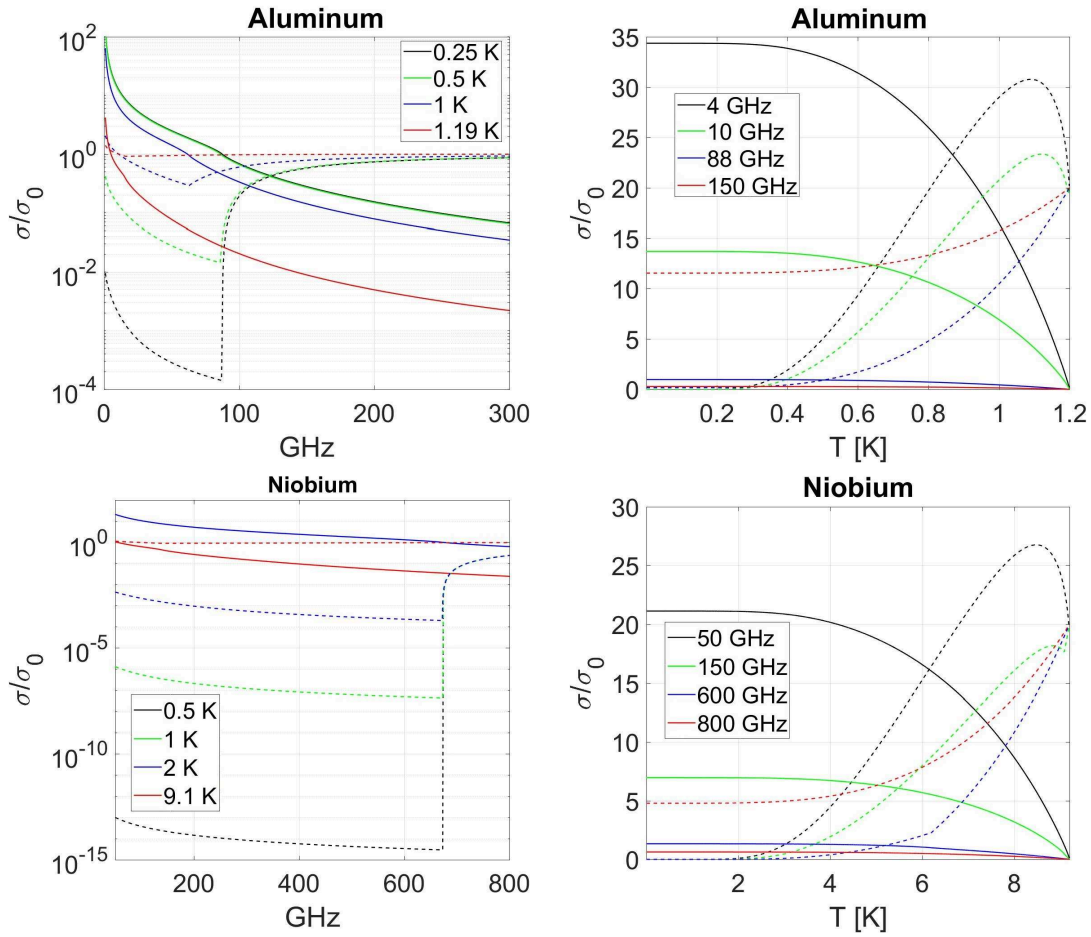

Figure 4.2.6: Real part (dashed lines) and imaginary part (solid lines) of the complex conductivity for aluminum ($T_c = 1.2\ K$) and niobium ($T_c = 9.2\ K$). Values of σ_1 are scaled by a factor 20 when plotted versus temperature. Note that differences in niobium σ_2 plotted versus frequency at 0.5 K, 1 K and 2 K are within the line width for frequencies above 690 GHz.

[71], we obtain

$$\frac{\partial^2 \mathbf{E}}{\partial z^2} = \sigma\mu_0 \frac{\partial \mathbf{E}}{\partial t} + \varepsilon\varepsilon_0\mu_0 \frac{\partial^2 \mathbf{E}}{\partial t^2} \tag{4.2.13}$$

where we are assuming a non-magnetic metal with $\mu_r \approx 1$, which gives $\mu \approx \mu_0$. The second term in the right-hand side of 4.2.13 represents the time variation of the vector field which takes into account the internal charge of materials. This is called displacement current and can be neglected at microwave frequencies, since $\sigma \gg \omega\epsilon\epsilon_0$. A solution for $\mathbf{E}$ can be found using the equation of motion of an exponential decay wave along the z direction

$$\mathbf{E} = \mathbf{E}_0 \exp\left(ikz - i\omega t\right) \exp\left(-\frac{z}{\delta}\right)$$

which lead to

$$\left(ik + \frac{1}{\delta}\right)^2 = i\omega\mu_0\sigma$$

where the quantity δ is the *skin depth*, the distance from the surface where the field is reduced by a factor e, defined as

$$\delta = \sqrt{\frac{2}{\omega\mu_0\sigma}}$$

and we can rewrite Z_s as

$$Z_s = \frac{(1+i)}{\sigma\delta}$$

Moving to the superconducting phase the complex conductivity can be written combining 4.2.9 and 4.2.7, we obtain

$$\sigma_1 - j\sigma_2 = \frac{n_n}{n}\sigma_n - j\frac{1}{\omega\mu_0\lambda_L^2\left(T\right)}$$

which, using 4.2.12, gives

$$Z_s \approx \frac{1}{2}\omega^2\mu_0^2\sigma_n\lambda_L^3\left(T\right) + i\omega\mu_0\lambda_L^2\left(T\right)$$

As in the case of the complex conductivity, an expression for the surface impedance can be derived depending on the scale involved. In some cases Ohm's law is no more valid and deriving Z_s need a more complete mathematical description of the phenomena. A great effort in this direction has been done by J. Gao [72], which gives an expression of Z_s in terms of σ_1 and σ_2. We can distinguish three cases:

- **Thick film in the extreme anomalous limit**: this condition is verified when $\xi_0 \gg \lambda_L(0)$ AND $l \gg \lambda_L(0)$, we obtain

$$Z_s = \frac{j\sqrt{3}\mu_0\omega}{2}\left[\frac{3\pi\omega}{4v_0\lambda_L^2(0)}\frac{\sigma_2 + j\sigma_1}{\sigma_n}\right]^{-1/3}$$

- **Thick film, local (dirty) limit**: this condition is verified when $\xi_0 \ll \lambda_0(0)$ OR $l \ll \lambda_0(0)$

$$Z_s = \sqrt{\frac{j\omega\mu_0}{\sigma_1 - j\sigma_2}}$$

- **Thin film**: in this case the film thickness $t \ll l$, hence the Cooper pair mean free path is limited by surface scattering. The Ohm's law is valid when $l \ll \xi_0$ AND $l \ll \lambda_0(T)$

$$Z_s = \frac{1}{(\sigma_1 - i\sigma_2)\,t}$$

4.3 KIDs sensitivity

4.3.1 Response

All the information about resonator properties can be inferred from the feedline. The readout node for a KIDs array usually involves IQ mixing for producing the tones to be sent along the feedline, hence resonances can be represented on the IQ plane or with S-Parameters. We can now consider the case of a feedline coupled to several detectors as in Fig. 4.1.4 and examine the transmission parameter S21: at the frequencies corresponding to the resonators natural frequencies, the power along the feedline is transferred to the resonators and the transmission drops as shown in Fig. 4.3.1 (left). Each resonator produces a resonance peak as in Fig. 4.3.1 (right). The transmission response can be described by the single-pole approximation [86] as

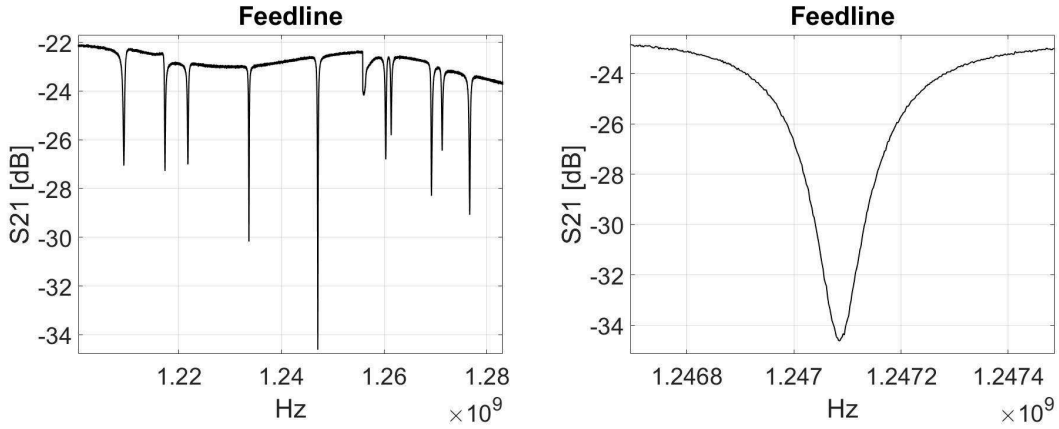

Figure 4.3.1: Left: typical transmission parameter of a KIDs readout. Each peak along S21 corresponds to a resonator. Right: Zoom on one pixel. The total quality factor is calculated at $-3\ dB$ from the baseline.

$$S_{21}(\omega) = 1 - \frac{Q_i}{Q_c}\frac{1}{1 + 2jQ_i x}$$

where Q_i is the internal quality factor of the resonator and

$$x = \frac{\omega - \omega_0}{\omega_0}$$

is the fractional detuning from the resonant frequency ω_0. The coupling quality factor Q_c can be inferred from 4.1.3 considering the $\min(|S_{21}|) = 1 - Q_{tot}/Q_c$

$$Q_c = \frac{Q_{tot}}{1 - \min(|S_{21}|)}$$

and consequently, because of 4.1.3, we obtain

$$Q_i = \frac{Q_{tot}}{\min(|S_{21}|)}$$

The resonance is affected by the readout power delivered on the feedline. The power P_{res} dissipated in the resonator is of the form $P_{res} = R_c I_c^2$, with R_c the resistance of the coupling and I_c the current flowing from the feedline to the resonator, which has the form [87]

$$I_c = V_{source}\frac{Z_c}{Z_0/Z_c + 2}$$

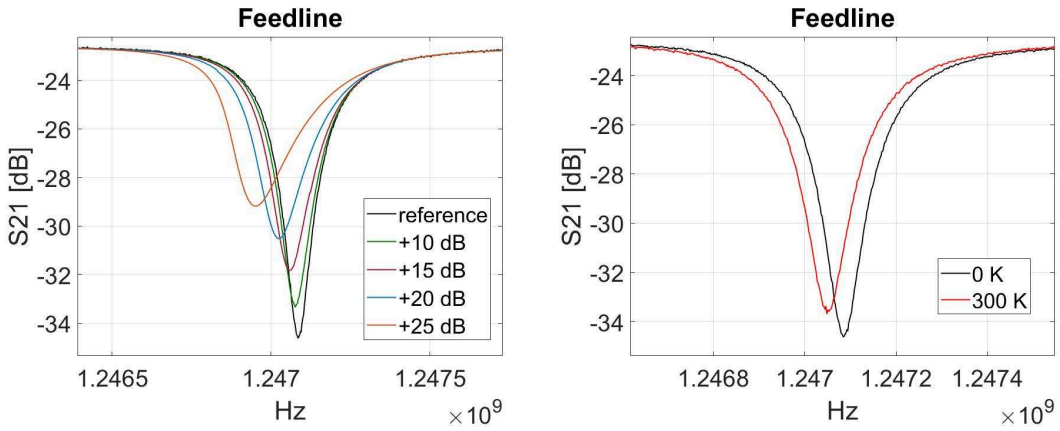

Figure 4.3.2: Left: Effect of rising up the readout power. The peak becomes skewed and eventually the resonance may disappear for very high readout power. Right: Typical detector resonance shift under the exposure of different black body sources.

where Z_0 is the characteristic impedance of the feedline and V_{source} is the Thévenin equivalent voltage of the source. The peak current occurs at resonance, which is temperature dependent. Therefore, we can define a resonant temperature for a particular readout frequency. Fig. 4.3.2 (left) shows a typical peak distortion due to high readout power. The same figure (right) also shows a typical resonant frequency shift due to millimeter waves absorption along the KID inductor.

The resonant frequency shift can be inferred directly from 4.1.2. Typically, the phase is more sensitive and the response of a KID is calculated in terms of the phase shift. Therefore, we are interested at the phase change over the Cooper pair variation $d\theta/dN_{qp}$. Considering a metal of volume V, thickness t and penetration depth λ, an expression for $d\theta/dN_{qp}$ can be found in literature [88, 89, 90]

$$\frac{d\theta}{dN_{qp}} = -\frac{\alpha\zeta Q_{tot}}{|\sigma|\,V}\frac{d\sigma_2}{dn_{qp}} \tag{4.3.1}$$

where the parameter ζ is given by

$$\zeta = 1 + \frac{2t/\lambda}{\sinh(2t/\lambda)}$$

and

$$\alpha = \frac{L_{kin}}{(L_g + L_{kin})}$$

is the kinetic inductance fraction of the superconducting line. From 4.3.1 we infer that the resonator response increase both with α, which is temperature dependent, and Q. The response also increases by diminishing the volume of the metal, hence the detector benefits from thin metal layers. Nevertheless, we must take in mind that pushing up the responsivity by decreasing the volume will result in a limitation in terms of dynamic range.

4.3.2 Characteristic sources of noise

g-r noise

Cooper pair population is calculated by balancing the generation and recombination time. Recombination occurs with a phonon emission. The average time necessary for a Cooper pair to recombine is the quasiparticle lifetime τ_{qp}. For detectors made out of superconducting resonators this value is also related to the time constant. It determines how fast the detector returns to its original state after a single detection. Resonant detectors do not integrate signals as in the case of CCD, but rather measure the flux in a temporal scale of τ_{qp}. An expression for the quasiparticle lifetime can be found in [73] as follows:

$$\frac{1}{\tau_{qp}} = \frac{\sqrt{\pi}}{\tau_0}\left(\frac{2\Delta}{k_B T_c}\right)^{5/2}\left(\frac{T}{T_c}\right)^{1/2}\exp\left[-\frac{\Delta}{k_B T}\right]$$

where τ_0 is a material dependent constant. The ring down time of a standard resonator depends on the quality factor and resonant frequency as follows [77]:

$$\tau_{res} = \frac{Q_{tot}}{\pi f_0}$$

Considering a superconducting resonator with quality factor of 10^5 and a resonant frequency of few GHz, we obtain a ring down time of the order of the μs. Typical quasiparticle lifetime for a 100 nm thick aluminum layer at 100 mK can be found in [78] of the order of few hundreds of μs. Hence, the quasiparticle lifetime will dominate the time constant of a superconducting detector.

Because of the thermal excitation, the number of quasiparticle fluctuates in time from the generation and recombination processes; this effect leads to a source of

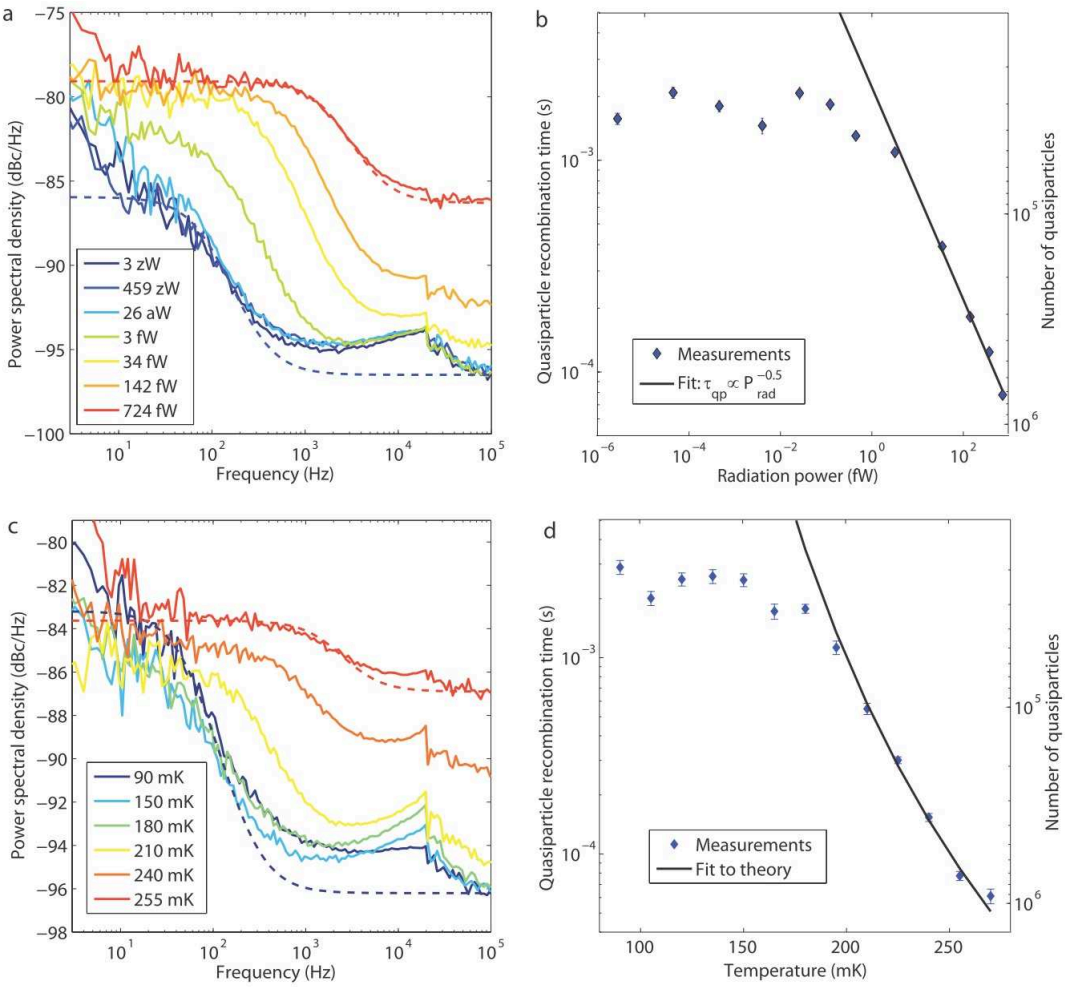

Figure 4.3.3: The device tested is a half wavelength CPW resonator coupled to an X-slot antenna. The CPW strip is a 50 nm thick layer of aluminum. Power spectral density for different values of radiation power and tempperature (a,c) lead to an estimation of τ_{qp} (b,d). Dashed lines represent Lorentzian fit to the corresponding spectrum. Credit: De Visser et Al. [80].

statistical noise, called g-r noise, which is the fundamental noise limit for KIDs. The associated NEP_{gr} can be estimated from the average value of quasiparticles $\langle N_{qp} \rangle$ as calculated in [79]

$$NEP_{gr} = 2\Delta\sqrt{\frac{\langle N_{qp}\rangle}{\tau_{qp}}} \propto \exp\left(-\frac{\Delta}{k_B T}\right)$$

According to the equation of the quasiparticle lifetime, the g-r noise starts to decrease exponentially when cooling down well below T_c. Measurements of the power spectral density (PSD) of an Al antenna coupled resonator made by De Visser et Al. [80] are shown in Fig. 4.3.3. Both the temperature and the radiation power effect on the PSD is considered. From the spectra they also inferred the values of τ_{qp} and N_{qp}.

Expected NEP at 6 GHz from a 3 μm strip of 220 nm thick Aluminum resonator on sapphire with $\tau_{qp} = 200\,ms$ is of the order of $10^{-20}\,W/\sqrt{Hz}$ at 100 mK. It increases up to $10^{-17}\,W/\sqrt{Hz}$ at 300 mK [89]. These values are sufficient for photon noise limited observation of CMB polarization at 150 GHz.

Two level system noise

The dominant source of noise in superconducting microwave resonators is often due to surface layer of two-level system (TLS) defects on metal interfaces or dielectrics [81]. Resonators generate an electric field that can couple to dipole moments on TLS, which results on local fluctuations in the electric field strength. These fluctuations affect the local value of ϵ_{eff}. As a consequence, we observe an increase in losses and a jittering capacitance value in the resonator. The most sensible component of a LEKID to TLS noise is the capacitor, in which the electric field is stronger than in any other part of the circuit. The TLS noise has been extensively studied in [72, 82, 83] and represents an excess noise that prevents microwave resonators to reach the fundamental limit. The major results obtained are summarized as follows:

- The power readout $P_{readout}$ determines the electric field strength along the resonator. As a consequence, it also affects the coupling with the dipole moments. The frequency noise $S_f = df/f^2$ decreases with the readout power

$$S_f \propto P_{readout}^{-1/2}$$

- The temperature affects the phase noise as well as the resonance frequency f_0 and the internal quality factor. The TLS theory gives an explanation for all of these affected parameters [72]. The frequency noise decreases with the temperature

$$S_f \propto T^{-k} \quad with \quad 1.73 < k < 2$$

- The TLS noise is material dependent and it is influenced only by the interface between a superconductor and the substrate/dielectric. The bulk properties does not seem to affect the excess noise. The main contribution is the oxide layer which form on the material surface, other contributions may come from impurities and chemical residues left from fabrication. Some techniques has been developed for reducing the TLS, like etching the substrate [85], or using

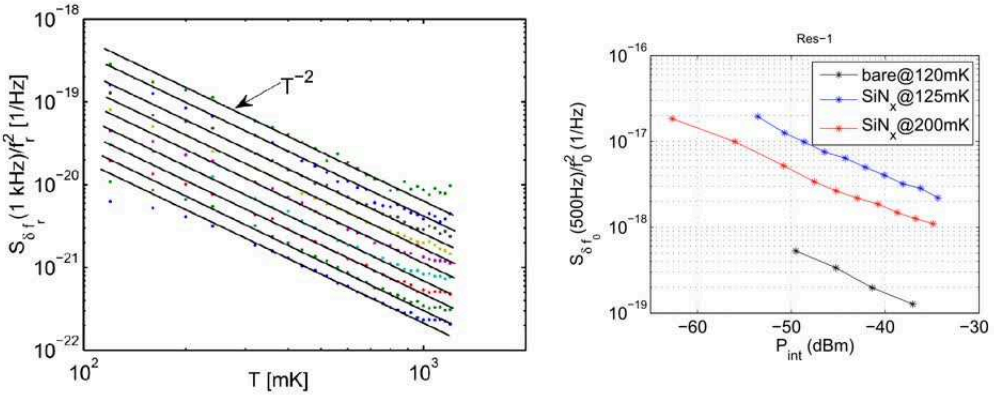

Figure 4.3.4: Left: TLS noise of a Nb quarter wave resonator as a function of temperature. The readout power increases from -105 dBm for the upper curve to -73 dBm for the bottom curve with a step of 4 dBm. Right: TLS noise of a bare Al quarter wave resonator deposited over sapphire (black plot) and the effect of dielectric deposition (red and blue plots). Credit to J. Gao [72].

materials that does not oxide, like the TiN.

- Using larger transmission lines results in a reduction of the TLS noise. This is particularly true at those points where the electric field is stronger, like inside the capacitor or at the transmission line open ends.

Fig. 4.3.4 shows some noise measurement of a Nb coplanar quarter wave resonator as a function of temperature and readout power. It also shows the effect of dielectric deposition over a bare resonator.

4.4 Conclusion

Microwave resonators are an attractive solution for B-Modes observation. Planar structures are simple to fabricate and large arrays of KIDs are less expensive than more common bolometers. The main advantage of using KIDs is the multiplexing factor. Currently, bolometer multiplexing is also possible but it requires low temperature electronics for a lower multiplexing rate. Contrary to TESs, kinetic inductance detectors work well below the critical temperature, which is a region of more stability and thus they are less sensitive to temperature fluctuations.

The critical point in KIDs development remains the TLS noise that can prevent the detector to reach the photon noise limit. This is particularly true for antenna-coupled detectors, for which the antenna adds some constraints on the pixel design and may

require the deposition of extra dielectric layers. Another limitation is the binding energy of common metals that makes KID technology ineffective for detection of frequencies below 100 GHz.

Chapter 5

Antenna-Coupled LEKID

As opposed to bolometers, the coupling of an antenna to LEKIDs is complex to design since the resonator is a closed circuit and only the inductive part is sensitive to Cooper Pair breaking. Therefore, the connection with an external transmission line may require extra metal and/or dielectric layers that can potentially degrade the performance in terms of noise and sensitivity. In this chapter, I present my original solution to couple an antenna to a LEKID. The high frequency signal is filtered on a diplexer and each sub-band is coupled to one detector resonating at low frequency. Every component has been simulated with full wave simulation software. The receiver and the diplexer-LEKID coupling have been simulated with CST Microwave Studio, the diplexer and the superconducting resonator with Sonnet Software.

5.1 Electromagnetic field solvers

An ideal full wave simulation will give the same results regardless of the solver type, the choice of one solver over another will only affect the simulation time. In practice each solving approach is optimized for certain cases. Usually, the choice depends on the size of the simulation box compared to the involved wavelengths. Other discriminating factors can be the shape of the structure, the excitation signal and model resonances. In the following sections I will explain the three solvers I have used to run simulations in CST and Sonnet.

Finite Integration Technique (FIT) in CST

The time domain solver, or transient solver, of CST Microwave studio uses the Finite Integration Technique to infer the S-parameters. This algorithm is suited for hexahedral mesh, which defines a finite calculation domain. CST solves the Maxwell's equations on two orthogonal sets of meshes [91, 92]. Electric voltages e and magnetic fluxes b are defined on the primary mesh grid G, while the dielectric fluxes d and magnetic voltages h are defined on the dual meshing grid $\widetilde{G}$. Each side of a single cell in G describes one side of the Faraday's law

$$\int_A \vec{E} \cdot d\vec{s} = -\frac{\partial}{\partial t} \iint_A \vec{B} \cdot d\vec{A}$$

which can be analytically solved introducing the topological matrix C

$$Ce = -\frac{\partial}{\partial t} b$$

The same procedure is performed on the grid $\widetilde{G}$ with the Ampere's law. We obtain a set for the Maxwell's equations in the hexahedral mesh, or the *Maxwell's Grid Equations* (MGEs)

$$\begin{aligned} Ce = -\frac{d}{dt} b \qquad & \widetilde{C}h = \frac{d}{dt} d + j \\ \widetilde{S}d = q \qquad & Sb = 0 \end{aligned}$$

which can be solved considering the averaged material parameter on the area and edges of each cell of the mesh.

The transient solver carries out the excitation in time domain and recovers the spectrum with a Fourier Transform. Therefore, it is particularly indicated for broadband analysis or arbitrary time signal excitation. It is also the best choice when the structure size d under study is electrically large. This is true in the case of $d \gg \lambda_{min}$ where λ_{min} is the smaller wavelength simulated. When simulating strong resonant structures, the energy remains in the system for a certain time after the excitation. If the simulation ends before the resonance amplitude decays to zero, the Fourier Transform will be calculated with a truncated signal, which may lead to inaccurate

results. Typically, we observe ripples in the S-parameters when some of the input energy remains in the simulation.

I have used the transient solver to simulate the antenna and the antenna-coupling design.

Frequency domain solver in CST

This algorithm is suited for tetrahedral and hexahedral mesh. The Maxwell's equations can be transformed into the frequency domain when the fields are characterized by a time-harmonic dependence. These can be described by

$$\vec{E}(t) = \Re\left\{\vec{E}(\omega)\exp(i\omega t)\right\}$$

The software calculates a solution of the linear equation system frequency by frequency and then interpolates the points to obtain the spectrum. The frequency domain solver is particularly preferred when simulating narrow band spectra or in cases of electrically short size structure, which means $d < \lambda$. It is generally more robust than the transient solver, on the other hand the tetrahedral mesh cannot be refined by the user. Whatever the solver, CST allows creating custom materials with frequency depended properties, which is convenient for modeling superconducting metals.

I have used the frequency solver to validate simulations run with the transient solver.

EM in Sonnet Software

Simulations in Sonnet are enclosed in a metal box of which two opposite sides can be opened to free space. The software divides the 2.5D structure in subsections and adopts a modified Method of Moments (MoM) analysis based on Maxwell's equations [93, 94]. The analysis includes every possible electromagnetic effect (dispersion, losses, coupling, ...) and uses the Fast Fourier Transform (FFT) to calculate S-parameters. Sonnet is particularly effective with planar structures which are modeled in layers, such as planar transmission lines, and when $d \ll \lambda$, which is the case of lumped elements. Sonnet allows creating custom materials with fixed character-

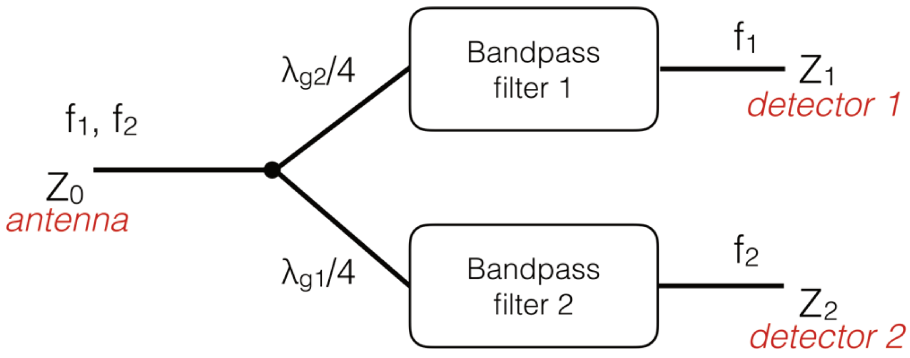

Figure 5.2.1: Detection chain block diagram. The receiver is a dual resonant slot antenna coupled to a diplexer. The power of each sub-band is absorbed on lumped resonator.

istics without a detailed frequency dependence. This feature can be a limitation for broadband simulations of superconducting metals, for which the impedance may vary considerably with frequency.

I have mainly used Sonnet for low frequency simulations in order to calculate the detector resonant frequency.

5.2 Concept drivers

To develop a technological demonstrator, I aim to design an architecture that can attain the following features:

- Sensitive to linear polarization according to the CMB polarimetry requirement.
- Operational frequency range around 150 GHz. The lower limit is given by the superconducting Aluminum which has a cutoff frequency at about 100 GHz. The upper limit is given by the laboratory equipment which allows to illuminate the detector with monochromatic radiation up to 200 GHz. Moreover, this is the frequency range of most interest for CMB.
- Detector resonance frequency in the range $1 - 3$ GHz according to the low temperature amplifier operational frequency range available at APC.
- Easy to fabricate.
- Avoid dielectric deposition over the resonator to reduce the impact of TLS.

The block diagram of the dual-color antenna-coupled LEKID is shown in Fig. 5.2.1.

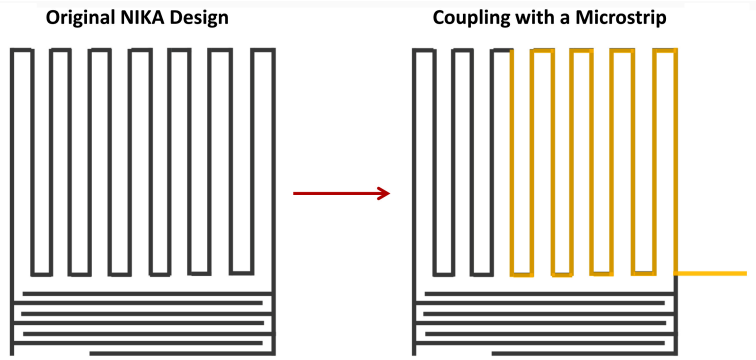

Figure 5.3.1: Basic idea of coupling a microstrip (yellow) with the NIKA pixel (dark gray) by overlapping the two strips.

The receiver is a dual resonant slot antenna, which is sensitive to linear polarization. The bandwidth is large enough to obtain two sub-bands, each one coupled to a superconducting resonator. The same architecture is suitable for different types of microstrip excited antennas. These are preferred because they can easily accommodate bandpass filters. The diplexer is composed by two 5th order Chebyshev open-circuited stub bandpass filters centered at 140 GHz and 160 GHz respectively. Each LEKID is then coupled with one filter.

5.3 Antenna-coupling KIDs

The problem of planar antenna-coupling KID can be reduced to a microstrip coupling with a superconducting resonator. Indeed, the coupling technique is independent from the antenna and filter design as long as we use a microstrip excited antenna. Since we plan to fabricate the antenna and the detector on the same ground plane, the microstrip must lie on a different metal layer.

5.3.1 Basic idea

The starting geometry I have considered to design a resonator is the NIKA pixel [95] shown in Fig. 5.3.1. A simple coupling can be achieved by overlapping the antenna microstrip with the inductor. The microstrip will be fabricated in Nb, which has negligible resistivity in the operational frequency range, so that only the Aluminum resonator will contribute to signal absorption. The resonator is a closed geometry for which is topologically impossible not to create a T-junction at the coupling point. It

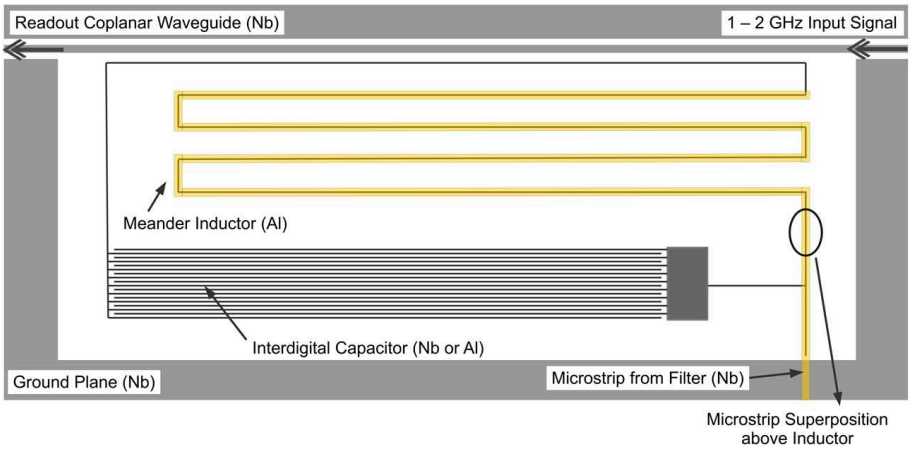

Figure 5.3.2: First detector prototype. The microstrip antenna (yellow) is coupled to the inductor. Because of the ground plane discontinuity most of the signal is reflected back to the antenna.

is crucial that the absorption occurs along the inductor, which is the sensitive area, so we must prevent power dissipation over the capacitor.

To design a first prototype I have reshaped the inductor to maximize the coupling with the feedline. In order to take care of the T-junction I have designed a patch on one side of the capacitor as shown in Fig. 5.3.2. The patch is located at distance $\lambda/4$ to prevent the microstrip signal to couple with the capacitor. Since the resonator is a lumped element, the patch does not affect the resonance at $1\,GHz$. The main problem of this design is the ground plane discontinuity between the resonator and the microstrip ground plane. The microstrip must have a consistent reference ground plane to avoid reflection back to the antenna. It is clear that this problem is due to the fact that the resonator is physically disconnected from the ground. Thus, in a second attempt to couple the microstrip I have redesigned the resonator out of a coplanar waveguide as shown in Fig. 5.3.3. The two ground planes are in Niobium while the inductor central strip is partially in Niobium and partially in Aluminum. The capacitor is entirely made of Niobium since we do not want any power dissipation over it. By using this design the microstrip-to-detector transition can be reduced to a simple microstrip-to-CPW transition for which several techniques can be found in literature. Moreover, the power can be transmitted directly along the inductor without the microstrip overlapping technique, thus eliminating the requirement of dielectric deposition. The main concern of using a CPW is that it is necessary to keep the two ground planes at the same potential, which is quite troublesome especially because of the T-junction. The implementation of airbridges across the two ground planes would introduce a significant effort in terms of microfabrication.

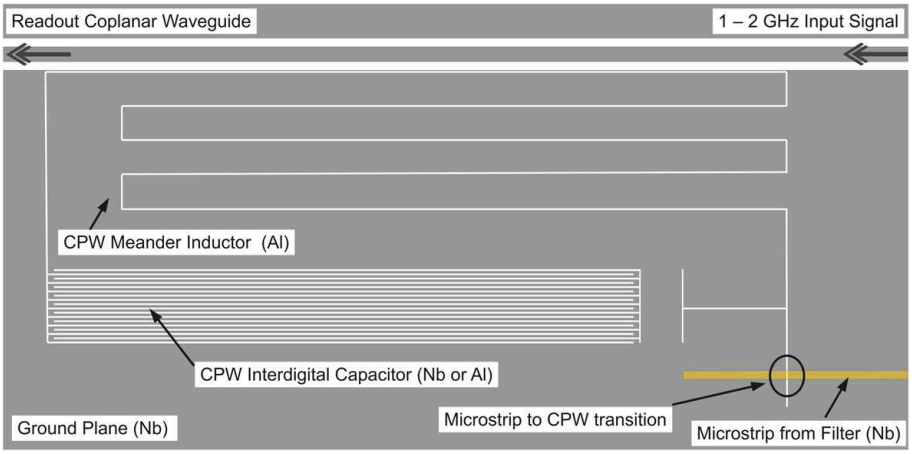

Figure 5.3.3: Second detector prototype. The coplanar waveguide allows to couple the antenna microstrip (yellow) without generating ground plane discontinuities.

Furthermore, the signal can propagate with different modes along a CPW, including the slotline mode, which may lead to inefficient power absorption on Aluminum. I found a solution to these problems by producing a short circuit along the inductor as explained below.

5.3.2 Detector

A schematic of the final detector design and its equivalent circuit is shown in Fig. 5.3.4. The structure is entirely modeled out of a Nb CPW, except for an Aluminum absorber located along the inductor. The interdigital capacitor has 12 arms per electrode as shown in Fig. 5.3.5, each arm is separated from the adjacent by a 3 μm gap. The inductor is a 3 μm Nb strip in a meander shape which has been short circuited. Such a design has multiple benefits:

- The short circuit has the advantage to assure the two ground planes to be electrically in contact without implementing airbridges.

- The microstrip signal power is transferred to the resonator so that the geometry does not require an overlap with the inductor. This technique allows the resonator to see free space on one side, thus reducing the impact of potential TLS generated by dielectric deposition.

- The short circuit has the supplementary advantage of improving the microstrip-to-CPW transition since it allows to excite the coplanar mode along the induc-

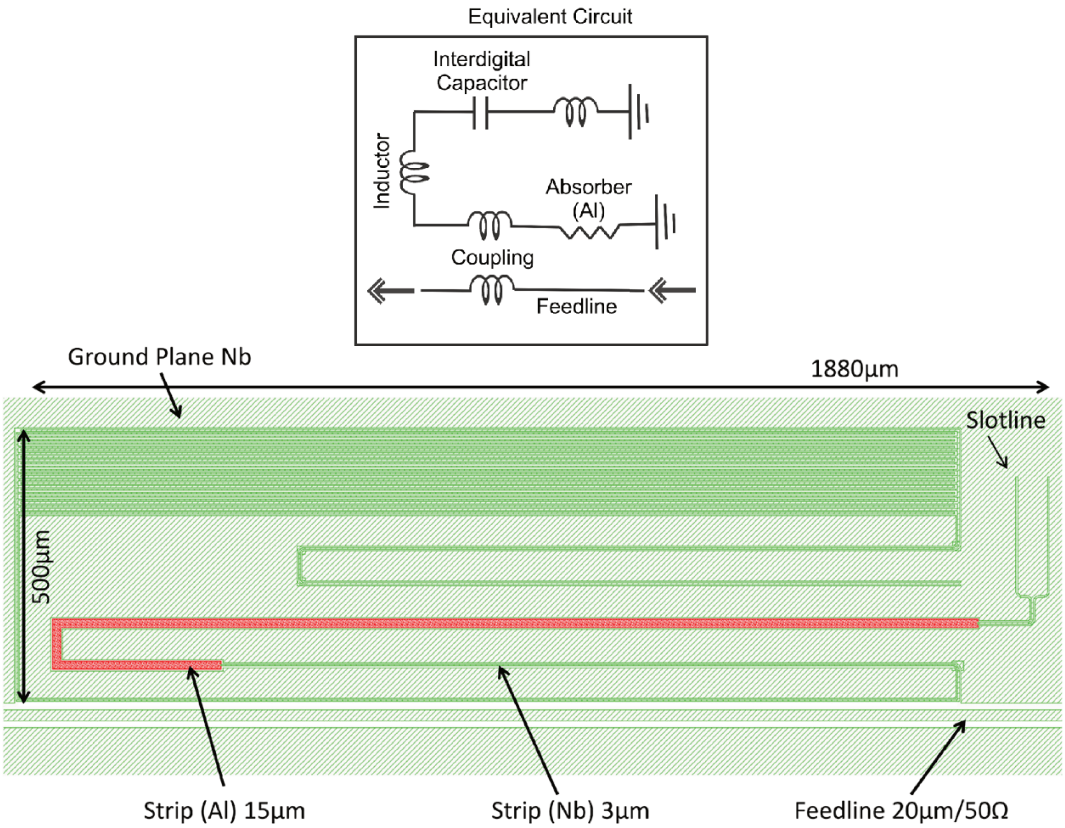

Figure 5.3.4: Detector layout and its equivalent circuit. The distance from the feedline is left as a parameter and varies in some pixels of the fabricated chips. The gap between the inductor and the feedline ranges from 15 μm to 20 μm. A strip of ground plane separates the two when the gap is > 15 μm.

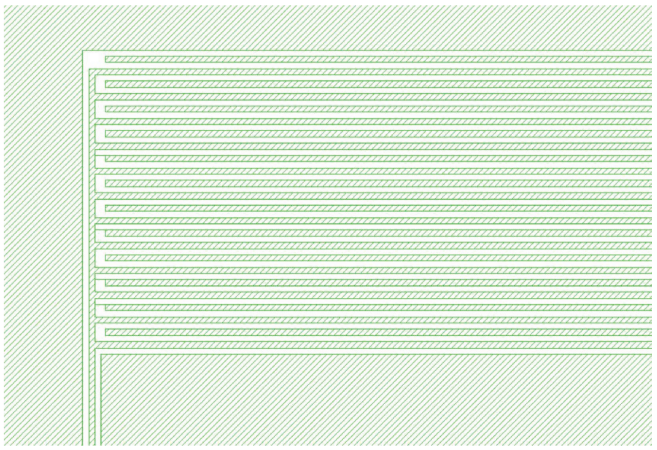

Figure 5.3.5: Zoom on one end of the interdigital capacitor.

tor more easily, thus enhancing the performance in terms of power absorbed on the Aluminum strip.

One of the two short circuited ends is used to couple the LEKID to the microstrip network above. The inductor includes a 2 mm long Aluminum strip to absorb the millimeter signal coming from the bandpass filter. The absorber is 15 μm wide with 3 μm gaps between the ground planes. The Aluminum width has been chosen to match the characteristic impedance of the Nb line. This has been calculated in CST as well as the characteristic impedance of the Aluminum CPW. The Niobium has been modeled with PEC and the Aluminum with a 2-D layer having a complex conductivity calculated from the Mattis-Bardeen integrals discussed in section 4.2.4 for 20 nm thick Aluminum at 300 mK (table of values in Appendix).

The feedline provides the tone for the resonator. When the signal frequency along the feedline is equal to the natural frequency of the resonator, the current flows through the LEKID. I have developed two different LEKID coupling geometries with the feedline:

1. The feedline central strip and the inductor are separated by 15 μm gap.

2. A narrow strip of ground plane divides the feedline from the inductor. The LEKID is from 3 μm to 9 μm more distant from the feedline with respect to the gap-separated geometry.

Fig. 5.3.6 shows the current distribution inside the LEKID and along the feedline as simulated in Sonnet. At resonance, the power flows through the resonator and the current has its maximum along the inductor and at the two sides of the capacitor. To multiplex different resonators along the same feedline I have changed the length of the inductor. Fig. 5.3.7 shows how much the resonant frequency change by reducing the Nb inductor of about 100 μm. I aim to multiplex up to 14 detectors in a bandwidth narrower than 150 MHz, which should be large enough to minimize potential resonance overlaps.

5.3.3 Coupling

Bandpass filters are connected with the resonators via capacitive coupling. The design focuses on avoiding the excitation of a slotline mode along the absorber that

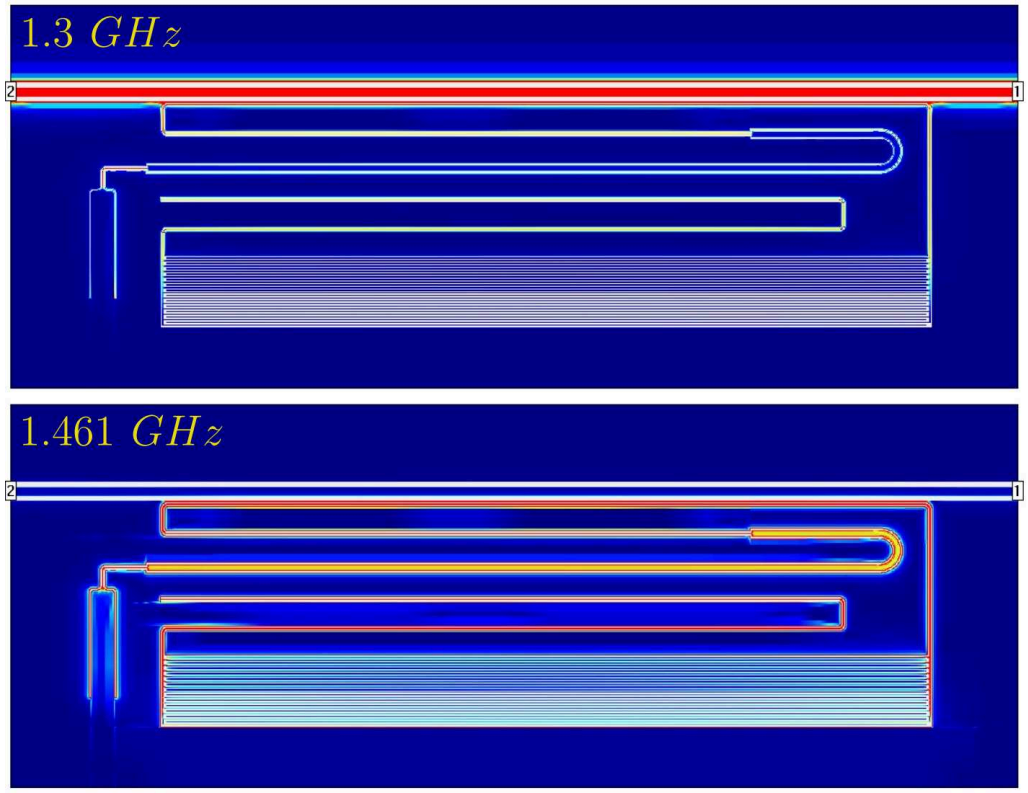

Figure 5.3.6: Current simulated in Sonnet for a LEKID resonating at 1.461 GHz. Colors go from blue (minimum intensity) to red (maximum intensity). The resonator is insensitive for frequencies different from $f_0 \pm (Q_{tot} \times f_0)$ and the current only flows along the feedline (top). At resonance, the transmission coefficient of the feedline drops down; the current flows inside the LEKID inductor and at the two sides of the capacitor (bottom). The electric field is maximum across the interdigital capacitor arms.

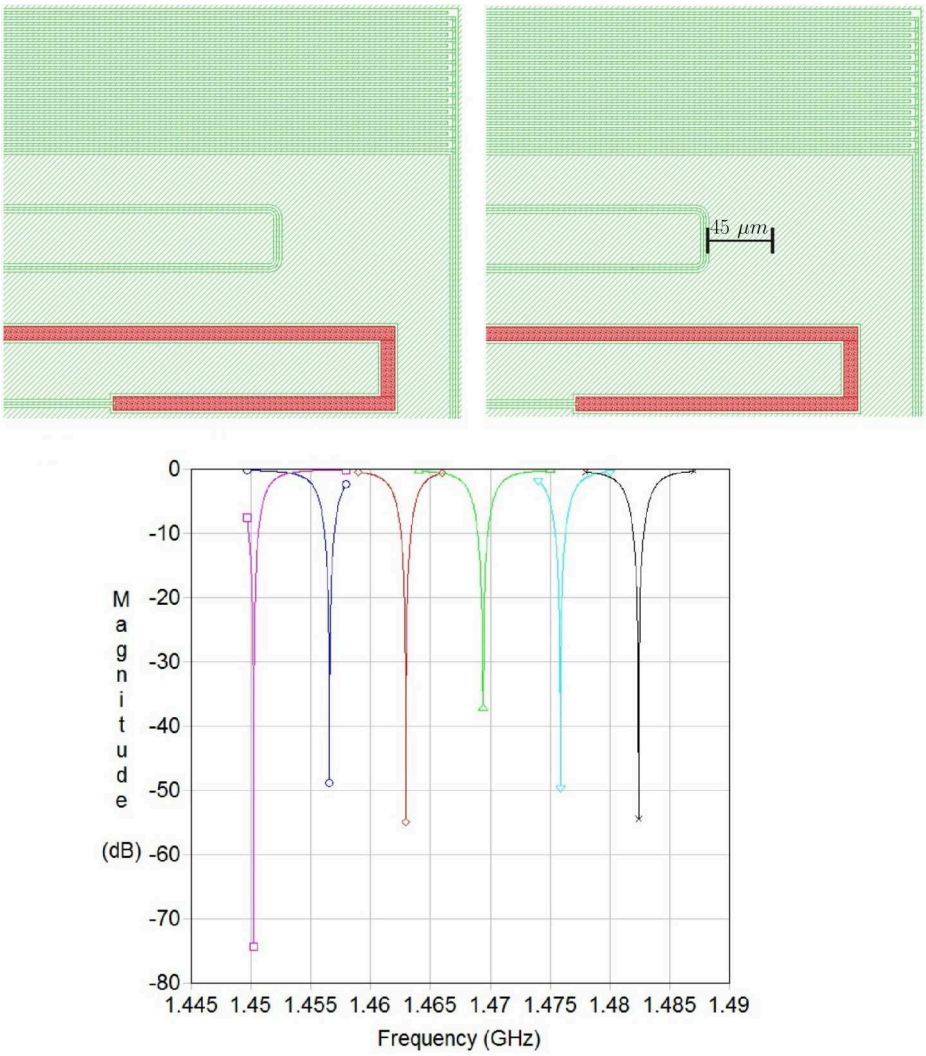

Figure 5.3.7: By reducing the length of the inductor (top) we increase the resonant frequency. The plot shows a resonance shift of more than 7 MHz for six resonators with progressive inductor reduction of about 100 μm.

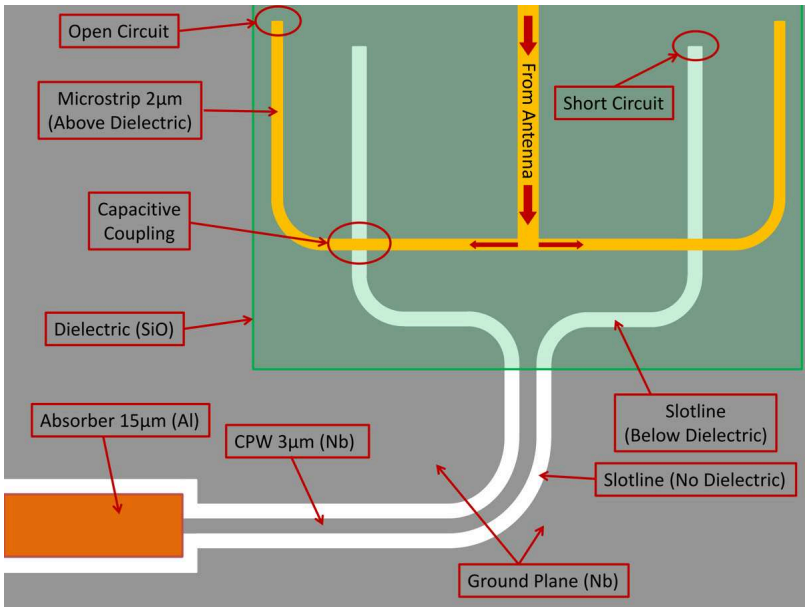

Figure 5.3.8: Sketch of the LEKID coupling with the bandpass filter output microstrip line. The two gaps of the incuctor are coupled with the two microstrip above. The phase shift between the two capacitive couplings assures the coplanar mode excitation along the inductor.

would suddenly decrease the absorption efficiency. For this reason I have decided to couple both the gaps of the CPW inductor. The output of each filter is a 2 μm wide microstrip, which becomes 5 μm wide after a 600 μm long tapered line, and terminates in a power divider above one shorted end of the LEKID inductor. The two lines are separated by 500 nm of silicon oxide. The two ends of a power divider must have twice the impedance of the input line. Thus, as shown in Fig. 5.3.8, the power divider requires the two microstrips to be 2 μm wide, which is the reason of the tapered line. In fact, dividing the original 2 μm strip would require a design quite demanding in terms of microfabrication. The two gaps of the CPW lines split into two slotlines. Each of these is orthogonal to the microstrips above and is capacitively coupled with one of them. Both the slotlines and the microstrips have a reactive termination at their ends. The slotlines end with a short-circuited stub, the microstrips end with an open-circuited stub. The impedance matching involves also the aluminum strip, which is a reactive element. In total, I have three parameter to set for matching the impedance, the two stubs length and the distance between the aluminum strip and the coupling point. I have run simulations in CST to determine these parameters. These simulations include the power divider, the transition and the aluminum strip. I have used few 2D surfaces for adjusting the mesh. A snapshot of the 3D model is shown in Fig. 5.3.9. The power enters the simulation in the

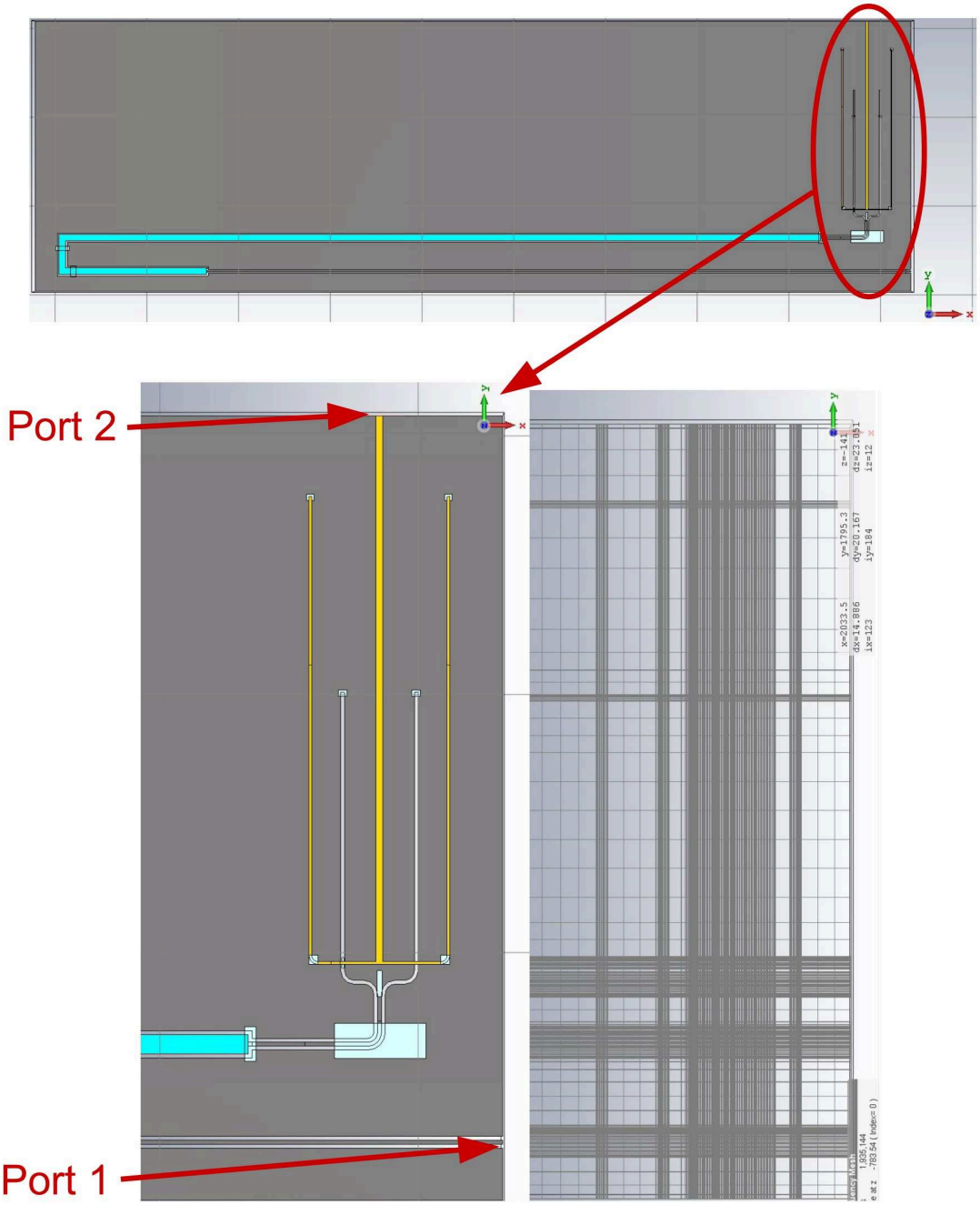

Figure 5.3.9: Front view of the LEKID-filter coupling 3D model in CST (top). Zoom on the coupling (left-bottom) and mesh grid (bottom-rigth). Millimeter waves enter the simulation on port 2, pass through the microstrip-CPW transition and are absorbed on the aluminum strip. Any residual power came out the simulation through port 1. Reflection on port 2 is influenced by the impedance mismatching at the transition.

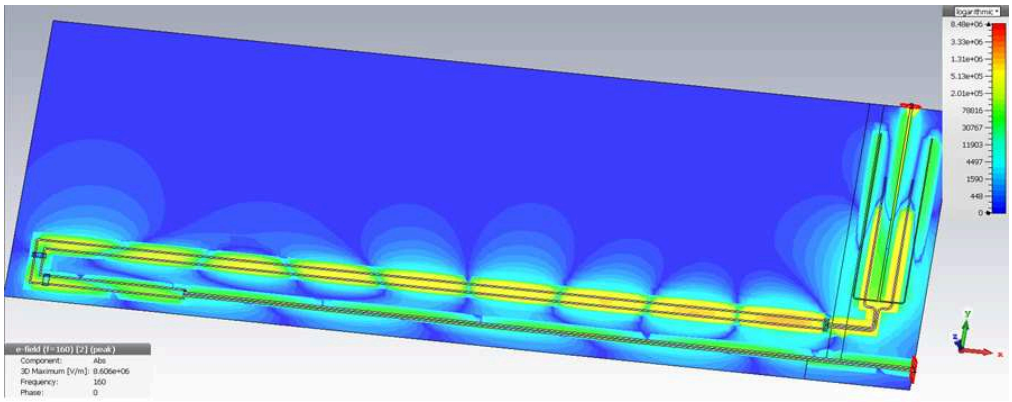

Figure 5.3.10: Electric field strength along the absorber at 160 GHz.

form of millimeter wave along the microstrip line. If the impedance matching at the coupling point is carried out correctly, the signal flow through the slotlines below with minimal reflection. The two slotlines combine together to form the inductor CPW. The design symmetry assures that there is $\lambda/4$ of phase shift between the two microstrip-slotline transitions, thus the two signals combine in such a way that the two ground planes are at the same potential. In other words, the symmetry assures the coplanar mode along the CPW. Absorption occurs along the aluminum strip, which has been simulated as a 2D layer with a frequency dependent conductivity according to the Mattis-Bardeen theory. The inductor ends on a waveguide port, so that I can recover any potential unabsorbed signal. Once the aluminum properties in terms of resistance and reactance are set, the power absorbed depends only on the aluminum strip length. Note that because of the inductive behavior of the line, changing the Al strip length may require a different set of parameters for the impedance matching at the LEKID-filter transition. Simulation results are shown in Fig. 5.3.10 and Fig. 5.3.11. Stub tuning at the transition is different for the 140 GHz and 160 GHz sub-bands to take into account the different wavelengths. Most of the power is absorbed in about two lambda along the aluminum strip, which corresponds to about 880 μm at 140 GHz and 740 μm at 160 GHz. The simulation gives more than 95% of absorption for both the sub-bands along the 2 mm aluminum strip, the reflection on the excitation port is below -20 dB.

Critical points of the design are the stubs length and the system symmetry. They affect the performance as follows:

- Reducing the microstrip stub length by 27 μm and the slot stub length by 10 μm will result in a frequency shift of $+10$ GHz of the coupling operational

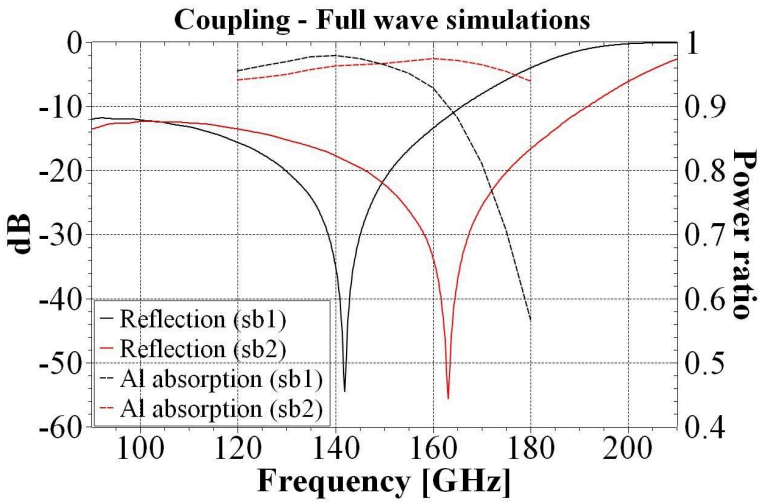

Figure 5.3.11: Simulation results for the 140 GHz and 160 GHz sub-bands. The absorption on Aluminum is calculated as the power absorbed on Aluminum over the total power contained in the simulation.

frequency range. Those values has been taken into account for sweeping some parameters as described in section 6.4.

- A misalignment of the microstrip network with respect to the slotlines will result to an incorrect excitation of the coplanar mode along the inductor.

- The length of the Aluminum strip sets the total reactance of the line and so it contributes to the impedance matching.

5.3.4 Slot antenna

The receiver is a dual resonant slot antenna as described in section 3.2.3. The resonance has been simulated with the transient solver in CST. Fig. 5.3.12 shows a screenshot of the CST 3D modeler. The ground plane is simulated as a 2D layer of Perfect Electric Conductor (PEC), which is a good approximation for a 120 nm thick Niobium cooled down to sub-kelvin temperature. The silicon substrate is loss free with a dielectric constant of 11.9 while the SiO layer is simulated as an ideal material with dielectric constant of 3.7. The microstrip is also modeled with PEC and has one end excited by a waveguide port, which is 12 times larger than the microstrip and 20 time higher than the dielectric. The port size must be large enough to accommodate the electric field around the strip. The slot antenna is largely affected by the boundary conditions. These set the effective size of the ground plane and determine

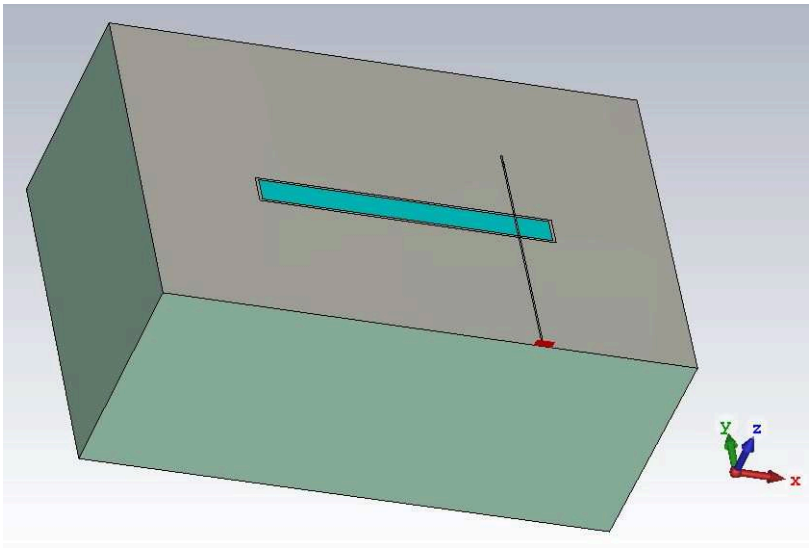

Figure 5.3.12: Dual resonant slot antenna modeled in CST. The SiO dielectric is not shown. The size of the box (450 $\mu m \times 700$ μm) has a minimal effect on the resonance since the open boundary conditions in y and x assures the ground plane to be infinite in size.

how the substrate mode of the antenna is dissipated on the simulation box edges. The final chip has the size of around 4 cm^2, hence the ground plane is electrically large compared to the simulation box and can be approximated as of infinite size. I have used open boundary both in the x and y axis to simulate an infinite structure. The open boundary is a perfect impedance match with the geometry in contact and represents a virtual extension of the 3D structure to infinity. Along the z axis, in both directions, the boundaries are open with extra space between the 3D structure perimeter and the simulation box to allow the emitted signal to be dissipated in free space.

By default, CST generates a mesh grid which is insufficient to calculate the fields at the point of the microstrip-slot coupling. To adjust the mesh, I have included two 2D meshing surfaces as shown in Fig. 5.3.13 which are not taken into account for the fields calculation but are effective to alter the mesh. One meshing surface is centered on the slot and is 6 μm longer than the slot width and 8 μm larger than the slot length. These dimensions assure that the surface covers the slot edges and provides a meshing grid for the magnetic current. I have chosen 1 μm of mesh cell size on the x axis, which is the main direction of the microstrip electric field, and 2 μm along the y axis. The other meshing surface is an extension of 12 μm of the microstrip open ends and provides a mesh cell of 1 μm in the y axis to resolve the electric field at the line termination. Adjusting the mesh has the disadvantage that

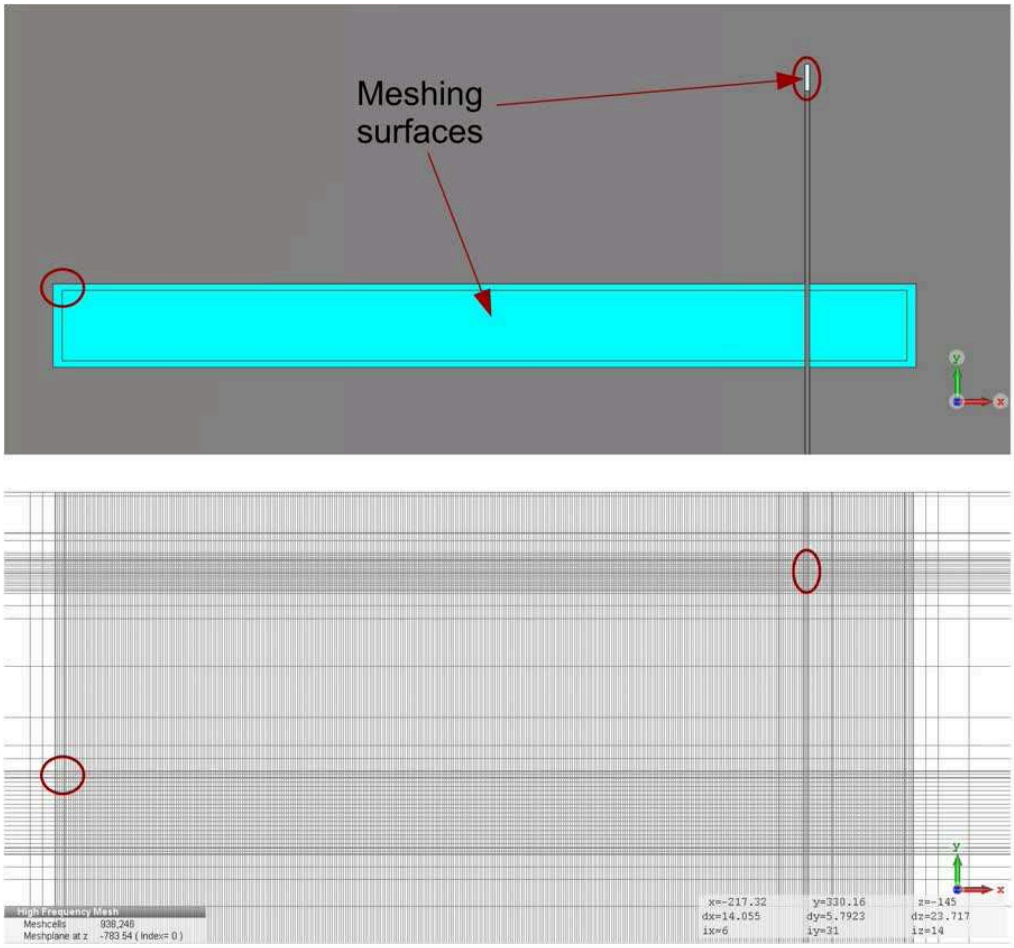

Figure 5.3.13: Top: The two meshing surface used to adjust the mesh around the slot and at the microstrip end. Bottom: The mesh grid in the xy plane generated by the two surfaces.

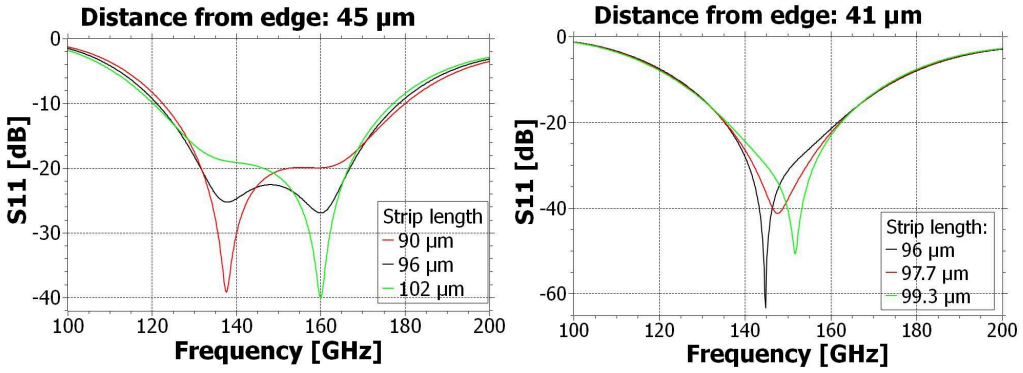

Figure 5.3.14: Strip length sweep for two different microstrip distances from the edge. Accordingly with the expected behavior of a dual resonant slot the distance from the edge sets the maximum antenna bandwidth and the strip length selects the resonance λ and λ_s.

the generated meshing grid is not local but extends across the whole simulation box, drastically increasing the number of mesh cells and so the simulation time.

Simulations for a slot of size 32 $\mu m \times 382$ μm are in good agreement with expectations. As shown in Fig. 5.3.14 the microstrip length can select the standard $\lambda/2$ resonance or the short circuited $\lambda_s/2$ resonance. In the case of λ close to λ_s, choosing an average value of the strip length will result in the dual resonant slot. Approaching the strip to the slot edge, λ become closer to λ_s and the antenna bandwidth decreases. The final design is a slot excited with a 2 μm strip which is 44 μm distant from one edge and ends 90 μm after the slot. This configuration provides a resonance with a bandwidth of almost 40% at -10 dB centered at 150 GHz. The resonance of such antenna is plotted in the next section (Fig. 5.3.17) in comparison with the two sub-bands.

The boundary conditions used to simulate the infinite ground plane also affect the farfield calculation. CST needs extra space at the boundary for a proper farfield calculation, which in the case of the slot would result in a finite ground plane. An infinite ground plane could be simulated if its size is larger than several wavelengths. This condition with the extra space at the boundaries is memory consuming for a standard computer since the mesh refining around the slot would spread across the entire ground plane. Furthermore, the excitation propagating through the ground plane wouldn't be able to escape the simulation and the transient solver would give a truncated calculation of the Fourier Transform. The effect of the boundaries on the farfield is shown in Fig. 5.3.15 for three ground plane sizes. Boundaries on the xy plane are fixed, I have considered two cases for the boundary below the silicon

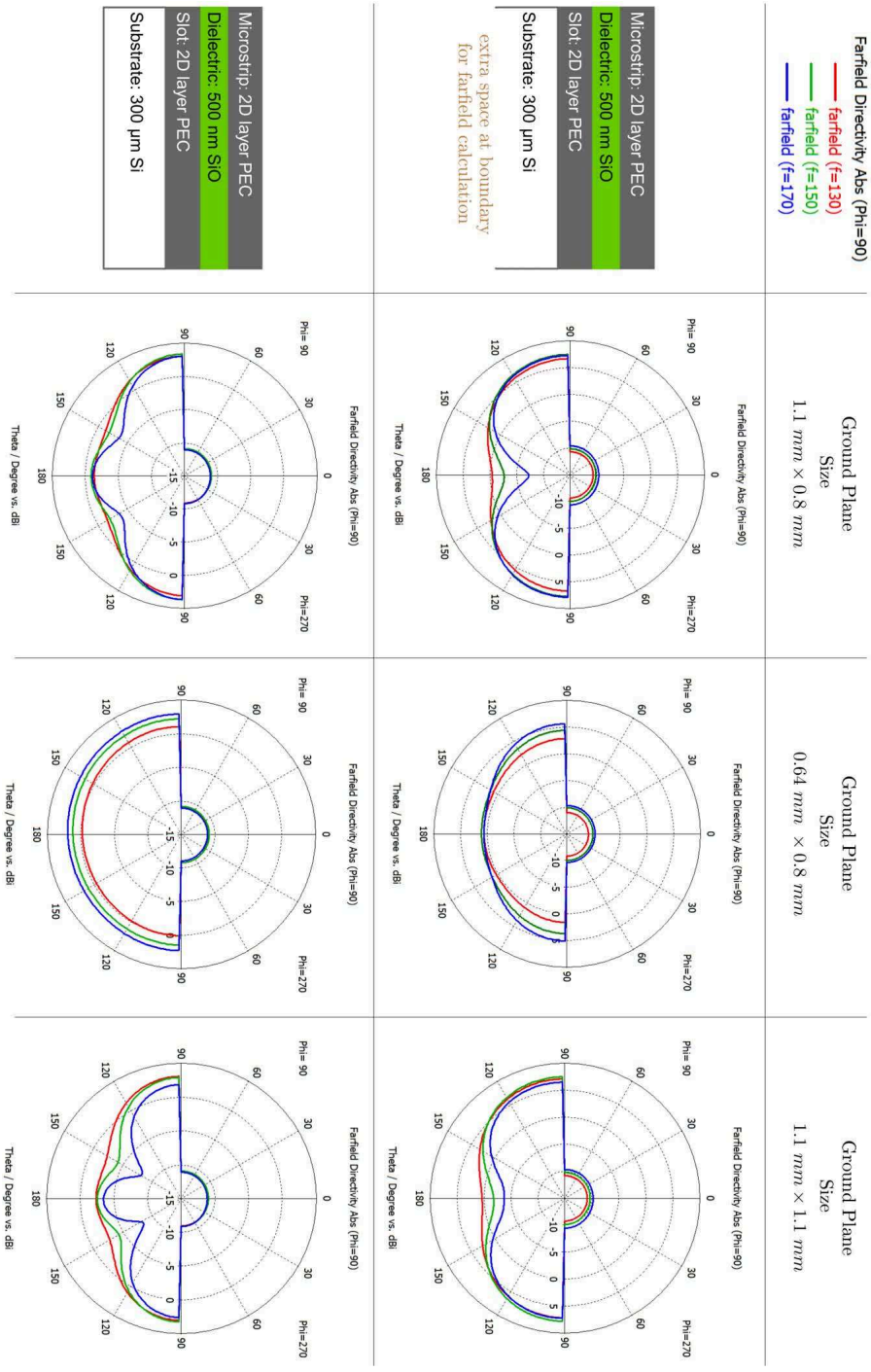

Figure 5.3.15: Farfield calculation in CST for different simulation box sizes and boundary condition below the silicon substrate.

substrate: extra space and normal open boundary in which no extra space is added. In some cases the calculated farfield shows extra structures compared to the expected dipole.

5.3.5 Diplexer

The microstrip network has been simulated with Sonnet Software. I have decided to use the 5th order Chebyshev open-circuited stub bandpass to filter the signal. The reasons are the following:

- I want to avoid filters with capacitive-coupled lines that can excite some propagation modes over the ground plane/dielectric.
- Stepped impedance filters are also an option but are less flexible than stubs and the microstrip line width is already pushing the fabrication limit.
- Short-circuited stub filters have the advantage of being physically shorter with respect to the open-circuited stub filters. On the other hand, the short circuit is implemented by connecting one strip end with the ground plane, thus it requires more effort during the fabrication.

The diplexer includes two bandpass filters with bandwidth of about 10%, which is tuned to fit in the antenna bandwidth and minimize the cross talk. The central frequencies are 140 GHz and 160 GHz respectively. Each bandpass filter is composed by ten stubs, five of which are quarter wavelength long and five are half wavelength long. The half wavelength stubs are an extension of the quarter wavelength stubs and together they form five elements of a Chebyshev filter. The size of each element in Fig. 5.3.16 has been calculated starting from the admittance as derived in section 2.3.5. The millimeter signal from the antenna is filtered on a T-junction. The filters are located at distance $\lambda/4$ the central frequency of the adjacent filter as shown in Fig. 5.3.17 to avoid reflection back to the antenna. In this manner the three lines of the diplexer can share the same impedance and no additional impedance matching is needed. This is advantageous because the mainline is only 2 μm wide and the T-junction would require to further reduce the strip width, which already approaches the microfabrication limit.

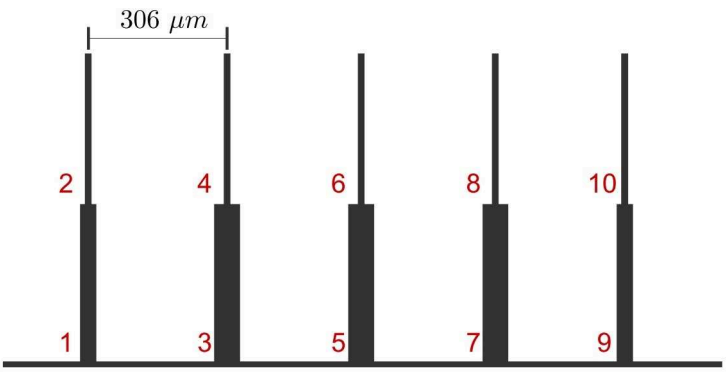

$width_1 = width_9 = 8\ \mu m$ $width_2 = width_{10} = 3\ \mu m$

$width_3 = width_5 = width_7 = 17\ \mu m$ $width_4 = width_8 = width_8 = 6\ \mu m$

$length_1 = length_9 = 290\ \mu m$ $length_2 = length_{10} = 600\ \mu m$

$length_3 = length_5 = length_7 = 280\ \mu m$ $length_4 = length_6 = length_8 = 580\ \mu m$

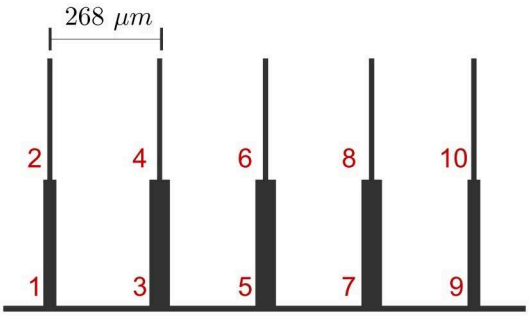

$width_1 = width_9 = 8\ \mu m$ $width_2 = width_{10} = 3\ \mu m$

$width_3 = width_5 = width_7 = 17\ \mu m$ $width_4 = width_8 = width_8 = 6\ \mu m$

$length_1 = length_9 = 290\ \mu m$ $length_2 = length_{10} = 600\ \mu m$

$length_3 = length_5 = length_7 = 280\ \mu m$ $length_4 = length_6 = length_8 = 580\ \mu m$

Figure 5.3.16: Calculated size of each filter considering a 2 μm wide transmission line at ends, passband ripple of 0.01 dB and the attenuation pole around 90 GHz. Top: filter centered at 140 GHz. Bottom: filter centered at 160 GHz.

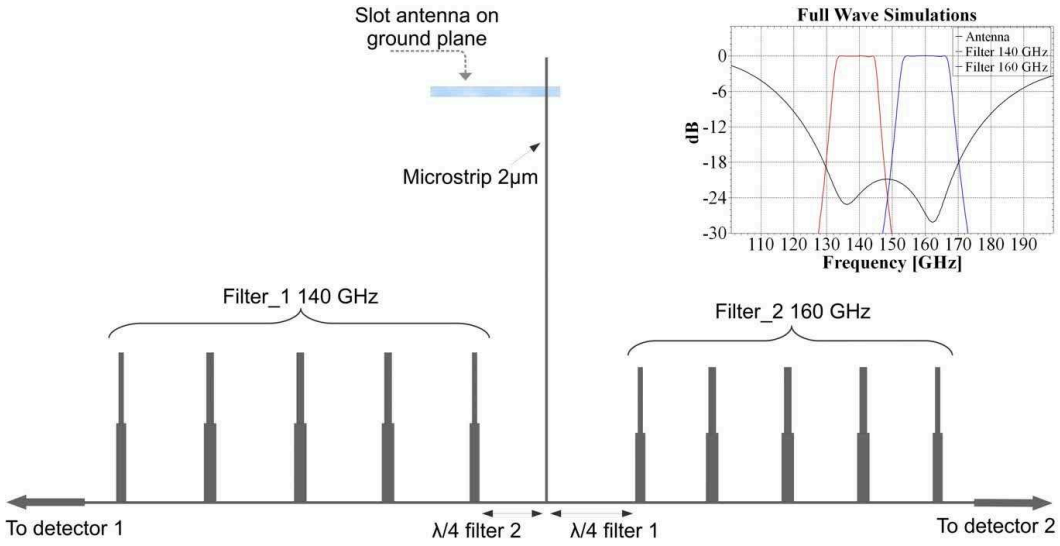

Figure 5.3.17: Filters displacement within the diplexer. The plot shows the two bands compared with the antenna resonance.

5.4 Pixel Design

The final design of the dual-color pixel is shown in Fig. 5.4.1 along with the fabrication levels. The millimeter wave from the antenna is processed on the microstrip network which consists of a 120 nm thick Nb layer[1] deposited over a 0.5 μm Silicon oxide. The dielectric is also deposited over the antenna to avoid dielectric constant discontinuities along the slot. The resonators and the antenna lie on the same level, which consists of a 120 nm thick Nb ground plane. The LEKID-filter coupling is capacitive, the power is transferred to a Nb CPW which is part of the LEKID inductor. The CPW transits to an aluminum strip 20 nm thick. The strip is about 2 mm long and assures the millimeter wave to be absorbed in the metal via Cooper Pair breaking.

5.5 Conclusion

The final pixel design requires only four depositions, no further structures are necessary to be implemented after fabrication (airbridges, VIAs, ...). This is a clear advantage for fabricating a prototype device.

Simulations show good overall efficiency: both the antenna and the coupling impedance

[1] The thickness has been increased to 300 μm during the microfabrication for mechanical stability as described in Chapter 6.

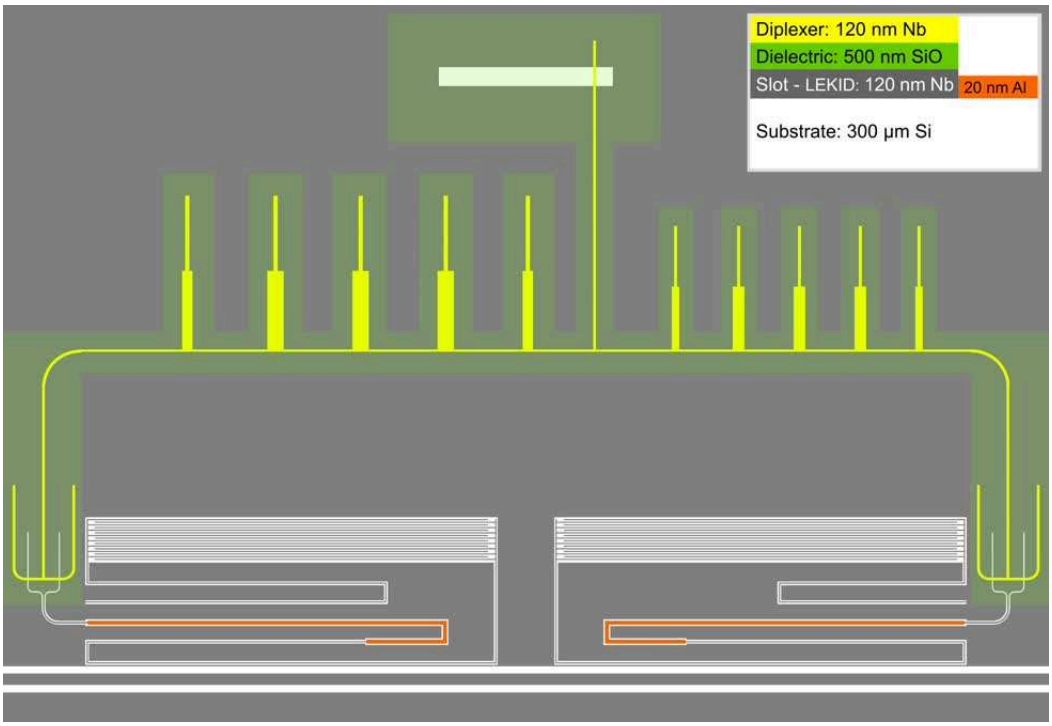

Figure 5.4.1: Sketch of the pixel design and fabrication levels. The antenna and the resonator are deposited over a silicon substrate. The resonator includes an Aluminium strip. The dielectric is deposited in correspondence of the microstrip network and over the antenna. The scale of the antenna is exaggerated in this illustration.

matching generate reflected signals of the order of 1% in the operational frequency range. Nevertheless, the design relies on several parameters and we haven't fabricated a demonstrator for each component. Therefore, we need to test different prototypes with several parameter sweeps to effectively determine the real performance. Major critical points are the antenna effective operational frequency range and the coupling performance. At this stage of development we plan to multiplex less than 14 detectors on a single chip. For this reason the resonance quality factor is not among the priorities, thus I have focused mainly on the global efficiency of the pixel when deciding which parameter to sweep. In the next chapter I will explain the microfabrication process and I will give accurate details about these sweeps.

Chapter 6

Microfabrication

Microfabrication is used in several different areas since the first development of the transistor. These include microelectronics (integrated circuits, ...), micromachines (robotics, mechatronics, ...) and nanotechnology. Clean room for microfabrication requires strict environmental parameters regulation such as temperature, atmospheric pressure and most of all the number of contaminant particles per square meter.

In this chapter I will explain the microfabrication process with particular emphasis on the technique used to fabricate KIDs. While this is not the core of my work, I have collaborated with F. Boussaha, S. Beldi and C. Chaumont at Paris Observatory to designed the photomasks used for fabricating some demonstrators. We have used liftoff techniques for depositing dielectrics (evaporation) and metals (sputtering).

6.1 Deposition

Several techniques exist for depositing thin material layer of thickness down to few nanometers. I will focus on two of them, evaporation and sputtering, which have been exploited for KID development at Paris Observatory. Both are a type of Physical Vapour Deposition (PVD) technique [96].

- **Evaporation** happens by heating the material in a high vacuum chamber. Once exceeded the evaporation point, atoms move through the vacuum on a

straight line from the source to the substrate. In order to improve the uniformity of the film thickness, the substrate is located in a rotating platform. Clean room at Paris Observatory uses a Joule effect heating system to evaporate the dielectric layer (SiO).

- **Sputtering** allows for a more uniform deposition, and so it is preferred in case of large wafers. At Paris Observatory sputtering is used in the clean room to deposit metals (Al, Nb). The rotating wafer and the material to deposit are located in two different facing platforms, which are two electrodes. The anode is the wafer platform and the cathode is the material platform. The chamber is then filled with neutral gas, usually Argon. A strong electric field is applied between the two platform, ionizing the gas. Positive ions hit the material and eject some atoms by collisions. These can have energy of few eV, which corresponds to a temperature of about 60000 K, and reach the wafer after many collision with the argon gas, which is at $T = 300\ K$. This process is called *thermalization*. It reduces the flux on the wafer and decreases the energy of the deposited material leading to less re-sputtering back to the cathode.

6.2 Lithography

Microfabrication process consists of several depositions of different layers over a substrate. This is usually a portion of a silicon block of certain diameter which is cut in sections of definite thickness. The result is a disk shaped silicon substrate that is called *wafer*. At Paris Observatory we have used 3 inches wide (76 mm) silicon wafers with a thickness of 300 μm. Depending on the technology, lithography allows the fabrication of components with details smaller than a micron. The process of depositing a thin layer of fixed geometry requires *photomasks* and photosensitive films (or *photoresist*s). The photomask is irradiated with UV light and produces a shadow on the photoresist. It will then be dissolved with chemicals. The wavelength used will determine the smaller detail achievable. The photoresist can be negative or positive, which defines its *polarity*. Positive photoresists are soluble after being irradiated with light. Negative photoresists have the inverse behavior. The photoresist will also affect the polarity of the photomask. We can distinguish two cases:

- Negative photoresist: the UV light irradiates the photoresist following the

photomask shape. A thin layer of material to be shaped is deposited below the photoresist. When dissolved, the non-irradiated part of the photoresist disappear and what remains is the negative of the photomask which has the desired shape for the layer below. Then, part of the bare thin layer can be etched via chemicals of physical processes. The photoresist acts as a mask during this step.

- Positive photoresist: in this case the irradiated part of the photoresist disappear with the chemical and remains the positive of the photomask. The thin layer is then deposited over the photoresist. A chemical is used to dissolve the photoresist and consequently the associate thin layer above. This technique is referred as *liftoff*.

The same result can be achieved by inverting the photoresist polarity and the liftoff/etching technique. In those cases, pictures worth more than words. Fig. 6.2.1, 6.2.2, 6.2.3 and 6.2.4 show the required steps to fabricate the negative or the positive shape of a photomask by using etching or liftoff technique. For KIDs fabrication at Paris Observatory we have used liftoff both for metals and dielectric deposition.

6.3 Chips fabrication

In order to fabricate the samples described in Chapter 5 I have designed four photomasks in total. These contain the design of each deposited material. The order of deposition is the following:

1. Niobium ground plane, which includes the design of the slot antenna, part of the LEKID and the feedline.
2. Aluminum strips.
3. Dielectric (SiO).
4. Niobium microstrip network, which include the antenna excitation and filters.

Each mask includes the design of five chips contained within a three inches large wafer. Pixel design and parameter sweep will be discussed later in section 6.4. The first fabrication attempt was unsuccessful: the photoresist used to deposit the di-

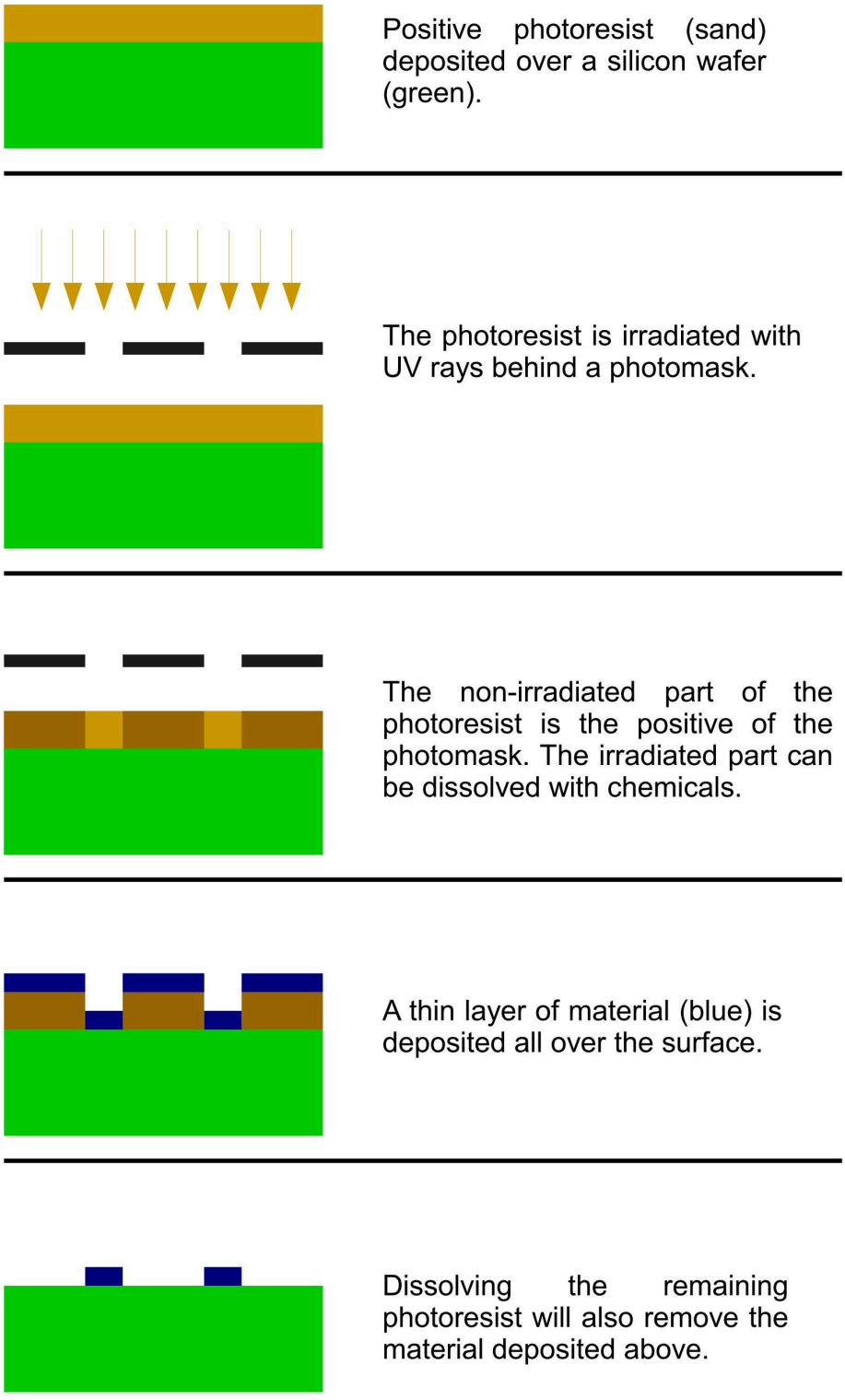

Figure 6.2.1: Liftoff with positive photoresist.

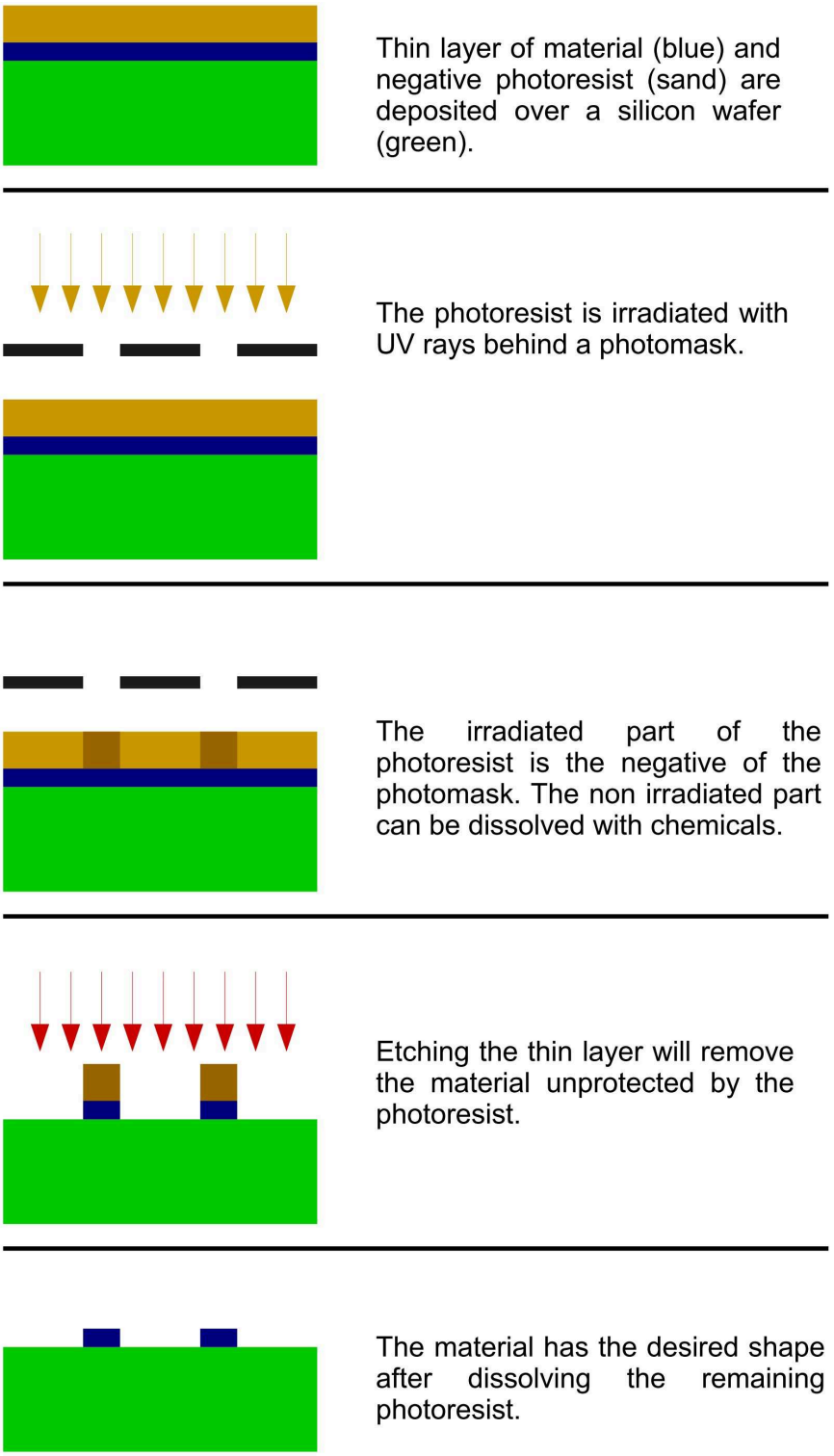

Figure 6.2.2: Etching with negative photoresist.

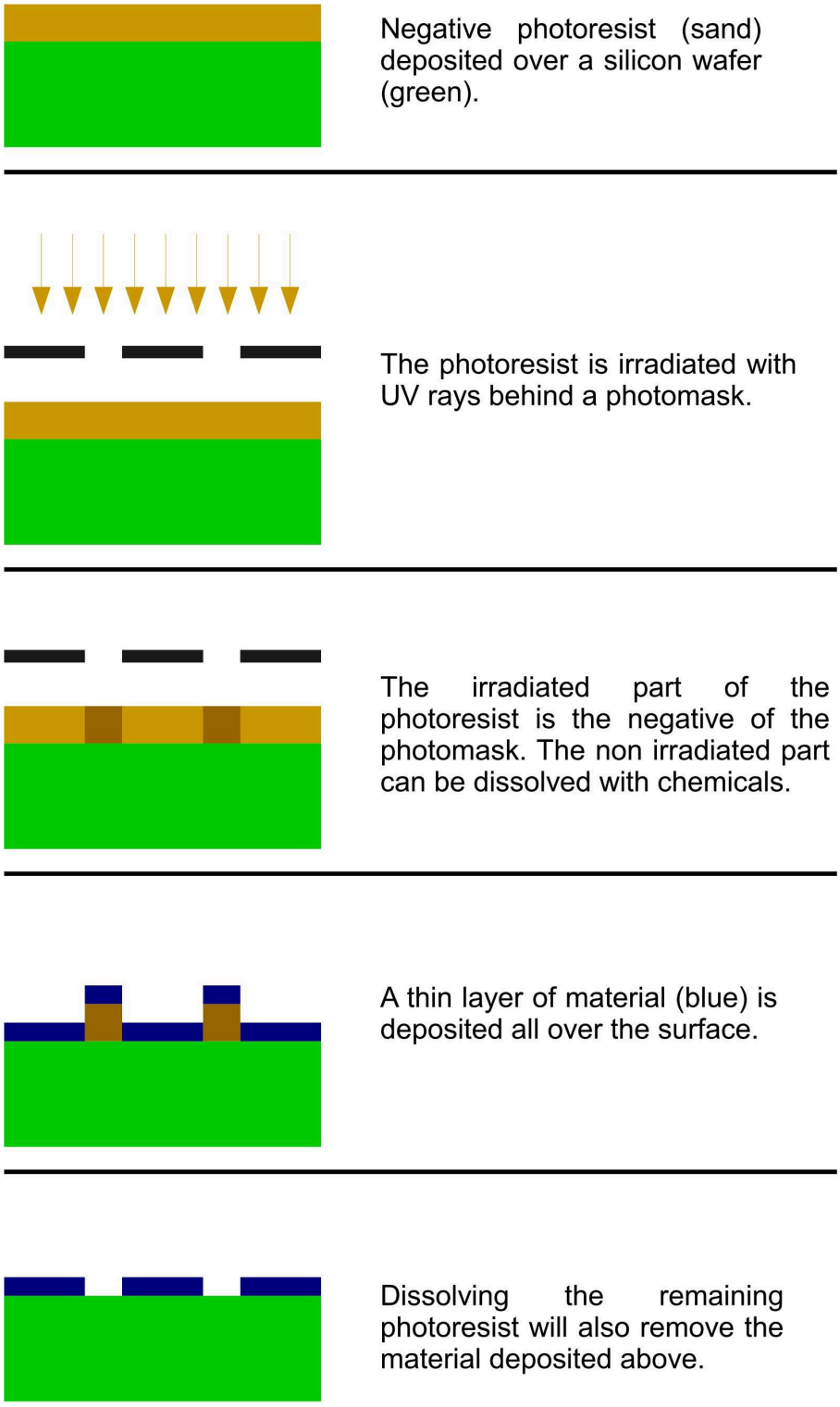

Figure 6.2.3: Liftoff with negative photoresist.

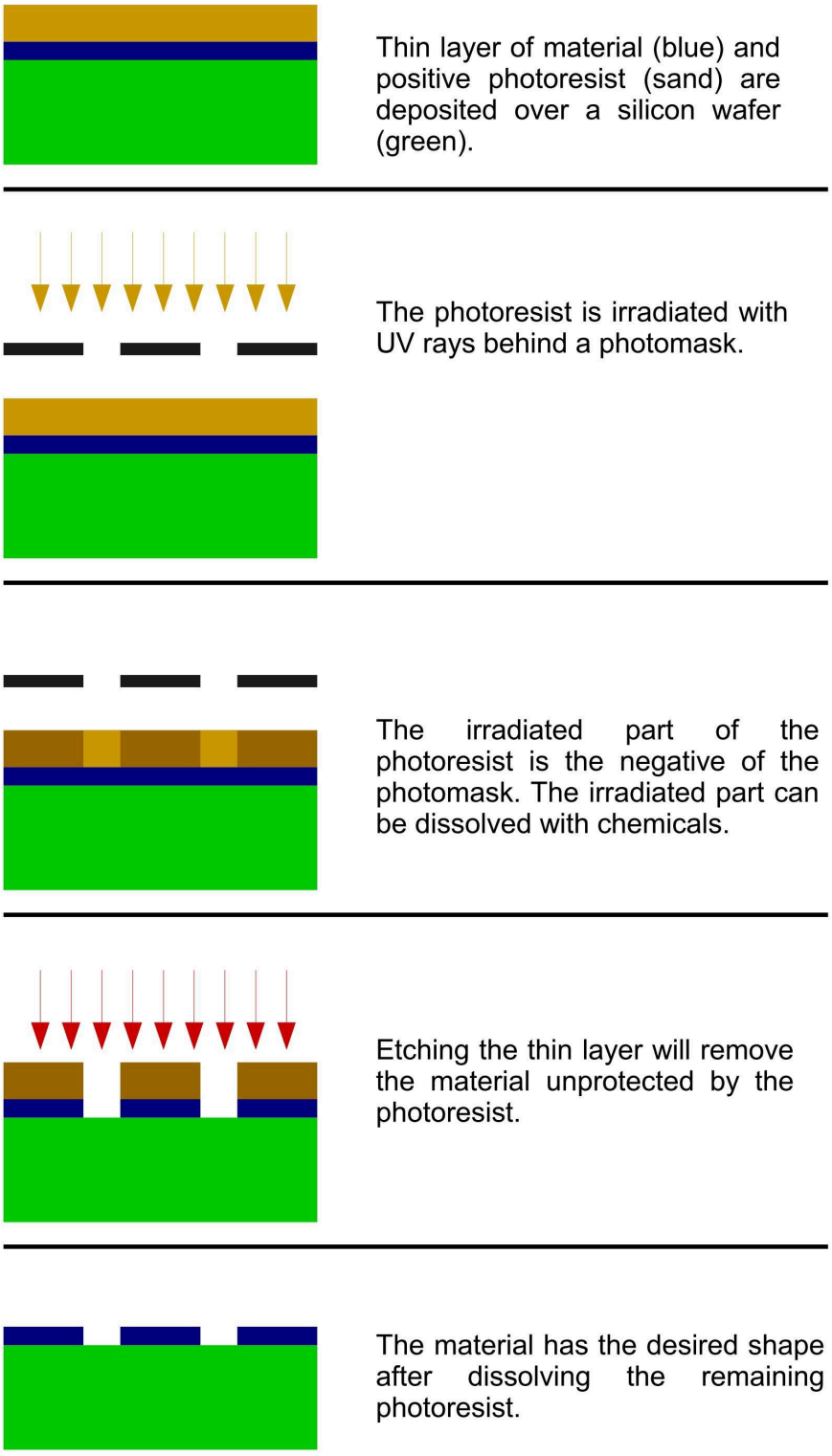

Figure 6.2.4: Etching with positive photoresist.

electric removed any aluminum deposition below once dissolved with chemicals. To fix the problem, we took advantage of the fact that the aluminum sees free space on one side, so we changed the fabrication order and deposited the aluminum at last as follows:

1. Niobium ground plane.

2. Dielectric (SiO).

3. Niobium microstrip network.

4. Aluminum strips.

This fabrication order allowed indeed to deposit the aluminum. Nevertheless, once tested, chips showed some problems in terms of performance. These will be discussed in detail in section 7.2. The GEPI group at the Observatory figured out that the main disadvantage of reordering the fabrication process was the contaminants left from previous depositions which add up and affect the aluminum deposition. We then fabricated a third chip set, keeping the same photomask order, using an acid to clean the wafer surface before depositing the aluminum. Fabrication techniques used for different fabrication attempts are shown in Fig. 6.3.1.

The GEPI group at Paris Observatory produced two sets of chips on a $3''$ silicon wafers. Each wafer includes five different chips that I tested at APC in a 300 mK cryostat and at Institut NEEL in a 50 mK cryostat. The two sets are equivalent in terms of geometry but differs in the fabrication process. After the fabrication we observed few chips that contains small defects on the geometry, these chips have been discarded. We tested in total five different chips, two from the first fabrication set and three from the second. Fig. 6.3.2 and Fig. 6.3.3 show a sample chip set layout. Each chip contains:

- Two dual-band pixels

- One or two uncoupled detectors for reference

- Up to nine antenna coupled LEKIDs

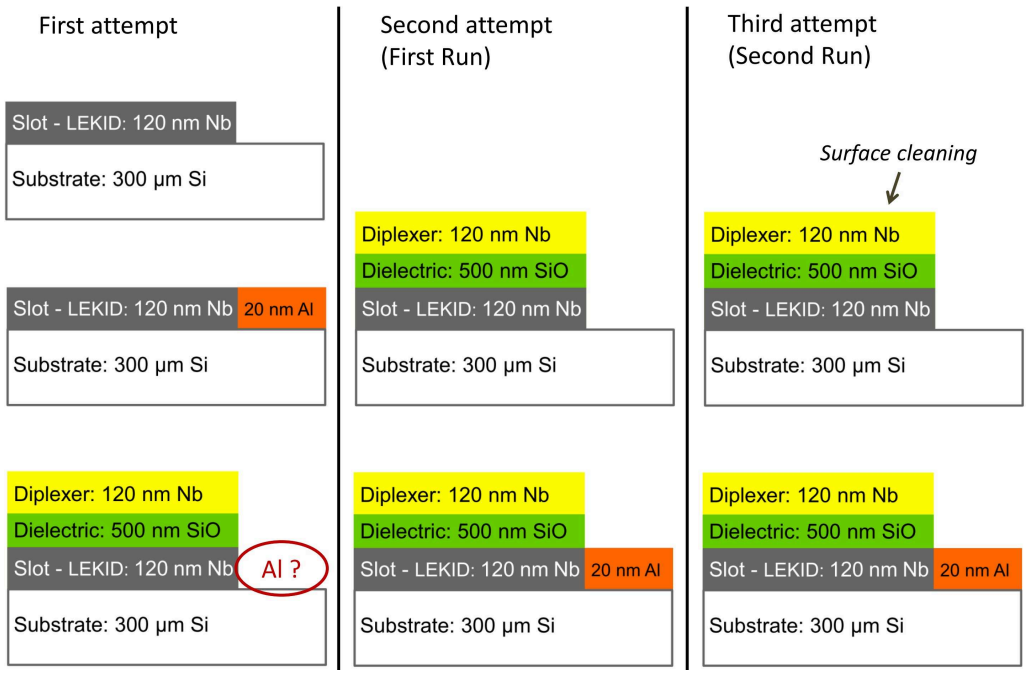

Figure 6.3.1: Fabrication order for the three fabrication attempts. The aluminum was completely washed out by further depositions in the first attempt. First chip measured (first run) has been fabricated with a different deposition order for which the aluminum is deposited last. In order to optimize the aluminum performance we fabricated a third chip set with particular effort on cleaning the wafer surface.

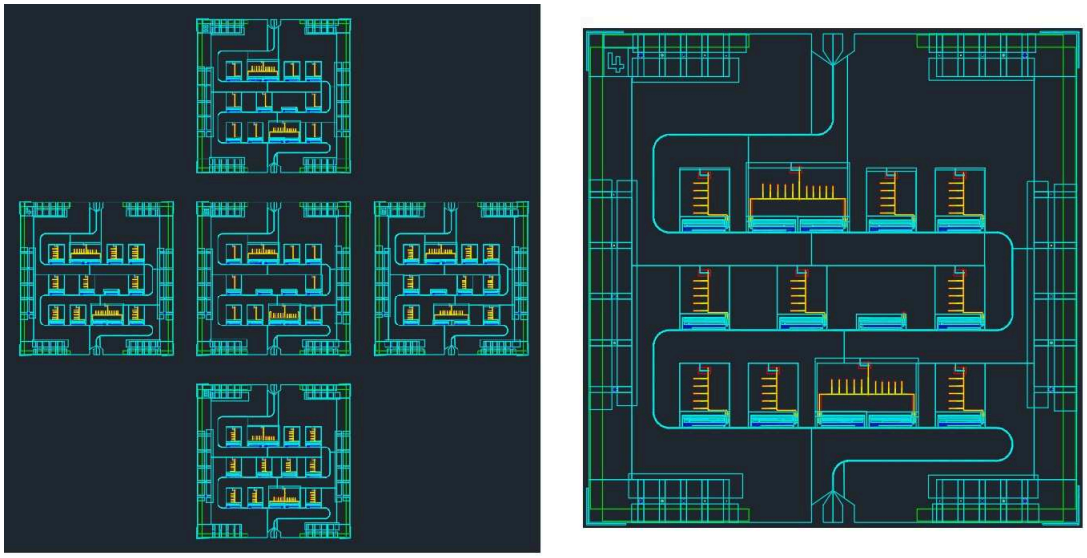

Figure 6.3.2: Layout of five chips on a 3 inches wafer (left). Zoom on one chip (right) with 2 dual band pixels, 9 single filter pixels and a spare uncoupled detector.

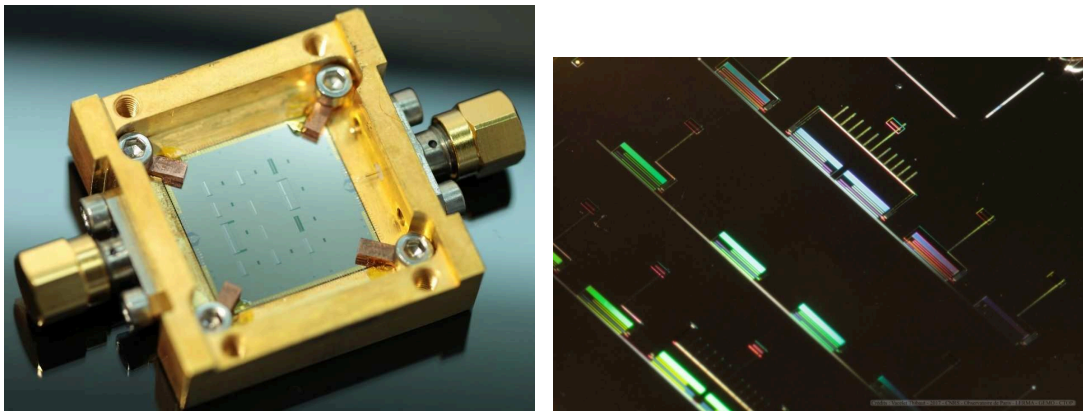

Figure 6.3.3: One chip mounted on a chip holder with two 50 Ω coaxial cable connectors (left). Zoom at microscope (right).

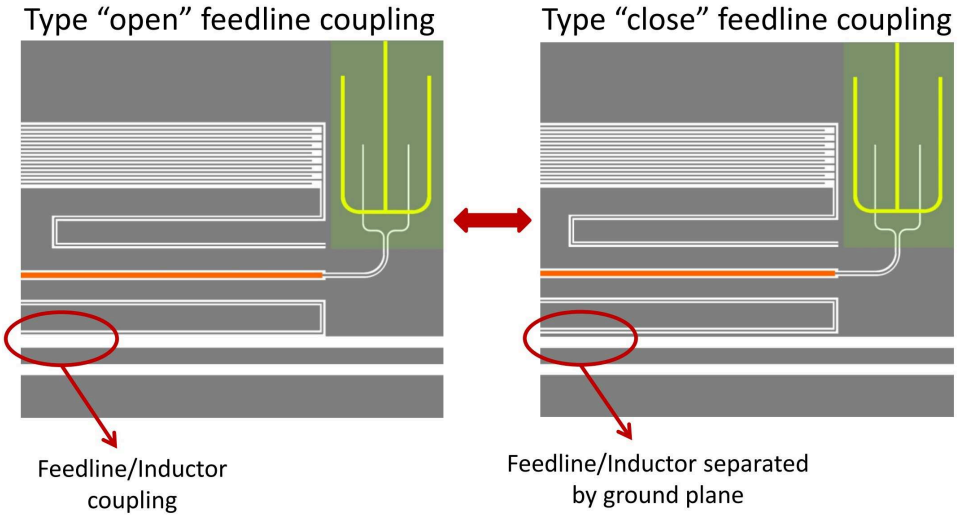

Figure 6.4.1: LEKID-Feedline coupling geometry sweep. In one case the two lines are separated by 3 μm - 5 μm ground plane.

6.4 Parameter sweeps

The three-inches wafer has enough space to fit five chips of size 2 $cm \times 2$ cm in it. These chips have different pixel geometry, which has been used to sweep some parameters as shown in Fig. 6.4.1, Fig. 6.4.2 and Fig. 6.4.3. In total I have considered six sweeps in the design:

- The main difference among the pixels is the technique used to couple the LEKID with the feedline. In some cases the two CPW are separated by a strip of ground plane (type “close” feedline coupling), in other chips the two central strips are coupled with no ground plane in between (type “open” feedline coupling). The reason of this sweep lies on the fact that in simulation the

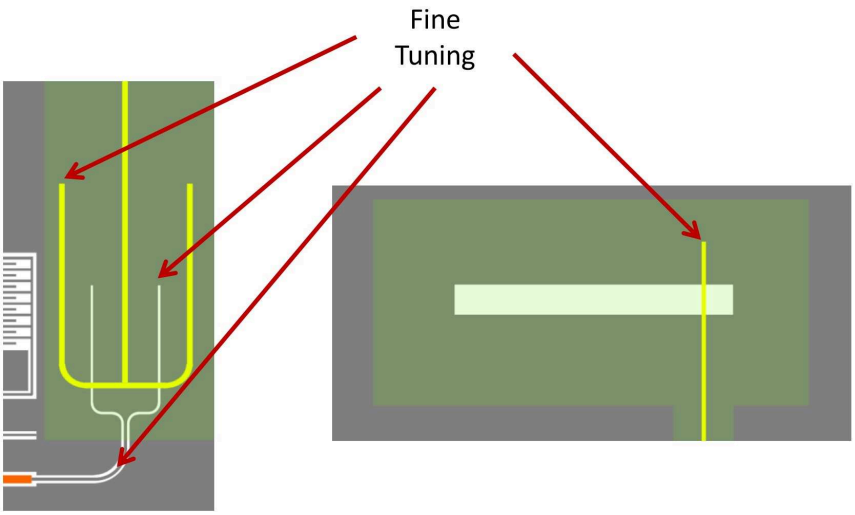

Figure 6.4.2: Microstrip-CPW transition (rigth) and Antenna (left) parameter sweeps.

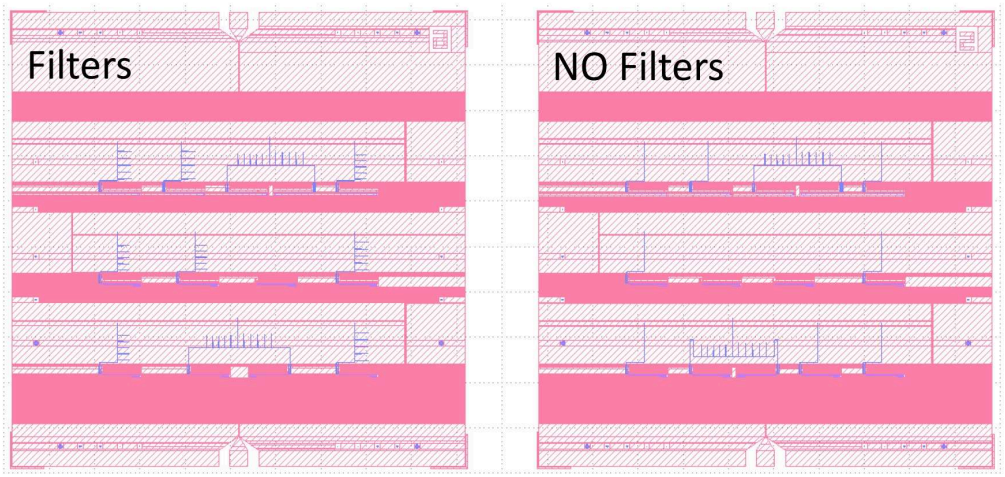

Figure 6.4.3: Two versions of the same LEKID geometry, one with filters and the other with the antenna directly coupled to the LEKID. The two dual color pixels have filters in any case due to the nature of the diplexer.

open geometry gives a deeper resonance. Nevertheless, the close geometry is preferred to avoid rough discontinuity in the ground plane and consequently preserve the coplanar mode along the feedline.

- The various impedance matching are carried out by all the stubs along the transmission lines. The lengths of these stubs are tuned around the value calculated in CST to find out which one gives the best performance. This fine tuning involves the line terminations at the LEKID-filter coupling, the distance of the Al strip from the transition and the microstrip termination at the slot antenna.

- I have considered two versions for each chip; one includes filters and a second one with the antenna directly coupled to the detectors. The dual color pixels lack of this latter variation since the filters are part of the diplexer impedance matching.

6.5 Chips layout

The following pictures show the layout of the five fabricated chips. If not specified differently, the indicated sub-band expresses the type of filter adopted and consequently the impedance matching at the LEKID-filter transition.

LEGEND

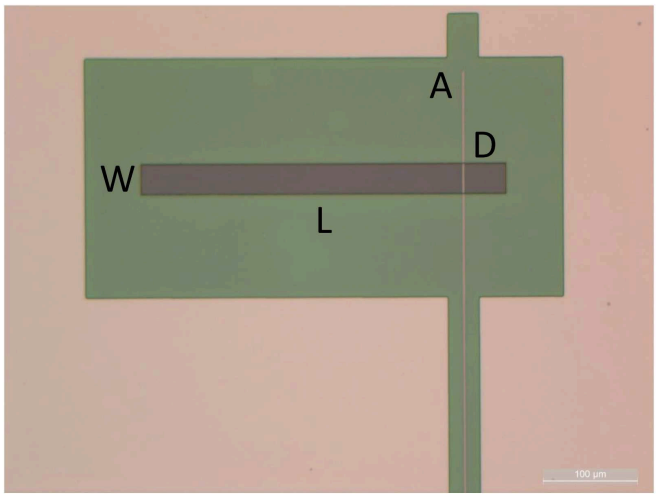

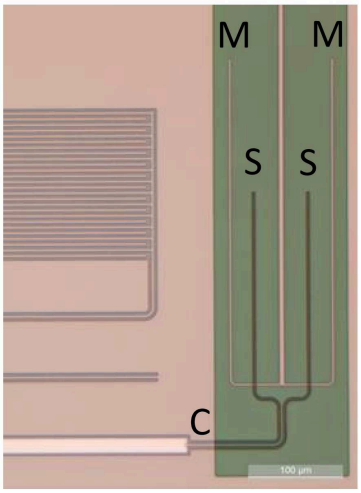

W = Slot width = 32 µm
L = Slot length = 382 µm
A = Antenna microstrip stub length = 90 µm
D = Antenna microstrip distance from the edge = 44 µm
S = Slotline length = 229 µm (140 GHz sub-band) 208 µm (160 GHz sub-band)
M = Microstrip length = 440 µm (140 GHz sub-band) 386 µm (160 GHz sub-band)
C = Aluminium strip distance from CPW - slotlines transition = 136 µm

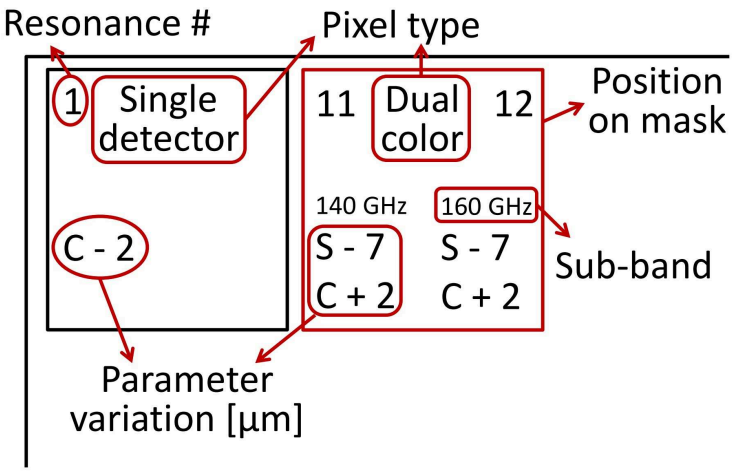

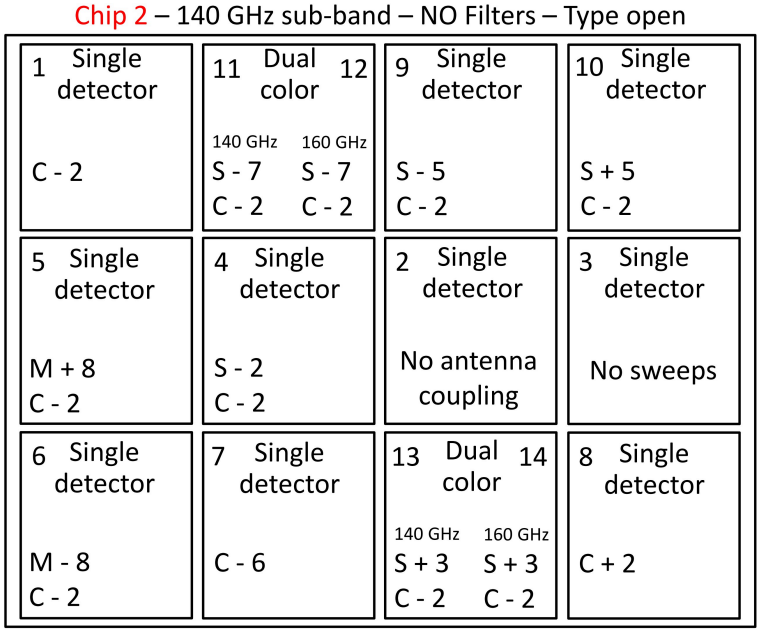

Figure 6.5.1: Layout of Chip_2. All the detectors, except for the dual color pixels, are coupled to the antenna with the impedance matching adapted for the 140 GHz centered sub-band. This chip does not include filters in single band pixels. The feedline coupling is of type "open".

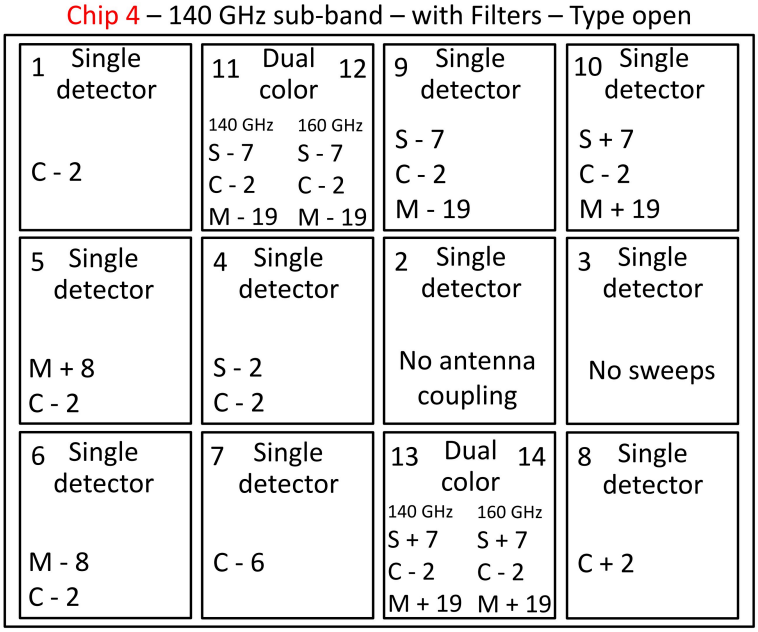

Figure 6.5.2: Layout of Chip_4. All the detectors, except for the dual color pixels, are coupled to the antenna with the impedance matching adapted for the 140 GHz centered sub-band. This chip includes filters in single band pixels. The feedline coupling is of type "open".

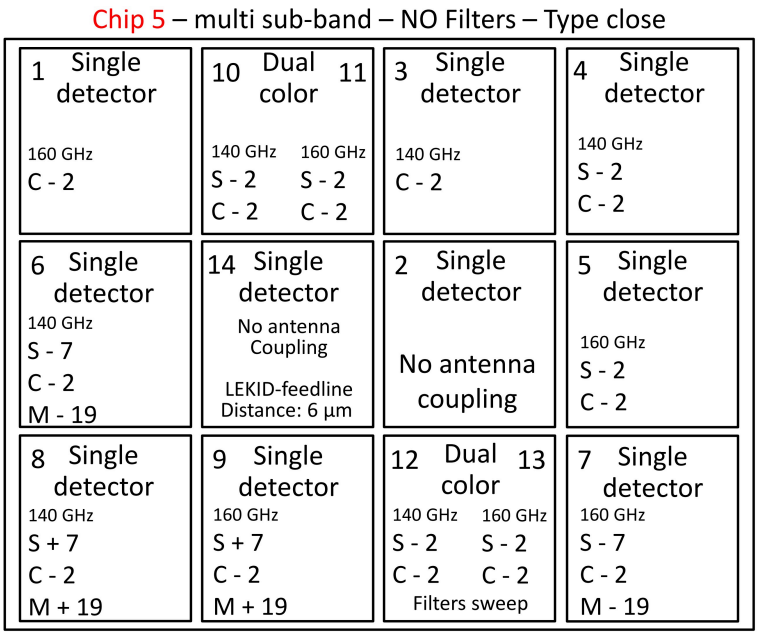

Figure 6.5.3: Layout of Chip_5. This chip includes both the two sub-bands with filters, the feedline coupling is of type "close" with 3 μm ground plane between the inductor and the feedline. One of the two dual color pixels has the 140 GHz filter coupled with the 160 GHz optimized slotline-CPW transition and vice-versa. The last detector (resonance #14) is a spare LEKID moved 3 μm away from the feedline.

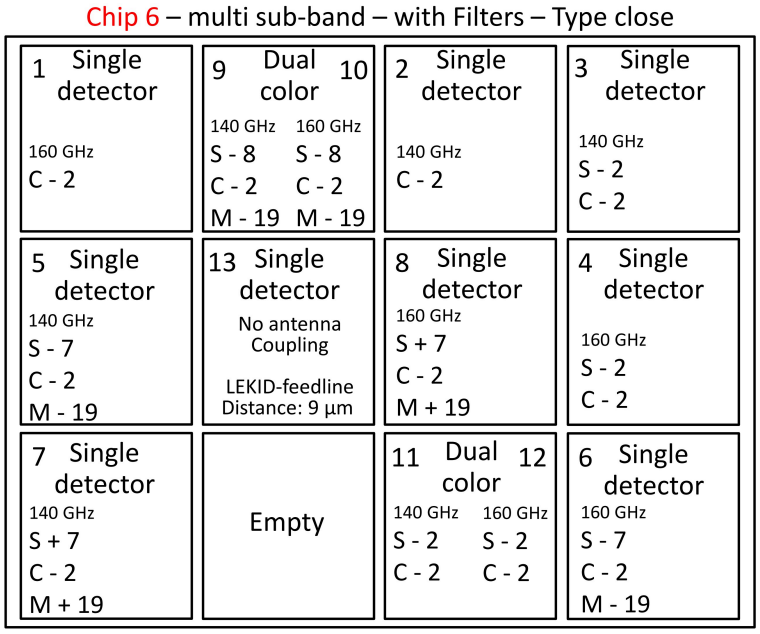

Figure 6.5.4: Layout of Chip_6. This chip includes both of the two CPW-slotline coupling configuration but does not include filters. The feedline coupling is of type "close" with 3 μm ground plane between the inductor and the feedline. The last detector (resonance #13) is a spare LEKID moved 6 μm away from the feedline.

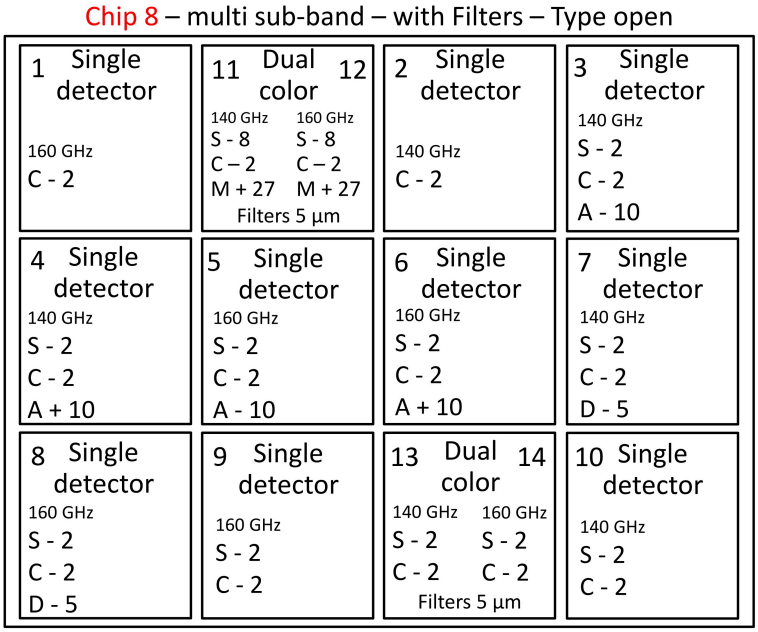

Figure 6.5.5: Layout of Chip_8. This chip includes some sweeps on the antenna geometry. The two dual color pixels have filters based on 5 μm microstrip line.

Chapter 7

Measures

In this chapter I will discuss the measurements I did of prototype chips. First, I will describe the setup I have used to test the chips at APC and Institut NEEL, then I will discuss the main results we have obtained from each prototype. We have completed two measurement runs. The first run includes chips from the second fabrication attempt as described in previous Chapter. The second run includes another chip set with identical design for which we have improved the fabrication process.

7.1 Test setup

7.1.1 APC setup

I have used a pulse tube cryostat equipped with a monochromatic millimeter source and a Vector Network Analyzer to test the chips at 300 mK. This temperature is achieved with two adsorption pumps for Helium-4 and Helium-3 single-shot cycle. The cryostat includes a 5 cm window at the bottom to illuminate the pixels. Fig. 7.1.1 shows some pictures of the equipment in the millimeter laboratory. Chips are measured with two coaxial cables; the setup consists of one variable attenuator, five DC-blocks and one low temperature amplifier as shown in Fig. 7.1.2. DC-blocks allow for thermal decoupling of the attached coaxial cables as well as suppressing low frequency noise. The main source of heat inside the cryostat is the amplifier connected to the 4 K plate, therefore one extra Dc-block is connected to the output line. The measurement is performed with a commercial Vector Network Analyzer

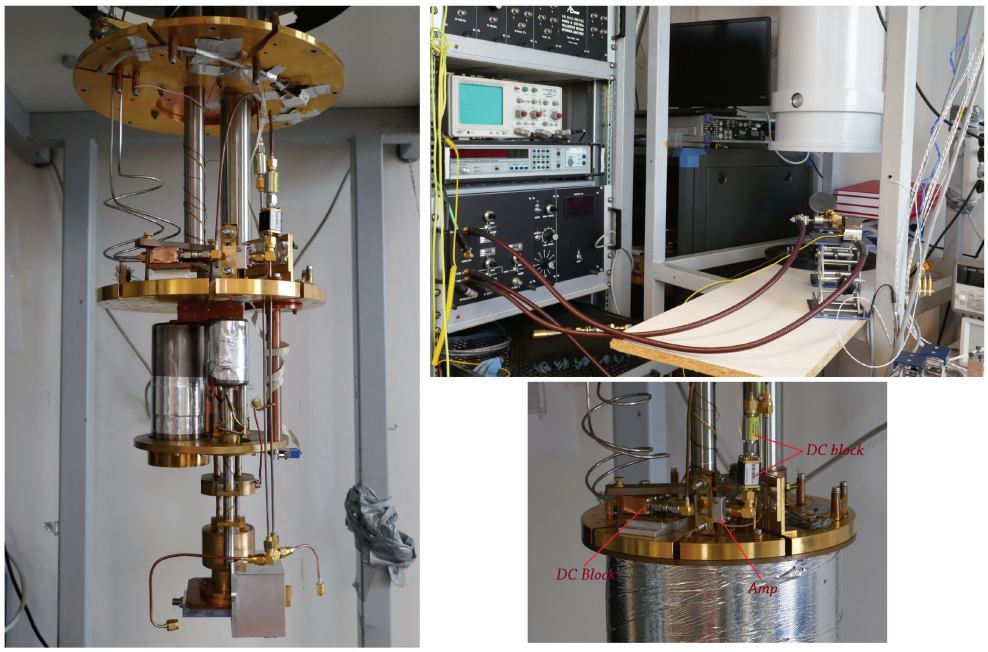

Figure 7.1.1: Pulse tube cryostat with two adsorption pump (left). Millimeter wave source (top right) and cryostat setup at 4 K (bottom right).

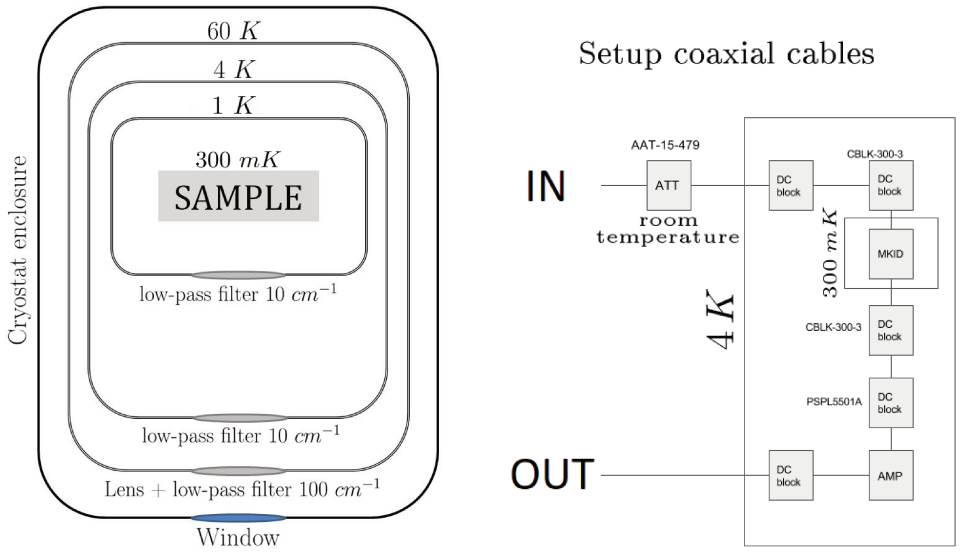

Figure 7.1.2: Cryostat optical setup (left) and coaxial cables arrangement (right - image credit to Alejandro Almela).

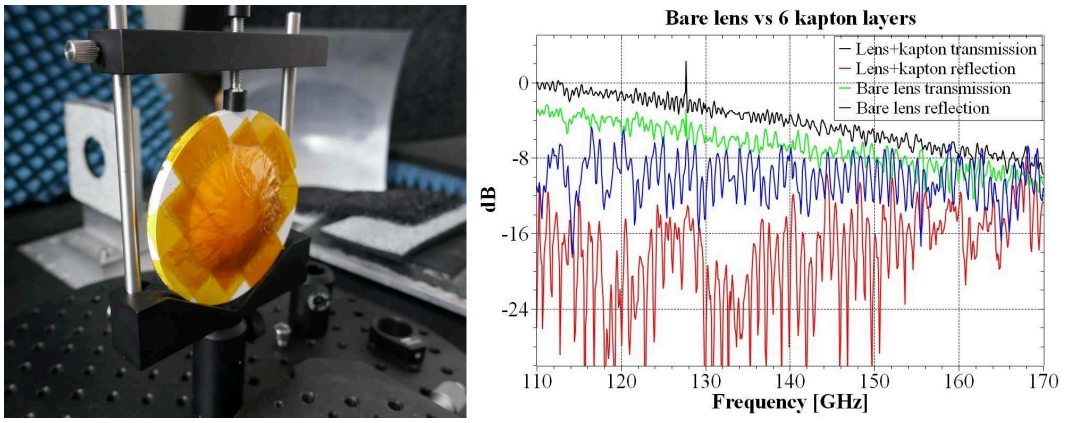

Figure 7.1.3: Lens with six layers of Kapton (left) and S-parameters measured on the optical bench (right).

(VNA). The optical setup includes one lens at 60 K in front of the main cryostat circular window. Three cold stop low-pass filters are located at 60 K, 4 K and 1 K. To improve the lens performance we have attached six layers of Kapton in both sides. Considering the thickness of the Kapton scotch and the dielectric constant of about 3.4 [97], six layers of Kapton reproduces the effect of an anti-reflection coating. Measures on the optical bench in Fig. 7.1.3 show the effect of the made-up coating on the lens transmission and reflection coefficients. The setup at APC allows for measures of resonances up to 3GHz. The bottleneck is represented by the amplifier operational frequency range.

7.1.2 Institut NEEL setup

The HELFA group[1] at Institut NEEL is active on KIDs development and characterization in several projects, including the New IRAM Kid Array (NIKA) [98]. I had access to a 50 mK cryostat [99] and to instruments dedicated to KIDs characterization:

- Fast readout electronic: it allows for following up to ten resonances at a rate of 23.8 Hz. The software includes a full resonance characterization in terms of noise and quality factor.
- Martin-Pupplet interferometer to measure the spectral sensitivity.
- Sky simulator to simulate the image of a moving planet on the sample.

[1] Hélium: du Fondamental aux Applications.

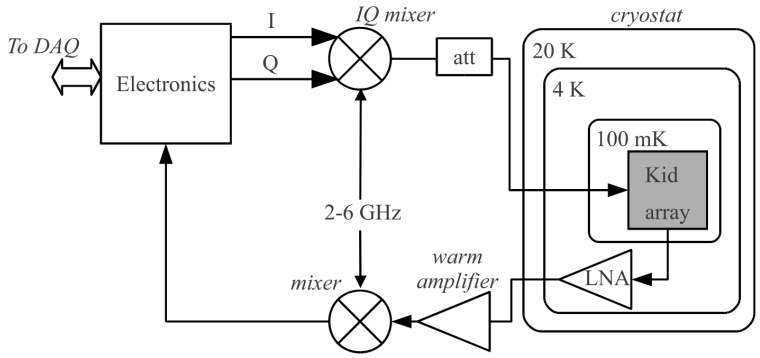

Figure 7.1.4: Block diagram of the readout setup to monitor an array of KIDs. Source: O. Bourrion et al., arXiv:1102.1314v3

Readout Electronic

The readout electronic generates a frequency comb to send along the feedline in order to excite the resonators. Resonant frequencies of KIDs are too high for any electronics, so they are generated at baseband and up-converted by hybrid mixers. The KID array output signal containing all the frequencies of the comb is multiplied by a sine and cosine wave of the tone of interest and filtered on a low-pass filter. This method generates the I and Q components which are continuously monitored to recover the amplitude $A = \sqrt{I^2 + Q^2}$ and phase $\phi = \arctan(Q/I)$ of the signal. The schematic of a standard readout setup is shown in Fig. 7.1.4. The KID array is preceded by an attenuator, to control the input power, and followed by a Low Noise Amplifier at $4\,K$.

Murtin-Pupplet

The Martin-Pupplet interferometer (MPI) is a Fourier transform interferometer which uses two modulated black body sources to produce an interferogram once demodulated. The basic scheme is shown in Fig. 7.1.5. Two black bodies at $300\,K$ and $77\,K$ respectively are modulated by a polarizer rotating at angular speed ω. A polarizing grid oriented at 45° with respect to the modulator splits the beam into two different optical paths. Two mirrors flip the polarization by 90° so that the reflected signal has the opposite polarization on the polarizing grid. One of the two mirrors is moving continuously. The beam produced by the MPI has intensity I given by the power difference between the two sources modulated at 2ω [101]. Fig. 7.1.6 shows the MPI in front of the cryostat.

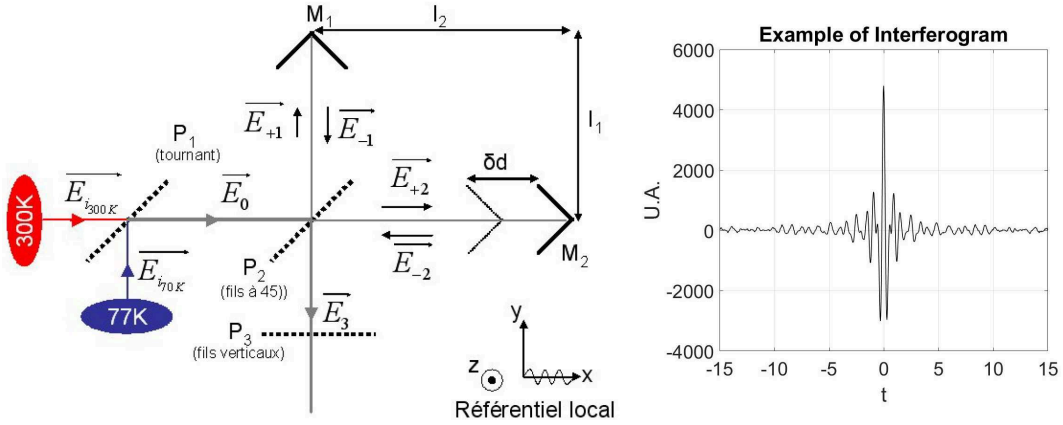

Figure 7.1.5: Scheme of a Martin-Pupplet interferometer (left - credit to Thomas Durand [101]) and example of interferogram generated after demodulation.

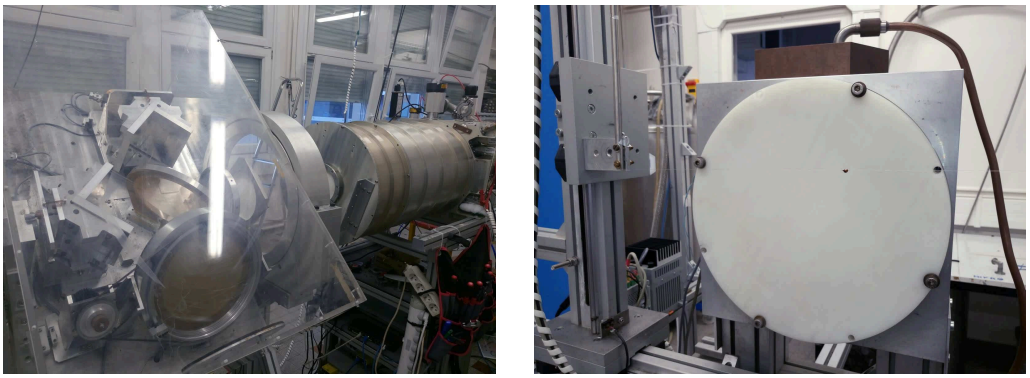

Figure 7.1.6: The Martin-Pupplet interferometer in front of the cryostat (left). Picture of the sky simulator (right). The nylon wire is attached on a motorized XY stage which moves the ball over a cold screen.

Sky Simulator

The sky simulator produces the image of a moving planet with a low emissivity ball hold by a nylon wire. The ball is free to move in two axis over a cold screen of temperature down to 50 K and reflects the surrounding 300 K, simulating a hot spot over the cold sky. A picture of the instrument is shown in Fig. 7.1.6.

7.2 First run

The first run includes chip 2 and chip 5, all other chips presented fabrication defects and have been discarded. First preliminary tests consist of measurements at APC with temperature and black body sweeps. I also attempted to measure the spectral sensitivity with the polarized millimeter source.

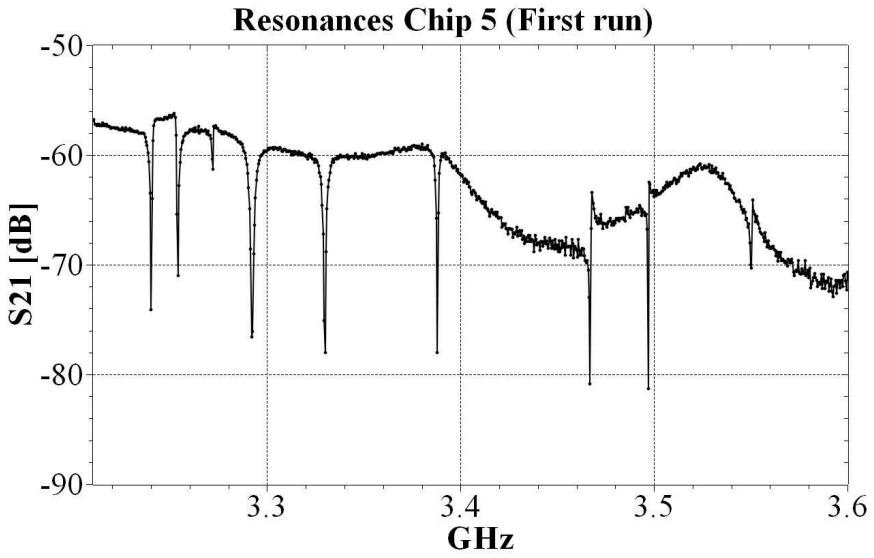

Figure 7.2.1: Resonances of chip_5 measured at 320 mK. The total quality factor is about 10^4.

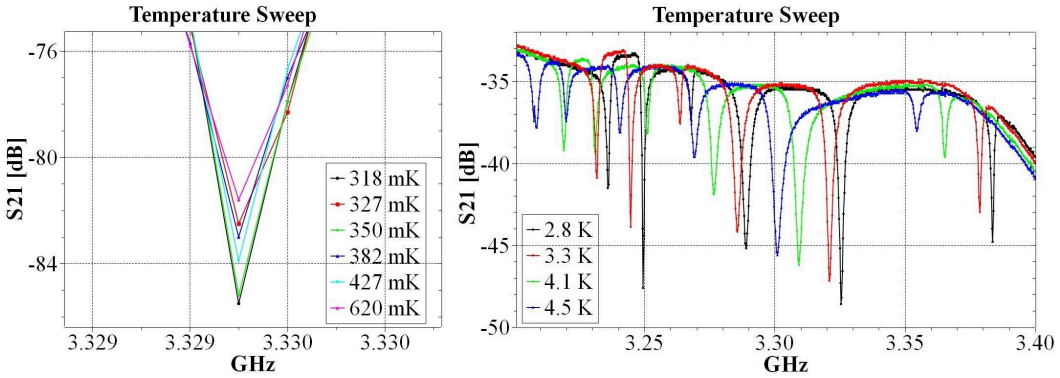

Figure 7.2.2: Temperature sweep of one pixel (left). The temperature does not affect the resonant frequency for $T < 1\ K$. The sensitivity increases at higher temperatures (right).

7.2.1 Chip 5

This sample contains 14 detectors: two dual-band pixels, two spare resonators and ten antenna coupled LEKIDs without signal filtering. Measures with the VNA at 320 mK (Fig. 7.2.1) show nine resonances around 3.4 GHz, which is much higher than expected, in a bandwidth of 300 MHz. The calculated total quality factor is of the order of 10^4. Changing the black body source does not affect the resonances, so I raised up the temperature to measure the resonance response. Fig. 7.2.2 shows that the resonance shift is null for $T < 1\ K$. Resonances start moving at temperature greater than the aluminum critical temperature, thus the aluminum does not contribute to the resonance which just might be due to the niobium feedline. Another explanation is that the aluminum deposition has some fabrication defects and only

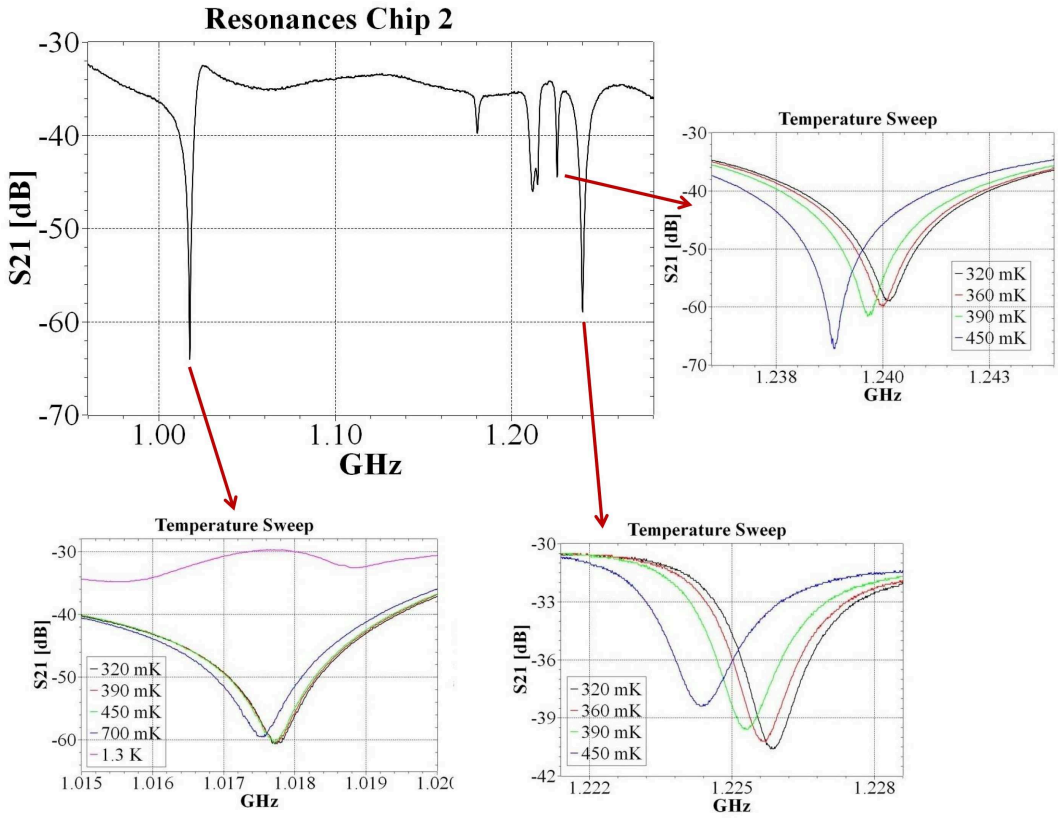

Figure 7.2.3: Resonances of chip_2 disappear at temperature above T_c of aluminum. The quality factor increases with temperature in one pixel.

part of the LEKID resonates.

7.2.2 Chip 2

Contrary to chip_5, this sample has the type "open" feedline coupling. Measures at 320 mK show only few resonances at around 1.2 GHz, which is the expected band, and with a poor quality factor of about 10^3. Chip_2 is responsive to the temperature sweep accordingly to aluminum. Fig. 7.2.3 shows the resonance shift increasing the temperature. One pixel presents a quality factor which increases with temperature. In any case resonances disappear when the temperature rise above the critical temperature of aluminum, confirming that we are looking at the LEKIDs.

7.2.3 Conclusion

During the first run of tests I have encountered several issues regarding the pixel performances. These are summarized as follows:

- The total quality factor seems to depend on the feedline coupling geometry. It approaches 10^4 for the type "close" and reduces to 10^3 for the type "open".
- One of the two chips tested is not responsive to the temperature accordingly with the aluminum strip. In the other case one pixel shows the unexplained behavior of increasing its quality factor with temperature.
- None of the chips tested has a number of resonances equal to the number of detectors. In case of chip_2 the resonance number is less than half the number of detectors.
- Only chip_2 has resonances in a frequency band consistent with simulations.

Detectors of chip_2 are slightly sensitive when illuminated with a black body or with the monochromatic light. In this latter case resonances shift only for certain frequencies of the source with a periodicity of roughly few GHz. I tried to change the optical setup of the cryostat in attempt to reduce the impact of potential Fabry-Perot effect which can produce a frequency selection along the optical path. I didn't find any significant improvement by removing some elements like the lens or a low-pass filter. Some further tests are required to investigate the optical performance of the cryostat, in particular the stray light control.

7.3 Second run

The second measurement attempt includes a brand new fabricated chip set with the same masks. During the fabrication process more effort has been made to remove contaminants during metal depositions, in particular on the aluminum strip, as described in Chapter 6. The second run involves measurements both at APC and Institut NEEL.

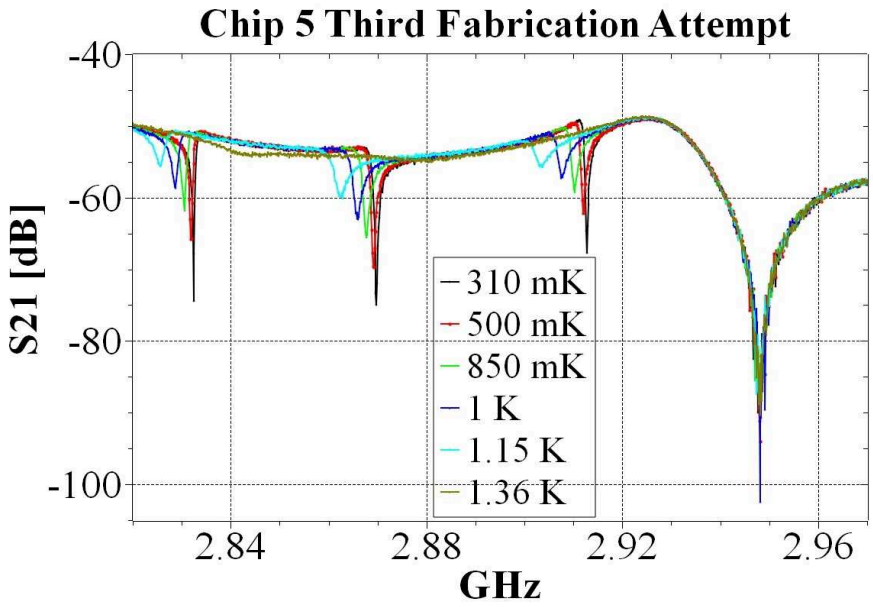

Figure 7.3.1: Temperature sweep of Chip_5. Compared to the analogous chip of previous fabrication process this chip is sensitive to temperature in the temperature range of superconducting aluminum.

7.3.1 Chip 5

Although the geometry of this chip is exactly the same to that of the chip_5 tested during the first run, the new fabricated chip presents a number of different features. As shown in Fig. 7.3.1 the resonant frequencies are decreased of about 500 MHz and are sensitive to temperature. Above 1.15 K resonances disappear accordingly to the aluminum transition to normal state. The quality factor of 10^4 is preserved. Despite the shift in frequency, resonances are still in a frequency range not consistent with simulations. In addition, the separation between two resonances is much greater than what expected since all the 14 LEKIDs are supposed to fit within a bandwidth of about 120 MHz. Fig. 7.3.2 shows a low frequency resonance which is sensitive to temperature greater than 500 mK but does not disappear above the critical temperature of aluminum, suggesting some other excitation modes of the LEKID which are mainly driven by the niobium ground plane and/or the microstrip network.

7.3.2 Chip 4

This sample includes 14 detectors: two dual-band pixels, eleven antenna coupled LEKIDs with the bandpass filter centered at 140 GHz and one spare resonators. Every pixel has the type "open" feedline coupling. Measure in Fig. 7.3.3 has been

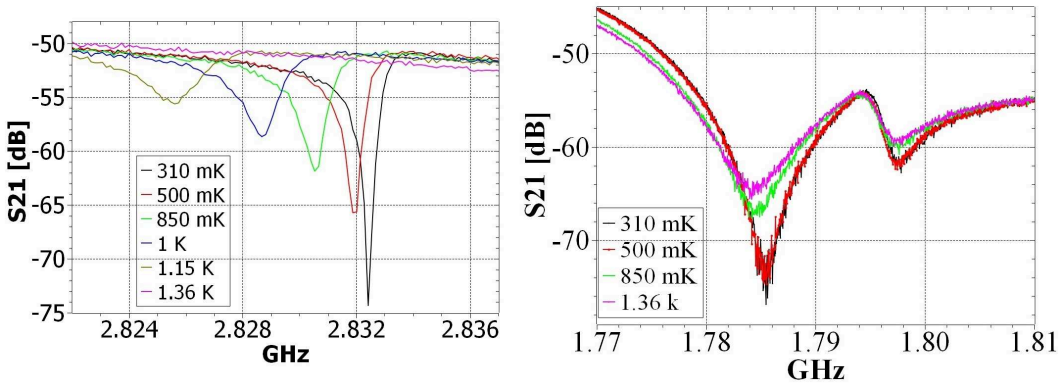

Figure 7.3.2: Zoom on some pixels of Chip_5. The plot on the left shows a correct aluminum driven temperature sweep for one high frequency resonance. The plot on the right shows an unexplained resonance at low frequency which is sensitive to the temperature only above 500 mK and does not disappear when temperature is greater than the aluminum critical temperature.

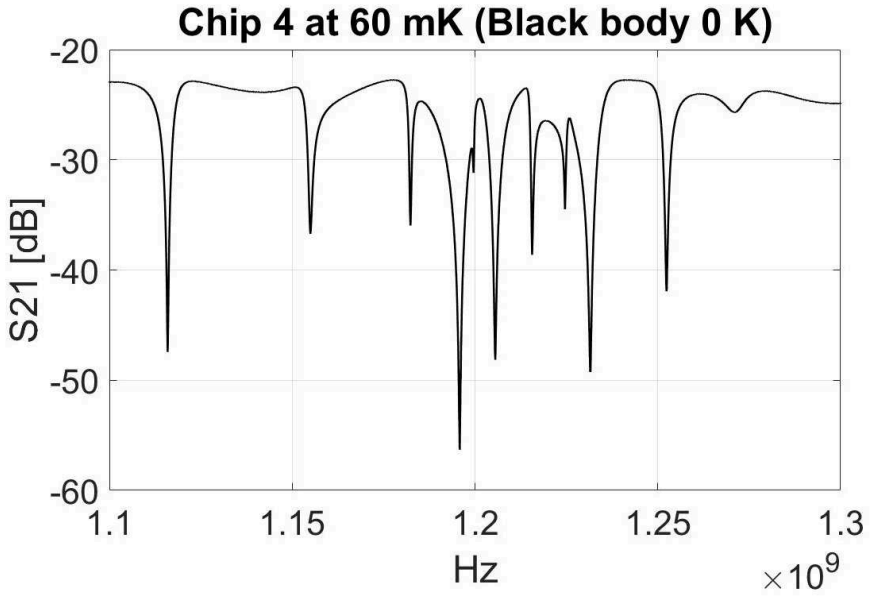

Figure 7.3.3: VNA scan at 60 mK with an equivalent black body temperature of 0 K.

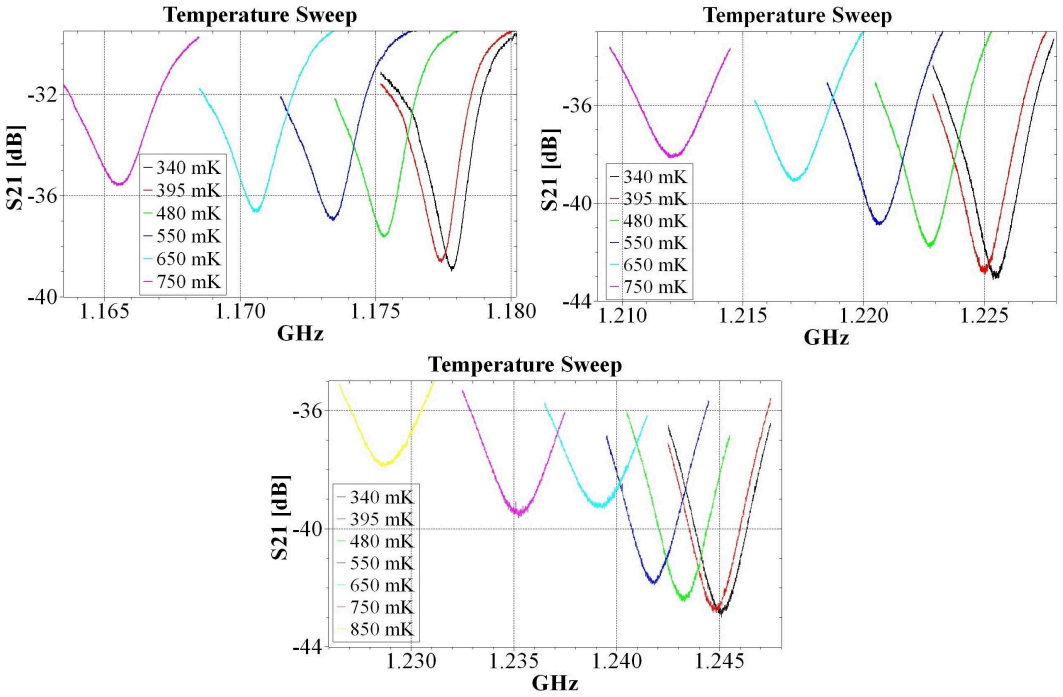

Figure 7.3.4: Temperature sweep for some pixels in Chip_4. All the resonances are sensitive to aluminum.

taken at Institut NEEL. Resonances show a poor quality factor of 10^3, which is comparable to those on Chip_2 first run. The frequency range and distance between resonances is consistent with values found in simulations. Compared to the first run, measures in NIKA0 shows almost twice the number of resonances of Chip_2, suggesting that the new fabrication process improved the chips performance. The temperature sweep (Fig. 7.3.4) presents a frequency shift in agreement with the superconducting aluminum. Fig. 7.3.5 shows that the quality factor is strongly affected by the input power on the feedline and above a certain value some resonances disappear. Each pixel has been characterized in terms of spectral response both with black body sweep and the Martin-Pupplet interferometer. Results of black body sweep are shown in Fig. 7.3.6. Resonance labeled as '8' presents the higher signal to noise ratio and is among the most sensitive. As in Chip_2 first run, one pixel show an unexplained inverse frequency shift. Measures with the Martin-Pupplet interferometer shows two different types of spectrum:

1. Resonances 4, 7, 8, 9 and 10 are responsive in a band centered nearby 100 GHz, which is close to the aluminum frequency threshold. Detectors also show some response below 90 GHz, leading to confusion about the detection mechanism.

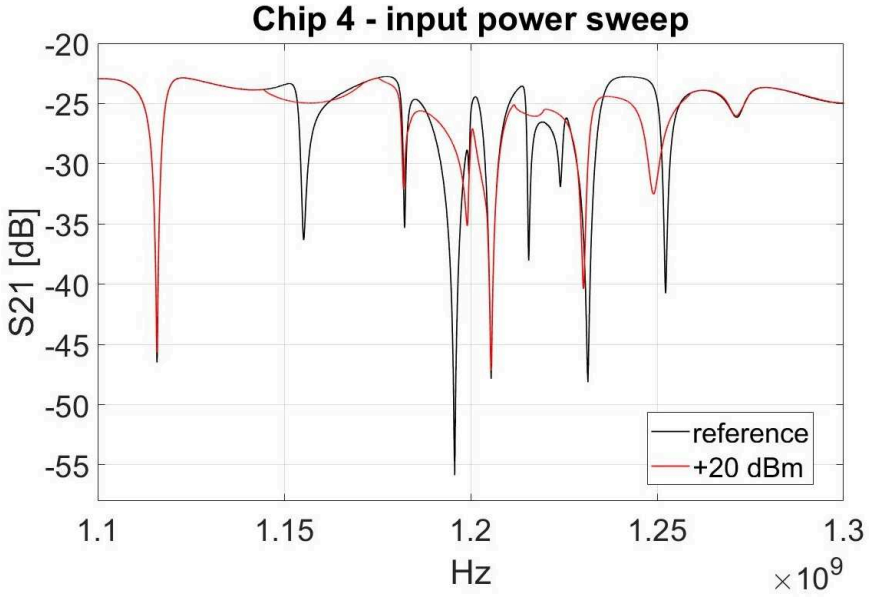

Figure 7.3.5: Resonances of chip 4 are sensitive to the input power on the feedline. The quality factor decrease while increasing the power, above a certain value most of the pixels shift in frequency, decrease in amplitude or disappear.

2. Resonances 1, 3, 5 and 6 show a more broad spectrum with particular sensitivity around 180 GHz. This frequency band should be rejected by the filters; furthermore, the spectra don't present the antenna cutoff above 180 GHz. A second slightly less intense peak is present at frequencies around 300 GHz.

Spectra of the two types are shown in Fig. 7.3.7. Pixels are also sensitive to linear polarization (Fig. 7.3.8). Pol and Cross-pol are measured with respect to the antenna polarization. Sensitivity of type 1 pixels almost disappear in cross-pol, while type 2 pixels is half sensitive than in pol case. The sky simulator shows a local response of pixels on the mask, even though due to the high noise level and the poor spatial resolution I was not able to properly extract the information about the pixel location. Furthermore, the planet scan speed is not constant and introduces a systematic error in the planet chart as shown in Fig. 7.3.9. In order to measure Pol and Cross-pol, we mounted the chip at 45° inside the cryostat. This is observable from the 45° feature on charts which is generated by the planet holding nylon wire.

7.3.3 Chip 6

This sample has the type "close" feedline coupling and includes 11 pixels: two dual color pixels, four antenna coupled LEKIDs with the bandpass filter centered

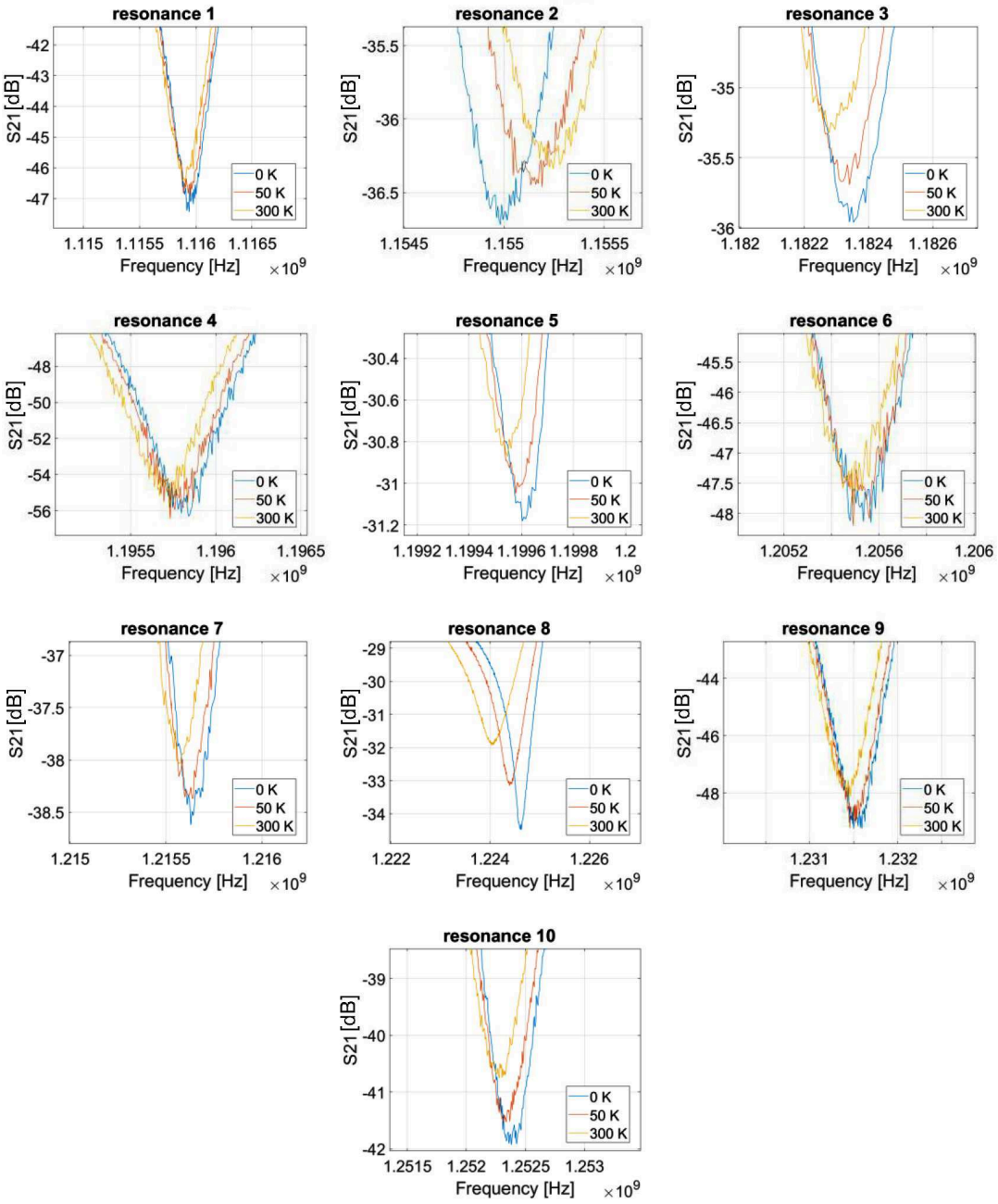

Figure 7.3.6: Resonances of Chip_4 for three different black body sources. Noise level and sensitivity varies on each pixel. Resonance labeled as '2' has the unexplained behavior of shifting frequency on the wrong side while the black body temperature increases. The same effect has been noticed on Chip_2 first run.

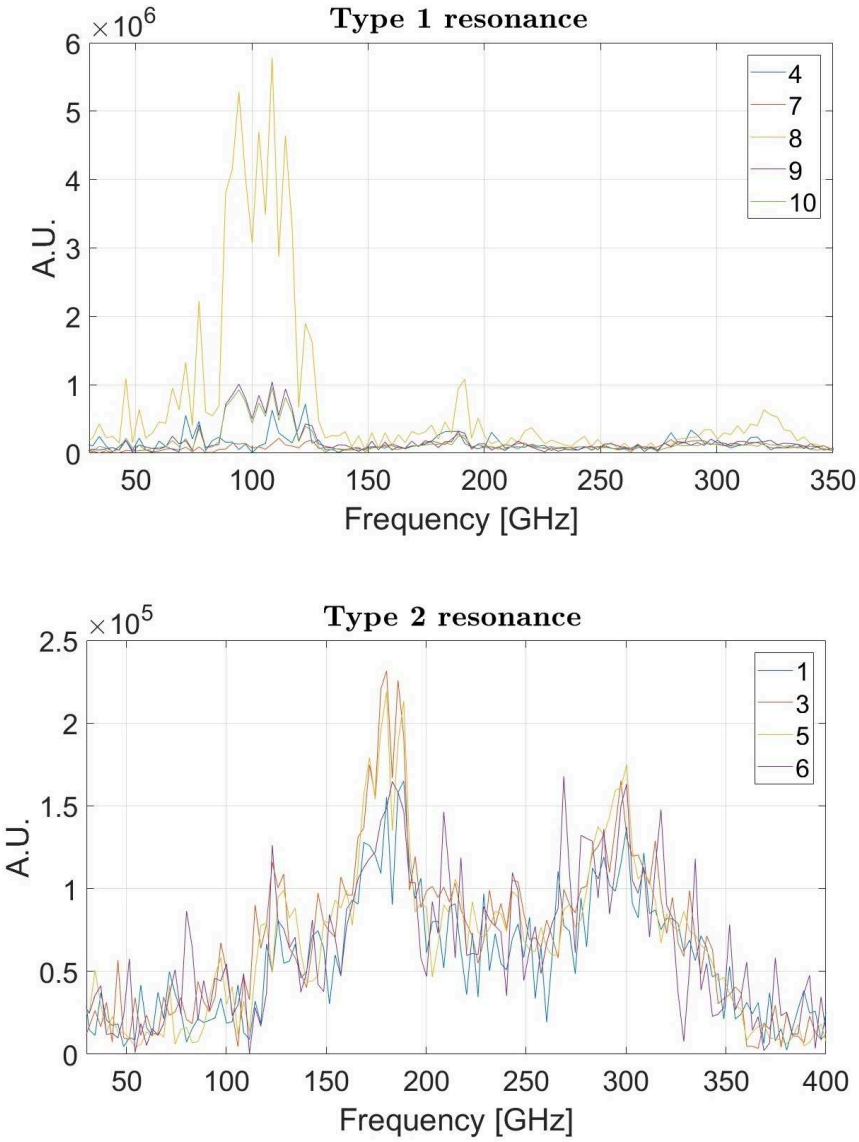

Figure 7.3.7: Type 1 and type 2 spectrum of pixels in Chip_4. Resonance sensitivity below 100 GHz can't be explained with Cooper Pair breaking.

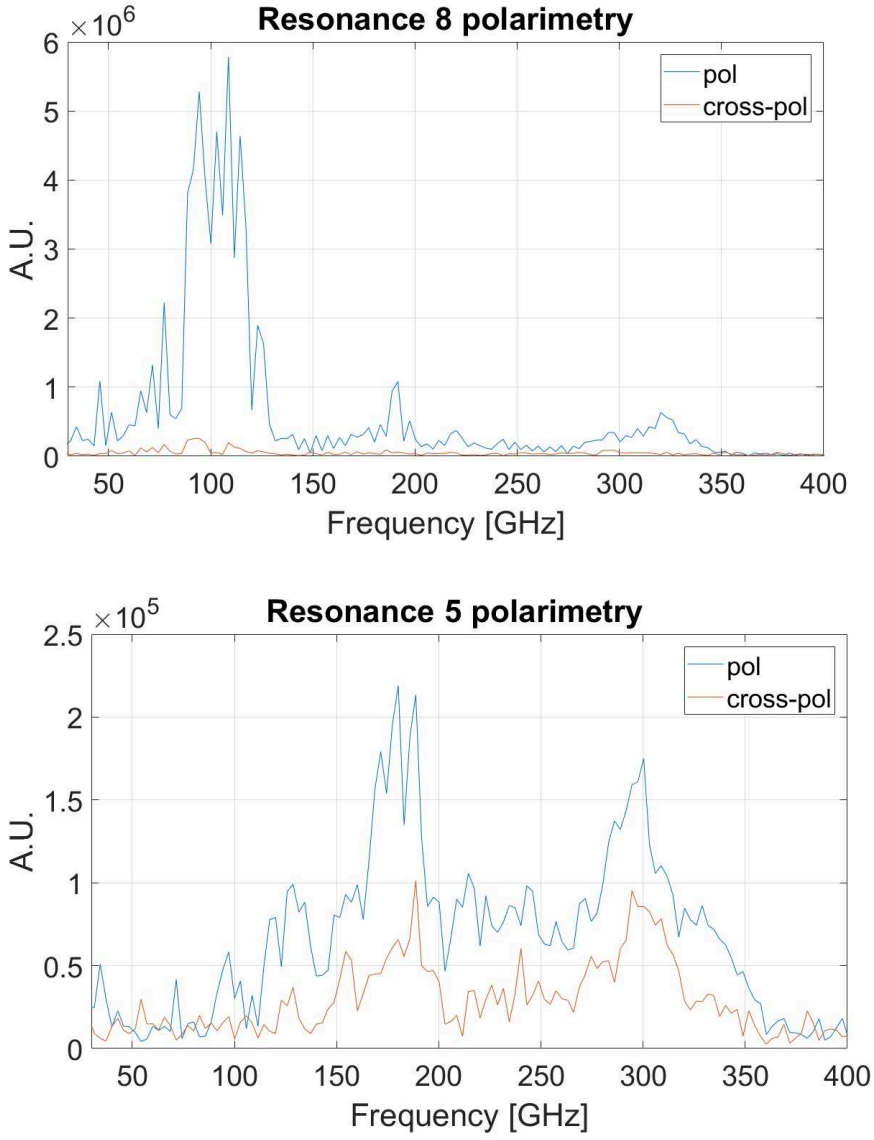

Figure 7.3.8: Polarimetry of pixel 8 (type 1 spectrum) and pixel 5 (type 2 spectrum). These are the pixels with the best noise performance for each spectrum type.

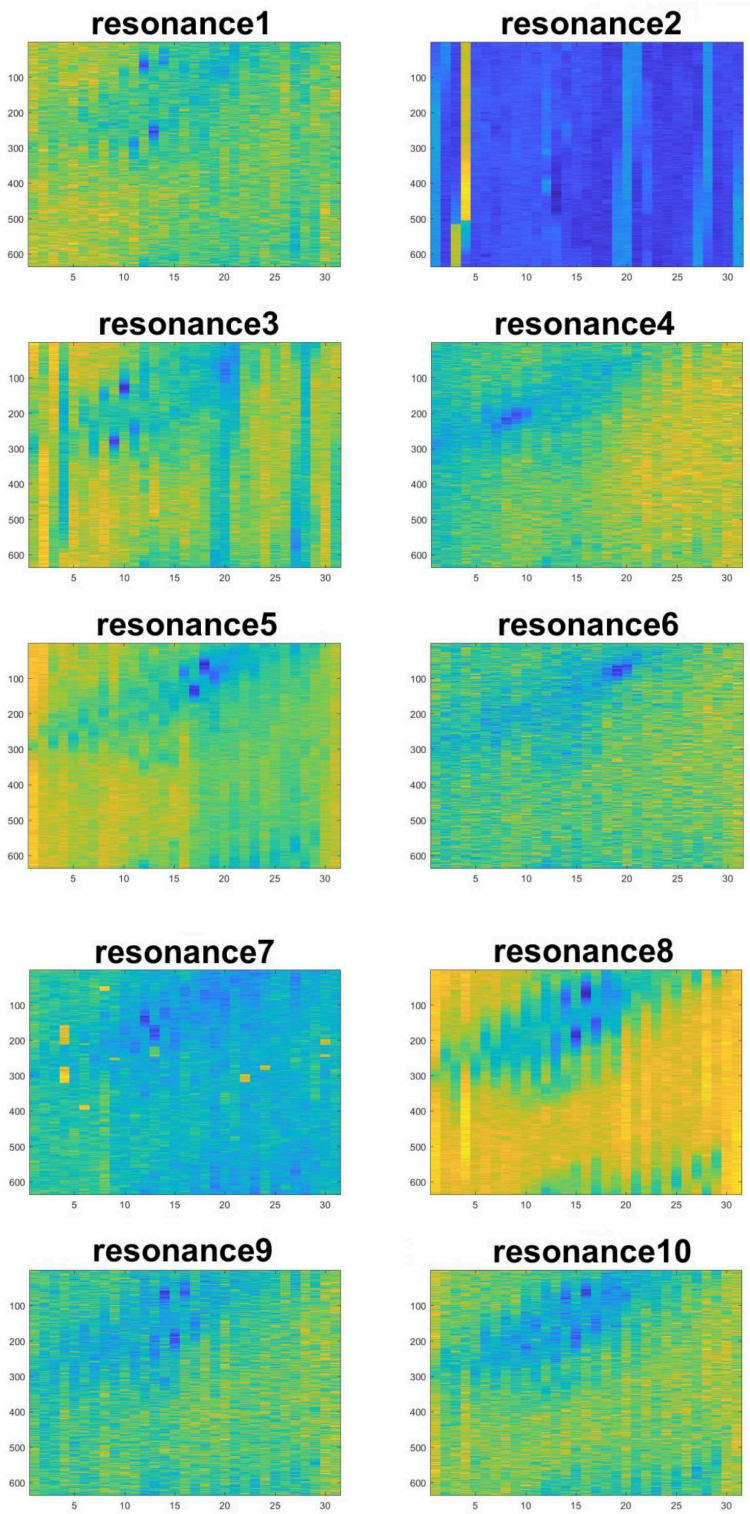

Figure 7.3.9: Planet chart for each resonance of Chip_4. Pixel 8 present a decent contrasts due to better signal to noise ratio. It is clear that the planet position on the chart differs for every pixel. In addition to the planet, a linear shadow 45° tilted, which is generated by the holding nylon wire, is also visible.

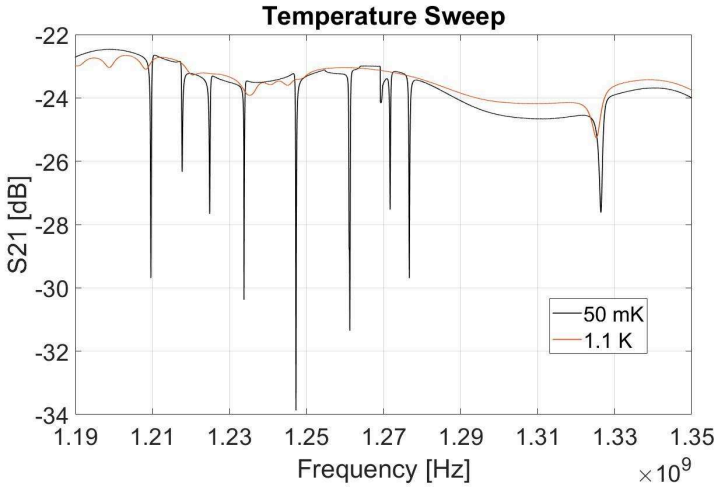

Figure 7.3.10: VNA scan of Chip_6 at 50 mK. Quality factors are consistent with the closed type coupling as in Chip_5. Resonance at 1.32 GHz does not disappear with temperature even though the amplitude decreases significantly. Such a behavior may be due to some local defects in the aluminum. As seen in Chip_5 first run, pure niobium resonances are quite insensitive below 1 K.

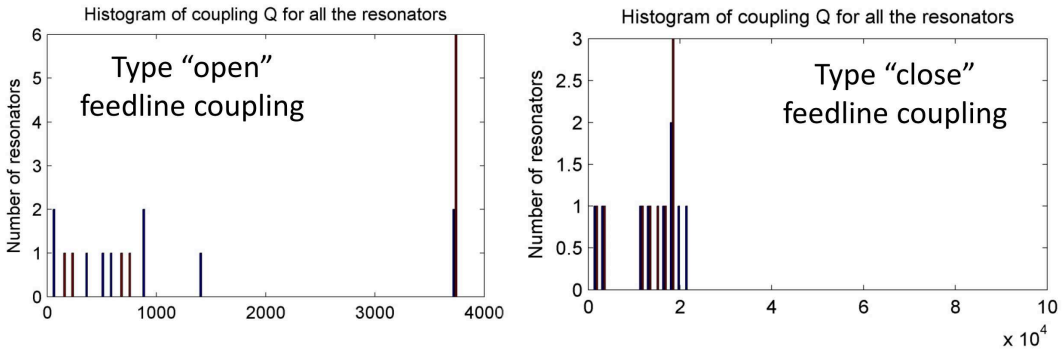

Figure 7.3.11: Comparison of Q_c of Chip_4 (left) with Q_c of Chip_6 (right). The latter is ten time greater, which explains the higher total quality factor of Chip_6. Both histograms are generated by the NIKA software.

at 140 GHz, four antenna coupled LEKIDs with the bandpass filter centered at 160 GHz and one spare resonator. This latter LEKID is 6 μm more distant from the feedline respect to the others. Measures in Fig. 7.3.10 show ten pixels with quality factor of 10^4, which is coherent with the other "close" feedline coupling-like chips, but contrary to them, resonances are in the expected frequency range. Chip_6 is the first tested among the set that have both high quality factor and resonances consistent with simulations in terms of frequency range and separation. Comparing pixels of Chip_4 with pixels of Chip_6 (Fig. 7.3.11) we notice that the quality factor is determined by the coupling quality factor. The black body sweep is less noisy than any other chip among the set (Fig. 7.3.12) and none of the pixels show the inverse resonance shift feature. Due to the lower noise, the planet charts have

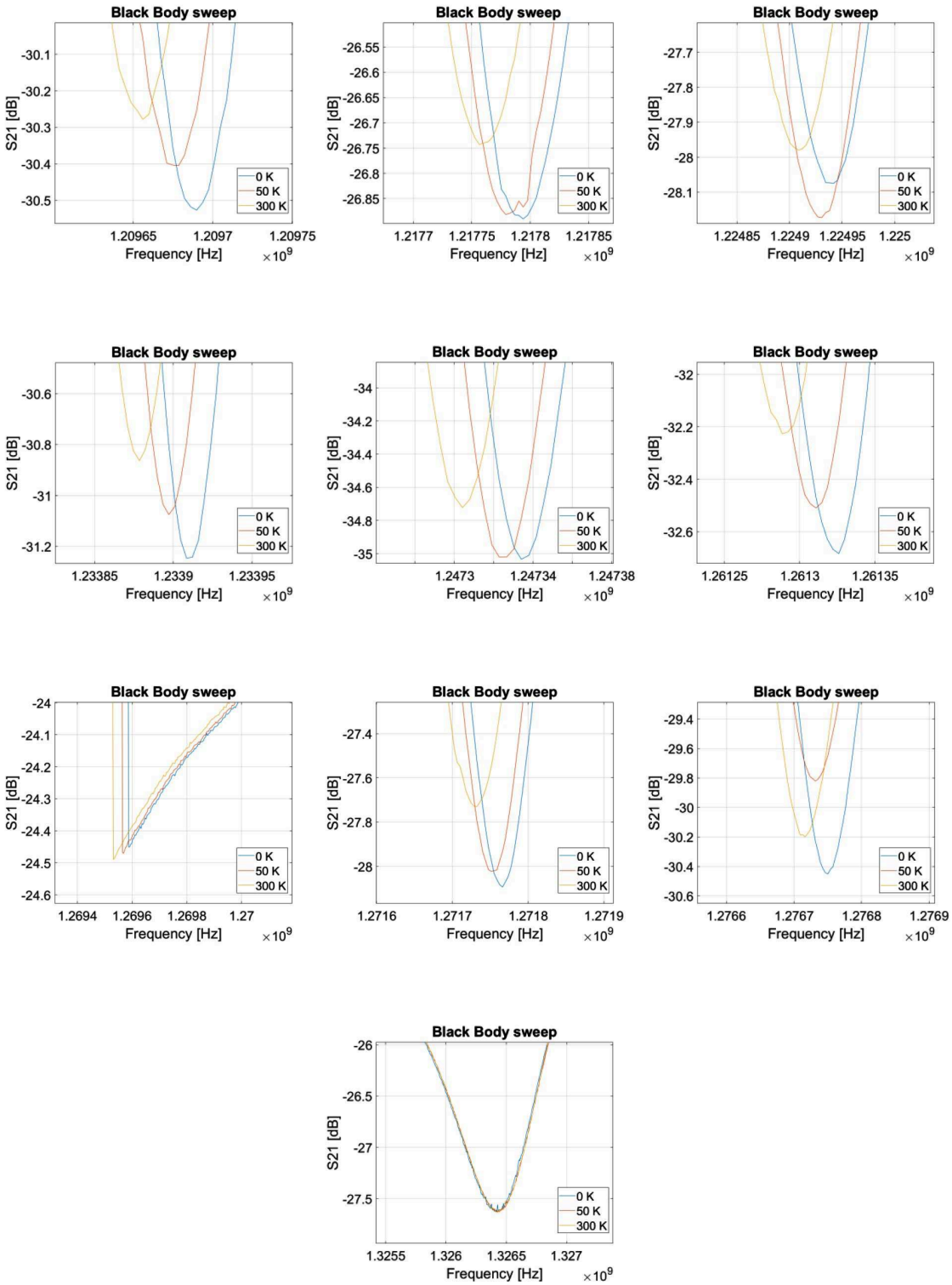

Figure 7.3.12: Chip_6 black body sweep. The last pixel, which does not disappear with temperature, is also totally insensitive to radiation. The rest of the resonances move to the left while increasing the black body temperature.

more contrast but are affected by some systematic effects which make difficult to recover the position of each resonance on the mask. As shown in Fig. 7.3.13, the resonance that show a skewed feature (resonance 7) appears to be sensitive regardless of the planet position. Contrary to Chip_4, all resonances present the same spectrum features except for pixels 4, 7 and 10 (Fig. 7.3.14). One pixel (4) presents a narrow peak at around 80 GHz, below the aluminum frequency threshold, which does not depend on polarization. Noise level has been characterized by the NIKA software with a sample rate of 23.8 Hz, which gives a Nyquist frequency of 11.9 Hz. Fig. 7.3.15 shows the frequency deviation in time of one resonance. The calculated signal-to-noise ratio varies between $10^6 - 10^7$ depending on the resonance.

7.3.4 Conclusion

Measures at Institut NEEL added some valuable information about chip performance and allowed to characterize more in detail the detector response. Main results obtained are summarized as follows:

- Measures of different feedline coupled chips confirm that the coupling affects the total quality factor of resonators. Analysis done by the NIKA software shows that such effect is due to the different coupling quality factor between the two geometries.

- The new fabrication technique improved the resonance responsiveness to black body radiation, suggesting that the aluminum deposition procedure is crucial to fabricate high quality resonances. Others fabrication techniques (like etching) should be also investigated.

- As in the first run, only resonant frequencies on chips with filters are in agreement with simulations.

- Pixels with the type "open" feedline coupling are strongly influenced by the input power. The limitation in the input power during the measures affected the noise performance in Chip_4.

- Spectra and Pol/Cross-pol measures suggest that the signal is coupled directly to detectors instead of to the antenna. The detection mechanism is still unclear and set a priority for further tests.

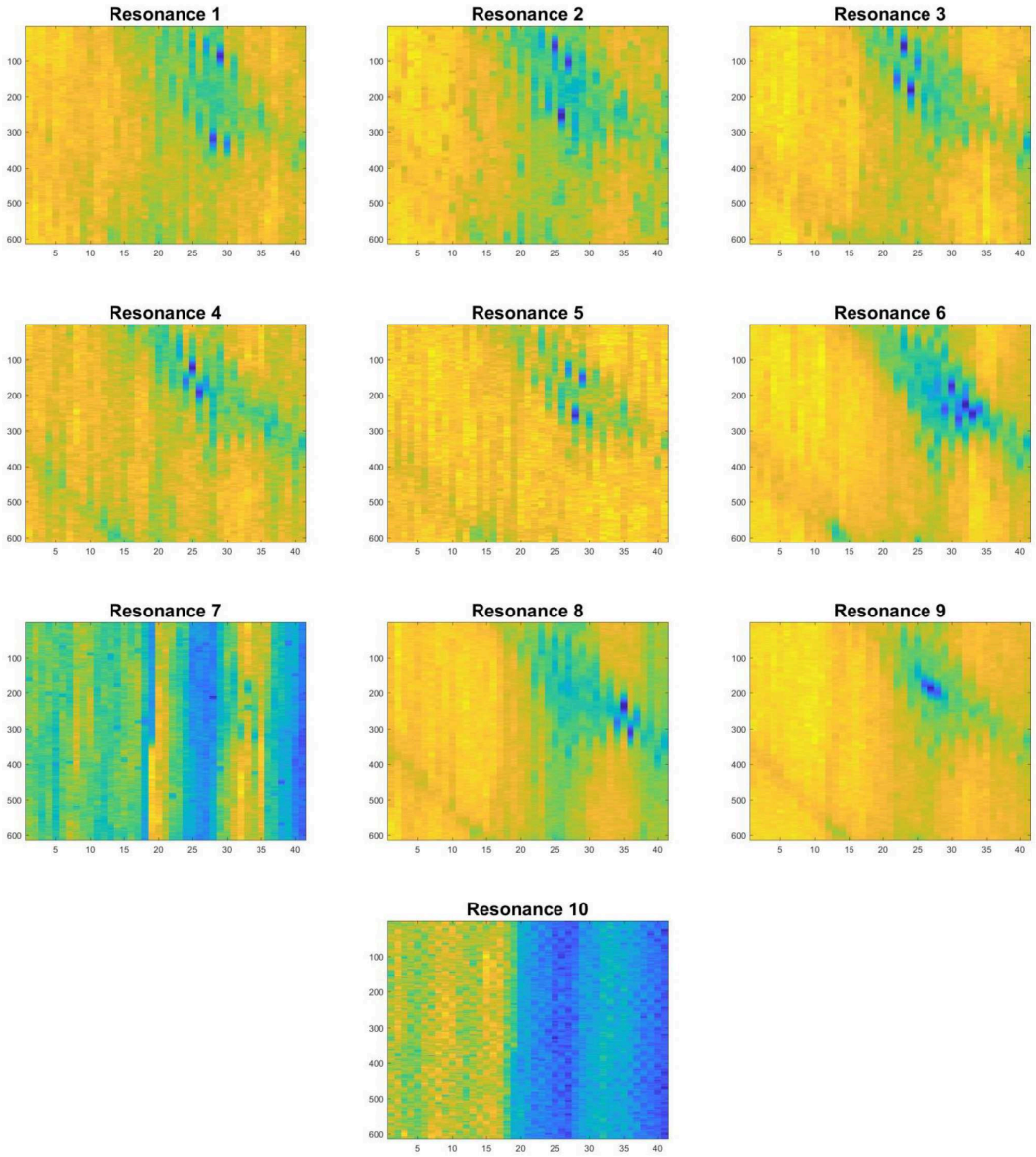

Figure 7.3.13: Chip_6 planet chart for each resonance. Resonance 9 shows a sharp image of the planet and the nylon wire at 45°.

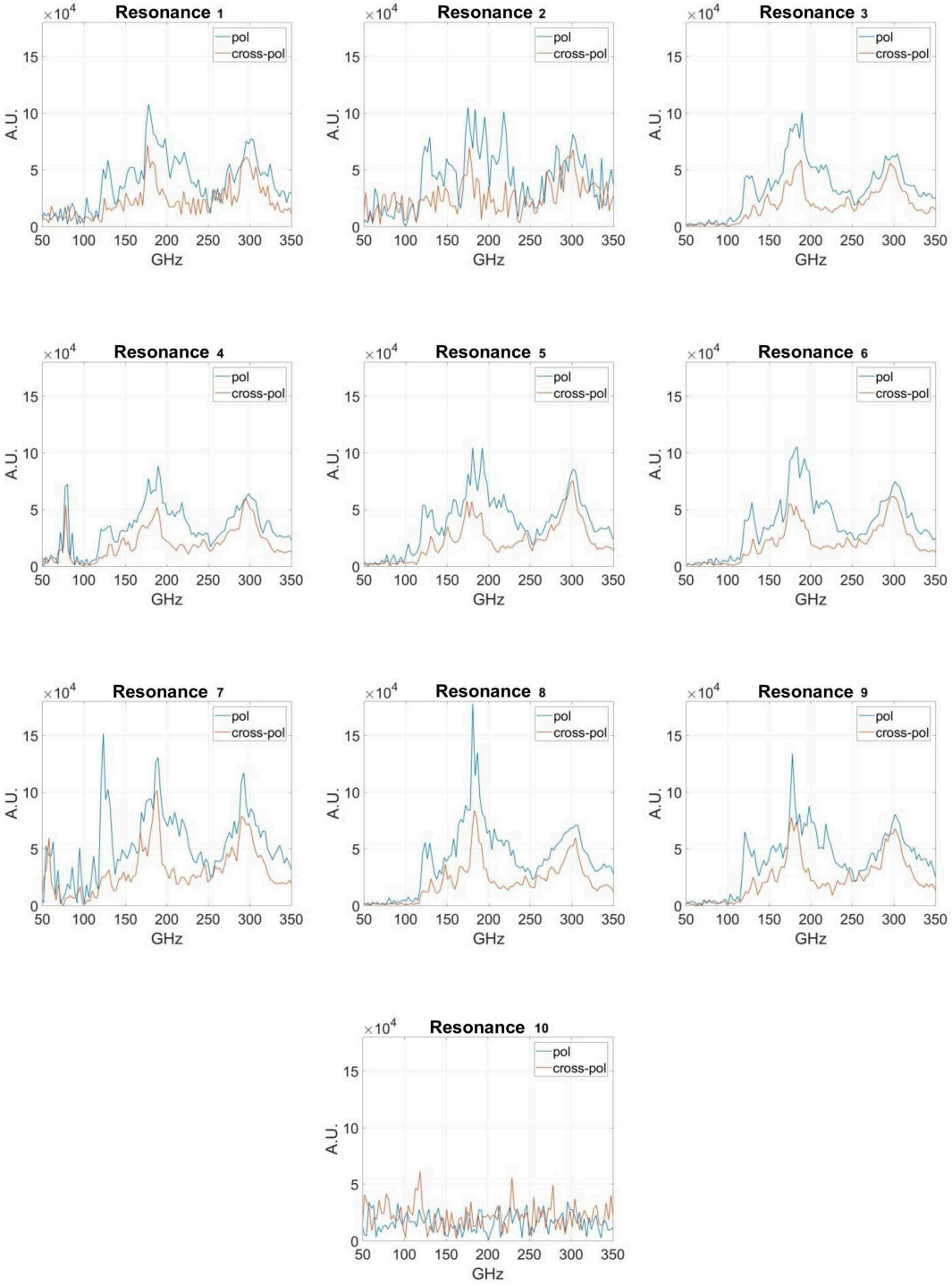

Figure 7.3.14: Chip_6 pixels polarimetry. Every working pixel has two peaks, one at 180 GHz and one at 300 GHz. Resonance 4 presents an extra peak centered at 80 GHz, which is below the aluminum frequency threshold. Pixels lose about half of the signal in some frequency bands when illuminated in Cross-pol.

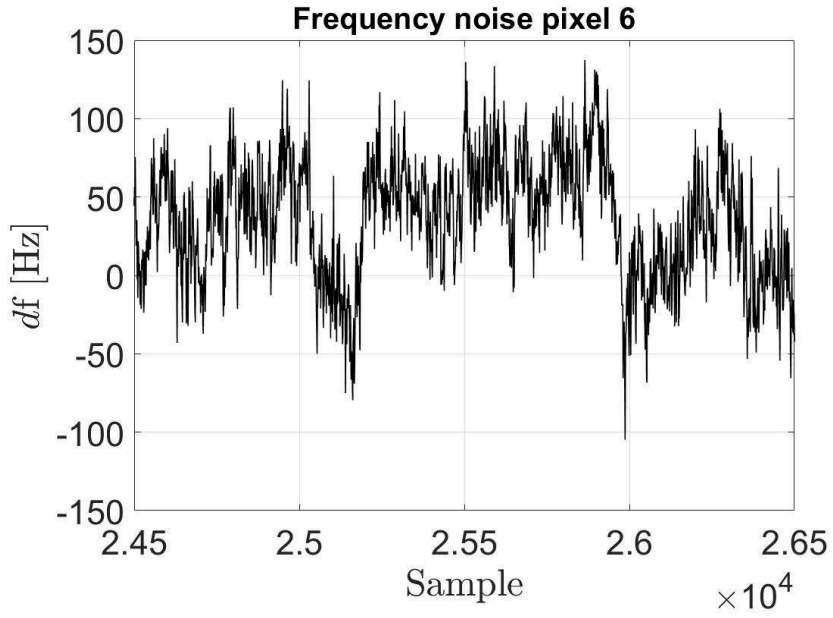

Figure 7.3.15: Frequency deviation of a pixel resonating at around 1.26 Ghz, which gives a signal-to-noise ratio of the order of 10^7. Samples have been taken at 23.8 Hz.

- Measures with the sky simulator suggest that the pixel response is local. Therefore, despite the detection mechanism is unclear, the resonance shift depends mainly on some kind of on-pixel power absorption.

7.4 Lens on Chip 6

A further step towards the understanding of the detection mechanism can be achieved by coupling the antenna with a lens. Focusing the radiation on the antenna will significantly reduce both the radiation incoming on the resonator and the antenna spillover. We have used a silicon lens adapted for a dipole. The lens shape takes also into account the 300 μm silicon substrate which sets the focal length. Because of its large diameter (> 1 cm) with respect to the chip size, the lens has been coupled to the antenna which is closer to the chip center (pixel #8). Nevertheless, part of the lens extends out of the chip, therefore the chip holder is re-adapted to accommodate the lens has shown in Fig. 7.4.1. Despite the focus is on one single slot antenna, the lens diameter cover several pixels. We expect a significant loss of signal in these corresponding resonators.

I firstly have tested the lens mounted chip at APC to verify the mechanical stability

Figure 7.4.1: Chip_6 illuminated side with the lens mounted. Because of its size, it has been necessary to enlarge the chip holder window.

at low temperature. After validating the result, resonances have been characterized with the NIKA cryostat. Fig. 7.4.2 shows the differences between resonance spectra calculated on Chip_6 and the same resonances on Chip_6 with lens. Resonances become polarization insensitive except for resonance number 7 which we then suppose to be the pixel coupled to the lens. Furthermore, the resonance number is coherent with the expected resonance number for that pixel (number 8). This resonance shows the same feature as in the chip without the lens, thus suggesting that the antenna is not the dominant source of resonance shift.

7.5 Conclusion

After testing seven different chip configurations I managed to determine what is necessary to test for further developments. The main result I have obtained is the contribution of the coupling quality factor to the total quality factor. Next prototypes will be fabricated only with the "close" type coupling geometry. Further investigation of performance in terms of quality factor should involve the tuning of the inductor impedance to study the effect of impedance mismatches along the feedline.

Resonances are sensitive to different black body sources and the response is given by some sort of on-pixel absorption. Nevertheless, the detection mechanism is still unclear and we need to test a chip with a dedicated geometry to decouple the effect of direct absorption on Aluminum from the antenna detection. Moreover, detectors seems to resonate differently for different arrangements of the microstrip network. Therefore, it is necessary to fabricate a dedicated prototype to investigate if there is

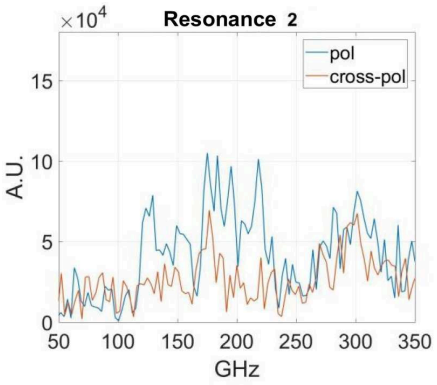
Resonance 2
×10^4
pol
cross-pol
A.U.
GHz

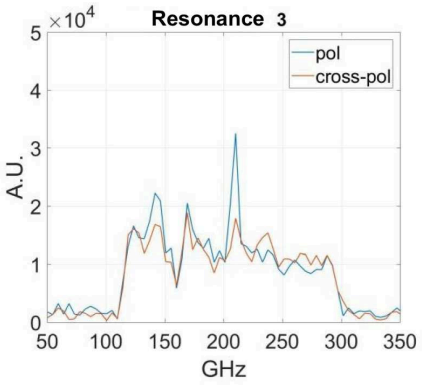
Resonance 3
×10^4
pol
cross-pol
A.U.
GHz

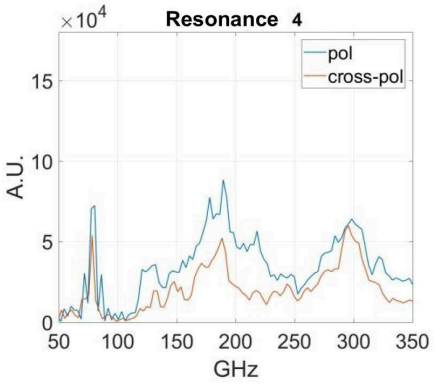
Resonance 4
×10^4
pol
cross-pol
A.U.
GHz

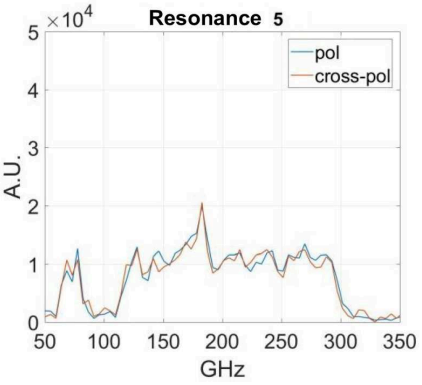
Resonance 5
×10^4
pol
cross-pol
A.U.
GHz

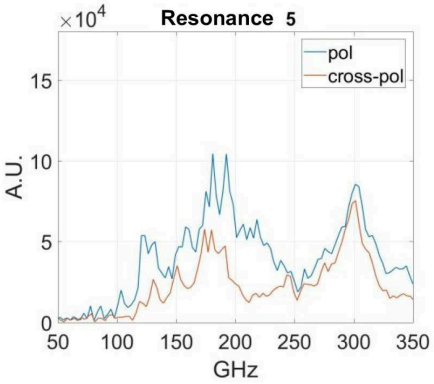
Resonance 5
×10^4
pol
cross-pol
A.U.
GHz

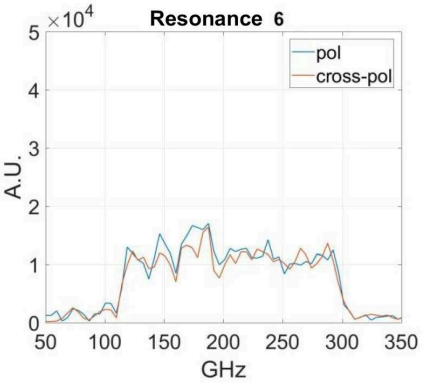
Resonance 6
×10^4
pol
cross-pol
A.U.
GHz

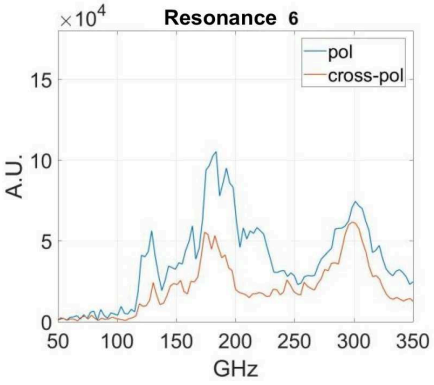
Resonance 6
×10^4
pol
cross-pol
A.U.
GHz

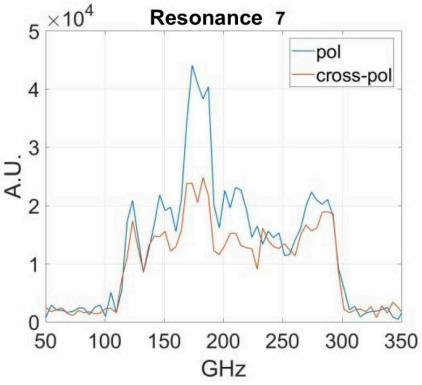
Resonance 7
×10^4
pol
cross-pol
A.U.
GHz

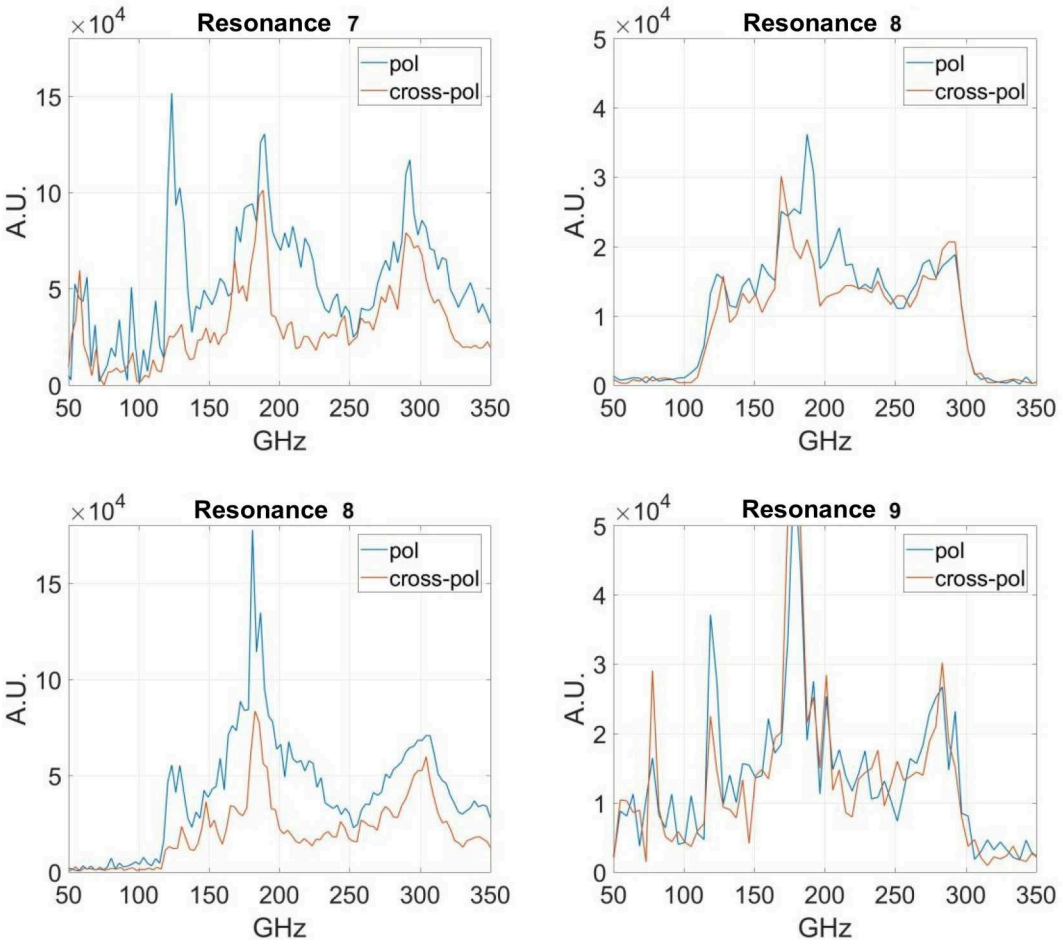

Figure 7.4.2: Measured spectra of Chip_6 (left) and measured spectra of Chip_6 with lens (right). We have used a different numeration for the two measures and resonance names differ of a factor 1.

		Resonant Frequencies	Quality factor	Temperature Sweep (0.3K - 1K)	Signal-to-Noise ratio	Spectra
First Run	**Chip 5** • **Close** • **No filters**	3 GHz	10^4	Insensitive	-	-
	Chip 2 • **Open** • **No filters**	1 GHz	10^3	Sensitive	One resonance: 10^7 Others: 10^6 or less	-
Second Run	**Chip 5** • **Close** • **No filters**	3 GHz	10^4	Sensitive	-	-
	Chip 4 • **Open** • **Filters**	1 GHz	10^3	Sensitive	-	Two kinds of spectra: • One peak centred at around 100 GHz • Broadband spectrum
	Chip 6 • **Close** • **Filters**	1 GHz	10^4	Sensitive	10^7	Broadband spectrum, no clear distinction between pixels

Figure 7.5.1: Performance comparison between different chips.

an effective contribution of the bandpass filter to the detector resonance.

We have revised several time the microfabrication process. The latest chips seem to be improved with the microfabrication, suggesting that we should investigate more fabrication techniques, especially for the Aluminum. In any case, the knowledge acquired by both APC and Paris Observatory in terms of KIDs fabrication is among the positive results of these preliminary tests. Table in Fig. 7.5.1 shows some fundamental properties comparison between the measured chips.

Chapter 8

New Chip Design

Results discussed in previous do not reflect all the simulated performance. Therefore, I have decided to run new simulations and develop a new design by using different parameters.

8.1 Parameter Adjustments

8.1.1 Dielectric constant

In chapter 5 I have chosen the dielectric constant of SiO in analogy with the value of the SiO_2. Literature suggests a value of $\epsilon_r = 5.7$ [102, 103, 104] for the SiO, which is almost twice the value I have considered. The dielectric constant affect pixel components as follow:

- **Antenna**: The wavelength along the microstrip is a function of ϵ_r and its value determines the stub length used to tune the dual-resonant slot.
- **Bandpass Filter**: The filter central frequency decreases as the dielectric constant value increases. This effect may lead to a mismatch between the filter pass band and the antenna resonance.
- **Coupling**: The impedance matching is carried out by four stubs. As for the antenna, stub length depends on the dielectric constant.

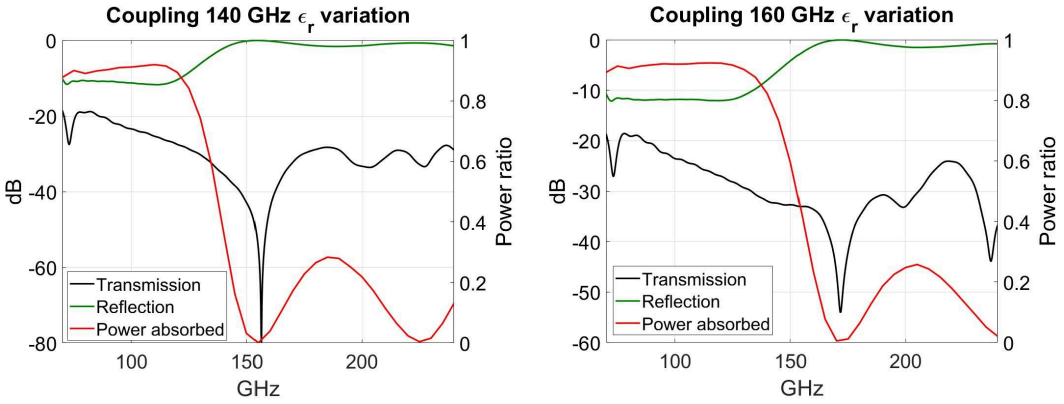

Figure 8.2.1: Simulated S-parameters of the coupling geometry (left axis) and power absorbed on Aluminum (right axis) for the two sub-bands. The geometry is the same described in Chapter 5 while the simulations take into account the value of $\epsilon_r = 5.7$ for the SiO and the kinetic inductance of Niobium.

Because of these effects, it is reasonable that the coupling efficiency between the antenna and the detector is highly degraded due to a wrong assumption on the dielectric constant. The detector performance is not affected since we have avoided dielectric deposition above the resonator.

8.1.2 Kinetic inductance of Niobium

I have taken into account the effect of superconducting niobium in the new design. Instead of using a perfect electric conductor as in previous design I have solved the Mattis-Bardeen integrals to infer the small kinetic inductance of Nb (table of values in Appendix). This is of the order of $10^{-1} pH/\square$ for a thin layer of 120 nm and about $4 \times 10^{-2} pH/\square$ for a 300 nm thin layer. I have used the kinetic inductance values of a 120 nm thick Nb layer for the ground plane and the values for a 300 nm thick Nb layer for the microstrip network.

8.2 Simulations

I have simulated each component of the pixel with the assumptions described above. Fig. 8.2.1 shows the effect of changing the dielectric constant and Niobium properties on the coupling design: the power dissipated on Aluminum decreases dramatically as a consequence of the high reflection due to impedance mismatching. Therefore, I have designed a new coupling geometry to recover the same performance obtained

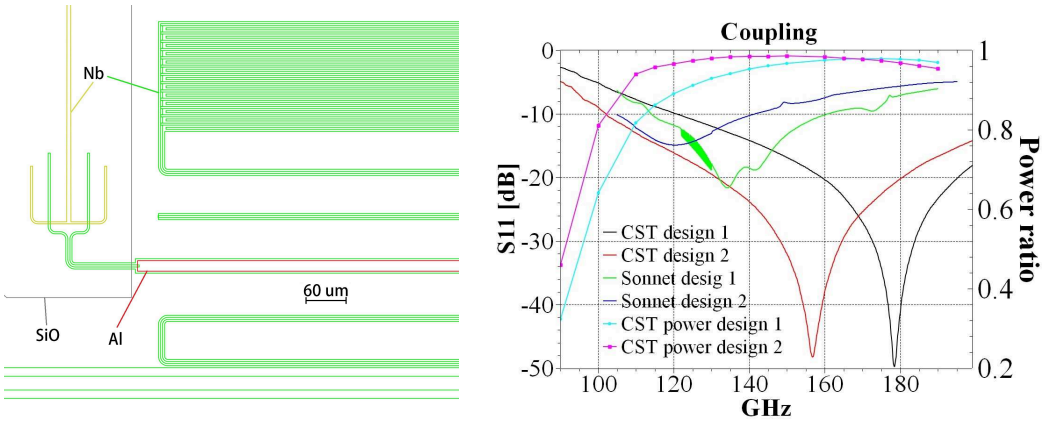

Figure 8.2.2: Autocad layout of coupling design 1 (left). Performance simulated with CST and Sonnet (right). Aluminum characterization in Sonnet is less accurate because of the kinetic inductance dependence on frequency. Note that simulation accuracy in CST is limited to -35 dB. Design 1 is optimized to be consistent with both software in the operational frequency range. Design 2 is optimized with CST only. Right axis shows the power absorbed on aluminum normalized to the total power entering the simulation.

in Chapter 5. To validate the coupling simulations run in CST I also simulated the same design with Sonnet. The reason I preferred CST in the first place is that it allows to create custom materials with given frequency-dependent surface impedance. Sonnet allows custom material to only have fixed kinetic inductance. This feature contrasts with the superconducting aluminum property for which the kinetic inductance doubles its value in the operational frequency range. Since different software give slightly different results for the same geometry, I decided to adopt two different designs in developing new photomasks. In order to facilitate the data understanding we plan to fabricate new chips with only single-band pixels centered at 150 GHz. The filter bandwidth is wider compared to the previous design to minimize potential frequency mismatch with the antenna resonance due to wrong assumption of the dielectric constant. Fig. 8.2.2 and Fig. 8.2.3 show the simulated performance of the new coupling and bandpass filter design.

8.3 Realization

I have developed five new chips as follows:

- The first chip has the same design of **chip_6** used in second run. In this version I have removed all the antennas on ground plane and the microstrip network on half of the pixels. This arrangement is dedicated to study the microstrip

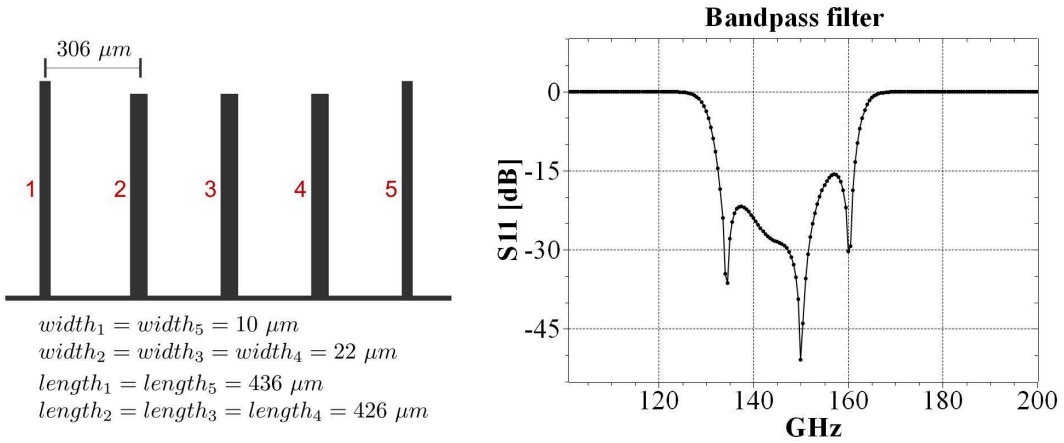

Figure 8.2.3: Filter layout (left) and simulated bandwidth with Sonnet (right). Stubs distances, lengths and widths are shown in μm.

network effect on the resonance. Moreover, I can compare the spectral response of bare resonators with the old chip_6 in order to evaluate antenna detection over direct absorption.

- **Chip 2 & 3** include nine pixels: three antenna-coupled detectors with one filter, three simple antenna-coupled detectors and three not coupled detectors. This design is dedicated to study the detection mechanism and if the resonant frequency depends on the microstrip network.

- **Chip 4 & 5** include five pixels. The design focuses on keeping the antenna at least 7 mm away from the detectors, allowing for a better understanding of the detection mechanism when illuminated with the sky simulator. One antenna is located at the chip center to optimize the coupling with a silicon lens.

Chips 2, 3, 4 and 5 have antennas tilted by 45° in order to measure pol and cross-pol more easily with the Martin-Pupplet interferometer. Pixels layout and schematic are shown in the following pictures.

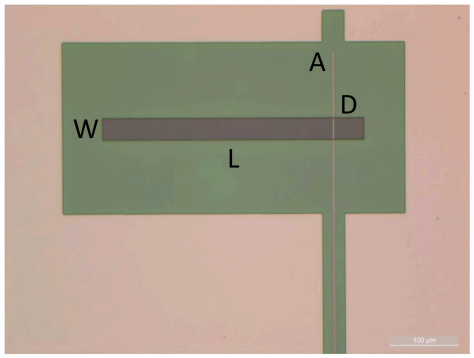

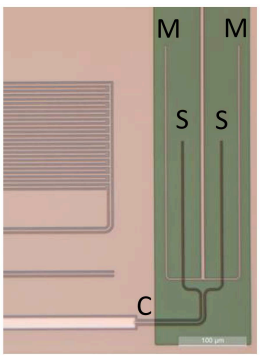

W = Slot width = 32 µm
L = Slot length = 382 µm
A = Antenna microstrip stub length = 62 µm
D = Antenna microstrip distance from the edge = 44 µm
S = Slotline length = 91.5 µm (design 1) 99.5 µm (design 2)
M = Microstrip length = 84 µm (design 1) 102 µm (design 2)
C = Aluminium strip distance from CPW - slotlines transition = 136 µm

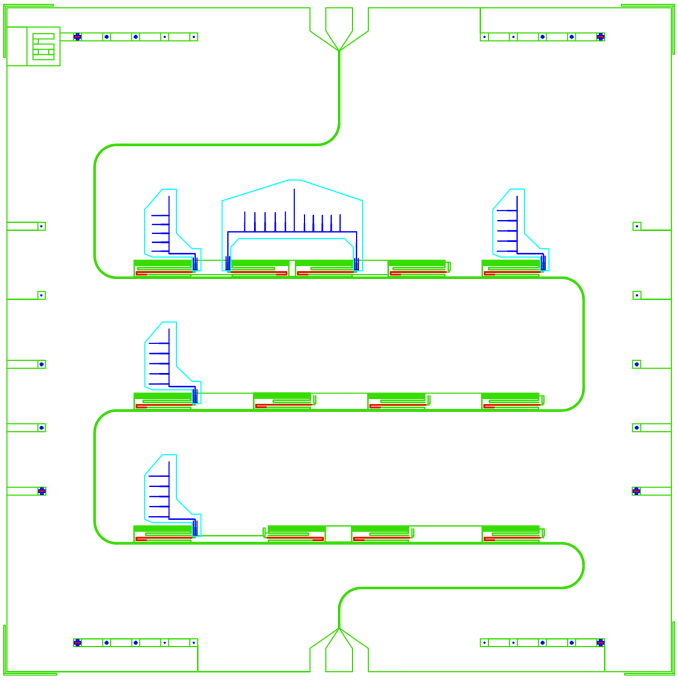

Chip 1 – no antennas

1 Single filter 160 GHz C - 2	9 Diplexer 10 140 GHz S - 8 C - 2 M - 19 / 160 GHz S - 8 C - 2 M - 19	2 Bare resonator	3 Single filter 140 GHz S - 2 C - 2
5 Single filter 140 GHz S - 7 C - 2 M - 19	13 Bare resonator	8 Bare resonator	4 Bare resonator
7 Single detector 140 GHz S + 7 C - 2 M + 19	11 Bare resonator	12 Bare resonator	6 Bare resonator

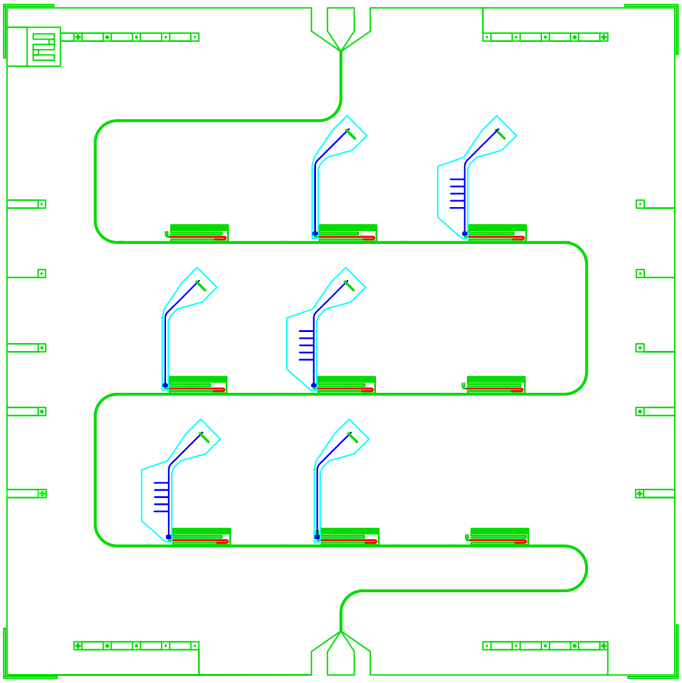

Chip 2 – 9 pixels

3 No Antenna Coupling	9 Antenna Coupling Design 1	6 Antenna Coupling + filter Design 1
8 Antenna Coupling Design 1	5 Antenna Coupling + filter Design 1	2 No Antenna Coupling
4 Antenna Coupling + filter Design 2	7 Antenna Coupling Design 2	1 No Antenna Coupling

Chip 3 – 9 pixels

3 No Antenna Coupling	9 Antenna Coupling Design 2	6 Antenna Coupling + filter Design 2
8 Antenna Coupling Design 2	5 Antenna Coupling + filter Design 2	2 No Antenna Coupling
4 Antenna Coupling + filter Design 1	7 Antenna Coupling Design 1	1 No Antenna Coupling

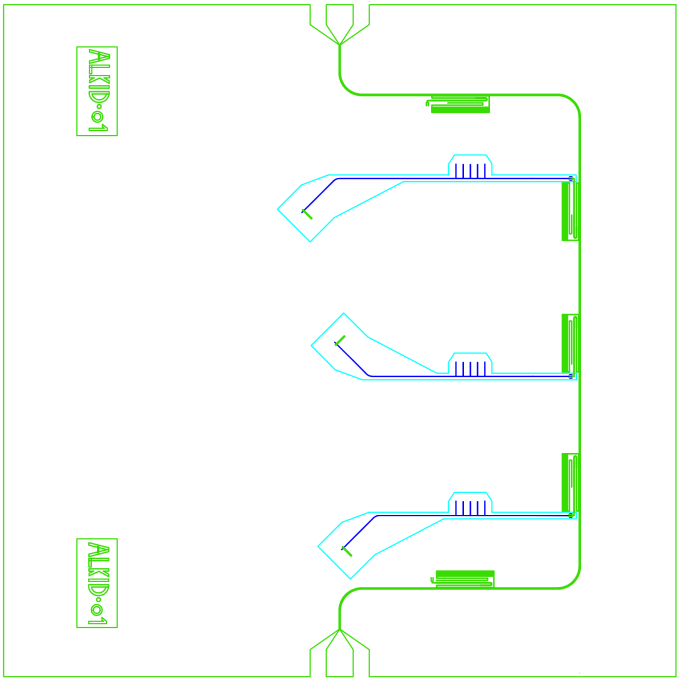
ALKID-01
ALKID-01

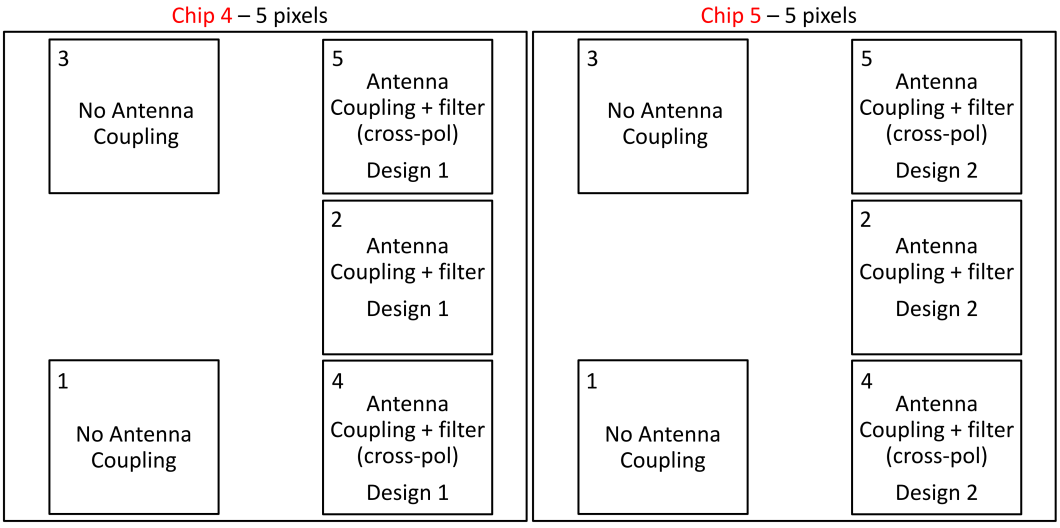
Chip 4 – 5 pixels
3
No Antenna Coupling
5
Antenna Coupling + filter (cross-pol)
Design 1
2
Antenna Coupling + filter
Design 1
1
No Antenna Coupling
4
Antenna Coupling + filter (cross-pol)
Design 1
Chip 5 – 5 pixels
3
No Antenna Coupling
5
Antenna Coupling + filter (cross-pol)
Design 2
2
Antenna Coupling + filter
Design 2
1
No Antenna Coupling
4
Antenna Coupling + filter (cross-pol)
Design 2

Chapter 9

Conclusions

During these three years I have developed and tested an original detection chain dedicated to CMB polarimetry. At first, I have simulated each component with full wave simulation software. The performance of a dual-resonant slot antenna exploiting a fictitious short-circuit effect simulated in CST Microwave Studio appears to be an attractive solution for future focal planes. The simulated bandwidth of about 35% is adequate to obtain two sub-bands of about 10% bandwidth. However, performance in terms of radiation pattern has not been simulated properly. Due to the thin dielectric and particular microstrip geometry, I couldn't realize a low frequency demonstrator in short time scale using the substrates available at APC. This step is required to validate both the antenna bandwidth and radiation pattern.

The diplexer has been chosen to keep the design as simple as possible. The two bandpass filters are fabricated along with the microstrip network in one deposition step.

I have developed the detector geometry focusing on the coupling technique. Since the filtering network requires a ground plane on the detector layer, I have decided to develop a CPW resonator. This choice allows the microstrip not to have ground discontinuities. The simulated performance of the coupling in terms of reflection and absorption on aluminum are adequate in the entire sub-band bandwidth. Again, a technology demonstrator should be the preferred way to validate the simulations. This is quite hard to accomplish because the superconducting metals do not have the same properties at low frequencies. Therefore, such a demonstrator would be

tested with high frequency signals.

We fabricated three times five chips over a three inches large wafer, each time we have improved the chip performance. The knowledge acquired will be precious for future development of KIDs both at APC and Paris Observatory.

Measurements at APC and institut NEEL shown several features which require further investigation. Mainly, the spectral response of the pixels seems to be the same regardless of the filter presence and filter pass band. Nevertheless, we have got promising results in terms of quality factor of the order of 10^4. Measurements with a lens coupled pixel did not improve the performance, thus it is necessary to further investigate the detection mechanism.

One possible explanation for the measured spectral response could be a poor estimation of the dielectric constant used for evaluating the impedance matching along the microstrip network. Therefore, I have developed a new pixel design for which I took into account the kinetic inductance of niobium, which was neglected in previous design, and a different value of ϵ_r according to values found in literature. Tests of this design are ongoing both at APC and Institut NEEL. These measurements will provide more data for analyzing the detection mechanism and resonant frequencies of the pixels.

Further investigation of pixel performance should involve the fabrication of low frequency demonstrators. A dual-resonant slot antenna operating in the frequency range around $3\,GHz$ can be tested at APC both in terms of antenna resonance and radiation pattern. An equivalent low frequency demonstrator of the coupling impedance matching cannot be fabricated due to the Aluminum cutoff at $100\,GHz$. Nevertheless, it would be of great interest to design and test a similar microstrip to CPW transition to validate the simulation setup. Another demonstrator of the pixel design could be realized by exaggerating the component size to reduce the impact of microfabrication defects.

Future improvement of pixel design may come from external collaborators. In particular, the dual-resonant slot antenna can be replaced with a sinuous antenna or a seashell antenna currently under development within the ESA Technology Research Programme (TRP) dedicated to the development of future CMB focal planes.

Appendix

Aluminum layer 20 nm **thick at** 300 mK

GHz	$R\,[\Omega/\square]$	$X\,[\Omega/\square]$	GHz	$R\,[\Omega/\square]$	$X\,[\Omega/\square]$
120.00	1.8764e+00	3.7873e+00	151.00	2.3950e+00	6.2058e+00
121.00	1.9192e+00	3.8572e+00	152.00	2.3953e+00	6.2926e+00
122.00	1.9596e+00	3.9276e+00	153.00	2.3951e+00	6.3801e+00
123.00	1.9977e+00	3.9986e+00	154.00	2.3945e+00	6.4680e+00
124.00	2.0335e+00	4.0700e+00	155.00	2.3935e+00	6.5566e+00
125.00	2.0671e+00	4.1420e+00	156.00	2.3922e+00	6.6457e+00
126.00	2.0985e+00	4.2146e+00	157.00	2.3906e+00	6.7353e+00
127.00	2.1278e+00	4.2877e+00	158.00	2.3887e+00	6.8255e+00
128.00	2.1550e+00	4.3613e+00	159.00	2.3865e+00	6.9163e+00
129.00	2.1803e+00	4.4354e+00	160.00	2.3841e+00	7.0077e+00
130.00	2.2037e+00	4.5101e+00	161.00	2.3814e+00	7.0996e+00
131.00	2.2253e+00	4.5854e+00	162.00	2.3785e+00	7.1920e+00
132.00	2.2451e+00	4.6612e+00	163.00	2.3755e+00	7.2851e+00
133.00	2.2633e+00	4.7375e+00	164.00	2.3723e+00	7.3787e+00
134.00	2.2800e+00	4.8144e+00	165.00	2.3689e+00	7.4728e+00
135.00	2.2952e+00	4.8918e+00	166.00	2.3654e+00	7.5675e+00
136.00	2.3090e+00	4.9698e+00	167.00	2.3618e+00	7.6628e+00
137.00	2.3214e+00	5.0483e+00	168.00	2.3580e+00	7.7587e+00
138.00	2.3326e+00	5.1274e+00	169.00	2.3542e+00	7.8551e+00
139.00	2.3427e+00	5.2070e+00	170.00	2.3502e+00	7.9520e+00
140.00	2.3517e+00	5.2872e+00	171.00	2.3462e+00	8.0496e+00
141.00	2.3596e+00	5.3679e+00	172.00	2.3421e+00	8.1477e+00
142.00	2.3665e+00	5.4492e+00	173.00	2.3379e+00	8.2464e+00
143.00	2.3726e+00	5.5310e+00	174.00	2.3337e+00	8.3456e+00
144.00	2.3778e+00	5.6134e+00	175.00	2.3295e+00	8.4454e+00
145.00	2.3822e+00	5.6964e+00	176.00	2.3252e+00	8.5458e+00
146.00	2.3859e+00	5.7799e+00	177.00	2.3208e+00	8.6467e+00
147.00	2.3889e+00	5.8640e+00	178.00	2.3165e+00	8.7482e+00
148.00	2.3913e+00	5.9486e+00	179.00	2.3121e+00	8.8502e+00
149.00	2.3931e+00	6.0338e+00	180.00	2.3077e+00	8.9529e+00
150.00	2.3943e+00	6.1195e+00			

Niobium layer 120 nm **thick at** 300 mK

GHz	$R\,[\Omega/\square]$	$X\,[\Omega/\square]$	GHz	$R\,[\Omega/\square]$	$X\,[\Omega/\square]$
120.00	8.8636e−26	8.6765e−02	166.00	1.0926e−25	1.2083e−01
121.00	8.9095e−26	8.7498e−02	167.00	1.0970e−25	1.2158e−01
122.00	8.9553e−26	8.8232e−02	168.00	1.1014e−25	1.2233e−01
123.00	9.0011e−26	8.8966e−02	169.00	1.1059e−25	1.2308e−01
124.00	9.0467e−26	8.9701e−02	170.00	1.1103e−25	1.2383e−01
125.00	9.0923e−26	9.0436e−02	171.00	1.1147e−25	1.2458e−01
126.00	9.1379e−26	9.1171e−02	172.00	1.1191e−25	1.2533e−01
127.00	9.1834e−26	9.1906e−02	173.00	1.1236e−25	1.2608e−01
128.00	9.2288e−26	9.2642e−02	174.00	1.1280e−25	1.2683e−01
129.00	9.2742e−26	9.3378e−02	175.00	1.1324e−25	1.2758e−01
130.00	9.3195e−26	9.4114e−02	176.00	1.1368e−25	1.2834e−01
131.00	9.3647e−26	9.4850e−02	177.00	1.1412e−25	1.2909e−01
132.00	9.4099e−26	9.5587e−02	178.00	1.1457e−25	1.2984e−01
133.00	9.4551e−26	9.6324e−02	179.00	1.1501e−25	1.3060e−01
134.00	9.5002e−26	9.7061e−02	180.00	1.1545e−25	1.3135e−01
135.00	9.5453e−26	9.7799e−02			
136.00	9.5903e−26	9.8537e−02			
137.00	9.6353e−26	9.9275e−02			
138.00	9.6802e−26	1.0001e−01			
139.00	9.7251e−26	1.0075e−01			
140.00	9.7699e−26	1.0149e−01			
141.00	9.8147e−26	1.0223e−01			
142.00	9.8595e−26	1.0297e−01			
143.00	9.9042e−26	1.0371e−01			
144.00	9.9489e−26	1.0445e−01			
145.00	9.9936e−26	1.0519e−01			
146.00	1.0038e−25	1.0593e−01			
147.00	1.0083e−25	1.0668e−01			
148.00	1.0127e−25	1.0742e−01			
149.00	1.0172e−25	1.0816e−01			
150.00	1.0216e−25	1.0890e−01			
151.00	1.0261e−25	1.0965e−01			
152.00	1.0305e−25	1.1039e−01			
153.00	1.0350e−25	1.1113e−01			
154.00	1.0394e−25	1.1188e−01			
155.00	1.0439e−25	1.1262e−01			
156.00	1.0483e−25	1.1336e−01			
157.00	1.0527e−25	1.1411e−01			
158.00	1.0572e−25	1.1486e−01			
159.00	1.0616e−25	1.1560e−01			
160.00	1.0660e−25	1.1635e−01			
161.00	1.0705e−25	1.1709e−01			
162.00	1.0749e−25	1.1784e−01			
163.00	1.0793e−25	1.1859e−01			
164.00	1.0838e−25	1.1933e−01			
165.00	1.0882e−25	1.2008e−01			

Niobium layer 300 nm **thick at** 300 mK

GHz	$R\,[\Omega/\square]$	$X\,[\Omega/\square]$	GHz	$R\,[\Omega/\square]$	$X\,[\Omega/\square]$
120.00	3.8153e−26	5.1716e−02	166.00	4.6990e−26	7.1888e−02
121.00	3.8350e−26	5.2152e−02	167.00	4.7179e−26	7.2330e−02
122.00	3.8546e−26	5.2587e−02	168.00	4.7368e−26	7.2772e−02
123.00	3.8742e−26	5.3023e−02	169.00	4.7557e−26	7.3214e−02
124.00	3.8938e−26	5.3459e−02	170.00	4.7746e−26	7.3657e−02
125.00	3.9134e−26	5.3895e−02	171.00	4.7935e−26	7.4100e−02
126.00	3.9329e−26	5.4331e−02	172.00	4.8124e−26	7.4543e−02
127.00	3.9525e−26	5.4767e−02	173.00	4.8313e−26	7.4986e−02
128.00	3.9719e−26	5.5204e−02	174.00	4.8502e−26	7.5429e−02
129.00	3.9914e−26	5.5640e−02	175.00	4.8691e−26	7.5872e−02
130.00	4.0108e−26	5.6077e−02	176.00	4.8880e−26	7.6316e−02
131.00	4.0302e−26	5.6514e−02	177.00	4.9069e−26	7.6760e−02
132.00	4.0496e−26	5.6951e−02	178.00	4.9258e−26	7.7203e−02
133.00	4.0690e−26	5.7388e−02	179.00	4.9447e−26	7.7648e−02
134.00	4.0883e−26	5.7825e−02	180.00	4.9636e−26	7.8092e−02
135.00	4.1077e−26	5.8262e−02			
136.00	4.1270e−26	5.8699e−02			
137.00	4.1462e−26	5.9137e−02			
138.00	4.1655e−26	5.9575e−02			
139.00	4.1847e−26	6.0012e−02			
140.00	4.2039e−26	6.0450e−02			
141.00	4.2231e−26	6.0888e−02			
142.00	4.2423e−26	6.1327e−02			
143.00	4.2615e−26	6.1765e−02			
144.00	4.2806e−26	6.2204e−02			
145.00	4.2998e−26	6.2642e−02			
146.00	4.3189e−26	6.3081e−02			
147.00	4.3380e−26	6.3520e−02			
148.00	4.3571e−26	6.3959e−02			
149.00	4.3762e−26	6.4398e−02			
150.00	4.3952e−26	6.4837e−02			
151.00	4.4143e−26	6.5277e−02			
152.00	4.4333e−26	6.5717e−02			
153.00	4.4524e−26	6.6156e−02			
154.00	4.4714e−26	6.6596e−02			
155.00	4.4904e−26	6.7036e−02			
156.00	4.5094e−26	6.7477e−02			
157.00	4.5284e−26	6.7917e−02			
158.00	4.5474e−26	6.8358e−02			
159.00	4.5663e−26	6.8798e−02			
160.00	4.5853e−26	6.9239e−02			
161.00	4.6043e−26	6.9680e−02			
162.00	4.6232e−26	7.0122e−02			
163.00	4.6422e−26	7.0563e−02			
164.00	4.6611e−26	7.1004e−02			
165.00	4.6800e−26	7.1446e−02			

Bibliography

[1] M. Longair - *The Cosmic Century, A history of Astrophysics and Cosmology* - Cambridge University Press - 2006

[2] A. Einstein - *On the Influence of Gravitation on the Propagation of Light* - Annalen der Physik, 35, pp. 898-908 - 1911

[3] M. Realdi, G. Peruzzi - *Einstein, de Sitter and the Beginning of Relativistic Cosmology in 1917* - Springer Science - DOI 10.1007/s10714-008-0664-y - 2008

[4] L. Bergstrom, A. Goobar - *Cosmology and Particle Physics* - Springer - 2006

[5] C. O'Rdtaifeartaigh - *The Contribution of V. M. Slipher to the Greater Discovery of the Expanding Universe* - arXiv:1212.5499 - 2013

[6] Slipher V.M - *Proceedings of the American Philosophical Society* - vol. 56, p.403-409 - 1917

[7] Edwin Hubble - *A relation between distance and radial velocity among extragalactic nebulae* - 1929

[8] V. Bonvin, F. Courbin, S. H. Suyu, P. J. Marshall, C. E. Rusu, D. Sluse, M. Tewes, K. C. Wong, T. Collett, C. D. Fassnacht, T. Treu, M. W. Auger, S. Hilbert, L. V. E. Koopmans, G. Meylan, N. Rumbaugh, A. Sonnenfeld, C. Spiniello - *H0LiCOW V. New COSMOGRAIL time delays of HE0435-1223: H0 to 3.8% precision from strong lensing in a flat ΛCDM model* - arXiv:1607.01790 - 2017

[9] Steven Weinberg - *Cosmology* - Oxford University Press - 2008

[10] James Rich - *Fundamentals of Cosmology* - Springer - 2nd Edition - 2009

[11] Malcom S. Longair - *Galaxy Formation* - Springer - 2007

[12] A. G. Walker - *On Milne's Theory of World-Structure* - Proceedings of the London mathematical society - 1937

[13] Steven Weinberg - *Gravitation and Cosmology: principles and applications of the General Theory of Relativity* - John Wiley & Sons - 1972

[14] Planck Collaboration - *Planck 2015 results. XIII. Cosmological parameters* - arXiv:1502.01589 - 2016

[15] S. Perlmutter, G. Aldering, G. Goldhaber, R.A. Knop, P. Nugent, P.G. Castro, S. Deustua, S. Fabbro, A. Goobar, D.E. Groom, I. M. Hook, A.G. Kim, M.Y. Kim, J.C. Lee, N.J. Nunes, R. Pain, C.R. Pennypacker, R. Quimby, C. Lidman, R.S. Ellis, M. Irwin, R.G. McMahon, P. Ruiz-Lapuente, N. Walton, B. Schaefer, B.J. Boyle, A.V. Filippenko, T. Matheson, A.S. Fruchter, N. Panagia, H.J.M. Newberg, W.J. Couch - *Measurements of Omega and Lambda from 42 High-Redshift Supernovae* - arXiv:astro-ph/9812133 - 1999

[16] Adam G. Riess, Alexei V. Filippenko, Peter Challis, Alejandro Clocchiattia, Alan Diercks, Peter M. Garnavich, Ron L. Gilliland, Craig J. Hogan, Saurabh Jha, Robert P. Kirshner, B. Leibundgut, M. M. Phillips, David Reiss, Brian P. Schmidt, Robert A. Schommer, R. Chris Smith, J. Spyromilio, Christopher Stubbs, Nicholas B. Suntzeff, John Tonry - *Observational Evidence from Supernovae for an Accelerating Universe and a Cosmological Constant* - arXiv:astro-ph/9805201 - 1998

[17] P. Coles, F. Lucchin - *Cosmology, Theorigin and evolution of cosmic structure* - Jhon Wiley and Sons - Second edition - 2002

[18] Daniel Baumann - *Lectures in Cosmology* - Cambridge University

[19] H. MO, F. Van Den Bosh, S. White - *Galaxy Formation and Evolution* - Cambridge University Press - 2010

[20] Penzias, A. A.; Wilson, R. W. - *Measurement of the Flux Density of CAS a at 4080 Mc/s* - Astrophysical Journal, vol. 142, p.1149 - 1965

[21] Dicke, R. H.; Peebles, P. J. E.; Roll, P. G.; Wilkinson, D. T. - *Cosmic Black-Body Radiation* - Astrophysical Journal, vol. 142, p.414-419 - 1965

[22] lambda.gsfc.nasa.gov/product/cobe/

[23] wmap.gsfc.nasa.gov

[24] esa.int/Our_Activities/Space_Science/Planck

[25] Alan H. Guth - *Inflationary universe: A possible solution to the horizon and flatness problems* - Physical review D, Vol.23, Number 2 - 1981

[26] Stephen Serjeant - *Observational Cosmology* - Cambridge University press - 2010

[27] Andrew Liddle - *An Introduction to Modern Cosmology* - Wiley - 2003

[28] M.C. Guzzetti, N. Bartolo, M. Liguori, S. matarrese - *Gravitational Waves from Inflation* - DOI: 10.1393/ncr/i2016-10127-1 - arXiv:1605.01615

[29] John A. Peacock - *Cosmological Physics* - Cambridge University press - 1999

[30] J. Kovac, E. M. Leitch, C. Pryke, J. E. Carlstrom, N. W. Halverson, W. L. Holzapfel - *Detection of Polarization in the Cosmic Microwave Background using DASI* - arXiv:astro-ph/0209478

[31] J. Kaplan, J. Delabrouille, P. Fosalba, C. Rosset - *CMB Polarization as complementary information to anisotropies* - arXiv:astro-ph/0310650v3 - 2005

[32] W. Hu, M. White - *A CMB Polarization Primer*

[33] H. C. Chiang, P. A. R. Ade, D. Barkats, J. O. Battle, E. M. Bierman, J. J. Block, C. D. Dowell, L. Duband, E. F. Hivon, W. L. Holzapfel, V. V. Hristov, W. C. Jones, B. G. Keating, J. M. Kovac, C. L. Kuo, A. E. Lange, E. M. Leitch, P. V. Mason, T. Matsamura, H. T. Nguyen, N. Ponthieu, C. Pryke, S. Richter, G. Rocha, C. Sheehy, Y. D. Takahashi, J. E. Tolan, K. W. Yoon - *Measurement of Cosmic Microwave Background Polarization Power Spectra from Two Years of Bicep Data* - arXiv:0906.1181v3 - 2010

[34] Kevork N. Abazajian, Peter Adshead, Zeeshan Ahmed, Steven W. Allen, David Alonso, Kam S. Arnold, Carlo Baccigalupi, James G. Bartlett, Nicholas Battaglia, Bradford A. Benson, Colin A. Bischoff, Julian Borrill, Victor Buza, Erminia Calabrese, Robert Caldwell, John E. Carlstrom, Clarence L. Chang,

Thomas M. Crawford, Francis-Yan Cyr-Racine, Francesco De Bernardis, Tijmen de Haan, Sperello di Serego Alighieri, Joanna Dunkley, Cora Dvorkin, Josquin Errard, Giulio Fabbian, Stephen Feeney, Simone Ferraro, Jeffrey P. Filippini, Raphael Flauger, George M. Fuller, Vera Gluscevic, Daniel Green, Daniel Grin, Evan Grohs, Jason W. Henning, J. Colin Hill, Renee Hlozek, Gilbert Holder, William Holzapfel, Wayne Hu, Kevin M. Huffenberger, Reijo Keskitalo, Lloyd Knox, Arthur Kosowsky, John Kovac, Ely D. Kovetz, Chao-Lin Kuo, Akito Kusaka, Maude Le Jeune, Adrian T. Lee, Marc Lilley, Marilena Loverde, Mathew S. Madhavacheril, Adam Mantz, David J. E. Marsh, Jeffrey McMahon, Pieter Daniel Meerburg, Joel Meyers, Amber D. Miller, Julian B. Munoz, Ho Nam Nguyen, Michael D. Niemack, Marco Peloso, Julien Peloton, Levon Pogosian, Clement Pryke, Marco Raveri, Christian L. Reichardt, Graca Rocha, Aditya Rotti, Emmanuel Schaan, Marcel M. Schmittfull, Douglas Scott, Neelima Sehgal, Sarah Shandera, Blake D. Sherwin, Tristan L. Smith, Lorenzo Sorbo, Glenn D. Starkman, Kyle T. Story, Alexander van Engelen, Joaquin D. Vieira, Scott Watson, Nathan Whitehorn, W.L. Kimmy Wu - *CMB-S4 Science Book* - arXiv:1706.02464

[35] Kiyotomo Ichiki - *CMB foreground: A concise review* - Progress of Theoretical and Experimental Physics, Volume 2014, Issue 6, 1 June 2014 - doi.org/10.1093/ptep/ptu065

[36] C. L. Bennet et al. - *Nine Year Wilkinson Microwave Anisotropy Probe (WMAP) Observations: Final Maps and Results* - The Astrophysical Journal Supplement Series, 208:20 (54pp), 2013 October - doi:10.1088/0067-0049/208/2/20

[37] J.A. Kong - *Electromagnetic Wave Theory* - EMW Publishing - 2008

[38] Lioubtchenko, Tretyakov, Dudorov - *Millimeter-Wave Waveguides* - Springer - 2003

[39] R. Weber - *Introduction to Microwave Circuit* - IEEE Press - 2001

[40] M. Pozar - *Microwave Engineering* - John Wiley & Sons - 1998

[41] Leo G. Maloratsky - *Passive RF & Microwave Integrated Circuits* - Newnes, Elsevier - 2004

[42] Ingo Wol - *Coplanar Microwave Integrated Circuits* - John Wiley & Sons - 2006

[43] I. J. Bahl, D. K. Trivedi - *A Designer's Guide to Microstrip Line* - Microwaves - Vol.16 - May, 1977

[44] Ingo Wolff - *Coplanar Microwave Integrated Circuits* - John Wiley & Sons - 2006

[45] G. L. Matthaei, Leo Young, E. M. T. Jones - *Design of Microwave Filters* - Stanford Research Institute - 1963

[46] Jia-Sheng Hong, M. J. Lancaster - *Microstrip Filters for RF Microwave Applications* - John Wiley & Sons - 2001

[47] G. C. Temes, S. K. Mitra - *Modern Filter Theory and Design* - Wiley, New York - 1973is

[48] J. D. Rhodes - *Theory of Electrical Filters* - Wiley, New York - 1976

[49] M. Piat. - *Review of detector R&D for CMB polarisation observations* - Proc. 43ème Rencontres de Moriond, La Thuile, Italie, 15-22 mars 2008

[50] L. Thourel - *Les Antennes* - Cepadues Editions - 1990

[51] K. Rohlfs, T. L. Wilson - *Tools of Radio Astronomy* - Springer - Second Edition

[52] Constantine A. Balanis - *Antenna Theory* - John Wiley & Sons - 2005

[53] H. Booker - *Slot Aerials and Their Relation to Complementary Wire Aerials* - J. Inst. Elect. Eng. - 1946

[54] C. Jordan, K. Balmain - *Electromagnetic Waves and Radiating Systems* - Prentice-Hall INC - Second Edition

[55] N. Behdad, K. Sarabandi - *A Wide Band Slot Antenna Design Employing a Fictitious Short Circuit Concept* - IEEE transactions on Antennas and Propagation - 2005

[56] A. C. Rose-Innes, E. H. Rhoderick - *Introduction to Superconductivity* - Pergamon Press - 1978

[57] G. Stojanovic, L. Živanov, M. Damjanovic - *Compact Form of Expressions for Inductance Calculation of Meander Inductors* - Serbian Journal of Electrical Engineering - Vol. 1, No. 3, November 2004, 57 - 68

[58] W. H. Hayt, J. E. Kemmerly - *Engineering Circuit Analysis* - McGraw-Hill - 1971

[59] Richard C. Dorf, James A. Svoboda - *Introduction to Electric Circuit* - Wiley - 1996

[60] P.J. Ford, G.A. Saunders - *The Rise of the Superconductors* - CRC Press - 2004

[61] J. Bardeen, N. Cooper, R. Schrieffer - *Theory of Superconductivity* - Physical review volume 108 - 1957

[62] H. London - *The High-Frequency Resistance of Superconducting Tin* - 1940

[63] N. W. Ashcroft, N. D. Mermin - *Solid State Physics* - Holt, Rinehart & Winston - 1976

[64] Martino Calvo - *Development of Kinetic Inductance Detectors for the study of the Cosmic Microwave Background Polarization* - PhD Thesis - Università degli Studi di Roma "La Sapienza" - 2008

[65] Charles P. Poole, Horacio A. Farach, Richard A. Creswick, Ruslan Prozorov - *Superconductivity* - Elsevier - 2007

[66] F. London, H. London - *The Electromagnetic Equations of the Supraconductor* - Proceedings of the Royal Society of London Series - 1935 - 10.1098/rspa.1935.0048

[67] C. Kittel - *Introduction to Solid State Physics* - John Wiley & Sons - 2005

[68] M. Tinkham - *Introduction to Superconductivity* - 2° Ed. - Dover Publications - 1996

[69] D. Mattis, J. Bardeen - *Theory of the anomalous skin effect in normal and superconducting metals* - Physical review 111, 412 - 1958

[70] P. Turneaure, J. Halbritter, A. Schwettman - *The Surface Impedance of Superconductors and Normal Conductors: The Mattis-Bardeen Theory* - Journal of Superconductivity, Vol. 4, No. 5 - 1991

[71] David R. Tilley, John Tilley - *Superfluidity and Superconductivity* - Institute of Physics Publishing Bristol and Philadelphia - 1990

[72] J. Gao - *The physics of superconducting microwave resonators* - PhD thesis, Caltech - 2008

[73] S. Kaplan et al. - *Quasiparticle and phonon lifetimes in superconductors* - Phys. Rev. B 14, 4854–4873 - 1976

[74] J. Janssen - *Multiwavelength Observations of Active Galactic Nuclei* - PhD Thesis, Delft - 2017

[75] M. Rosch - *Development of lumped Element Kinetic inductance Detectors for mm-wave Astronomy at the IRAM 30 m Telescope* - PhD Thesis, KIT - 2013

[76] Simon Doyle - *Lumped Element Kinetic Inductance Detectors* - PhD Thesis - Cardiff University - 2008

[77] A. B. Pippard - *The Physics of Vibration* - Cambridge University Press - 1978

[78] J. Baselmans, C. Yates, R. bardens, Y. lankwarden, J. gao, H. Hoevers, T. Klapwijk - *Noise and Sensitivity of Aluminum Kinetic Inductance Detectors for sub-mm Astronomy* - Journal of low temperature Physics - 2007

[79] A. V. Sergeev, V. V. Mitin, B. S. Karasik - *Ultrasensitive hot-electron kinetic-inductance Detectors Operating Well Below the Superconducting Transition* - Appl. Phys. Lett. 80, 817 - 2002 - doi: 10.1063/1.1445462

[80] P.J. de Visser, J.J.A. Baselmans, J. Bueno, N. Llombart, T.M. Klapwijk - *Fluctuations in the Electron System of a Superconductor Exposed to a Photon ?ux* - ArXiv:1306.4238v1

[81] O. Noroozian, J. Gao, J. Zmuidzinas, H. G. LeDuc, B. A. Mazin - *Two-level System Noise Reduction for Microwave Kinetic Inductance Detectors* - arXiv:0909.2060

[82] S. Kumar, J. Gao, J. Zmuidzinas, B. A. Mazin, H. G. Leduc, and P. K. Day - *Temperature Dependence of the Frequency and Noise of Superconducting Coplanar Waveguide Resonators* - Applied Physics Letters 92 123503 - 2008

[83] R. Barends - *Photon-detecting Superconducting Resonators* - PhD Thesis, Delft - 2009

[84] L. J. Swenson, P. K. Day, B. H. Eom, H. G. Leduc, N. Llombart, C. M. McKenney, O. Noroozian, J. Zmuidzinas - *Operation of a Titanium Nitride Superconducting Microresonator Detector in the Nonlinear Regime* - arXiv:1305.4281 - 2013

[85] A. Bruno, G. de Lange, S. Asaad, K. L. Van der Enden, N. K. Langford, L. DiCarlo - *Reducing Intrinsic Loss in Superconducting Resonators by Surface Treatment and Deep Etching of Silicon Substrates* - arXiv:1502.04082 - 2015

[86] J. Zmuidzinas - *Superconducting Microresonators: Physics and Applications* - Annu. Rev. Condens. Matter Phys. 2012.3:169-214 - 2012

[87] P. J. de Visser, S. Withington, D. J. Goldie - *Readout-power Heating and Hysteretic Switching Between Thermal Quasiparticle States in Kinetic Inductance Detectors* - Journal of Applied Physics 108, 114504 - 2010

[88] R. Pöpel - *Surface Impedance and Reflectivity of Superconductors* - Journal of Applied Physics 66 , 5950 (1989); doi: 10.1063/1.343622

[89] B. Mazin - *Microwave Kinetic Inductance Detectors* - PhD Thesis, Caltech - 2004

[90] P. De Visser - *Quasiparticle Dynamics in Aluminium Superconducting Microwave Resonators* - PhD Thesis, Delft - 2014

[91] T. Weiland - *Time Domain Electromagnetic Field Computation with Finite Difference Methods* - International journal of Numerical Modelling, Vol. 9, 295 - 1996

[92] CST studio Suite Manual

[93] J. C. Rautio, R. F. Harrington - *An Electromagnetic Time-Harmonic Analysis of Shielded Microstrip Circuits* - IEEE Transaction on microwave theory, vol. 35 - 1987

[94] Sonnet software user manual

[95] A. Monfardini et al. - *NIKA: A millimeter-wave kinetic inductance camera* - A&A, 521 (2010) A29; doi.org/10.1051/0004-6361/201014727

[96] Sami Franssila - *Introduction to MicroFabrication* - Jhon Wiley & Sons - 2004

[97] www.dupont.com

[98] A. Catalano et all. - *Performance and calibration of the NIKA camera at the IRAM 30 m telescope* - arXiv:1402.0260 [astro-ph.IM] - 2014

[99] A. Monfardini et al. - *A Dual-band Millimeter-wave Kinetic Inductance Camera for the IRAM 30 m Telescope* - The Astrophysical Journal Supplement, Volume 194, Issue 2, article id. 24 - 2011

[100] O. Bourrion et al. - *Electronics and data acquisition demonstrator for a kinetic inductance camera* - arXiv:1102.1314v3 [astro-ph.IM] - 2011

[101] Thomas Durand - *Réalisation d'un interféromètre de Martin-Puplett pour le développement d'une caméra bolométrique* - Thesis, Institut NEEL - tel.archives-ouvertes.fr/tel-00181020 - 2007

[102] A. Larsen, H. D. Jensen, J. Mygind - *Self-Induced Steps in a Small Josephson Junction Strongly Coupled to a Multimode Resonator* - Physical Review B, Vol. 43, N. 13 - 1 May 1991

[103] M. Salez, F. Boussaha - *Fluxon modes and phase-locking at 600 GHz in superconducting tunnel junction nonuniform arrays* - Journal of Applied Physics 107, 013908 (2010); doi: 10.1063/1.3270403

[104] M. Salez, F. Boussaha - *Interference filter properties of nonuniform Josephson junction arrays* - Journal of Applied Physics 102, 083904 (2007); doi: 10.1063/1.2796108